Gelatin-based hydrogel foams – morphology and polymer functionality

Von der Fakultät Chemie der Universität Stuttgart
zur Erlangung der Würde einer Doktorin der Chemie (Dr. rer. nat.)
genehmigte Abhandlung

Vorgelegt von
Friederike Dehli
aus Fellbach

Hauptberichterin: Prof. Dr. Cosima Stubenrauch
Mitberichter: Prof. Dr. Andrea Barbetta
Prüfungsvorsitz: Prof. Dr. Bernhard Hauer

Tag der mündlichen Prüfung: 19.07.2022

Institut für Physikalische Chemie
der Universität Stuttgart
2022

Acknowledgements

First and foremost, I wish to thank *Prof. Dr. Cosima Stubenrauch* for giving me the opportunity to pursue a Ph.D. in her group and to work on this topic. Without her guidance and support, would not have been possible. Thanks to the investments she made into my work, I was able to learn so much and improve as a scientist. I am also grateful for the opportunity to attend several national and international conferences.

Moreover, I want to thank *Prof. Dr. Andrea Barbetta* for being the second examiner of my thesis and *Prof. Dr. Bernhard Hauer* for being the chair of the examination board.

Sincere thanks to *Dr. Alexander Southan* for all the meetings and discussions. Without his guidance and scientific advice, this work would not look the same.

I also wish to thank *Dr. Wiebke Drenckhan* for her guidance regarding foam physics and for being the co-author of one of my publications.

I also want to thank *Dr. Melanie Dettling* and *Sarah Schmidt* for their help with the gelatin modification. Furthermore, I want to thank *Dr. Stefan Eisler* and *Melanie Noack* for their support and assistance with the LSM. Special thanks to *Dr. Jan Guzowski* and *Dr. Marco Costantini* for welcoming me in their group and for fabricating the microfluidic chip. Furthermore, I want to thank *Dr. Nihal Vrana* for welcoming me in his group, and *Celine Muller* and *Emine Berber* for performing preliminary cell culture experiments with my samples.

Warm thanks to *Hailey Poole* and *Yanina Dreer*, who contributed to my work by doing a research internship on my project. Further thanks goes to *Diana Zauser*, *Gabriele Bräuning*, and the *mechanical* and *electrical workshop* for their support in the laboratories. I also want to thank *Dr. Herbert Dilger* and *Beate Holley* for taking care of the administrative issues.

I also want to thank all members of the *Stubenrauch* and *Sottmann* group for the nice working atmosphere, the shared lunch breaks, and scientific discussions. Special thanks also to *Philipp Menold*, *Ke Peng*, and *Tamara Schad*, who shared the office with me.

I am also very grateful to my friends and family, who supported me during this time. Thank you for your encouragement, understanding, and support. A special and heartfelt thank you to *Fabian Moczko*.

Abstract

Two different aspects that influence the properties of hydrogel foams are the morphology and the polymer functionality. In this work, both aspects were studied for hydrogel foams based on gelatin methacryloyl (GM) to broaden their tailorability and applicability.

To tailor the morphology, the pore opening diameters of the hydrogel foams were adjusted. For this purpose, the gas fraction and the bubble diameter during microfluidic foaming were decoupled using two complementary methods. We showed that the pore opening diameter $\langle d_p \rangle$ could be varied independently of the pore diameter $\langle D_p \rangle$, obtaining $\langle d_p \rangle / \langle D_p \rangle$ ratios between 0.14 and 0.28. A comparison of the experimentally obtained data with theoretical predictions for thin film diameter in liquid foams revealed that the experimental values lie between predictions for ordered and disordered foams. For low gas fractions, the obtained data agreed with predictions for disordered foams, suggesting that the pore opening diameters are determined by the thin film diameters in liquid foams.

Furthermore, the sorption and release of the cationic model drug metoprolol on GM-based hydrogel foams was characterized and compared to non-foamed samples. When examining equilibrium state, i.e. measuring sorption and release isotherms, no influence of the morphology was found. A maximum sorption capacity of ~ 530 µmol g^{-1} was obtained in both cases. Furthermore, the materials could be fully regenerated by immersion in a salt solution. When studying non-equilibrium state, i.e. measuring sorption and release kinetics, the morphology had a pronounced influence. Up to 10 times higher rate coefficients were obtained for the foamed samples, which can be explained by shorter diffusion paths in foamed hydrogels. Moreover, the rate coefficients for the foamed and the non-foamed samples depended on the ion concentration in the sorption or release medium.

In addition, we synthesized a new gelatin derivative by biotinylating the carboxyl groups in GM in a two-step procedure. Successful biotinylation was confirmed by TNBS- and HABA/Avidin assays as well as by ^{1}H-NMR. After having prepared hydrogel foams based on the biotinylated GM, the streptavidin-conjugated model enzyme horseradish peroxidase (Strep-HRP) was immobilized via the biotin-streptavidin interaction. A comparison of the substrate conversion rate r_A of Strep-HRP immobilized on foamed and non-foamed hydrogels showed that r_A is 12 times higher in foamed hydrogels. This suggests that r_A can be adjusted by tailoring the sample morphology.

Kurzzusammenfassung

Zwei verschiedene Aspekte, die die Eigenschaften von Hydrogelschäumen beeinflussen, sind die Morphologie und die Polymerfunktionalität. In dieser Arbeit wurden beide Aspekte für Hydrogelschäume auf Basis von Gelatine-Methacryloyl (GM) untersucht, um die Anwendbarkeit dieser Materialien zu erweitern.

Zur genauen Einstellung der Morphologie wurden die Porenöffnungsdurchmesser der Hydrogelschäume variiert. Dazu wurden Gasanteil und Blasendurchmesser während der Herstellung flüssiger Schaumtemplate entkoppelt, wozu zwei komplementäre Methoden verwendet wurden. Es konnte gezeigt werden, dass der Porenöffnungsdurchmesser $\langle d_p \rangle$ unabhängig vom Porendurchmesser $\langle D_p \rangle$ variiert werden kann, wodurch sich $\langle d_p \rangle / \langle D_p \rangle$-Verhältnisse zwischen 0.14 und 0.28 ergaben. Ein Vergleich der experimentell gewonnenen Daten mit theoretischen Vorhersagen für die Filmdurchmesser in flüssigen Schäumen ergab, dass die experimentellen Werte zwischen den Vorhersagen für geordnete und ungeordnete Schäume liegen. Bei niedrigen Gasanteilen stimmten die erhaltenen Daten gut mit den Vorhersagen für ungeordnete Schäume überein, was darauf hindeutet, dass die Porenöffnungsdurchmesser durch die Dünnschichtdurchmesser in flüssigen Schäumen bestimmt werden.

Darüber hinaus wurde die Sorption und Freisetzung des kationischen Modellwirkstoffs Metoprolol an GM-basierten Hydrogelschäumen charakterisiert und mit ungeschäumten Proben verglichen. Bei der Untersuchung des Gleichgewichtszustands, d. h. der Messung von Sorptions- und Freisetzungsisothermen, wurde kein Einfluss der Morphologie festgestellt. Für geschäumte und ungeschäumte Proben wurde dabei eine maximale Sorptionskapazität von ~ 530 µmol g^{-1} erhalten. Außerdem konnten die Materialien durch Immersion in eine Salzlösung vollständig regeneriert werden. Bei der Untersuchung des Nicht-Gleichgewichtszustands, d. h. der Messung der Sorptions- und Freisetzungskinetiken, hatte die Morphologie dagegen einen deutlichen Einfluss. Es wurden bis zu 10-fach höhere Geschwindigkeitskoeffizienten für die geschäumten Proben erhalten, was durch kürzere Diffusionswege in geschäumten Proben erklärt werden kann. Außerdem konnte gezeigt werden, dass die Geschwindigkeitskoeffizienten für geschäumte und ungeschäumte Proben durch die Ionenkonzentration im Sorptions- oder Freisetzungsmedium beeinflusst wird.

Darüber hinaus wurde ein neues Gelatinederivat durch Biotinylierung der Carboxylgruppen in GM synthetisiert. Die erfolgreiche Biotinylierung des Polymers wurde durch TNBS- und HABA/Avidin-Assays sowie durch ^{1}H-NMR bestätigt. Nach der Herstellung von Hydrogelschäumen auf Basis von biotinylierter GM wurde das Streptavidin-konjugierte Modellenzym Meerrettichperoxidase (Strep-HRP) über die Biotin-Streptavidin-Interaktion immobilisiert. Ein Vergleich der Substratumwandlungsraten r_A zwischen geschäumten und ungeschäumten Hydrogelen zeigte, dass r_A in geschäumten Hydrogelen 12-fach höher ist. Dies deutet darauf hin, dass r_A durch die Anpassung der Probenmorphologie eingestellt werden kann.

Erklärung über die Eigenständigkeit der Dissertation

Ich versichere, dass ich die vorliegende Arbeit mit dem Titel

Gelatin-based hydrogel foams – morphology and polymer functionality

selbständig verfasst und keine anderen als die angegebenen Quellen und Hilfsmittel benutzt habe; aus fremden Quellen entnommene Passagen und Gedanken sind als solche kenntlich gemacht.

Declaration of Authorship

I hereby certify that the dissertation entitled

Gelatin-based hydrogel foams – morphology and polymer functionality

is entirely my own work except where otherwise indicated. Passages and ideas from other sources have been clearly indicated.

Name/Name: _____

Unterschrift/Signed: _____

Datum/Date: _____

Publication List

1. Dehli, F.; Southan, A.; Drenckhan, W.; Stubenrauch, C. Tailoring and Visualising Pore Openings in Gelatin-Based Hydrogel Foams. *J. Colloid Interface Sci.* **2021**, *588*, 326–335. https://doi.org/10.1016/j.jcis.2020.12.064.
Impact Factor 2021: 8.1

2. Dehli, F.; Poole, H.; Stubenrauch, C.; Southan, A. Gelatin-Based Foamed and Non-Foamed Hydrogels for Sorption and Controlled Release of Metoprolol. *ACS Appl. Polym. Mater.* **2021**, *3* (11), 5674–5682. https://doi.org/10.1021/acsapm.1c00968.
Impact Factor: 4.0

3. Dehli, F.; Stubenrauch, C.; Southan, A. New gelatin-based hydrogel foams for improved substrate conversion of immobilized horseradish peroxidase. *Macrom. Biosci.*, **2022**, 2200139. https://doi.org/10.1002/mabi.202200139.
Impact Factor: 5.8

Contribution report

1. Responsible for writing the manuscript and for all experimental work. The co-authors revised the manuscript

2. Responsible for writing the manuscript and for most of the experimental work. The sorption isotherms for foamed and non-foamed samples, as well as the release isotherm for non-foamed samples, and one replicate of the sorption kinetics were measured by Hailey Poole during an internship which was supervised by Friederike Dehli. Cosima Stubenrauch and Alexander Southan revised the manuscript.

3. Responsible for writing the manuscript and all experimental work. The co-authors revised the manuscript.

List of Publications not included in this PhD Thesis

I. Highly Ordered Gelatin Methacryloyl Hydrogel Foams with Tunable Pore Size
Friederike Dehli, Lisa Rebers, Cosima Stubenrauch, Alexander Southan
Biomacromolecules **2019**, *20*, 2666-2674. https://doi.org/10.1021/acs.biomac.9b00433.

II. Monodisperse Liquid Foams via Membrane Foaming
Laura Carballido, Miriam Lucia Dabrowski, Friederike Dehli, Lukas Koch, Cosima Stubenrauch
Journal of Colloid and Interface Science **2020,** *568*, 46–53.
http://doi.org/10.1016/j.jcis.2020.02.036.

Table of Contents

Nomenclature

Abbreviations

ABTS	2,2′-Azino-di(3-ethylbenzthiazolin-6-sulfonic acid)
BSA	bovine serum albumin
EDA	ethylene diamine
EDC	1-ethyl-3-(3-dimethylaminopropyl)carbodiimide hydrochloride
EDS	equilibrium degree of swelling
FCC	face centered cubic
Gly	glycine
GM	gelatin methacryloyl
GM10	gelatin methacryloyl synthesized by adding a 10-fold excess of methacrylic anhydride with respect to free amino groups in gelatin
GM10E	gelatin methacryloyl aminoethyl
GM10EB	biotinylated gelatin methacryloyl aminoethyl
HABA	4'-hydroxyazobenzene-2 carboxylic acid
IEP	isoelectric point
LAP	lithium phenyl-2,4,6-trimethylbenzoylphosphinate
MAAnh	methacrylic anhydride
MMP	matrix metalloproteinase

NMR	nuclear magnetic resonance
PBS	phosphate buffered saline
pH	potentia hydrogenii
p-HEMA	poly(2-hydroxyethyl)methacrylate
RGD	arginine-glycine-aspartic acid
rpm	revolutions per minute
SEM	scanning electron microscope
SDS	sodium dodecyl sulfate
Strep-HRP	streptavidin-conjugated horseradish peroxidase
TMSP	sodium 3-trimethylsilylpropionate-2,2,3,3-d_4
TNBS	2,4,6-trinitrobenzenesulfonic acid
UV/VIS	ultraviolet-visible
wt %	weight percent
µ-CT	micro-computed tomography

Latin symbols

A	surface area
Bo	Bond number
Ca	Capillary number
c	concentration
c_0	initial solute concentration
$c_{e,a}$	equilibrium solute concentration after sorption

$c_{e,d}$	equilibrium solute concentration after release
c_t	solute concentration at time t
$c_{t,d}$	solute concentration in the release medium at time t
D	diffusion coefficient
D_b	bubble diameter
D_h	diffusion coefficient within hydrogel matrix
D_p	pore diameter
D_w	diffusion coefficient in water
d	mean squared displacement
d_b	contact zone diameter
d_{max}	maximum diffusion path
d_p	pore opening diameter
DB	biotin content
DE	amino group content
DM	methacryloyl group content
G'	storage modulus
g	gravitational acceleration
H	mean curvature
$\tilde{h}$	reduced foam height
J	diffusion flux
K	compressive modulus
K_s	equilibrium constant
k_a	sorption rate coefficient

k_r	release rate coefficient
m	mass
n	amount of substance
p	gas pressure during microfluidic foaming
p_c	capillary pressure
p_g	gas pressure
p_l	liquid pressure
PDI	polydispersity index
Q_g	gas flow rate
Q_l	liquid flow rate
$q_{e,a}$	amount of sorbed solutes per sample mass in equilibrium
$q_{e,d}$	amount of released solute per sample mass in equilibrium
q_{max}	maximum sorption capacity
$q_{t,a}$	amount of sorbed solute per sample mass at time t
$q_{t,d}$	amount of sorbed solute per sample mass at time t during release
R	bubble radius
r_A	substrate conversion rate
Re	Reynolds number
t	time
U	energy
V	volume

V_a	volume of sorption medium
V_d	volume of release medium
V_f	free volume
v	velocity
v_L	liquid flow rate
v_A	liquid flow rate of additional polymer solution
We	Weber number
x	spatial position

Greek symbols

γ	surface tension
η	viscosity
ρ	density
τ	characteristic diffusion time
ϕ	gas fraction
ϕ_c	critical gas fraction
φ	liquid fraction

1. Introduction

1.1 Motivation

Whether in packaging, insulation, or protective gear, macroporous materials are widely used in our daily life [Lee07]. One subgroup of macroporous materials are hydrogel foams which are defined by a continuous phase consisting of a hydrogel matrix, and a dispersed phase consisting of a gas or a liquid [Dje21]. Due to the unique combination of the porous foam structure with the high water content of a hydrogel, these materials have gained increasing attention in many research fields, including tissue engineering [Bar08, Lin11], drug delivery [Gup10], or wastewater treatment [Wu20]. In tissue engineering, for example, the hydrogel matrix ensures biocompatibility, while the porous structure enables an increased transport of oxygen and nutrients. One major challenge in these application fields is the generation of hydrogel foams with defined properties, i.e. tailor-made hydrogel foams. The properties of hydrogel foams generally depend on two different length scales: (1) the microscale, which is defined by the morphology of the hydrogel foam, and (2) the nanoscale, which is defined by the network structure and composition of the hydrogel matrix (Figure 1.1).

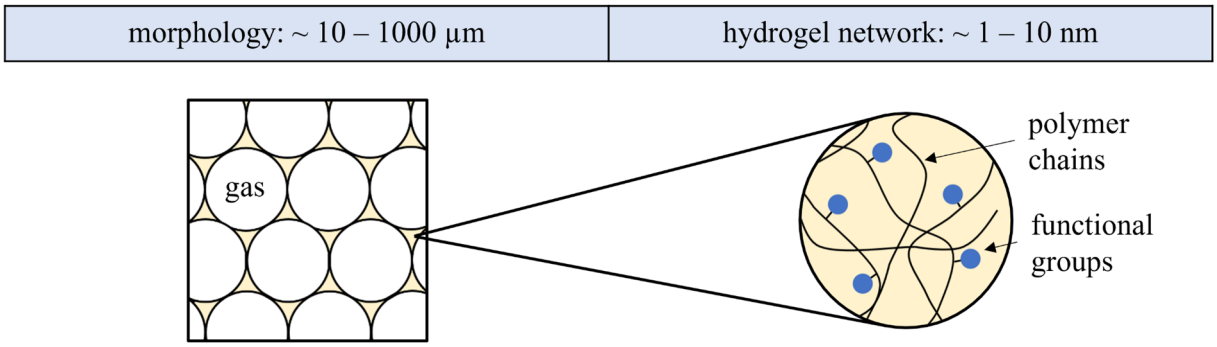

Figure 1.1: (left) Schematic drawing of a hydrogel foam. The hydrogel matrix is drawn in yellow, whereas the gas-filled pores are white. (right) Schematic drawing of the hydrogel network structure. The black lines represent the polymer chains and the blue circles represent the functional groups.

The morphology of a hydrogel foam is defined by its structural parameters, namely the pore diameter, the pore diameter distribution, and the pore connectivity. The influence of these parameters was examined in e.g. tissue engineering, where relations between the distribution and differentiation of cells and the pore diameter and pore diameter distribution were found in various studies [Lee13, Cos16]. Both the pore diameter and pore diameter distribution of

hydrogel foams can be adjusted by liquid foam templating via microfluidic foaming. In this approach, a liquid foam template based on a hydrogel precursor solution is generated and subsequently solidified by e.g. homo- or copolymerization of monomers [Hsi16] or cross-linking of polymer chains with reactive groups [And17]. During this process, a three-dimensional hydrogel network is generated. Figure 1.2 shows a schematic drawing of foam templating via microfluidic foaming.

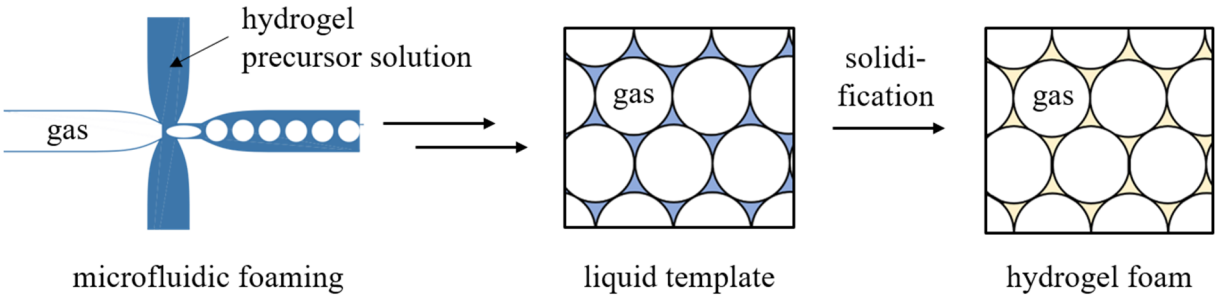

Figure 1.2: Generation of hydrogel foams via liquid foam templating using microfluidic foaming. During solidification, the structure of the liquid foam template is retained. The blue areas represent the hydrogel precursor solution, while the yellow areas represent the cross-linked hydrogel matrix. The gas phase is drawn in white.

The solidification of the liquid foam template usually causes a rupture of the thin films between neighboring bubbles, which leads to the formation of pore openings. Thus, an interconnected porous structure that can also be filled with an aqueous solution is generated. As the structure of the liquid template is retained during solidification, the structure of the hydrogel foam can be adjusted by controlling the structure of the liquid template. A powerful tool to control the structure of the liquid template is microfluidic foaming, which was used to generate hydrogel foams with a defined pore diameter [Cos15, And17, Deh19], a controlled degree of polydispersity [And18a], or a gradient in pore diameter [Cos19]. However, control over the pore openings independent of the pore diameter is still a challenge.

Besides the morphology, the network structure and composition of the hydrogel matrix also play an important role when generating hydrogel foams with defined properties. The network structure and composition depend primarily on the type of polymer, as well as the type and density of cross-linking [Bas20], or the presence of specific functional groups. The influence of the network structure on the hydrogel foam properties was for instance demonstrated for hydrogel foams based on poly(acrylamide), for which a direct correlation between the degree of cross-linking and the osteogenesis of mesenchymal stromal cells was found [Hsi16]. In addition, the influence of functional groups within the hydrogel matrix was studied for

hydrogels based on chitosan, where a different swelling behavior was found depending on the charge of the functional groups [Pie09]. Furthermore, it was shown that the sorption of cholate ions on hydrogels based on quaternary ammonium-modified dextran depends on the structure of the functional groups [Nic00] in the hydrogel matrix. Specific functional groups can either be inherently present in the polymer and in the cross-linker, respectively, or can be introduced by additional modification.

In this thesis, both the morphology and the effects of the polymer functionality are studied for hydrogel foams based on gelatin methacryloyl (GM). GM is a derivative of the biopolymer gelatin, which is synthesized by modifying amine and hydroxyl groups in polypeptide side chains of gelatin with methacrylic anhydride [Bul00]. Figure 1.3 shows a drawing of methacryloylated gelatin.

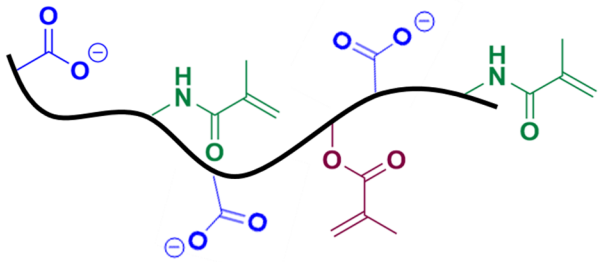

Figure 1.3: Schematic drawing of gelatin methacryloyl (GM). Reprinted with permission from [Deh21b]. Copyright 2021 American Chemical Society.

In presence of a suitable photo initiator, the methacryloyl groups can be radically cross-linked by irradiation with UV light to form hydrogels. The modification of gelatin also results in a decreased viscosity compared to non-modified gelatin [Hoc12], which facilitates foam production via microfluidics and allows for the solubilization of an increased amount of polymer in the continuous phase. Moreover, GM is both biodegradable [Ste02] and biocompatible [Sir13], which makes hydrogel foams based on GM attractive for many applications. During methacryloylation, the carboxyl groups of gelatin are unaffected and are thus available for further chemical modification [Cla19]. Based on a previous study, which deals with adjusting the pore diameter of GM-based hydrogel foams [Deh19], this work seeks to further expand the tailorability and applicability of these materials by (1) adjusting the pore opening diameters in GM hydrogel foams, (2) studying the sorption and release of a cationic drug on GM hydrogel foams, which most likely occurs on the inherently present carboxyl groups of GM, and (3) chemically modifying the carboxyl groups to add another dimension of functionality to the hydrogel foams.

1.2 Task Description

In order to address both the morphology and the polymer functionality of gelatin-based hydrogel foams, this thesis is divided into three parts, each focusing on a different feature of the material.

In the first part, the morphology of the hydrogel foam is further tailored by adjusting the pore opening diameters. To tackle this goal, a method to decouple the gas fraction and the bubble diameter during foam production via microfluidics has to be developed. This is because both the pore opening diameter and the pore diameter of a hydrogel foam are connected to the gas fraction of the liquid template when producing the templates via microfluidics. Furthermore, a suitable method for characterizing the pore openings of hydrogel foams in their swollen equilibrium state has to be found. In addition, the obtained values for the pore opening diameters are compared with theoretical predictions for thin film diameters in the liquid state, to examine whether there is a direct relation between these parameters.

In the second part, the properties entailed by the functional groups of GM are examined. For this purpose, the sorption and release of a cationic model drug, which, according to our hypothesis, occurs on the carboxyl groups of GM, is investigated. A suitable model drug is metoprolol, whose chemical structure is depicted in Figure 1.4 (left). The sorption behavior of metoprolol is studied in both equilibrium and non-equilibrium conditions by measuring sorption isotherms and kinetics. Furthermore, the release of the model drug is examined. Equally to the sorption, the release behavior is examined by measuring release isotherms and kinetics. To elucidate the role of the hydrogel morphology, the sorption and release behavior of foamed hydrogels with a defined pore diameter is compared to the sorption and release behavior of non-foamed samples.

In the third part, additional functionality is introduced to the hydrogel foams by modifying the carboxyl groups. A suitable functional group for this purpose is biotin, as this might allow for building a bioconjugation platform via the biotin-streptavidin interaction. Figure 1.4 (right) depicts the chemical structure of biotin.

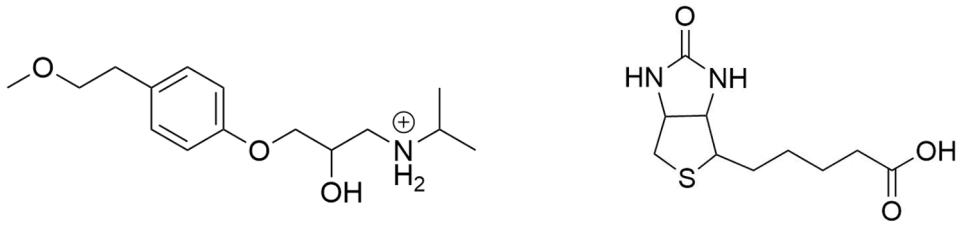

Figure 1.4: Chemical structure of metoprolol (left) and biotin (right).

In order to introduce biotin to the polymer chains, a suitable functionalization strategy has to be developed. Moreover, the amount of functionalized carboxyl groups has to be quantified. After having functionalized and characterized the polymer, hydrogel foams have to be produced via microfluidic foaming. The potential of these materials for building a bioconjugation platform is examined by immobilizing the streptavidin-conjugated model enzyme horseradish peroxidase (Strep-HRP) via the biotin-streptavidin interaction. In addition to that, the substrate conversion rate of Strep-HRP immobilized on functionalized hydrogel foams is compared to the substrate conversion rate of enzymes immobilized on non-foamed samples to examine the influence of the hydrogel morphology. Figure 1.5 shows the different dimensions of hydrogel foams studied in this thesis.

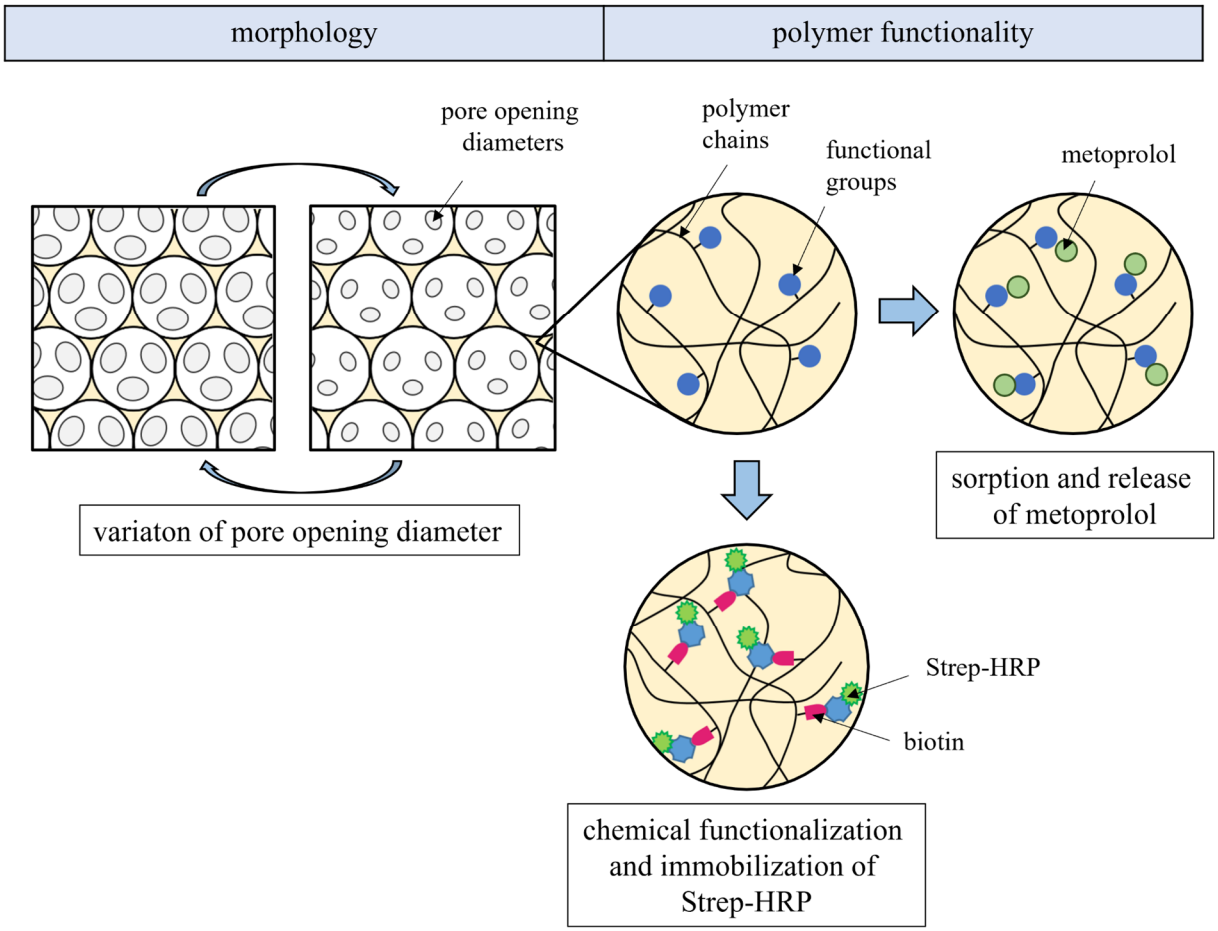

Figure 1.5: Schematic drawing of the dimensions of hydrogel foams studied in this thesis. The grey circles represent the pore openings, while the white circles represent the pores. The cross-linked hydrogel matrix is drawn in yellow. The black lines represent the polymer chains with functional groups drawn as blue circles. The green circles represent metoprolol, while the pink shapes represent biotin. The green and blue shapes represent streptavidin-conjugated horse-radish peroxidase.

2. Theoretical Background

2.1 Hydrogels

2.1.1 Definition

Typical hydrogels are polymeric materials that consist of a three-dimensional cross-linked hydrophilic polymer network [Hoa08]. Due to the hydrophilic network, hydrogels can take up and retain large amounts of aqueous media [Ahm15, Sla09]. Hydrogels can be distinguished according to different criteria, such as the origin of their building blocks or the nature of cross-linkages. Regarding the origin of their building blocks, hydrogels can be synthetic or natural hydrogels [Dje21]. Synthetic hydrogels are usually based on polymers of non-renewable origin such as poly(vinyl alcohol) [Zha12], poly(acrylamide) [Kim10], or poly(hydroxyl ethyl methacrylate) [Rat72]. By contrast, natural hydrogels are based on plant- or animal-derived biopolymers such as gelatin [Hoc12], hyaluronic acid [Bur11], or xanthan [Bue13]. Furthermore, hybrid hydrogels can be generated by combining synthetic and natural polymers [Wan99]. Regarding the nature of cross-linkages, hydrogels can be physical and chemical hydrogels. Physical cross-linkages in hydrogels are formed by transient bonds [Var17], which result from physical interactions such as hydrogen bonds, hydrophobic interactions, ionic interactions, crystallites, or entanglements [Dje21]. The biggest advantage of physically cross-linked hydrogels is that the network formation is reversible, which allows, for example, producing self-healing materials [Zha12] or easy recycling [Men21]. However, the resulting materials are often not stable over a wide range of pH, ionic strength, or temperature, which strongly limits their application. By contrast, the cross-linkages in chemically cross-linked hydrogels are formed by covalent bonds and are therefore permanent. Chemically cross-linked hydrogels can be obtained by homo- or copolymerization of water-soluble monomers [Ahm15] or by directly cross-linking polymers with reactive groups [Klo16]. In the latter case, the cross-linking can either occur via a cross-linking agent that reacts with specific functional groups of the polymer [And17], or by polymerization of reactive side chains that are present within the polymer [Hoc13]. Figure 2.1 shows a schematic drawing of a physically and a chemically cross-linked hydrogel.

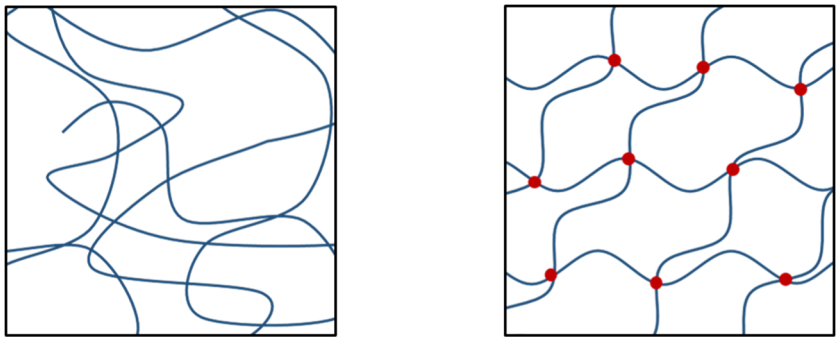

Figure 2.1: Schematic drawing of a physically (left) and chemically (right) cross-linked hydrogel.

The first application of hydrogels dates back to 1960 when hydrogels based on poly(hydroxyl ethyl methacrylate) were first used as materials for contact lenses [Wic60]. Since then, their application has continued to expand to fields like agriculture [Rud12], cosmetics [Mit20], or biomedicine [Par96]. Other application fields include the sorption and release of ions, or the immobilization of enzymes (see Sections 2.3 and 2.4). One challenge for all applications is the generation of biocompatible and biodegradable materials, preferably from renewable sources. Thus, hydrogels based on biopolymers such as chitosan [Ahs20], alginate [Aug06], or gelatin [Hoc12] are intensively examined.

2.1.2 Hydrogels based on gelatin

Gelatin: Gelatin is a mixture of proteins produced by partial hydrolysis of the biopolymer collagen [Bab96] with which it shares many similarities. Collagen is part of the natural extracellular matrix of animals [Alb02] and consists of polypeptide chains that self-assemble into triple-helical domains stabilized by hydrogen bonds. In order to form the characteristic triple helices, every third position in the polypeptide chain of collagen must be occupied with glycine [Tra71], which is the smallest proteinogenic amino acid. Consequently, the triple-helical domains of collagen consist of repetitive tripeptide units $(Gly\text{-}X\text{-}Y)_n$ [Ram98]. During the hydrolysis of collagen, the chemical bonds between and within the peptide chains are broken, resulting in the transformation of water-insoluble collagen to water-soluble gelatin [Bab96]. Gelatin is widely used in the field of biomaterials science as it contains asparagine-glycine-aspartic acid (RGD)-sequences, which are relevant for cell adhesion. Furthermore, it contains target sequences for matrix-metalloproteinases (MMP), which impart biodegradability [Ste02]. Depending on the hydrolysis conditions, two different types of gelatin can be

distinguished. Gelatin type A is produced by acidic hydrolysis, while gelatin type B is produced by basic hydrolysis. Due to the different hydrolysis conditions, gelatin type A and gelatin type B differ significantly in their charge patterns, which is also illustrated by their isoelectric points (IEPs). Gelatin type A has an IEP of 8.8, which closely resembles the IEP of native collagen. In contrast, gelatin type B has an IEP of 4.9 [Sew18]. This decrease is due to the basic hydrolysis conditions, under which the amino acids asparagine and glutamine are hydrolyzed to aspartic and glutamic acid [Bab96]. Consequently, additional negative charges are introduced to the polypeptide backbone.

Physical and chemical hydrogels based on gelatin: Aqueous solutions of both gelatin type A and gelatin type B can undergo thermo-reversible sol-gel transitions [Miy15, Sew18]. Upon cooling an aqueous gelatin solution, the polypeptide chains partially re-associate to the triple helix structure of collagen and form a physically cross-linked hydrogel. When increasing the temperature above the melting point of the hydrogel, the structure is disturbed due to the thermal motion of the polypeptide chains and the hydrogel starts to melt. The gelling, as well as the melting point of physically cross-linked gelatin hydrogels, strongly depends on the polymer concentration as well as the heating or the cooling rate. The melting point of a physical gelatin hydrogel with a mass fraction of 10 wt. % is 31 °C [Sew18]. Figure 2.2 shows a schematic drawing of the sol-gel transition of gelatin.

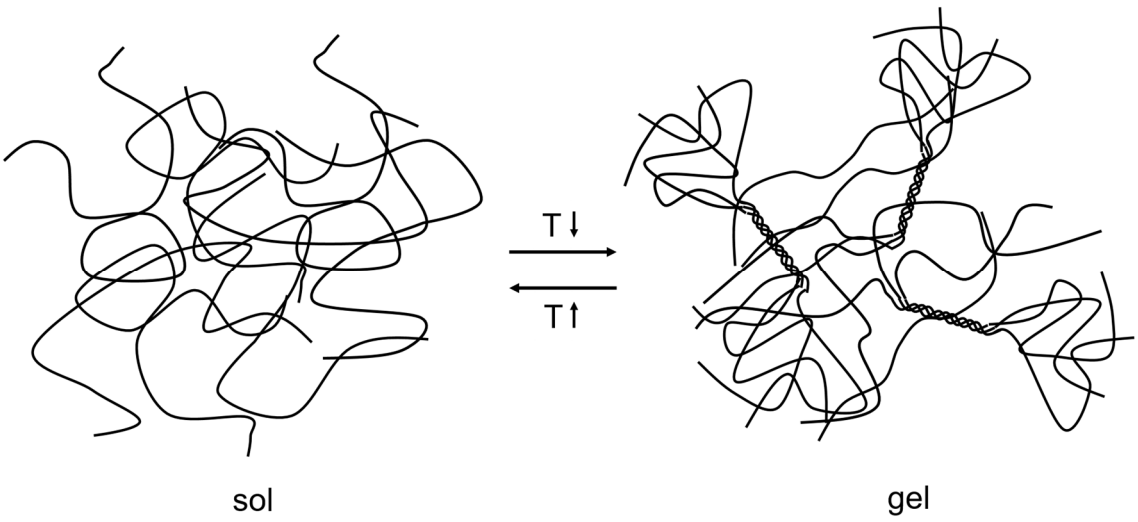

Figure 2.2: Schematic drawing of the sol-gel transition of gelatin. Upon cooling an aqueous gelatin solution (left), the polymer chains re-associate to triple helices (right).

Chemically cross-linked gelatin hydrogels can be generated by reaction of amino groups in amino acid side chains with cross-linkers such as e.g. 1-Ethyl-3-(3-dimethyl aminopropyl)

carbodiimide (EDC) [Bar09], genipin [Yao04], or glutaraldehyde [Big08]. As an alternative, gelatin can be chemically modified to introduce polymerizable groups into the polymer. One well-known example is methacryloylated gelatin (GM), which was first reported by van den Bulcke [Bul00]. GM is synthesized by the reaction of gelatin with methacrylic anhydride at a constant pH, resulting in methacryloylation of amino and hydroxy groups in polypeptide side chains [Cla18a]. The degree of substitution can be controlled by adjusting the amount of added methacrylic anhydride [Hoc12]. The reaction scheme for the synthesis of GM is shown in Figure 2.3.

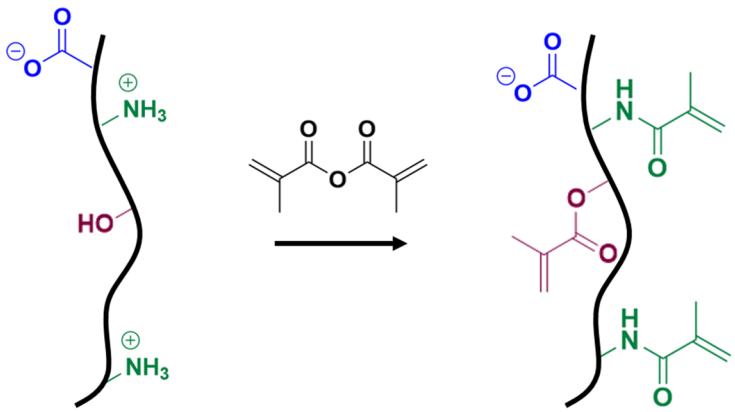

Figure 2.3: Synthesis of methacryloylated gelatin via methacryloylation of amine and hydroxyl residues in gelatin. Adapted with permission from [Deh21b]. Copyright 2021 American Chemical Society.

The methacryloylation of gelatin also results in a decreased IEP due to the conversion of the positively charged amino groups in lysine residues. For gelatin type A, an IEP of 4.5 is obtained, whereas an IEP of 4.1 is obtained for gelatin type B [Sew18]. Thus, GM is a polyanion at neutral pH, regardless of its source. During methacryloylation, the carboxylate groups of asparagine and glutamine acid residues in gelatin are unaffected and thus available for further modification. This has been used to prepare GM with an isoelectric point of 9.9 [Cla19], which was achieved via functionalization of the carboxyl groups with ethylenediamine.

The methacryloyl groups of GM can be cross-linked by radical polymerization in presence of a suitable initiator [Klo16]. Depending on the type of initiator, the cross-linking can be triggered thermally or photo-chemically. However, a photo-chemical initiation is widely preferred as it allows for spatio-temporal control of cross-linking. One example of a photo-initiator that is commonly used for cross-linking of GM is lithium phenyl-2,4,6-trimethylbenzoylphosphinate (LAP) [Mon18], whose maximum molar extinction coefficient is at 375 nm [Fai09]. Thus,

cross-linking can easily be triggered by irradiation with UV-A light. Compared to other commonly used UV-active photo-initiators such as Irgacure 2959, LAP has a much higher molar extinction coefficient [Fai09] and good water solubility [Maj91], which allows for solubilizing an increased amount of initiator. This is particularly important for cross-linking of thin structures. In this case, the inhibition of the cross-linking procedure by oxygen from the surrounding atmosphere can be circumvented by simply adding a larger amount of photo initiator. The cross-linking of methacryloyl groups and the chemical structure of LAP are shown in Figure 2.4.

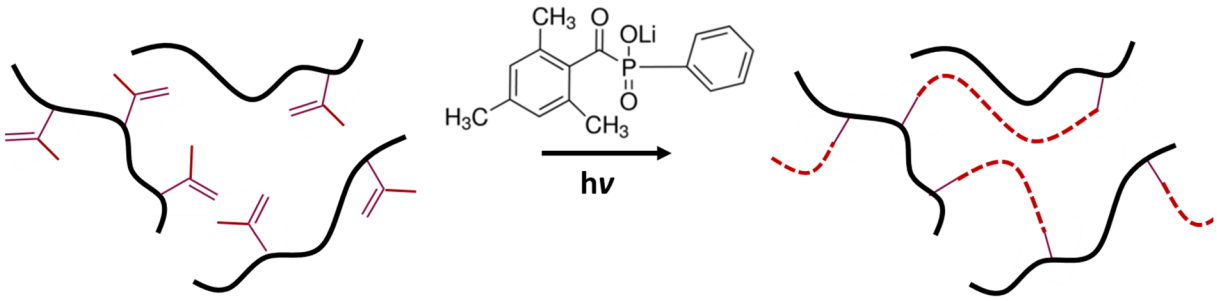

Figure 2.4: Photo-chemical cross-linking of GM in presence of LAP.

It has to be noted that the methacryloyl groups disturb interactions between the gelatin peptide chains, resulting in a reduced viscosity of aqueous solutions [Hoc13, Sew18]. Compared to non-modified gelatin, this allows handling of aqueous gelatin solutions with increased concentrations at room temperature. The properties of GM hydrogels strongly depend on the GM mass fraction and the degree of substitution. It was shown that the compressive modulus *K* and the storage modulus *G'* of GM hydrogels increase with increasing degree of substitution as well as increasing GM mass fraction [Che12, Nic10, Hoc12]. By contrast, the equilibrium swelling degree (EDS) of GM hydrogels decreases with increasing degree of substitution and mass fraction [Hoc12] which can be attributed to a decreased mesh size. It was also shown that in addition to chemical cross-linking, physical interactions in GM hydrogels affect the hydrogel properties. Regardless of the degree of substitution, increased compressive strengths σ_b were obtained when GM hydrogel precursor solutions were cooled before chemical cross-linking [Reb19]. The mechanical properties of GM hydrogels can also be adapted by varying the initiator concentration or the UV exposure time [Bul00]. GM hydrogels can be fabricated in various shapes and microstructures [Yin18, Nic10, Ald19]. Of particular interest are macroporous hydrogels, which are also known as hydrogel foams, since they combine the

unique properties of hydrogels with the large surface area and short diffusion lengths of a porous material. One method to generate GM hydrogel foams is liquid foam templating [Deh19].

2.2 Liquid foam templating for the generation of hydrogel foams

Liquid foam templating aims at generating solid foams by solidifying the continuous phase of a liquid foam template. During the solidification, the structure of the template is retained. Thus, control over the solid foam structure can be gained by adjusting the structure of the liquid foam template. In the following paragraph, the physical properties of liquid foams are outlined, followed by the generation of hydrogel foams via liquid foam templating. Finally, microfluidics for the generation of liquid foams is described.

2.2.1 Liquid foams

Key parameters of liquid foams: Liquid foams are dispersions of gas bubbles within a continuous liquid phase [Wea99], which are generated by either physical, chemical, or biological foaming methods. In physical foaming methods, bubbles are created by phase transitions or mechanical forces. Chemical foaming, on the other hand, is the result of gas release during chemical reactions [Hec98]. A well-known example of this is the generation of poly(urethane) foams [Zha13], during which CO_2 is released by the decomposition of isocyanides. In biological foaming, the gas is generated by microorganisms such as yeast [Uhl15]. What all these methods have in common is that they supply the energy that is required to generate an interface between the gas and the liquid. The least amount of energy U that is required to generate one bubble is defined as [Dre15]

$$U = \gamma {D_\mathrm{b}}^2, \tag{2.1}$$

with γ being the surface tension and D_b being the diameter of the bubble. To prevent the coalescence of the generated bubbles, stabilizing agents such as surfactants, polymers or proteins are added to the liquid phase [Tch08].
Liquid foams are defined by their average bubble diameter $\langle D_\mathrm{b} \rangle$ and its distribution, which can be described by the polydispersity index (*PDI*). The *PDI* is given as

$$PDI = \frac{\sqrt{\langle {D_\mathrm{b}}^2 \rangle - \langle D_\mathrm{b} \rangle^2}}{\langle D_\mathrm{b} \rangle}. \tag{2.2}$$

The generated bubbles are considered monodisperse if the *PDI* is below 5 % [Dre10]. Another important parameter in liquid foams is the gas fraction ϕ, which is defined by the ratio of the gas volume to the total foam volume. At a critical gas fraction ϕ_c the gas bubbles touch each other. For monodisperse bubbles that order in a close-packed structure, the critical gas fraction is $\phi_c = 0.74$ [Mae13], whereas, for monodisperse, disordered bubbles, the critical gas fraction is $\phi_c = 0.64$ [Ast08]. Note, however, that a close-packed structure is energetically more favorable compared to a randomly packed structure. Thus, monodisperse bubbles self-order under the influence of gravity and confinement if the gas fraction is sufficiently low to allow for a rearrangement of bubbles [Dre10]. If the gas fraction is sufficiently high so that two bubbles touch, a contact zone is formed, which is subject to capillary forces. Consequently, the contact zone is reduced to a thin liquid film, whose thickness is determined by the equilibrium between the capillary pressure p_c and the interactions of the surfactant layers [Höh21]. It holds for the capillary pressure

$$p_\mathrm{c} = p_\mathrm{g} - p_\mathrm{l} = 2\gamma H, \tag{2.3}$$

where p_l is the pressure of the liquid, p_g is the gas pressure, γ is the surface tension, and H is the mean curvature of the interface between the bubble and the liquid. The diameter of the contact zone d_b between touching bubbles depends on both the bubble diameter and the gas fraction. The larger the bubble diameter and the higher the gas fraction, the larger are the diameters of the contact zones. For monodisperse disordered foams [Prin88, Ard04] this relation is given as

$$\langle d_\mathrm{b} \rangle = \frac{0.6}{\phi^{\frac{1}{3}}} \left(1 - \frac{1.74}{\left(\frac{\phi}{1-\phi} + 1.3 \right)^{\frac{1}{2}}} \right)^{\frac{1}{2}} \cdot \langle D_\mathrm{b} \rangle. \tag{2.4}$$

Foam degradation: As liquid foams are thermodynamically unstable, they suffer from time-dependent foam degradation. Generally, there are three foam degradation mechanisms: Drainage, coarsening, and coalescence.

Drainage is the gravity-driven loss of liquid and results in a liquid fraction gradient along with the height of the foam. It holds for the liquid fraction gradient along the foam height [Dre15]

$$\varphi(\tilde{h}) = \frac{\varphi_c}{(1+\tilde{h})^2}, \tag{2.5}$$

with φ being the liquid fraction, φ_c being the critical liquid fraction, and $\tilde{h}$ being the reduced foam height. The liquid fraction φ is the ratio of the liquid volume to the total foam volume and is related to the gas fraction as follows: φ = 1 - ϕ. Thus, the gradient in the liquid fraction also generates a gradient in the gas fraction along the foam height. To decrease the influence of drainage in liquid foams, foams with a small foam height or a small bubble diameter can be generated [Mae13]. Furthermore, drainage can be slowed down by increasing the viscosity of the continuous phase or blocking the liquid channels between neighboring bubbles with particles such as laponite [Gui09]. Note that drainage only affects the liquid fraction of the foam, but does not change the bubble size and the bubble size distribution. However, the diameters of the contact zones between neighboring bubbles are influenced, because their size is determined by the gas fraction of the foam.

Coarsening is the transport of gas through thin liquid films within a foam, leading to an increase in the mean bubble size. Coarsening is driven by the *Laplace* pressure difference *Δp* between bubbles, which is given as [Wea99]

$$\Delta p = \frac{2\gamma}{R}, \tag{2.6}$$

with *R* being the bubble radius. Coarsening can be slowed down by generating foams with a very low polydispersity, as this decreases the *Laplace* pressure differences between the bubbles. Furthermore, the transport of the gas can be slowed down by using a gas with a low solubility [Wea99] or creating a densely packed surfactant layer [Var11]. Another method to slow down coarsening is the addition of water-insoluble gases, such as fluorocarbons, to the dispersed phase [Wea90]. In this way, a difference in osmotic pressure is generated, which counterbalances the *Laplace* pressure difference.

Coalescence is the merging of bubbles caused by the rupture of thin films, ultimately leading to an increase in bubble size and a decrease in bubble number. Coalescence can be slowed down by stabilizing the interface with e.g. particles [Rio14] or "catanionic" surfactant mixtures [Var11]. Furthermore, coalescence can be slowed down by fluorocarbon vapors [Ste21].

2.2.2 Liquid foam templating

To generate solid foams via liquid foam templating, the continuous phase of the liquid template has to be solidified. Depending on the composition of the continuous phase, this can be achieved via different methods [And18b]. In monomer-based systems, solidification occurs by polymerizing monomers that are either dissolved in the continuous phase [Net09] or constitute the continuous phase [Bon06]. Well-known polymer foams generated by solidifying a monomer-based continuous phase are poly(urethane) foams [Tes13]. In polymer-based systems, solidification occurs by cross-linking a polymer that either constitutes [Rod05] or is a component of the continuous phase [Tes10, And17, Deh19]. Solid foams can also be generated by solidifying dispersion-based systems. In these systems, the continuous phase consists of a suspension [Won09] or an emulsion [Els17a, Dab21]. For successful foam templating, the timescale of solidification has to be matched to the timescale of foam generation and foam degradation, and vice versa, to avoid pre-mature cross-linking or foam degradation. In an ideal case, the solidification occurs rapidly and can be controlled by an external stimulus.

During solidification, the structure of the liquid foam template is retained. Thus, the liquid foam's key structural parameters determine the solid foam's key structural parameters. The pore diameter D_p and the pore diameter distribution, for instance, are fixed by the bubble diameter D_b and the bubble diameter distribution. This has been demonstrated for numerous cases [And17, And18a, Deh19]. However, one has to bear in mind that those parameters are also influenced by shrinkage occurring during solidification [Deh19] or foam degradation prior to solidification. The porosity of the solid foam, which describes the relative amount of gas and solid phase, is fixed by the gas fraction of the liquid template [And18b]. Figure 2.5 shows a solid foam with a gradient in porosity due to drainage. At the top of the foam (high gas fraction) a high porosity can be observed, whereas at the bottom (low gas fraction) a low porosity is observed.

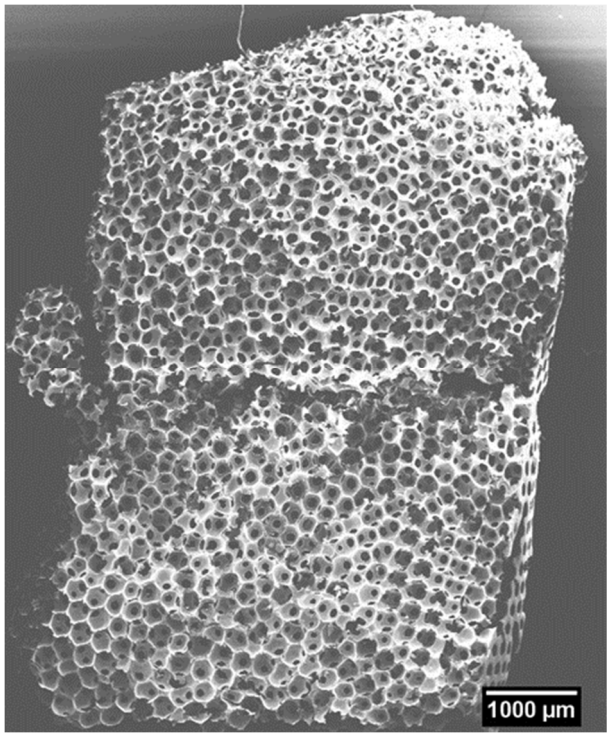

Figure 2.5: SEM image of a dried free-standing solid foam based on methacryloylated gelatin. Taken from [Deh19]. Reprinted with permission from [Deh19]. Copyright 2019 American Chemical Society.

In many systems, pore openings between neighboring pores are generated during solidification or further material processing. While the exact mechanism of the pore opening process is still unknown, a widely accepted hypothesis is that the formation of pore openings is caused by the rupture of thin films between neighboring bubbles. According to this, the pore opening diameter is directly determined by the diameter of the thin liquid films between neighboring bubbles, which is, in turn, determined by the gas fraction (see Section 2.2.1). This was also shown qualitatively for poly(urethane) foams, in which the pore opening diameter d_p increased with increasing gas fraction [Tes13]. The relation between gas fraction and pore opening diameter can be seen qualitatively in Figure 2.5. Due to the formation of pore openings, the foams can be filled with liquids (Figure 2.6). Technically, the term “foam” does not apply to water-filled structures (Figure 2.6 (right)) since foams are defined as dispersions of gas bubbles within a continuous phase. However, to be consistent with the existing literature, these structures will still be referred to as foams throughout this thesis. In closed-cell solid foams, which are obtained when the liquid foam templates are stabilized with particles [Won10] or when the formation of thin films is prevented by rapid solidification, the pores are permanently filled with gas.

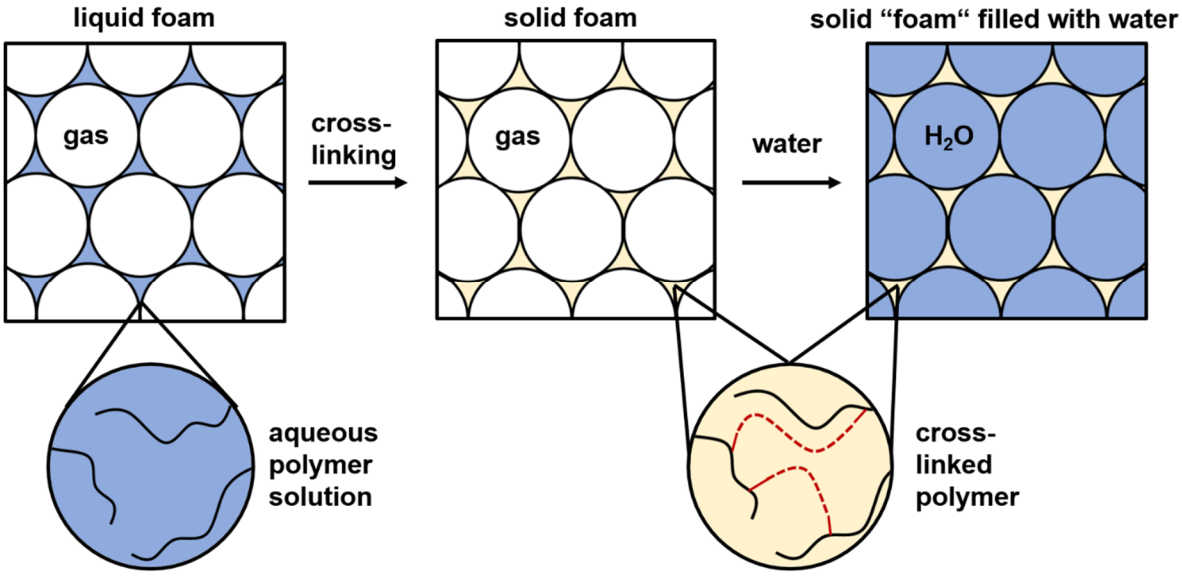

Figure 2.6: Liquid foam template (left) consisting of an aqueous polymer solution and gas. Upon cross-linking, a solid foam filled with gas is generated (middle). If pore openings are generated during solidification, the generated foams can be filled with water (right).

If the continuous phase of liquid foam templates consists of hydrophilic monomers or polymers dissolved in an aqueous solution, a hydrogel matrix is generated during solidification. Consequently, the resulting materials are called hydrogel foams. The most characteristic feature of hydrogel foams is that their continuous phase is permeable for small molecules such as water and gases [Maj17]. Thus, hydrogel foams swell to equilibrium in aqueous media, which also influences their pore size [Deh19]. Upon drying, dried hydrogel foams are generated, which, depending on the drying method, have an additional microporous structure [Dje21]. Hydrogel foams can be prepared by the monomer-based approach [Net09] and the polymer-based approach [And17]. However, the polymer-based approach is used more commonly as fewer components are needed in the continuous phase and solidification usually occurs faster. Furthermore, foams based on aqueous polymer solutions can be more effectively stabilized by surfactants, because the continuous phase is significantly more polar than in monomer-based systems. Figure 2.7 shows images of various hydrogel foams prepared by the polymer-based approach.

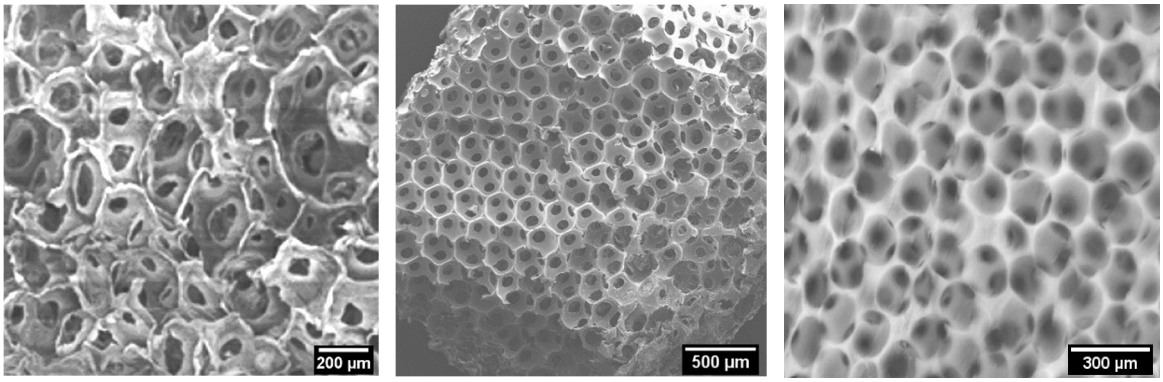

Figure 2.7: SEM images of hydrogel foams based on chitosan (left), methacryloylated gelatin (middle), and alginate (right). (left) Reprinted with permission from [And18a]. Copyright 2018 American Chemical Society. (middle) Reprinted with permission from [Deh19]. Copyright 2019 American Chemical Society. (right) Reprinted with permission from [Cos15]. Copyright 2015 American Chemical Society.

To prepare solid foams with a defined structure, the structure of the liquid foam template needs to be precisely controlled. One way to adjust the structure of the liquid template is microfluidic foaming. In this technique, a defined flow field is generated, which allows producing liquid foams with defined bubble diameters and bubble diameter distributions [Lin11, Tes13, Cos16, And18a, Deh19]. Furthermore, the spatial organization of the bubbles can be controlled, enabling the generation of hydrogel foams with a pore size gradient [Cos19]. The following section will outline the fundamentals of microfluidic foaming.

2.2.3 Microfluidic foaming

Microfluidics deal with the control and behavior of liquids and gases in micrometric dimensions and are applied in various research fields such as chemical engineering [Sun16] or chemical and biomedical analysis [Hae07]. Compared to the macroscale, the behavior of fluids in micrometric dimensions is notably different. First of all, the influence of viscous forces dominates over inertia, which becomes evident when looking at the *Reynolds* number. The *Reynolds* number is a dimensionless number, which describes the ratio of stress created by inertia to stress created by the fluid's viscosity [Rot90]. The *Reynolds* number reads

$$Re = \frac{\rho v D}{\eta} = \frac{\text{inertial stress}}{\text{viscous stress}}, \tag{2.7}$$

with ρ being the density, v being the velocity, D being the characteristic length scale, and η being the dynamic viscosity of the fluid. Due to the small characteristic length scales in

microfluidics, the influence of viscous stresses usually dominates over the influence of inertial stresses, which leads to a viscosity-driven flow in microfluidic devices.

To generate bubbles with microfluidics, a gas and a liquid need to be simultaneously injected into a microfluidic chip. As soon as the gas and liquid meet at a constriction, an interface between gas and liquid is created, which is deformed until a bubble with a diameter D_b is pinched off [Dre15]. If the flow rate of gas Q_g and liquid Q_l are set to appropriate values, the generation of bubbles occurs periodically, which can result in the formation of monodisperse liquid foams. The shape of bubbles moving in a surrounding fluid can be described by the *Bond*-number, which represents the ratio of gravitational to interfacial stress [Hag12]. The *Bond* number reads

$$Bo = \frac{\Delta\rho g D^2}{\gamma} = \frac{\text{gravitational stress}}{\text{interfacial stress}}, \tag{2.8}$$

with $\Delta\rho$ being the density difference of the fluids, g being the gravitational acceleration and γ being the surface tension. As the characteristic length scale in microfluidic chips is very small, the influence of gravity on the bubbles can be neglected. The bubble pinch-off inside the microfluidic chip is primarily influenced by the geometry of the constriction, as this determines the flow field at the interface between gas and liquid [Dre15]. The most commonly used geometries are cross-flow, co-flow, and flow-focusing (Figure 2.8).

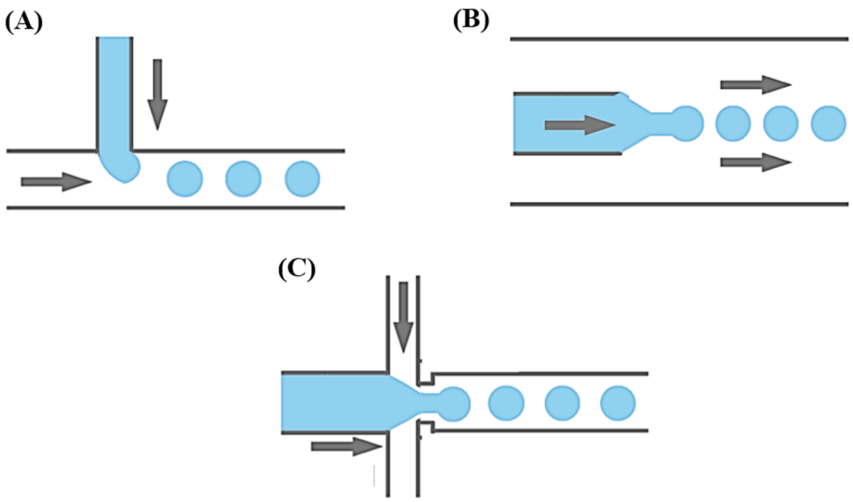

Figure 2.8: Schematic drawings of commonly used bubbling geometries in microfluidic channels. (A) cross-flow geometry (T-junction), (B) co-flow geometry, (C) flow-focusing geometry. The arrows indicate the direction of flow. Adapted from [Ma17] with permission from MDPI, open access journal.

If the liquid and gas meet at an angle between 0 – 180 °, the geometry is denoted as cross-flow. This geometry is also called “T-junction” if the gas and liquid inlet channels are perpendicular. In the co-flow geometry, the two phases move parallel to each other, whereby the channel of the liquid phase surrounds the channel of the gas phase. In the flow-focusing geometry, both fluid channels are focused in a constriction, which allows for an even more controlled bubble break-up. Recently, a flow-focusing chip with a reconfigurable constriction was developed [Cos19].

Irrespective of the chip geometry, the bubble break-up strongly depends on the flow conditions. Three different bubbling regimes can be discerned according to the relative extent of acting stresses. Besides the Reynolds number, the bubbling regimes are determined by the *Capillary* number and the *Weber* number. The *Capillary* number describes the ratio of viscous stress and interfacial stress [Squ05] and reads

$$Ca = \frac{\eta v}{\gamma} = \frac{\text{viscous stress}}{\text{interfacial stress}}. \tag{2.9}$$

The *Weber* number describes the ratio of inertial and interfacial stress [Yau16] and reads

$$We = \frac{\rho v^2 D}{\gamma} = \frac{\text{inertial stress}}{\text{interfacial stress}}. \tag{2.10}$$

Figure 2.9 shows schematic drawings of the bubble generation in the different bubbling regimes.

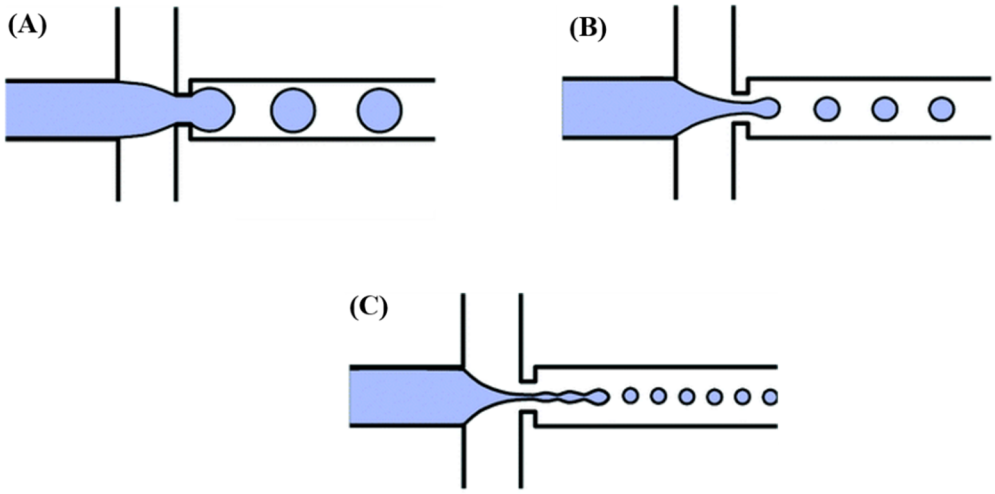

Figure 2.9: Generation of bubbles in different bubbling regimes in a flow-focusing geometry. (A) Squeezing regime, (B) dripping regime, (C) jetting regime. Adapted with permission from [Col15]. Copyright 2015 Royal Society of Chemistry.

In the squeezing regime (low *Ca*, low *We*, low *Re*), which is also known as the quasi-static regime, the dynamic stresses acting on the gas-liquid-interface can be neglected due to the low flow rates. During the generation of bubbles, the gas stream completely fills the constriction until the flow of the liquid leads to a pinch-off of the gas bubble. The generation of bubbles in the squeezing regime is shown in Figure 2.9 (A). Due to the quasi-static conditions, bubbles produced in the squeezing regime are highly monodisperse [Gar04]. However, this often comes at the expense of the production rate, as in the quasi-static regime low liquid and gas flow rates are used.

For increased flow rates (high *Ca*, low *We*, low *Re*), the bubble formation occurs in the dripping regime. In contrast to the squeezing regime, dynamic stresses are involved in the formation of bubbles, as the interfacial stresses are overcome by the viscous stresses. Figure 2.9 (B) shows the generation of bubbles in the dripping regime. Compared to the squeezing regime, an increased production rate is obtained when generating bubbles in the dripping regime. However, the influence of the flow rates on the bubble radius is stronger than in the squeezing regime. This leads to an increased polydispersity [Dre15] as small fluctuations of the gas or liquid flow rate have a strong influence on the bubble radius.

When increasing the flow rate further, bubble formation occurs in the jetting regime (high *Ca*, high *We*, high *Re*), where the generation of bubbles is dominated by inertial stresses. The jetting regime is characterized by the formation of a gas jet, which is subject to *Rayleigh*-Plateau instabilities and breaks up into bubbles to reduce its surface energy. The radius of the generated

bubbles depends on whether the external or the internal flow dominates the jetting. If the inertia of the internal flow dominates the jetting, the bubble radii are larger than the constriction. By contrast, bubble radii smaller than the constriction are obtained if the inertia of the outer fluid dominates the jetting. Figure 2.9 (C) shows the generation of bubbles in the jetting regime. Similar to the dripping regime, the production rates in the jetting regime are higher compared to the squeezing regime. However, an increased polydispersity is observed since the bubbles are generated due to the *Rayleigh*-Plateau instability [Dre15]. Regarding practical applications, the accessibility of the three bubbling regimes for a given microfluidic geometry is strongly influenced by the flow behavior of the fluids as well as the fluid flow rates, which are limited by the setup. Furthermore, the flow of the gas phase is often controlled by the gas pressure p to avoid long equilibration times that usually occur in flow rate-controlled setups.

Across all regimes, the diameters of the generated bubbles D_b are proportional to the ratio of gas and liquid flow rate to the power α. The higher the gas flow rate and the lower the liquid flow rate, the larger are the generated bubbles [Tes12]. It holds for the bubble diameter

$$D_b \propto \beta \left(\frac{Q_g}{Q_l}\right)^{\alpha}, \tag{2.11}$$

where β is a constant related to the channel dimensions. Furthermore, the fluid flow rates also determine the gas fraction ϕ of the generated foams [Tes12]. It holds

$$\phi = \frac{Q_g}{Q_g + Q_l}. \tag{2.12}$$

As seen from equations 2.11 and 2.12, the gas fraction and bubble diameter are coupled and cannot be varied independently for a fixed liquid flow rate.

To conclude, microfluidic foaming is a widely used tool to produce liquid foams with a defined structure, as the bubble diameter can be adjusted by controlling the flow rates of the gas or liquid phase. In this way, monodisperse foams [Lin11], foams with a controlled polydispersity [And18a] or foams with a gradient in bubble size can be generated [Els17b]. Solid foams with a controllable structure are of great relevance in many applications, as the foam properties strongly depend on the morphology. In the following paragraphs, the theoretical background of two potential application fields of hydrogel foams is outlined.

2.3 Sorption and controlled release of ions

The sorption and (controlled) release of molecules or ions is used in many technologies relevant to our daily life, such as water purification [Ali07, Gre72], chromatography [Buf86], or drug delivery [Coc21]. The term sorption describes processes that lead to an accumulation of a substance, also called sorptive, within a phase or at the surface of a material, which is also called sorbent. Once sorption took place, the sorbed substance is called sorbate. The reverse process of sorption is called desorption and is accompanied by the release of sorbed molecules or ions. Sorption can be divided into two main categories, namely adsorption and absorption [Atk08]. Briefly, the term adsorption describes the accumulation of a substance on vacant sites at the interface between two phases, whereas absorption is the accumulation of a substance within a different phase, e.g. gases that are dissolved in liquids. If the sorptive is an ion and if the sorbent contains charged functional groups, sorption can also take place via ion exchange, which is defined as the reversible interchange of dissimilar ions due to electrostatic interactions. In the existing literature, the terms ion exchange and adsorption are often used interchangeably, as there is no clear categorization for ion exchange within the context of sorption. However, ion exchange differs from adsorption in that the variance of both systems, i.e. the number of independent concentration variables, is different [Gre08]. During adsorption, the number of occupied sorption sites continuously increases. By contrast, the number of occupied sorption sites remains constant in ion exchange, as the adsorption of ions on charged functional groups is always accompanied by a simultaneous desorption of dissimilar ions [Eve71]. Thus, ion exchange should be treated as a subcategory of sorption, which is closely related to adsorption. Depending on the charge of the functional groups in the exchanger phase, cations or anions can sorb on an ion exchanger material. The general reaction equation for the exchange of cations reads

$$A^{n+} + nBR \rightleftharpoons AR_n + nB^+,$$

with R representing a univalent, negatively charged functional group of the cation exchanger. Commonly used functional groups used for cation exchange include sulfonic acid or carboxylic acid groups. Anion exchange, on the other hand, occurs on positively charged groups such as quaternary ammonium groups or amino groups. Widely used materials for ion exchange include clay minerals [Hof03], aluminum oxide [Bro89], or hydrogels with permanently bound charged groups [Esc13]. The most prominent advantage of hydrogels is that ion exchange occurs

throughout the whole material volume, allowing for an efficient use of available functional groups. Note that in this case, the ions are absorbed by the material during sorption. During this process, the ions first have to diffuse through the polymer network before they interact with specific functional groups. The diffusion of ions through the polymer network is the rate-limiting step during ion exchange and determines the kinetics of ion exchange. To a first approximation, the diffusion of ions in a polymer network is driven by a concentration gradient and can be described by Fick's law of diffusion [Gei14]. In one dimension, the first law of diffusion reads

$$J = -D\frac{dc}{dx}, \tag{2.13}$$

where J is the diffusion flux, D is the diffusion coefficient, c is the concentration and x is the spatial position. The distance a molecule covers within a time t depends on the diffusion coefficient and can be expressed by the mean squared displacement d [Atk08]. It holds

$$d = \sqrt{2Dt}. \tag{2.14}$$

The diffusion coefficient of a substance inside a polymer network can be described by the free volume theory [Coh59]. It holds

$$D = \mathrm{a_i}\, \mathrm{e}^{\frac{-\mathrm{b_i}}{\langle V_\mathrm{f} \rangle}}, \tag{2.15}$$

with V_f being the free volume inside the polymer network, and $\mathrm{a_i}$ and $\mathrm{b_i}$ are constants. As the free volume in hydrogels depends on the hydrogel's mesh size, the diffusion of solutes and thus the rate of ion exchange is strongly influenced by the hydrogel network structure. In many cases, the time-dependent sorption of ions follows the pseudo-first-order equation developed by Lagergren [Lag98]. It holds

$$q_{t,\mathrm{a}} = q_{\mathrm{e,a}}(1 - \mathrm{e}^{-k_\mathrm{a} t}), \tag{2.16}$$

where $q_{t,\mathrm{a}}$ is the concentration of sorbed solutes at a time t, $q_{\mathrm{e,a}}$ is the concentration of sorbed solutes at equilibrium, and k_a is the sorption rate coefficient.

In an ideal case, equilibrium is attained when the ions are evenly distributed inside the hydrogel matrix. The sorption equilibrium at a specific temperature is defined by the sorption isotherm. Most commonly, the concentration of sorbed ions increases with increasing ion concentration in the surrounding medium until a plateau is reached. Isotherms that follow this behavior are usually analyzed according to the *Langmuir* model, which was originally developed for the adsorption of substances on surfaces [Lan18]. The basic assumptions of this model are (1) the sorbent possesses a defined number of equal sorption sites, which are accessible to all molecules, (2) each sorption site only sorbs one molecule, and (3) no or ideal interactions occur between molecules that are sorbed on adjacent sorption sites. It holds

$$q_{\mathrm{e,a}} = q_{\max} \frac{K_s c_{\mathrm{e,a}}}{1 + K_{\mathrm{s}} c_{\mathrm{e,a}}}, \tag{2.17}$$

where $q_{\max}$ is the maximum sorption capacity, K_{s} is the equilibrium constant, and $c_{\mathrm{e,a}}$ is the equilibrium concentration of ions in the surrounding medium. Typically, $q_{\mathrm{e,a}}$ is plotted against $c_{\mathrm{e,a}}$. Figure 2.10 shows a *Langmuir* sorption isotherm.

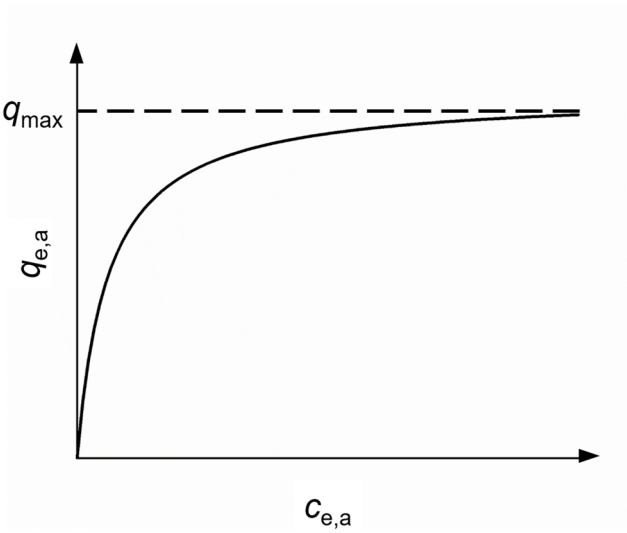

Figure 2.10: Schematic drawing of a *Langmuir* sorption isotherm.

For practical applications, high values of K_{s} and $q_{\max}$ are desired as they correspond to strong interactions between the sorptive and the sorbent (high K_{s}) and a high loading capacity of the sorbent (high $q_{\max}$). In order to regenerate the material, the sorbed ions can be released by replacing them with dissimilar ions. This can be achieved by immersing the material into a salt solution, e.g. a NaCl solution [Cla20]. Furthermore, ions could be released by protonating or

deprotonating the functional groups by changing the pH value [Raj20]. This is especially relevant for weak electrolytes, such as amino groups.

In both cases, the release of ions depends on an external stimulus and is thus a controlled process. This is of interest for drug delivery applications, where a controlled release of drugs is highly relevant. In particular, the prevention of a so-called "burst-release", which is the unpredictable and uncontrolled release of drugs, is important in this field. One material that is commercially used for the controlled release of the drugs via ion exchange is poly(stryrene-co-divinylbenzene) sulfonic acid. In these systems, drugs like morphine or noscapine [Voi10], are bound to sulfonic acid functional groups, and are replaced by either H^+-ions in the stomach or Na^+ or K^+ ions in the intestine. After being desorbed from the functional groups, the ions also diffuse through the hydrogel matrix before they are released into the surrounding medium. Thus, all physicochemical relations outlined above are also valid for the release of ions.

2.4 Enzyme Immobilization

2.4.1 Enzymes

Enzymes are biocatalysts that increase the rate of a reaction by lowering its activation energy [Atk08]. Like all proteins, enzymes consist of linearly connected amino acids, i.e. they are polypeptides. Due to the specific sequence of amino acids, the polypeptide chain forms a defined structure, which controls the primary function of the enzyme, i.e. the conversion of a substrate into a product. The conversion of a substrate occurs at the enzyme's active site, which consists of the binding site and the catalytic site [She82]. The binding site binds and sterically orients the substrate, whereas the catalytic site carries out the chemical reaction. Due to the defined structure of the active site, enzymes are highly specific and often display excellent chemo-, regio- and stereoselectivity [Dav01]. Enzymes are commonly categorized according to their enzymatic activity. Enzymes classified as oxidoreductases, for example, catalyze the transfer of electrons from one molecule to another. One well-known enzyme in the class of oxidoreductases is horseradish peroxidase (HRP), which catalyzes the reduction of hydrogen peroxide using heme as a co-factor [Vei00]. Figure 2.11 shows the ribbon structure of HRP.

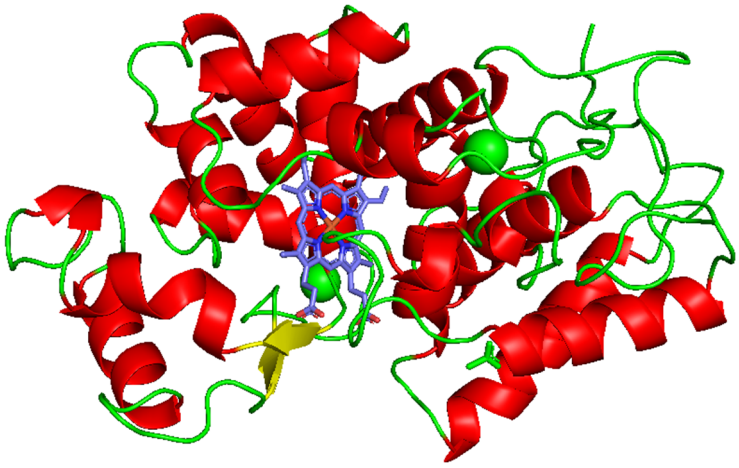

Figure 2.11: Ribbon structure of HRP. The image was created with PyMOL (version 2.5.2) using the protein sequence from [Ber02].

The catalytic cycle of HRP consists of three consecutive reactions [Vei00], during which two substrate molecules AH_2 are oxidized:

(I) $HRP + H_2O_2 \rightarrow HRP\text{-}I + H_2O$

(II) $HRP\text{-}I + AH_2 \rightarrow HRP\text{-}II + AH\bullet$

(III) $HRP\text{-}II + AH_2 \rightarrow HRP + AH\bullet$

In the first reaction, hydrogen peroxide is reduced to water, generating the HRP-I complex through the oxidation of heme. In the second reaction step, HRP-I oxidizes a substrate AH_2 and is thus reduced to HRP-II, which is followed by the oxidation of another substrate molecule in the third reaction step, thus regenerating HRP. HRP is able to catalyze the oxidation of various substrates, which often comes along with a significant change in the physicochemical properties, such as the generation of chemiluminescence [Kap97], the appearance of fluorescence [Zai80], or a shift in absorption wavelength [Cla18b]. One example is the oxidation of colorless 2,2'-azino-bis(3-ethylbenzothiazoline-6-sulfonic acid) (ABTS) to blueish-green $ABTS^{+\bullet}$ (Figure 2.12).

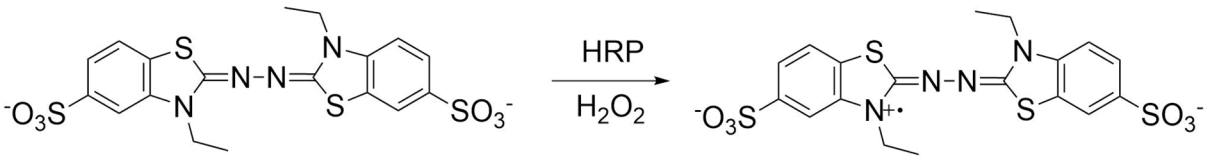

Figure 2.12: Oxidation of ABTS to $ABTS^{+\bullet}$ catalyzed by HRP.

The change in physicochemical properties upon substrate oxidation is often used in biotechnological applications [Kra13], such as coupled enzyme assays, biosensors, or diagnostic kits. In addition, HRP can be used in fine chemical synthesis [Das02] or wastewater treatment [Che06].

2.4.2 Methods for enzyme immobilization

In the past decades, the application of enzymes has continued to expand to many industrial processes. An essential issue in this field is the recovery and reuse of the applied enzymes, which can be facilitated by their immobilization on a solid support that can be easily removed from the reaction mixture. To date, many materials have been examined as solid supports, including polyketone polymers [Ago07], silica [Pie04], or gold nanoparticles [Pet12]. Furthermore, hydrogels are also widely investigated as materials for enzyme immobilization [Hom13] because they provide a suitable physiological environment for enzymes due to their high water content. Different strategies for the immobilization of enzymes include covalent binding, adsorption, entrapment, or affinity immobilization. Figure 2.13 schematically shows different immobilization strategies.

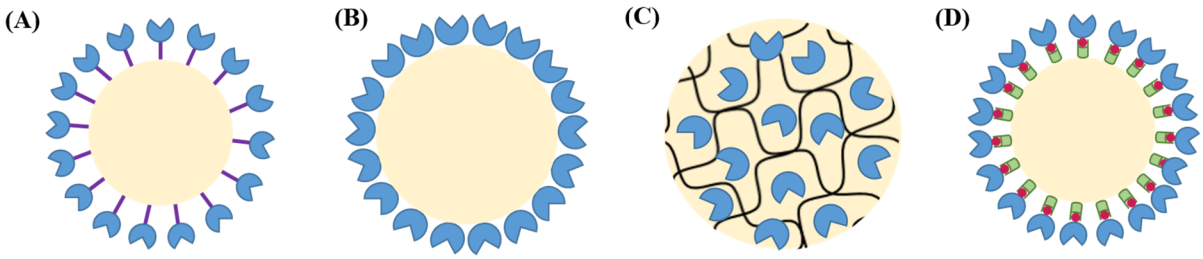

Figure 2.13: Different strategies for immobilizing enzymes. (A) covalent binding, (B) adsorption, (C) entrapment, (D) affinity immobilization. Adapted from [Lyu21] with permission from MDPI, open access journal.

Covalent binding: Covalent binding of enzymes involves the formation of chemical bonds between the enzyme and the support material. Typically, this occurs via the reaction of amino acid side chains with functional groups of the support material. Examples of this include (i) the reaction of amino groups in lysine residues with N-hydroxysuccinimide functionalized materials, which has been used for immobilizing glucose oxidase on silica [Jun11], or (ii) the reaction of thiol groups in cysteine residues with maleimide functionalized materials, which has been used for immobilizing beta-glucosidase on glass surfaces [Li18]. Covalent binding

provides a strong attachment and thus prevents enzyme leaching. In addition, it also results in a high loading efficiency [Dut17]. However, enzyme immobilization via covalent binding can lead to the loss of catalytic function or a decrease in enzyme activity as amino acid residues that maintain the enzyme's structural and functional properties might also be altered during the reaction [Lyu21].

Adsorption: Adsorption of enzymes on solid supports occurs via electrostatic interactions, hydrogen bonds, or hydrophobic interactions. Widely used materials for the immobilization of enzymes via adsorption include polylysine coated supports [Abo13] (electrostatic interactions), polyketone polymers (hydrogen bonds) [Ago07], or hydrophobic supports (hydrophobic interactions) [Li10]. In contrast to covalent binding, the formation of chemical bonds is not required. Thus, no additional chemical reagents are necessary, which leaves the procedure cheap and straightforward to perform. However, the adsorption of enzymes can also result in significant conformational changes [Hom13], which affect enzyme performance. Furthermore, the binding is relatively weak, resulting in the leaching of enzymes upon environmental changes such as pH or temperature changes [Han09].

Entrapment: Enzyme immobilization via entrapment occurs by physically trapping the enzyme within the meshes of a hydrogel. Consequently, the enzymes are protected from harsh environments, which prevents denaturation and preserves enzyme activity [Lyu21]. As network formation and enzyme entrapment occur simultaneously, careful attention must be paid to the cross-linking conditions, which can also damage the enzyme. Another downside of this method is that enzyme leakage can often not be entirely suppressed without additional covalent attachment [Cho08]. Furthermore, compared to other immobilization techniques, a limited mass transfer is observed as both substrate and product have to diffuse in and out of the polymer network. Due to the high turnover number of many enzymes, this results in the formation of a small (200 – 400 nm) catalytically active layer [Mar93]. Thus, enzymes immobilized inside the bulk of the material do not participate in substrate conversion, which can be considered a suboptimal use of both enzyme and support material. A particular case of entrapment is encapsulation, where enzymes are entrapped in lipid vesicles [Wal01].

Affinity immobilization: In affinity immobilization, specific interactions between proteins and small molecules are exploited. Familiar interactions used for affinity immobilization of enzymes are the chelation of transition metals by polyhistidine, which has been used for the

immobilization of His-tagged lipase [Woo10], or the interaction between biotin and the proteins avidin or streptavidin, which has been used for the immobilization of biotinylated glucose dehydrogenase [Mat18]. Even though this immobilization technique requires a chemical or biochemical modification of the enzyme prior to conjugation, affinity immobilization offers high selectivity and stability [Hom13]. This is especially true for the latter case, as the biotin-(strept)avidin interaction is the strongest non-covalent interaction occurring in nature ($K = 10^{14}$-10^{15}) [Liv93]. Both avidin and streptavidin are globular tetrameric proteins that possess four biotin binding sites. Figure 2.14 shows a schematic drawing of the biotin-(strept)avidin interaction and the chemical structure of biotin.

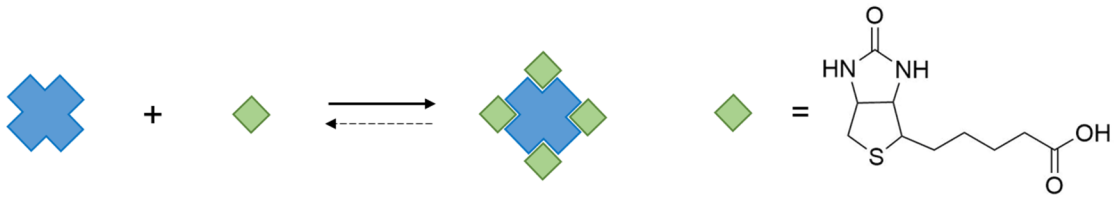

Figure 2.14: Schematic drawing of the biotin-(strept)avidin interaction (left), chemical structure of biotin (right).

3. Summary of Research

In this thesis, the tailorability and the effects of the polymer functionality of hydrogel foams based on gelatin methacryloyl (GM) are examined. The results are published in three publications [Deh21a (**Publication I**), Deh21b (**Publication II**), Deh22 (**Publication III**)]. In the following, the main results of this thesis will be summarized and discussed. The used gelatin methacryloyl was synthesized by adding a ten-fold excess of methacrylic anhydride with respect to the amino groups in gelatin, and will be abbreviated with GM10 in the following.

3.1 Tailoring and visualizing pore openings in gelatin-based hydrogel foams (Publication I)

Publication I deals with tailoring the pore opening diameter of GM10-based hydrogel foams at a constant pore diameter. To this end, two complementary methods were used to decouple the gas fraction from the bubble diameter in liquid foam templates. The obtained pore opening diameters were compared to theoretical predictions for thin film diameters in liquid templates.

3.1.1 Visualization of pore openings

All samples were characterized with confocal fluorescence microscopy for which they were stained with the cationic dye methylene blue. Figure 3.1 (bottom) shows the chemical structure of methylene blue. The staining process was followed by recording UV/VIS spectra of the staining solution at different times after immersion of the GM10 hydrogel foams (Figure 3.1, top, right). As can be seen from the UV/VIS spectra, the absorption of the staining solution decreases continuously as soon as the GM10 hydrogel foam is immersed. Therefore, it can be concluded that methylene blue not only penetrates the hydrogel matrix but also interacts with the polymer chains. This is further confirmed by the observation that no methylene blue visibly leaches out of the hydrogel matrix when immersing the stained sample in deionized water. We hypothesize that a cation exchange takes place during the sample staining, as the used GM10 contains negatively charged carboxyl groups. The isoelectric point (IEP) of GM10 is 4.2 [Sew18]. Thus, GM10 is a polyanion at neutral pH.

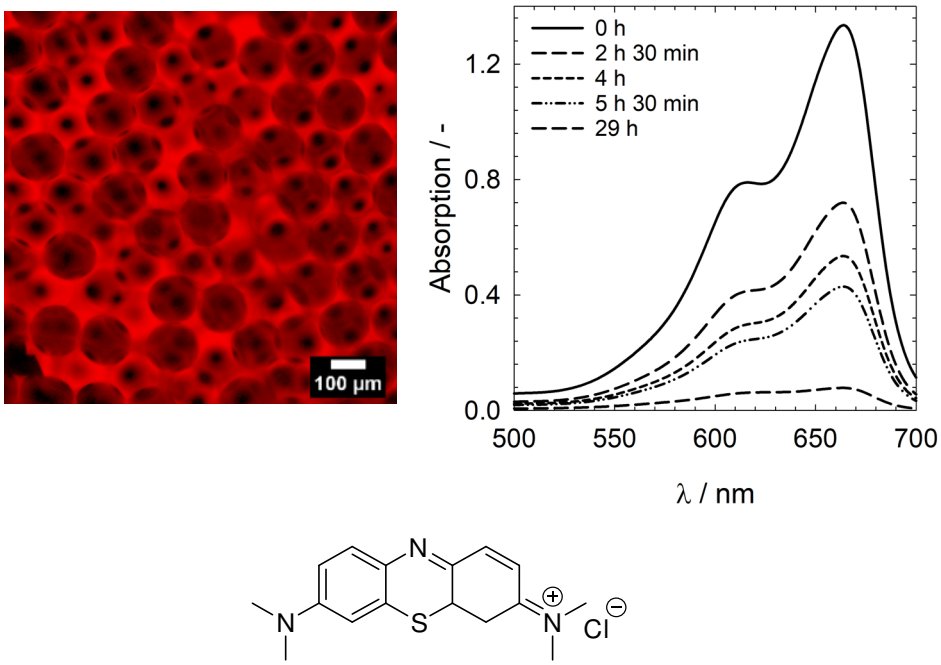

Figure 3.1: Confocal fluorescence microscopy image of a hydrogel foam stained with methylene blue (top, left) and absorption spectra of an aqueous methylene blue solution after immersion of a GM10 hydrogel foam (top, right). Chemical structure of methylene blue (bottom). Adapted from [Deh21a], Copyright 2021, with permission from Elsevier.

Compared to other methods commonly used for the characterization of hydrogel foams, confocal fluorescence microscopy offers several advantages. In our previous work, for example, GM10 hydrogel foams were characterized by scanning electron microscopy (SEM) and bright field microscopy [Deh19]. While SEM allows for the detailed visualization of both pores and pore openings, the characterization occurs in the dried state, which is disadvantageous, because the behavior of the hydrogel foams during drying, particularly the shrinkage of the pore openings relative to the shrinkage of the pores, is unknown. By contrast, bright field microscopy allows for visualizing the pores in their swollen equilibrium state. However, pore openings cannot be easily visualized due to the low contrast between the hydrogel matrix and the medium. As an alternative, confocal fluorescence microscopy allows for visualizing both pores and pore openings in the swollen state (Figure 3.1, top, left). Another commonly used method to characterize pores and pore openings in swollen hydrogel foams is micro computed tomography (µ-CT), which is undoubtedly the most precise method to visualize hydrogel foams in their swollen and dried states. However, a long acquisition time in the range of several hours, which increases enormously with increasing resolution, must be considered. Confocal fluorescence microscopy, on the other hand, offers short acquisition times in the range of minutes. Opposed to µ-CT, however, only the first pore layers can be seen with confocal

fluorescence microscopy, which is due to the scattering of light when measuring deep inside the samples.

3.1.2 Control over the pore opening diameter

To gain control over the pore opening diameters in GM10-based hydrogel foams, two different methods were used to decouple the gas fraction from the bubble diameter during microfluidic foaming. In the first method, the gas fraction of the liquid templates was adjusted by adding polymer solution to the liquid foam templates prepared at a constant liquid flow rate v_L and gas pressure p. In the second method, the gas fraction was varied by keeping the ratio of applied gas pressure to liquid flow rate constant, while increasing the absolute values of both parameters, thus varying the bubbling frequency. Figure 3.2 visualizes the experimental setup for each method.

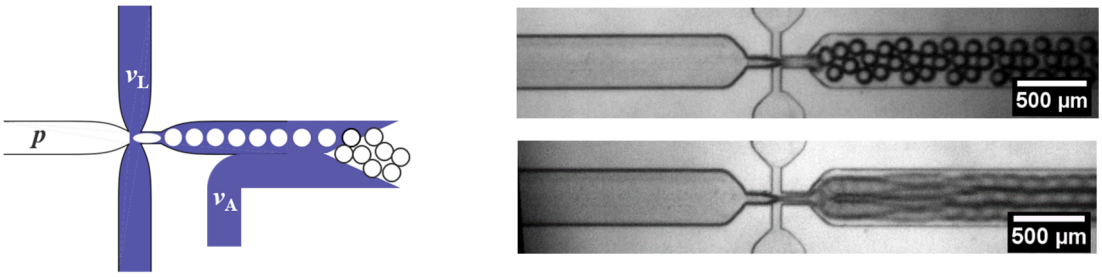

Figure 3.2: (left) Schematic drawing of the experimental setup used to add polymer solution with a liquid flow rate v_A to bubbles generated by applying a gas pressure p and a liquid flow rate v_L. (right) Generation of bubbles at different liquid flow rates and gas pressures. (top, right) v_L = 20 µL min^{-1}, p = 200 mbar, (bottom, right) v_L = 80 µL min^{-1}, p = 800 mbar. As can be seen, the bubbling frequency is considerably increased at higher absolute values of v_L and p, indicated by the blurry train of bubbles. Adapted from [Deh21a], Copyright 2021, with permission from Elsevier.

Addition of polymer solution: Pictures of samples generated by adding polymer solution to the liquid template are shown in Figure 3.3. The corresponding values for pore diameters and pore opening diameters as well as their ratios and the gas fraction of the foams are listed in Table 3.1.

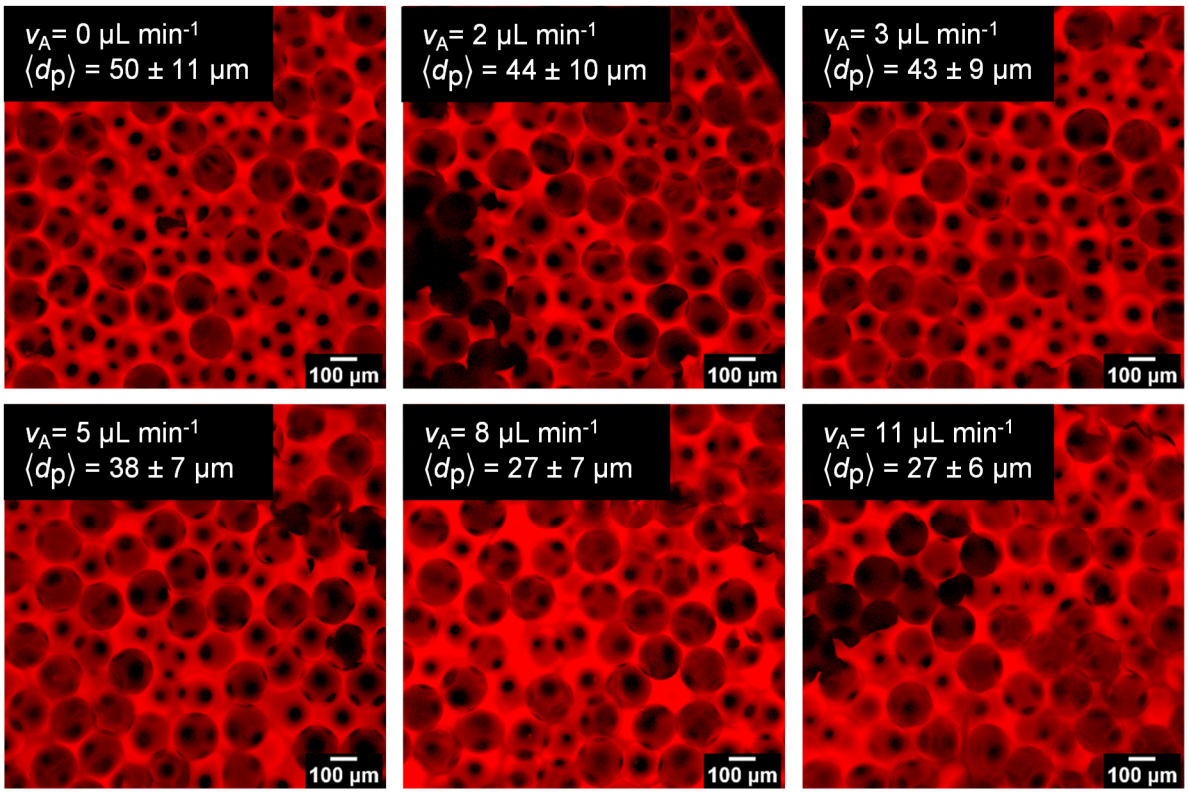

Figure 3.3: Pictures of GM10 foams produced at a liquid flow rate v_L of 7 µL min^{-1} and a gas pressure p of 260 mbar. Additional polymer solution was added to the liquid foam templates using the liquid flow rates v_A given in the insets. The pictures were taken with confocal fluorescence microscopy. All pores are filled with water. Adapted from [Deh21a], Copyright 2021, with permission from Elsevier.

Table 3.1: Liquid flow rates v_A of added GM solution, pore diameters $\langle D_p \rangle$, pore opening diameters $\langle d_p \rangle$, the ratio $\langle d_p \rangle / \langle D_p \rangle$ and the gas fraction ϕ of the liquid foams. All errors correspond to standard deviations. The liquid foam templates had a bubble diameter of $\langle D_b \rangle$ = 174 ± 2 µm. Adapted from [Deh21a], Copyright 2021, with permission from Elsevier.

v_A / µL min^{-1}	$\langle D_p \rangle$/ µm	$\langle d_p \rangle$ / µm	$\langle d_p \rangle / \langle D_p \rangle$	ϕ / %
0	178 ± 4	50 ± 11	0.28	82 ± 4
2	175 ± 4	44 ± 10	0.25	80 ± 1
3	181 ± 5	43 ± 9	0.24	79± 1
5	179 ± 3	38 ± 7	0.21	74 ± 1
8	178 ± 3	27 ± 7	0.15	67 ± 1
11	177 ± 4	27 ± 6	0.15	66 ± 0*

*As the gas fraction of samples produced with this liquid flow rate could only be determined from two samples that did not differ in weight, the obtained standard deviation is zero.

Looking at Table 3.1, one sees that the gas fraction of cross-linked hydrogel foams decreases from 82 % to 66 % when increasing the liquid flow rate of the additional polymer solution v_A from 0 µL min^{-1} to 11 µL min^{-1}. By contrast, a constant bubble diameter of 174 ± 2 µm and a constant pore diameter of ~ 178 µm were obtained. Furthermore, the mean pore opening

diameter decreases from 50 ± 11 µm to 27 ± 6 µm, which results in $\langle d_p \rangle / \langle D_p \rangle$ ratios ranging from 0.28 to 0.15. This confirms that the pore opening diameter can be adjusted at a constant pore diameter by decoupling the gas fraction from the bubble diameter during microfluidic foaming. As can be seen from Figure 3.1, left, this method allows for adding polymer solution to a generated liquid foam template outside the microfluidic chip. In this way, feedback loops on the bubble pinch-off at the constriction are avoided. However, this method is only suitable for liquid foam templates with high initial gas fractions and thus large bubble diameters.

Variation of bubbling frequency: To adjust the pore opening diameters in foams generated from liquid foam templates with low initial gas fractions and thus smaller bubble diameters, the bubbling frequency during foam generation inside the microfluidic chip was varied. Figure 3.4 shows pictures of the generated samples. The corresponding values for pore diameters and pore opening diameters as well as their ratios and the gas fraction of the foams are listed in Table 3.2.

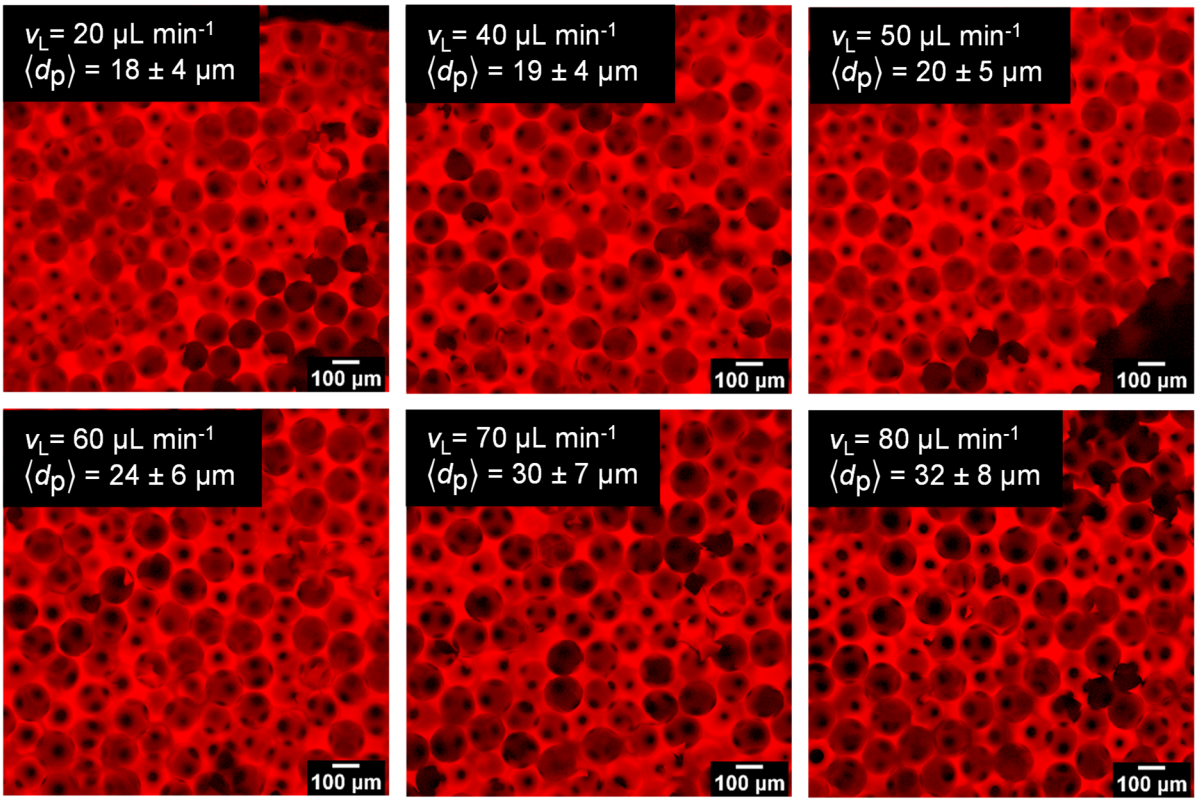

Figure 3.4: Exemplary pictures of GM10 foams produced with a ratio of liquid flow rate to gas pressure of 0.1 µL min^{-1} mbar^{-1}. The absolute values of the liquid flow rate v_L and the pore opening diameter are given in the insets. The pictures were taken with confocal fluorescence microscopy. All pores are filled with water. Adapted from [Deh21a], Copyright 2021, with permission from Elsevier.

Table 3.2: Liquid flow rates v_L and gas pressures p used to produce GM10 foams, bubble diameters $\langle D_b \rangle$, pore diameters $\langle D_p \rangle$, pore opening diameters $\langle d_p \rangle$, the ratio $\langle d_p \rangle / \langle D_p \rangle$ and the gas fraction ϕ of the liquid foams. The errors are standard deviations. Adapted from [Deh21a], Copyright 2021, with permission from Elsevier.

v_L / µL min^{-1}	p / mbar	$\langle D_b \rangle$/ µm	$\langle D_p \rangle$ / µm	$\langle d_p \rangle$ / µm	$\langle d_p \rangle / \langle D_p \rangle$	ϕ / %
20	200	140 ± 5	131 ± 6	18 ± 4	0.14	60 ± 4
30	300	135 ± 3	133 ± 3	19 ± 5	0.14	54 ± 1
40	400	138 ± 3	136 ± 3	19 ± 4	0.14	65 ± 1
50	500	145 ± 4	138 ± 3	20 ± 5	0.15	68 ± 1
60	600	144 ± 2	140 ± 3	24 ± 6	0.17	71 ± 1
70	700	144 ± 3	144 ± 3	30 ± 7	0.21	75 ± 2
80	800	142 ± 2	142 ± 4	32 ± 8	0.23	76 ± 1

Looking at Table 3.2, one sees that the gas fraction increases from 54 % to 76 % when increasing the absolute values of gas pressure and liquid flow rate. By contrast, the bubble diameter is kept constant at $\langle D_b \rangle$ ~ 140 µm, demonstrating that the gas fraction can be decoupled from the bubble diameter by varying the bubbling frequency. The obtained pore opening diameters range from 18 ± 4 µm to 32 ± 8 µm at a pore diameter of ~ 140 µm, resulting in $\langle d_p \rangle / \langle D_p \rangle$ values ranging from 0.14 to 0.23. Again, the obtained results show that pore opening diameter can be varied at a constant pore diameter by decoupling the gas fraction from the bubble diameter during microfluidic foaming.

Taking together the results of both methods, $\langle d_p \rangle / \langle D_p \rangle$ values between 0.14 and 0.28 are accessible. These values also represent the upper and lower limits of $\langle d_p \rangle / \langle D_p \rangle$ for the system examined in the thesis at hand. The upper limit, which corresponds to a gas fraction of 82 %, is set by the cross-linking chemistry of the system. As the hydrogel foams are solidified via radical cross-linking of the polymer chains, oxygen inhibition plays an increased role at high gas fractions. Indeed, liquid foam templates with gas fractions above 82 % could not be reliably cross-linked by irradiation with UV light. Larger $\langle d_p \rangle / \langle D_p \rangle$ values might be achieved by using a more rigorous inert gas atmosphere when collecting and cross-linking the liquid foam. The lower limit of accessible $\langle d_p \rangle / \langle D_p \rangle$ values is set by the drainage of liquid from the templates. Theoretically, the $\langle d_p \rangle / \langle D_p \rangle$ values should continuously decrease with decreasing gas fraction until $\langle d_p \rangle / \langle D_p \rangle$ equals zero below the critical packing limit, which is reached at ϕ = 63.5 % in monodisperse disordered foams. However, pore openings are still generated for foams with a gas fraction apparently below 63.5 % (see entries 1 and 2, Table 3.2). This apparent

contradiction can be explained by the instant drainage of the polymer solution from the liquid templates at gas fractions below 63.5 %. Consequently, a drainage layer is formed at the bottom of the sample, resulting in an increased gas fraction of the foam on top of the drainage layer and thus the formation of pore openings. Similar ranges for $\langle d_p \rangle / \langle D_p \rangle$ values were found for systems in which the pore openings were adjusted with different methods. In a study by Costantini et al., the pore opening diameters in alginate foams were adjusted by varying the surfactant concentration [Cos15], thus generating foams with different gas fractions by varying the interfacial tension. In this study, $\langle d_p \rangle / \langle D_p \rangle$ values ranging from 0.25 to 0.32 were obtained for surfactant concentrations between 0.6 wt. % and 5 wt. %. For geopolymer- or gelatin-based foams, $\langle d_p \rangle / \langle D_p \rangle$ values ranging from 0.15 to 0.38 were found [Tri19, Pit20a, Lan20]. In these studies, the gas fraction of the liquid templates was directly varied by mixing a geopolymer- or gelatin-containing dispersion/solution with a drained liquid precursor foam consisting of an aqueous surfactant solution.

3.1.3 Comparison of pore opening diameters to bubble contact zones in liquid foams

If the pore openings are generated by the rupture of thin films between neighboring bubbles, the pore opening diameters can be directly determined by the thin film diameters between neighboring bubbles. To examine this hypothesis, all experimentally obtained results for $\langle d_p \rangle / \langle D_p \rangle$ were plotted against the gas fraction (Figure 3.5) and were compared to theoretical predictions for $\langle d_b \rangle / \langle D_b \rangle$. $\langle d_b \rangle / \langle D_b \rangle$ is the ratio of the mean bubble contact zone diameter to the mean bubble diameter. As can be seen from Tables 3.1 and 3.2, the pore diameters of the cross-linked hydrogel foams are almost identical to the bubble diameters of the liquid templates. Consequently, it can be assumed that the shrinkage during cross-linking is counterbalanced by an isotropic swelling of the hydrogel matrix in deionized water, and that the gas fraction in the liquid templates equals the gas fraction in the cross-linked hydrogel foams. Thus, the gas fraction obtained for cross-linked hydrogel foams can be related to the gas fraction in the liquid state.

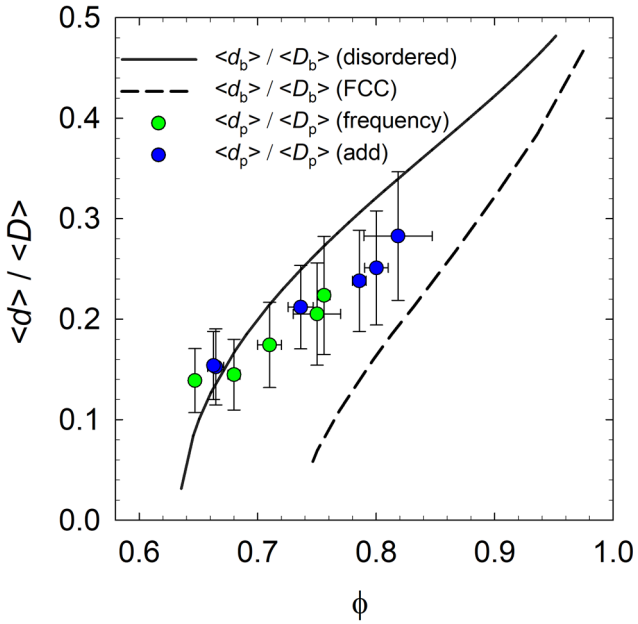

Figure 3.5: Experimentally determined values for $\langle d_p \rangle / \langle D_p \rangle$ obtained by adding polymer solution (blue) and varying the bubbling frequency (green) plotted against the gas fraction ϕ. The errors for $\langle d_p \rangle / \langle D_p \rangle$ were determined by an error propagation, whereas the errors for ϕ correspond to standard deviations. The solid line represents theoretical predictions for disordered foams and the dashed line represents theoretical predictions for ordered foams. Adapted from [Deh21a], Copyright 2021, with permission from Elsevier.

Note that values obtained for foams with gas fractions below 63.5 % are not shown as they cannot be compared to the other samples due to the formation of a drainage layer. Theoretical predictions for $\langle d_b \rangle / \langle D_b \rangle$ in Figure 3.5 were plotted for (a) monodisperse disordered systems [Prin88, Ard04] (solid line) and (b) monodisperse ordered systems (dashed line), obtained from Surface Evolver simulations for hexagonally close-packed (FCC) systems [Pit20a, Pit20b]. Looking at Figure 3.5, one sees that the experimental data lie between the predictions for ordered and disordered systems. At high gas fractions, the data points start to approach the predictions for ordered systems. Indeed, a similar trend can be observed when looking at foams with high gas fraction in Figure 3.4 and 3.5. For these samples, a higher degree of pore ordering can be observed. The increased degree of ordering at higher gas fractions is due to a stronger interaction between bubbles, which lead to the formation of the energetically more favorable FCC packing structure. For low gas fractions, the data points tend to be closer to the predictions for disordered systems, which indicates that the pore opening diameters in cross-linked hydrogel foams are indeed determined by the thin film diameters in the liquid templates.

In summary, two complementary methods to decouple the pore opening diameter from the pore diameter were introduced, which enable the systematic variation of the pore opening diameters in hydrogel foams independently of the pore diameter. Both methods complement existing

approaches as they allow for working at low surfactant concentrations and avoid using multiple formulations. The experimentally obtained values lie between predictions for disordered and ordered foams. For low gas fractions, the ratios $\langle d_p \rangle / \langle D_p \rangle$ correlate well with predictions for disordered foams, which indicates that the pore opening diameters are indeed determined by the thin film diameters in the liquid template.

3.2 Gelatin-based foamed and non-foamed hydrogels for sorption and controlled release of metoprolol (Publication II)

In **Publication II**, the properties of GM10 based hydrogel foams entailed by the polymer functionality were studied. As outlined in Section 3.1.1, staining of the GM10 hydrogel foams with methylene blue most likely takes place via an ionic interaction between the cationic dye methylene blue and the negatively charged carboxyl groups of GM10. To examine whether this effect can be transferred to other cationic molecules, we studied the interaction between the cationic model drug metoprolol and GM10. For this purpose, the sorption and release behavior of metoprolol was examined under both equilibrium and non-equilibrium conditions by measuring sorption and release isotherms and sorption and release kinetics. In addition, the results obtained for foamed hydrogels with a defined morphology ($\langle D_p \rangle$ = 147 ± 3 µm, $\langle d_p \rangle$ = 26 ± 6 µm) were compared to non-foamed samples to elucidate the role of the hydrogel morphology.

3.2.1 Sorption and release isotherms

The interaction between metoprolol and GM10 under equilibrium conditions was examined by measuring sorption and release isotherms. To obtain the sorption isotherm (Figure 3.6, left), the amount of sorbed metoprolol per sample mass, $q_{e,a}$, was plotted against the equilibrium concentration of metoprolol in the supernatant, $c_{e,a}$.

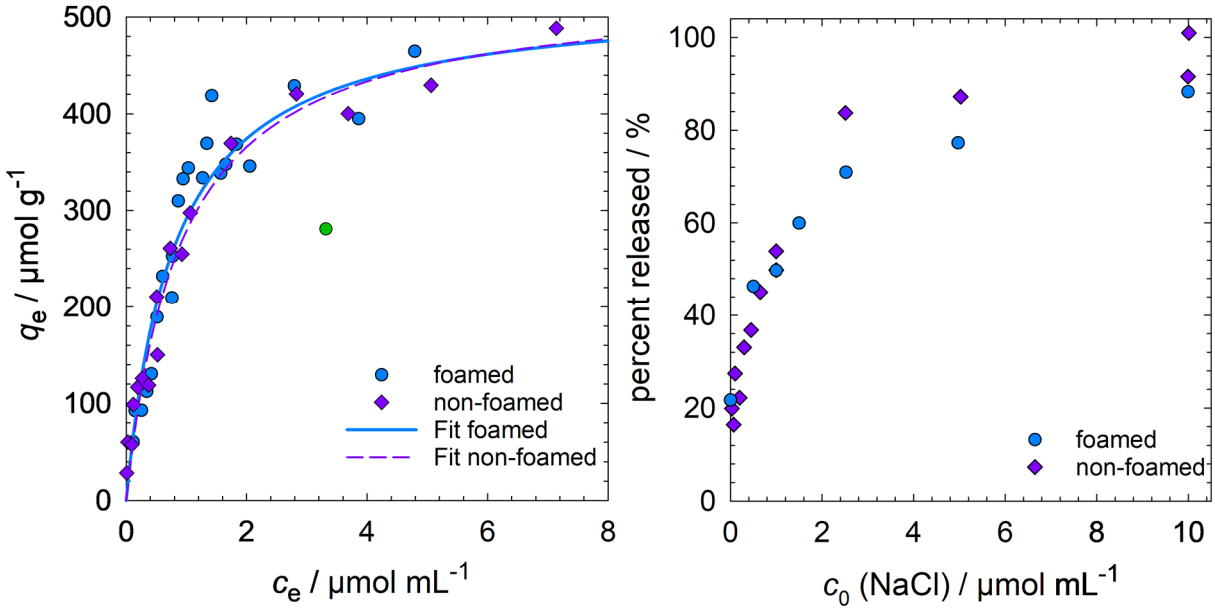

Figure 3.6: (left) amount of metoprolol $q_{e,a}$ inside foamed and non-foamed GM10 hydrogels plotted against the equilibrium concentration $c_{e,a}$ of metoprolol in the supernatants. The lines represent fits according to the Langmuir equation (see Equation 3.1). The data point marked in green was not included when fitting the data. (right) Percentage of released metoprolol for foamed and non-foamed hydrogels plotted against the concentration c_0 of NaCl in the surrounding medium. Before the release experiments, all samples were loaded with 248 ± 10 µmol g^{-1} metoprolol. Adapted with permission from [Deh21b]. Copyright 2021 American Chemical Society.

Regardless of the morphology, $q_{e,a}$ increases with increasing $c_{e,a}$ values until a plateau is reached. The two curves are very similar, which shows that the sample morphology does not influence the sorption behavior in equilibrium. Thus, it can be concluded that no size exclusion effects occur and that metoprolol has the same accessibility to all sorption sites. The obtained data were analyzed using the *Langmuir* model [Lan18]. It holds

$$q_{e,a} = q_{max} \frac{K_s c_{e,a}}{1 + K_s c_{e,a}}, \tag{3.1}$$

where K_s is the equilibrium constant, which represents the ratio of the sorption and the desorption rate constants, and q_{max} is the sorption capacity. The obtained values for K_s and q_{max} are listed in Table 3.3.

Table 3.3: *Langmuir* isotherm parameters for the sorption of metoprolol on foamed and non-foamed samples. The values are obtained by nonlinear regression. The data points were weighted using the reciprocal of the probability density function via the kernel density estimate. Adapted with permission from [Deh21b]. Copyright 2021 American Chemical Society.

	K_s / mL µmol^{-1}	q_{max} / µmol g^{-1}
foamed	1.3	522
non-foamed	1.1	531

Almost the same values are obtained for foamed and non-foamed samples, demonstrating again that the morphology does not influence the sorption behavior. The obtained values for K_s are close to one, which implies that the rate constants of sorption and desorption in both materials are approximately the same, i.e. that the interaction between metoprolol and GM10 is not very strong. Although metoprolol and heavy metal ions cannot be directly compared, much larger K_s-values are obtained for the sorption of Pb^{2+} ions on alginate/polyurethane foams (K_s ~ 11 mL µmol^{-1}) [Son09]. For q_{max}, values of 520 – 530 µmol g^{-1} were obtained, which amounts to approximately 142 mg g^{-1} of sorbed metoprolol. Surprisingly, this corresponds to only half the amount of carboxyl groups theoretically available in GM10 (1128 µmol g^{-1} for gelatin type B, composed of 427 µmol g^{-1} aspartic acid and 701 µmol g^{-1} glutamic acid [Sew19]) and might be due to unavailable carboxyl groups.

The release of sorbed metoprolol under equilibrium conditions was examined by immersing samples loaded with metoprolol ($q_{e,a}$ = 248 ± 10 µmol g^{-1}) into sodium chloride solutions with different concentrations. The percentage of released metoprolol was plotted against the initial sodium chloride concentration (Figure 3.6, right). Regardless of the morphology, the percentage of released metoprolol increases with increasing concentration of sodium chloride until a plateau is reached. Again, both curves are very similar, which demonstrates that the morphology of the hydrogel also does not play a role in the release behavior. The plateau corresponds to a release of up to 90 % - 100 %, indicating that the material can be fully regenerated upon immersion into sodium chloride solution. The results also suggest that the sorption of metoprolol occurs indeed via ion exchange with the hydrogel matrix. Upon immersion in PBS, 100 % of metoprolol is released as well. At a sodium chloride concentration of 0 µmol mL^{-1} (deionized water), 20 % of metoprolol is released. This might be due to the weak interaction between metoprolol and gelatin, which is also indicated by the low K_s value.

3.2.2 Sorption and release kinetics

The sorption and release behavior under non-equilibrium conditions was examined by measuring sorption and release kinetics. For this purpose, foamed and non-foamed GM10 samples were immersed into metoprolol solutions with concentrations of 0.2 µmol mL^{-1} and 1 µmol mL^{-1}. Figure 3.7 (top left and top right) shows the amount of sorbed metoprolol at a time t, $q_{t,\mathrm{a}}$, plotted against the time. It can be seen that $q_{t,\mathrm{a}}$ increases with increasing time until a plateau is reached. This plateau represents the amount of sorbed metoprolol per sample mass in equilibrium, $q_{\mathrm{e,a}}$, and is the same for both sample morphologies (see Section 3.2.1), demonstrating again that the morphology does not influence the equilibrium state. By contrast, the initial slopes of the $q_{t,\mathrm{a}}$ (t)-curves considerably differ for the two different morphologies. The data were analyzed using the *Lagergren* pseudo-first-order equation [Lag98]. It reads

$$q_{t,\mathrm{a}} = q_{\mathrm{e,a}}(1 - \mathrm{e}^{-k_{\mathrm{a}}t}), \tag{3.2}$$

where k_{a} is the sorption rate coefficient. The obtained values for $q_{\mathrm{e,a}}$ and k_{a} are listed in Table 3.4. A similar behaviour can be observed for the release kinetics, where samples loaded with 254 ± 10 µmol g^{-1} metoprolol were immersed into sodium chloride solutions with concentrations of 1 µmol mL^{-1} and 10 µmol mL^{-1}. Figure 3.7 (bottom left and bottom right) shows the amount of released metoprolol at a time t, $q_{\mathrm{e,a}} - q_{t,\mathrm{d}}$, plotted against the time. It can be seen that $q_{\mathrm{e,a}} - q_{t,\mathrm{d}}$ increases with increasing time until a plateau is reached. This plateau represents the amount of released metoprolol per sample mass in equilibrium, $q_{\mathrm{e,d}}$, and is again the same for both sample morphologies (see Section 3.2.1). By contrast, the initial slopes of the ($q_{\mathrm{e,a}} - q_{t,\mathrm{d}}$) ($t$)-curves considerably differ for the two different morphologies. The data were analyzed using equation 3.3. It reads

$$q_{\mathrm{e,a}} - q_{t,\mathrm{d}} = q_{\mathrm{e,d}}\,(1 - \mathrm{e}^{-k_{\mathrm{r}}t}), \tag{3.3}$$

where k_{r} is the sorption rate coefficient. The obtained values for $q_{\mathrm{e,d}}$ and k_{r} are listed in Table 3.4.

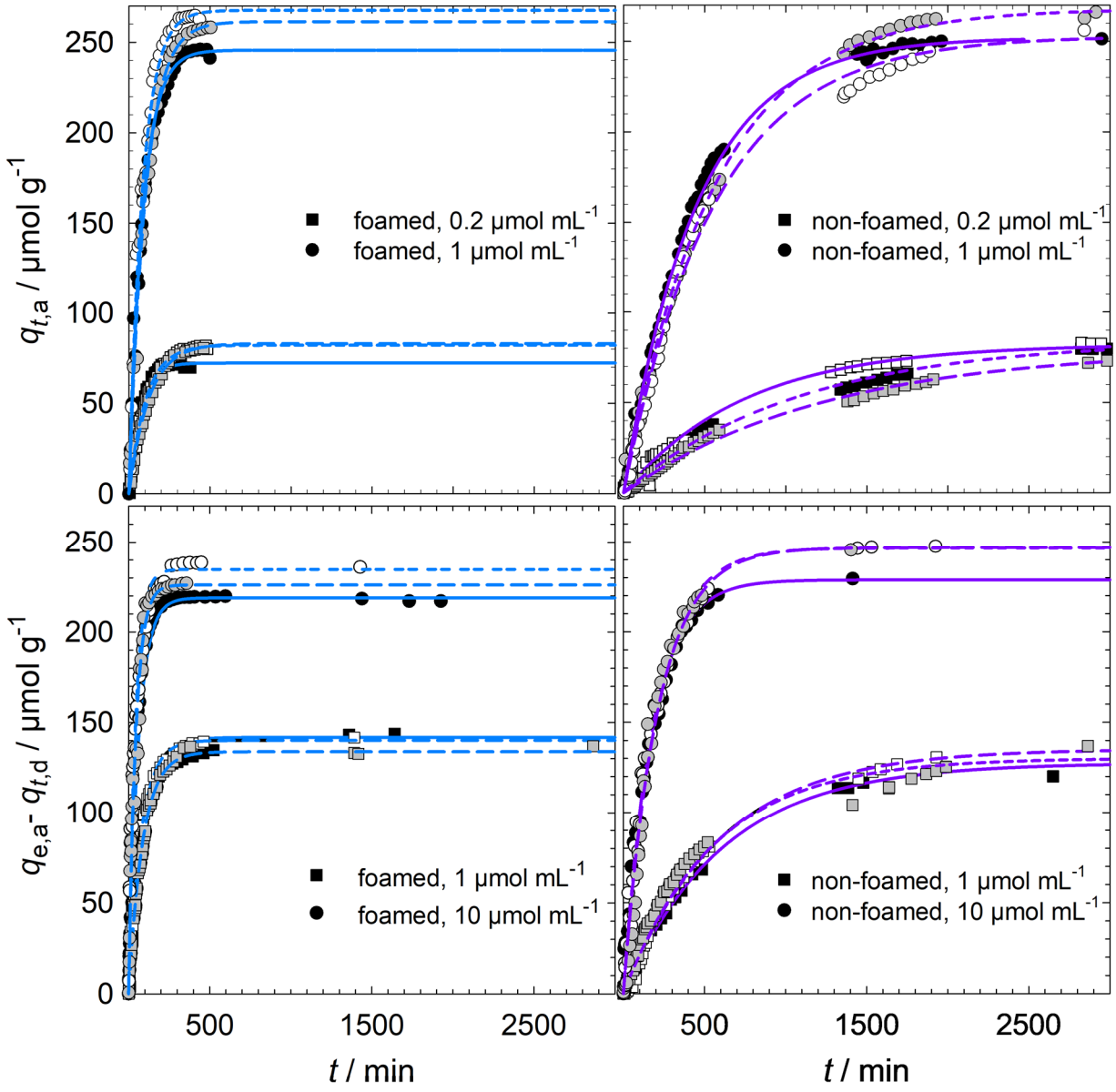

Figure 3.7: (top) Metoprolol concentrations $q_{t,a}$ inside foamed (left) and non-foamed (right) hydrogels against time t. c_0 = 1 µmol mL^{-1} and 0.2 µmol mL^{-1} metoprolol were used as starting concentrations. The solid lines represent fits according to equation (3.2). (bottom) Amount of released metoprolol, $q_{e,a} - q_{t,d}$, for foamed (left) and non-foamed (right) hydrogels against time t. Before the release experiments, the samples were loaded with 254 ± 10 µmol g^{-1} metoprolol. 10 µmol mL^{-1} and 1 µmol mL^{-1} sodium chloride solutions were used as release media. The solid lines represent fits according to equation (3.3). Adapted with permission from [Deh21b]. Copyright 2021 American Chemical Society.

Table 3.4: Kinetic parameters k_a and $q_{e,a}$ for the sorption of metoprolol on foamed and non-foamed hydrogels using different metoprolol concentrations c_0. Kinetic parameters k_r and $q_{e,d}$ for the release of metoprolol from foamed and non-foamed hydrogels using different sodium chloride concentrations c_0. Before the release experiments, all samples were loaded with 254 ± 10 µmol g^{-1} metoprolol. The values are obtained by nonlinear regression and the listed errors are standard deviations. The data points were weighted by using the reciprocal of the probability density function via the kernel density estimate. Adapted with permission from [Deh21b]. Copyright 2021 American Chemical Society.

		c_0 (metoprolol) / µmol mL^{-1}	k_a / hr^{-1}	$q_{e,a}$ / µmol g^{-1}
sorption	foamed	0.2	0.64 ± 0.19	79 ± 6
		1	0.67 ± 0.07	258 ± 11
	non-foamed	0.2	0.061 ± 0.017	82 ± 2
		1	0.12 ± 0.015	258 ± 9
		c_0 (NaCl) / µmol mL^{-1}	k_r / hr^{-1}	$q_{e,d}$ / µmol g^{-1}
release	foamed	1	0.71± 0.05	139 ± 4
		10	1.27 ± 0.23	227 ± 8
	non-foamed	1	0.102 ± 0.005	131 ± 4
		10	0.31 ± 0.03	241 ± 10

Looking at the values for k_a and k_r, one sees a pronounced difference between foamed and non-foamed samples. Compared to the non-foamed samples, the k_a- and k_r-values of the foamed samples are up to 10 times or 7 times higher, which can be ascribed to the larger surface area and the shorter diffusion paths in foamed hydrogels. During sorption, metoprolol crosses the surface of the hydrogel and diffuses through the meshes of the hydrogel network until it interacts with the polymer network. In an ideal case, equilibrium is attained when metoprolol is evenly distributed on the hydrogel network. The characteristic diffusion time τ of a metoprolol molecule is determined by the average distance d a molecule covers as well as the diffusion coefficient of metoprolol in the hydrogel matrix D_h. It holds for τ [Atk08]

$$\tau \sim \frac{d^2}{D_h}. \tag{3.4}$$

The average distance d can also be correlated to the penetrated volume V and the hydrogel surface A. It holds

$$d \sim \frac{V}{A}. \tag{3.5}$$

Looking at equations 3.4 and 3.5 and assuming that D_h is the same for all samples, one sees that a shorter diffusion path through the hydrogel results in a faster penetration of the whole sample volume, which, in turn, leads to a shorter equilibration time and thus to larger sorption rate coefficients. The difference in diffusion paths between foamed and non-foamed hydrogels is evident when looking at the shapes of the samples. Defining the maximum diffusion path as the maximum distance to the surface, $d_{max,1}$ is 1 mm in non-foamed hydrogels and is 30 µm or 17 µm for foamed hydrogels with a pore diameter $\langle D_p \rangle$ = 147 µm. For non-foamed samples, this value can be estimated based on the height of the sample. For foamed samples, $d_{max,2}$ equals the radius of tetrahedral or octahedral voids, assuming a hexagonal close packing of pores. It holds for the radius of octahedral (equation 3.6) and tetrahedral voids (equation (3.7))

$$d_{max,2} = \left(\sqrt{2} - 1\right) \cdot \frac{D_p}{2} \approx 0.207 \cdot D_p \tag{3.6}$$

and

$$d_{max,2} = \left(\frac{\sqrt{6}}{2} - 1\right) \cdot \frac{D_p}{2} \approx 0.112 \cdot D_p. \tag{3.7}$$

Figure 3.8 visualizes the sorption process in foamed and non-foamed hydrogels.

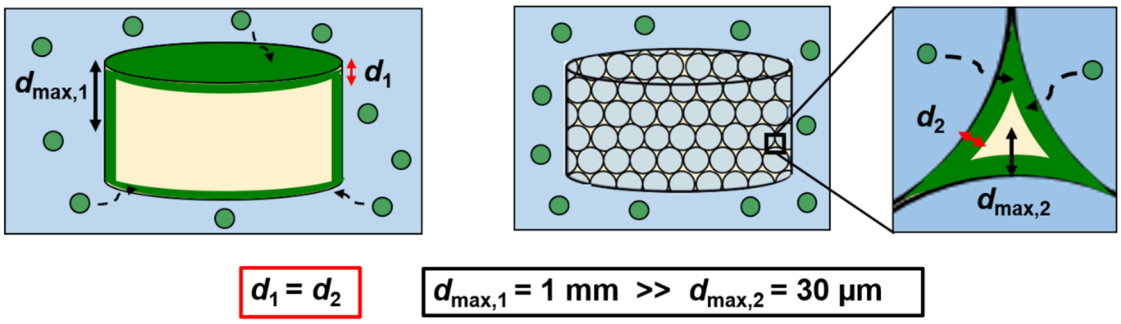

Figure 3.8: Schematic drawing of the sorption process in non-foamed (left) and foamed (right) hydrogels. The metoprolol molecules (green) cross the surface of the hydrogel matrix (yellow) and diffuse through the meshes of the hydrogel. The blue circles represent the water-filled pores. The average distance a metoprolol molecule has covered at a given time t is denoted as d, whereas the maximum distance to the surface is denoted as d_{max}. The indices 1 and 2 denote non-foamed and foamed samples, respectively. Note that $d_{max,2}$ is much shorter compared to $d_{max,1}$. Consequently, the metoprolol solution penetrates a bigger fraction of the available hydrogel matrix at a given time t. Adapted with permission from [Deh21b]. Copyright 2021 American Chemical Society.

In foamed hydrogels, metoprolol additionally diffuses through the water-filled pores. However, the diffusion coefficient of an ion in water, D_w, is much higher than that of an ion in the hydrogel matrix, D_h [Pot96]. Thus, the diffusion through the pores of the hydrogel foams can be neglected. Note that the properties of the hydrogel (e.g. the equilibrium swelling degree) might also change during sorption, which might, in turn, change D_h. Furthermore, D_h depends on the local occupation of sorption sites if the system is not in equilibrium.

As mentioned above, similar trends can be observed for the release of metoprolol. As the release of metoprolol is essentially the sorption of sodium ions on the sorption sites, the explanations given above can also be applied to the release of metoprolol. Thus, the higher k_r values can again be ascribed to shorter diffusion paths in the foamed samples. Surprisingly, the sorption and release rate coefficients are the same for initial concentrations of 1 µmol mL^{-1} metoprolol or sodium chloride. This implies that the sorption and release in this system are truly complementary processes.

In addition to the hydrogel morphology, the initial metoprolol or sodium chloride concentration also affects k_a and k_r. The influence of the initial metoprolol or sodium chloride concentration is more pronounced for non-foamed hydrogels, where k_a was two times higher when increasing the initial metoprolol concentration from 0.2 µmol mL^{-1} to 1 µmol mL^{-1}, or k_r was three times higher when increasing the sodium chloride concentration from 1 µmol mL^{-1} to 10 µmol mL^{-1}. By contrast, no increase in k_a was observed for foamed samples, while k_r was only 1.8 times higher. To explain why the concentration influences k_a and k_r, it is useful to consider the rate coefficients as a measure for the mass transfer of metoprolol or sodium ions, which is influenced by the gradient of $q_{t,a}$ or $q_{e,a} - q_{t,d}$ within the hydrogel matrix. As $q_{t,a}$ or $q_{e,a} - q_{t,d}$ are related to the concentrations via the *Langmuir* isotherm, which is only linear for small equilibrium concentrations $c_{e,a}$, the gradient $q_{t,a}$ or $q_{e,a} - q_{t,d}$ within the hydrogel matrix should differ for different concentrations, if higher $c_{e,a}$ values are obtained in the non-linear range of the *Langmuir* isotherm. The stronger influence of the concentration on k_a and k_r in non-foamed hydrogels compared to foamed hydrogels might again be ascribed to the larger diffusion paths in non-foamed samples. Finally, the obtained data also suggest that sodium and metoprolol have a similar affinity to the sorption sites. As seen from Table 3.4, ~ 139 µmol mL^{1} metoprolol are released when immersing loaded samples into a 1 µmol mL^{-1} sodium chloride solution and ~ 241 µmol mL^{-1} metoprolol are released when immersing the samples into a 10 µmol mL^{-1} sodium chloride solution. All samples were loaded by immersing them into a 1 µmol mL^{-1} metoprolol solution with the same volume as the release medium. The released amounts of

metoprolol correspond to a release of 55 % and 95 %, which would also be expected if both ions had the same affinity to the sorption sites.

In addition to the published results, the release of metoprolol was also examined for PBS as release medium, which has a total ion concentration of 151 µmol mL^{-1}. Figure 3.9 shows the amount of released metoprolol at a time t, $q_{e,a} - q_{t,d}$, plotted against the time.

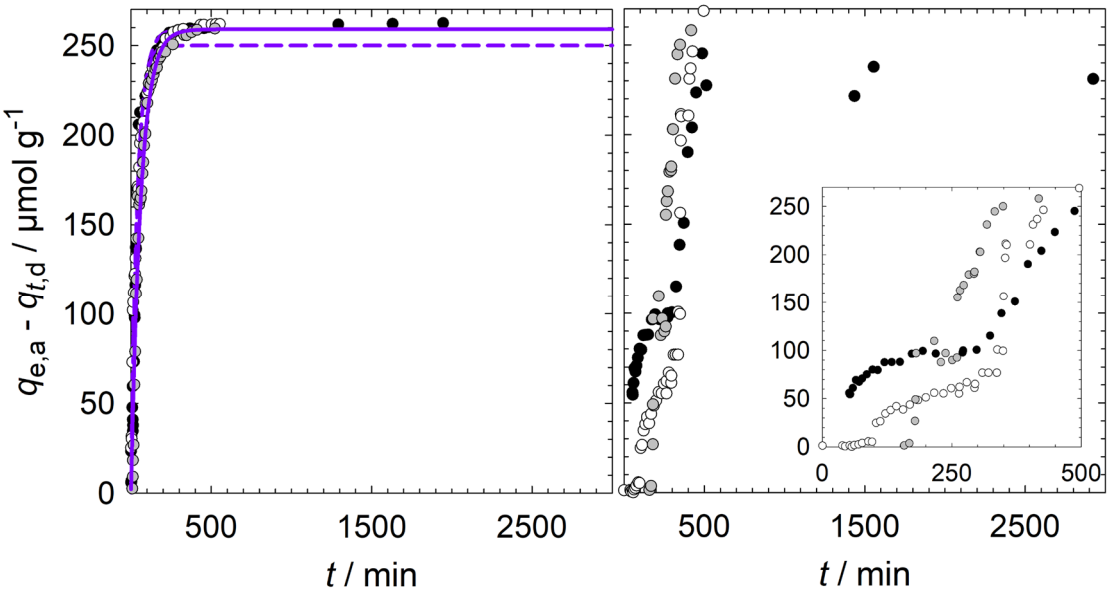

Figure 3.9: Amount of released metoprolol, $q_{e,a} - q_{t,d}$, for non-foamed (left) and foamed (right) hydrogels. The inset shows the release during the first 500 min. The release medium is PBS. Before the release experiment, the samples were loaded with 266 ± 4 µmol g^{-1} metoprolol. The solid lines represent the fits according to equation (3.3). The data points were weighted by using the reciprocal of the probability density function via the kernel density estimate.

For non-foamed hydrogels (Figure 3.9, left), $q_{e,a} - q_{t,d}$ increases with increasing time until a plateau is reached, which represents the amount of released metoprolol in equilibrium. The obtained data were analyzed using equation 3.3. The analysis resulted in a release rate coefficient $k_r = 1.4 \pm 0.3$ h^{-1} and an amount of released metoprolol in equilibrium of $q_{e,d} = 268 \pm 3$ µmol g^{-1}, which corresponds to a release of 100 %. The errors are standard deviations. Compared to the values obtained for sodium chloride as release medium, one sees that k_r is considerably increased and is even in the range of k_r values for foamed hydrogels. This effect can again be ascribed to the increased ion concentration in the release medium. While the increase in k_r for non-foamed hydrogels follows the trend already seen before, the behavior of foamed hydrogels is quite different. For foamed hydrogels, the amount of released metoprolol also increases with increasing time (Figure 3.9, right). However, metoprolol can only be detected in the supernatant after a certain induction period of ~ 60 – 150 min (see insets,

Figure 3.9, right). After this induction period, the amount of released metoprolol steeply increases until a plateau is reached at ~ 100 – 170 min. Afterward, the amount of released metoprolol increases again until 100 % of metoprolol is released. This is a rather surprising outcome, which might be explained by the volume shrinkage of the hydrogel matrix at high salt concentrations, occurring for both foamed and non-foamed hydrogels. While this process might occur over a longer time period in non-foamed hydrogels due to the larger diffusion path, the hydrogel matrix in foamed hydrogels might collapse instantaneously. This rapid volume shrinkage might also cause a collapse of the pore openings in foamed hydrogels, which would lead to an accumulation of metoprolol inside the water filled pores and thus to an irregular release of metoprolol. However, this effect must be further examined to explain it properly. For example, the release of metoprolol from hydrogel foams with different pore opening diameters could be examined.

In summary, the material properties entailed by the carboxyl groups in GM10 were examined by studying the sorption and release behavior of the cationic model drug metoprolol in hydrogels with two different morphologies. While the morphology did not influence the sorption and release behavior in equilibrium, a pronounced effect was observed for non-equilibrium conditions, i.e. sorption and release kinetics. For the foamed hydrogels, the rate coefficients were up to 10 times higher compared to the non-foamed hydrogels, which can be ascribed to the decreased diffusion length. Furthermore, the sorption and release rate coefficients are influenced by the initial metoprolol and sodium chloride concentrations, respectively, and increase with increasing concentrations. For very high ion concentrations, however, foamed hydrogels show an irregular release behavior, which might be caused by the volume shrinkage of the hydrogel matrix.

3.3 New gelatin-based hydrogel foams for improved substrate conversion of immobilized horseradish peroxidase (Publication III)

In **Publication III**, the carboxyl groups in GM10 were chemically modified to add a new functional group to the material. For this purpose, biotin groups were tethered to GM10 with the overall aim to immobilize the model enzyme streptavidin-horseradish peroxidase (Strep-HRP) on the hydrogel foams via the biotin-streptavidin interaction. Thus, **Publication III** deals with the synthesis of biotinylated GM10, the generation of foamed and non-foamed hydrogels based on this polymer, and the immobilization of Strep-HRP on the generated materials. Furthermore, the substrate conversion rate was assessed for different hydrogel morphologies.

3.3.1 Synthesis of biotinylated gelatin methacryloyl

Biotinylated gelatin methacryloyl (GM10EB) was synthesized via a two-step procedure starting from GM10. In the first reaction step, primary amino groups were introduced to GM10 by modifying the carboxyl groups of the polymer with EDA, using EDC as a coupling agent. The reaction product is referred to as GM10E. Afterward, biotin was tethered to the polymer backbone by reaction of amino groups with NHS-dPEG®4-biotin. The reaction product is referred to as GM10EB. Figure 3.10 shows the corresponding reaction scheme.

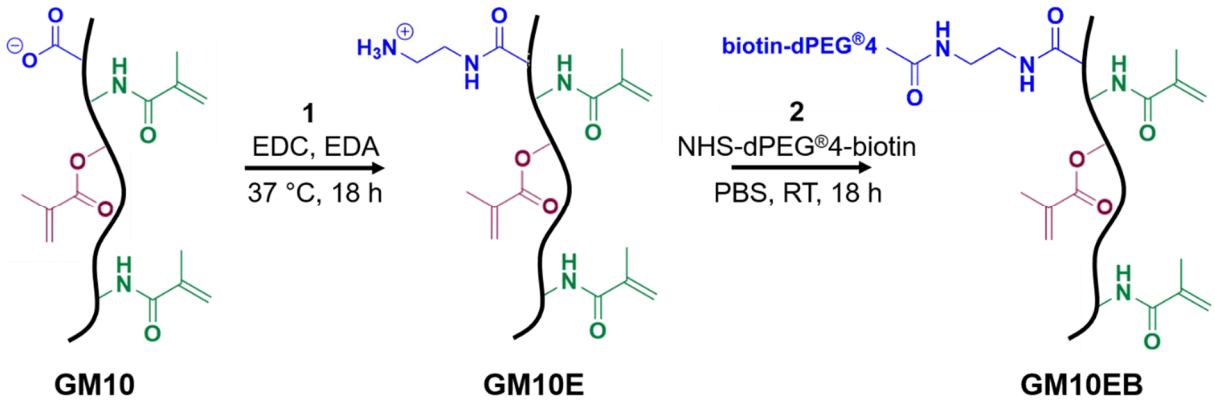

Figure 3.10: Reaction scheme for synthesizing biotinylated gelatin methacryloyl (GM10EB). Step 1: Synthesis of GM10E by modification of carboxyl groups in GM10. Step 2: Synthesis of GM10EB by biotinylating amino groups in GM10E with NHS-dPEG®4-biotin. Reprinted from [Deh22], with permission from Wiley-VCH, open access article.

The first reaction step was performed according to a procedure previously described by Claaßen et al. [Cla19]. Compared to the original procedure, less EDA and EDC were used to maintain a constant isoelectric point (IEP). This is because a high amino group content causes a considerably increased IEP [Cla19], which might lead to different non-specific protein interactions between different gelatin derivatives when immobilizing Strep-HRP. The obtained reaction product was completely soluble in PBS and deionized water, indicating that the polymer chains are not cross-linked, as is sometimes the case when a bifunctional reagent is used during amide coupling. The amino group content (*DE*) of GM10E was quantified with the TNBS-assay, which is based on the reaction of primary amino groups with 2,4,6-trinitrobenzenesulfonic acid. This reaction leads to a color development, which can be used to quantify the content of primary amino groups. A *DE* of 71 ± 2 µmol mg^{-1} was obtained. This corresponds to a modification of 6.8 % of carboxyl groups in GM10 or 0.8 % of all amino acids [Sew18] in gelatin. For comparison, the TNBS-assay was also performed for GM10, where no

amino groups were detected ($DE = -2 \pm 2$ µmol mg^{-1}). This is in accordance to previously obtained results [Cla18a]. Table 3.5 summarizes the obtained values.

Table 3.5: Methacryloyl group content (*DM*), amino group content (*DE*), and biotin content (*DB*) of different gelatin derivatives. The errors are standard deviations, except for *DB* (TNBS), where the error was derived from an error propagation. Adapted from [Deh22], with permission from Wiley-VCH, open access article.

gelatin derivative	*DM* / mmol g^{-1}	*DE* / µmol g^{-1}	*DB* (TNBS) / µmol g^{-1}	*DB* (HABA/Avidin) / µmol g^{-1}
GM10	0.94	-2 ± 2	-	-
GM10E	0.97	71 ± 2	-	-
GM10EB	0.94	38 ± 1	33 ± 3	26 ± 2

In the second reaction step, GM10E was biotinylated by reaction of amino groups with NHS-dPEG®4-biotin. The obtained reaction product (GM10EB) was completely soluble in PBS and deionized water, yielding a slightly opalescent solution. The amino group content of GM10EB was again determined with the TNBS-assay, yielding a considerably decreased *DE* of 38 ± 1 µmol g^{-1} (Table 3.5), which confirms the consumption of amine groups and is thus an indirect measure for the biotinylation. Consequently, the biotin content (*DB*) can be determined indirectly by subtracting the *DE* of GM10EB from the *DE* of GM10E. A *DB* of 33 ± 3 µmol g^{-1} was obtained (Table 3.5), which corresponds to 3.2 % of the carboxyl groups in GM10 or 0.4 % of all amino acids [Sew18]. In addition to this indirect method, the *DB* was also directly quantified with the HABA/Avidin-assay, in which 4'-hydroxyazobenzene-2-carboxylic acid coordinated to avidin is displaced by biotin. The displacement results in a color change at 500 nm that is used to quantify the biotin content. According to the HABA/Avidin assay, the *DB* of GM10EB is 26 ± 2 µmol g^{-1} (Table 3.5). This is in good agreement to the value obtained with the TNBS-assay. The slightly lower value of *DB* obtained with the HABA/Avidin assay might be ascribed to steric hindrance, resulting from biotin being bound to a large macromolecule. In addition, the lower value might also be caused by a slight overestimation of the *DE* in GM10E due to coordinatively bound EDA, which is removed during the second reaction step. The synthesized gelatin derivatives were also analyzed with ^{1}H-NMR to determine the methacryloyl content (*DM*) after each reaction step. Figure 3.11 shows the ^{1}H-NMR spectra of different gelatin derivatives in D_2O. The methacryloyl group content is particularly important for generating hydrogels and hydrogel foams based on these polymers, which occurs via radical cross-linking of methacryloyl groups. Furthermore, a high

methacryloyl group content also ensures a low viscosity of aqueous polymer solutions, which is essential for microfluidic foaming.

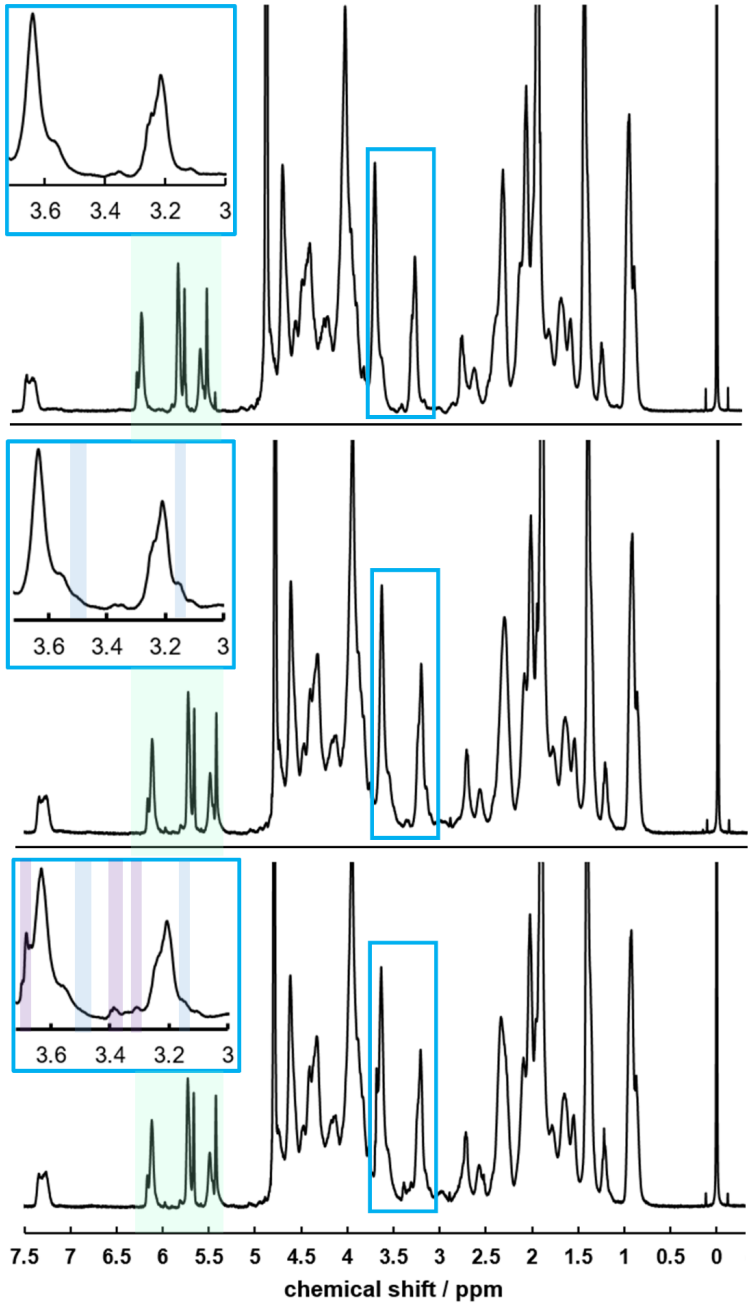

Figure 3.11: ^{1}H-NMR spectra of different gelatin derivatives (top: GM10, middle: GM10E, bottom: GM10EB) in D_2O. The signals of the acrylic protons of the methacryloyl groups are marked in green. The insets show signals between 3.7 ppm and 3.0 ppm. The EDA-related signals are marked in blue, while the signals related to dPEG®4 are marked in purple. Adapted from [Deh22], with permission from Wiley-VCH, open access article.

The *DM* was determined by analyzing the methacryloyl signals between 5.9 ppm and 5.6 ppm according to Claaßen et al. [Cla18a]. Table 3.5 summarizes the obtained values. Comparing the *DM* for different gelatin derivatives, the values are virtually unchanged. Thus, a high *DM* is

maintained throughout different synthesis steps. This is in contrast to previously published work, where a significant decrease in *DM* was obtained for GM10E [Cla19]. We ascribe the constant *DM* value obtained for GM10E in this thesis to the lower amount of EDA in the reaction mixture, which might prevent side reactions such as aminolysis or hydrolysis of methacryloyl groups. Looking at the ^{1}H-NMR spectra, one also sees that even though only a low amount of carboxyl groups was modified, additional signals appear in the spectra of GM10E and GM10EB. Compared to the ^{1}H-NMR spectrum of GM10 (Figure 3.11, top), the ^{1}H-NMR spectrum of GM10E (Figure 3.10, middle) shows two additional shoulders at 3.50 ppm and 3.15 ppm. These signals belong to the CH_2-groups of EDA, as was also shown in previously published work [Cla19]. Furthermore, new signals at 3.68, 3.39, and 3.31 ppm appear in the ^{1}H-NMR spectrum of GM10EB (Figure 3.11, bottom), which might either belong to CH_2-groups of the dPEG®4 spacer or might result from a shift of the EDA-related signals.
In addition, the effect of the modification on the isoelectric point (IEP) of synthesized gelatin derivatives was estimated using the ExPASy tool (https://web.expasy.org/compute_pi/, 22/04/22, 1.06 pm) as described previously [Cla19]. The calculated IEPs of GM10, GM10E, and GM10EB were 4.2, 4.4 and 4.3, respectively. This indicates that the modification of GM10 does not result in a pronounced change in the IEP. Thus, large differences in non-specific protein interactions between different gelatin derivatives and Strep-HRP are not expected when PBS is used as a buffer.

3.3.2 Preparation and characterization of foamed and non-foamed hydrogels

Hydrogel foams based on all synthesized gelatin derivatives were prepared with liquid foam templating using microfluidic foaming. The applied gas pressures p, the liquid flow rates v_L, and the obtained bubble diameter $\langle D_b \rangle$ are listed in Table 3.6.

Table 3.6: Liquid flow rate v_L and gas pressure p used for the generation of liquid foam templates from different gelatin derivatives via microfluidic foaming. Bubble diameter $\langle D_b \rangle$ of liquid foam templates, pore diameters $\langle D_p \rangle$, and pore opening diameters $\langle d_p \rangle$ of cross-linked hydrogel foams. The errors are standard deviations. Adapted from [Deh22], with permission from Wiley-VCH, open access article.

gelatin derivative	v_L / µL min^{-1}	p / mbar	$\langle D_b \rangle$ / µm	$\langle D_p \rangle$ / µm	$\langle d_p \rangle$ / µm
GM10	25	500	154 ± 2	147 ± 3	26 ± 6
GM10E	20	300	140 ± 3	128 ± 4	26 ± 6
GM10EB	20	290	154 ± 2	127 ± 3	31 ± 7

As can be seen from Table 3.6, very similar values for $\langle D_b \rangle$ were obtained, which demonstrates that the bubble diameter of the liquid foam templates can still be easily controlled during microfluidic foaming even though different gelatin derivatives are used. To achieve a similar bubble diameter, however, small changes in v_L and p are necessary, which implies that the physico-chemical properties of GM10E and GM10EB solutions are slightly different from those of GM10 solutions. Upon irradiation with UV light, hydrogel foams were obtained, indicating that the amino- or biotin functionalization does not hinder radical cross-linking. The generated samples were stained with methylene blue and then examined with confocal fluorescence microscopy. No methylene blue visibly leached out of the hydrogel foams when immersing them in deionized water. Thus, the functionalization of GM10 also does not impede the interaction between metoprolol and the hydrogel network. Figure 3.12 shows exemplary pictures of hydrogel foams based on different gelatin derivatives.

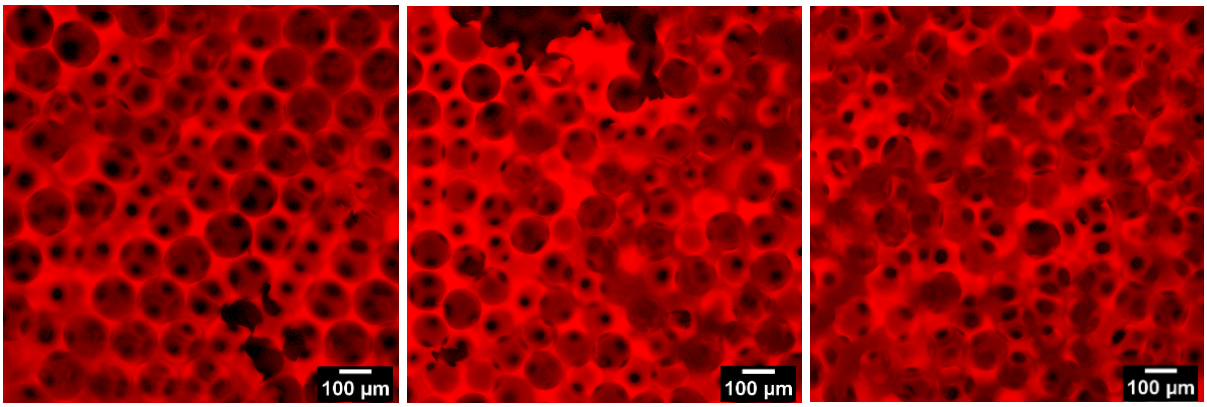

Figure 3.12: Confocal fluorescence microscopy images of hydrogel foams based on GM10 (left), GM10E (middle), and GM10EB (right). The samples were stained with methylene blue. Reprinted from [Deh22], with permission from Wiley-VCH, open access article.

Table 3.6 summarizes the obtained values for the pore diameter $\langle D_p \rangle$ and the pore opening diameter $\langle d_p \rangle$. All samples had similar values for $\langle d_p \rangle$. By contrast, the values for $\langle D_p \rangle$ varied for different gelatin derivatives when comparing them to the corresponding values for $\langle D_b \rangle$. This effect is most pronounced for hydrogel foams based on GM10EB, where the pore diameter is reduced by 18 % compared to the bubble diameter. In GM10 and GM10E hydrogel foams, the pore diameter is reduced by 5 % and 9 %, respectively, compared to the bubble diameter. This indicates that the functionalization also causes a different cross-linking behavior. The change of the pore diameter compared to the bubble diameter was calculated according to $\frac{\langle D_b \rangle - \langle D_p \rangle}{\langle D_b \rangle}$. Non-foamed hydrogels based on all gelatin derivatives were prepared by curing

aqueous solutions of the different polymers. Compared to GM10 and GM10E samples, which were optically clear, GM10EB samples were slightly opaque, which might be due to the introduction of hydrophobic biotin groups.

3.3.3 Strep-HRP immobilization and ABTS conversion

To examine whether the biotin groups are intact and accessible for the immobilization of Strep-HRP, foamed and non-foamed GM10EB samples were exposed to a Strep-HRP solution, using GM10 and GM10E samples as controls. All hydrogel samples were exposed to Strep-HRP only after hydrogel formation, because the large amount of radicals generated during cross-linking as well as subsequent sample processing in organic solvents and at elevated temperatures might damage the protein. To examine the immobilization of Strep-HRP, the 2,2′-azino-bis(3-ethylbenzothiazoline-6-sulfonic acid (ABTS)-assay was performed after thorough sample washing. In this assay, horseradish peroxidase oxidizes the colorless ABTS to blueish-green $ABTS^{+}\bullet$, which can be followed by UV/VIS spectroscopy. Figure 3.13 shows pictures of hydrogel samples after a reaction time of 30 min and the corresponding UV/VIS spectra of the supernatants.

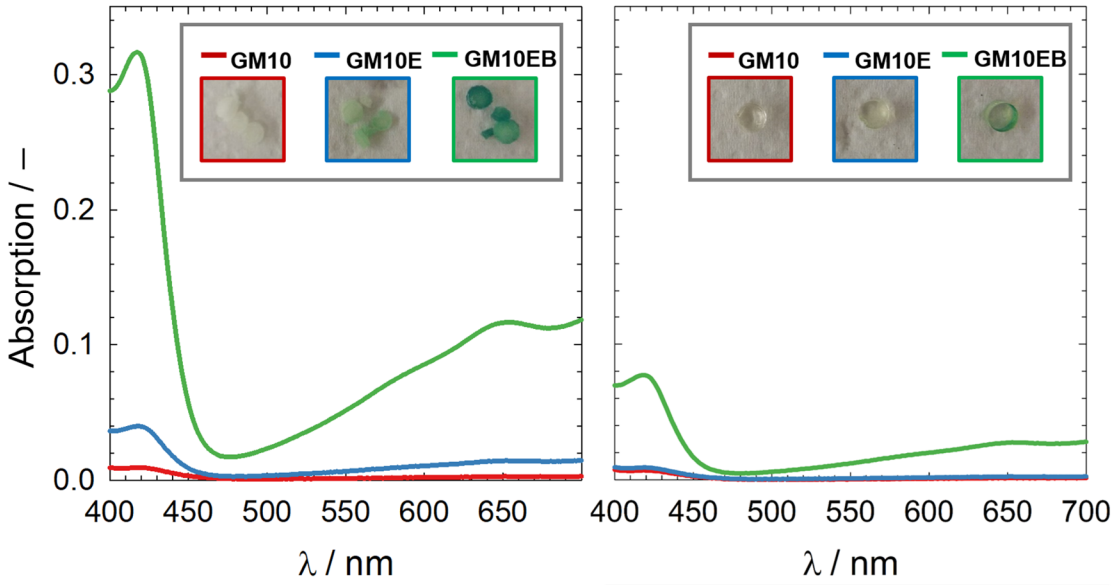

Figure 3.13: Representative UV/VIS-spectra of the supernatants of the ABTS assay after a reaction time of 30 min, using foamed hydrogels (left) and non-foamed hydrogels (right). The reaction was stopped by adding 1 % SDS solution. The insets show pictures of the respective hydrogel samples. Reprinted from [Deh22], with permission from Wiley-VCH, open access article.

As can be seen from Figure 3.13, the absorption for both foamed and non-foamed GM10EB samples (green lines) is considerably higher than that for GM10 and GM10E samples (red and blue lines). Furthermore, the GM10EB hydrogel samples are more stained than the GM10 and GM10E samples. Both observations indicate that Strep-HRP is predominantly immobilized via the biotin-streptavidin interaction and that non-specific protein interactions can be neglected. However, the absorption in the supernatants of GM10 and GM10E does not equal zero, which demonstrates that a certain degree of non-specific protein interaction occurs.

Comparing foamed to non-foamed samples, one also sees that the supernatants of foamed samples have a much higher absorption than non-foamed samples. This indicates a different ABTS conversion rate, which was examined more closely for foamed and non-foamed GM10EB samples. Figure 3.14 shows the time-dependent absorption for supernatants of foamed and non-foamed GM10EB samples at 416 nm.

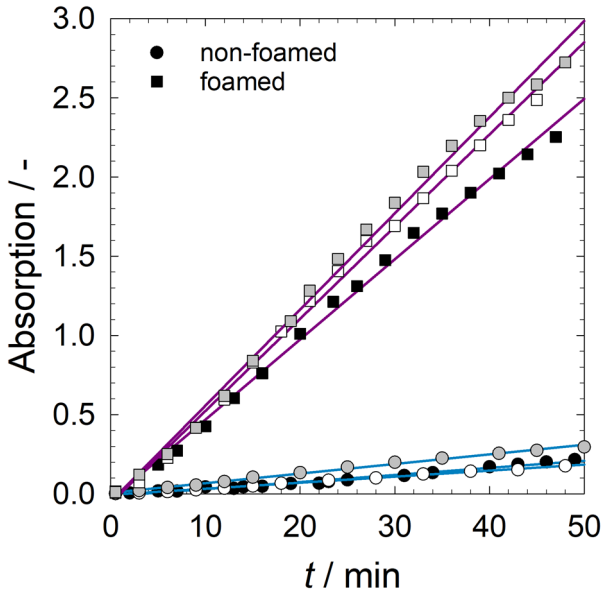

Figure 3.14: Time-dependent absorption of the supernatants at 416 nm for foamed (purple) and non-foamed (blue) Strep-HRP-loaded GM10EB hydrogels. Three independent measurements are shown for foamed and non-foamed hydrogels, respectively. Reprinted from [Deh22], with permission from Wiley-VCH, open access article.

The slopes of the linear regression lines represent the substrate conversion rates r_A. For the foamed samples, a 12 times higher rate of $r_A = 3.4 \pm 0.3\ h^{-1}$ was obtained compared to the non-foamed samples ($r_A = 0.29 \pm 0.07\ h^{-1}$). The errors are standard deviations. The difference in r_A might be explained by two different mechanisms depending on the location of the enzyme. If the enzyme is located near the surface of the samples, the increased surface area of the foamed

samples might lead to an increased amount of immobilized enzymes due to a larger number of accessible biotin groups, resulting in a higher r_A value. Based on a rough estimation, the surface area of the foamed samples is approximately $A \approx 1900$ mm^2 and thus 40 times larger than that of the non-foamed hydrogels of the same mass ($A \approx 50$ mm^2). On the other hand, if the enzyme is evenly distributed within the hydrogel matrix, the higher r_A value might be caused by diffusion, i.e., shorter diffusion lengths in the foamed samples (see Section 3.2) lead to a faster transport of substrate and product to and from the enzyme and thus to a larger r_A value. Note, however, that it has been shown that even if the enzyme is evenly distributed within the hydrogel matrix, the substrate conversion often occurs in a small catalytically active layer located 200 – 400 nm away from the surface [Mar93]. In such a case, r_A in foamed samples is higher compared to non-foamed samples due to a greater amount of enzymes being exposed to the substrate containing medium, which is caused by the larger surface area.

Further information on the enzyme distribution might be gained by quantifying the amount of immobilized Strep-HRP. However, the porous structure of the foamed hydrogels impedes an accurate characterization of proteins in the washing solutions. Thus, commonly used methods, such as quantifying Strep-HRP in the supernatant before and after loading, could not be successfully applied. Nonetheless, it can be strongly assumed that the immobilization of Strep-HRP on GM10EB hydrogels occurs near the surface of the hydrogel due to two reasons. Firstly, an excess of biotin groups is provided (~ 170 nmol biotin per samples of the same mass, compared to 4.7 pmol Strep-HRP in the loading solution), which increases the probability that Strep-HRP binds closely to the surface before it reaches the bulk of the hydrogel. Secondly, Strep-HRP has a relatively large hydrodynamic radius [Cla18b], which might also hinder its diffusion deep into the hydrogel matrix. Thus, we assume that the increased substrate conversion rate in foamed hydrogels is due to an increased amount of immobilized enzyme compared to non-foamed hydrogels, caused by the larger surface area. Note that in any case, the use of foamed hydrogels also allows for using both enzyme and generated polymer more efficiently, since the bulk of the hydrogels most likely does not participate in the substrate conversion.

In summary, a new biotinylated gelatin derivative (GM10EB) was synthesized, which allows for the immobilization of Strep-HRP via the biotin-streptavidin interaction. We showed that the new gelatin derivative GM10EB can also be used to generate hydrogel foams with defined pore diameters via microfluidic foaming. When comparing the substrate conversion rate r_A of Strep-HRP immobilized on foamed and non-foamed hydrogels, a 12 times larger rate was found for the foamed hydrogels, which is most likely due to an increased amount of immobilized enzyme

caused by the larger surface area of the foamed samples. The higher substrate conversion rate Strep-HRP immobilized on foamed hydrogels suggests that r_A can be adjusted by tailoring the hydrogel morphology.

4. Conclusions and Outlook

The objective of the present work was to extend the tailorability and applicability of gelatin methacryloyl (GM)-based hydrogel foams by focusing on both the morphology and polymer functionality of these materials. To this end, this work was divided into three parts.

In the first part, we tailored the morphology of GM-based hydrogel foams by adjusting the pore opening diameters $\langle d_p \rangle$ independently from the pore diameter $\langle D_p \rangle$. For this purpose, the gas fraction and the bubble diameter were decoupled during the generation of liquid foam templates via two complementary methods: (1) the addition of polymer solution to liquid foam templates produced at high initial gas fractions and thus large bubble diameters and (2) the variation of the bubbling frequency during the generation of liquid foam templates with low initial gas fractions and thus smaller bubble diameters. Decoupling the gas fraction and the bubble diameter was successful in both cases, which was confirmed by variable pore opening diameters at constant pore diameters. The results of both methods show that the ratio of the pore opening diameters to the pore diameters, $\langle d_p \rangle / \langle D_p \rangle$, can be varied from 0.14 to 0.28. The upper and lower limits of the accessible ratios were determined by oxygen inhibition during cross-linking and drainage of liquid from the foam templates, respectively. In future work, the range of $\langle d_p \rangle / \langle D_p \rangle$ might be further expanded by using a more rigorous inert gas atmosphere or slowing down drainage. Comparing the experimentally obtained data with predictions for thin film diameters in liquid foams, we found that our data lie between disordered and FCC-ordered foams. With increasing gas fractions, the experimental data tend more towards predictions for ordered foams, which is due to an increasing degree of pore ordering within the samples. By contrast, the experimental data for low gas fractions agree with predictions for disordered systems, which indicates that the thin film diameters in liquid foams indeed determine the pore opening diameters. Together with previously published work [Deh19], it is now possible to vary two key structural parameters of hydrogel foams, namely the pore opening diameter and the pore diameter, independently, which enables to study the influence of both parameters on specific material properties systematically. This might be particularly interesting in tissue engineering, where the influence of the hydrogel foam morphology on the behavior of cells should be studied.

In the second part, the hydrogel foam properties entailed by the inherently present functional groups were examined. For this purpose, the sorption and release of the cationic model drug metoprolol, which most likely occurs on the carboxyl groups of GM, was studied. Both

equilibrium and non-equilibrium conditions were examined and compared to non-foamed hydrogels to examine the influence of the hydrogel morphology. When studying equilibrium conditions, i.e. sorption and release isotherms, the hydrogel morphology did not influence the sorption and release behavior. The maximum sorption capacity was $q_{max} = 530$ µmol g^{-1}, corresponding to 142 mg g^{-1} metoprolol. The equilibrium constant of sorption was $K_s = 1.3$ mL µmol^{-1}, indicating a relatively weak interaction between metoprolol and GM. Upon immersion in sodium chloride solution or PBS, up to 100 % of sorbed metoprolol was released, which indicates that the sorption of metoprolol occurs via ion exchange and that the material can be entirely regenerated by immersion in salt solutions. When studying non-equilibrium conditions, i.e. sorption and release kinetics, the sample morphology had a pronounced influence on the sorption and release behavior. We obtained up to 10 times higher rate coefficients for foamed hydrogels, which we ascribe to the shorter diffusion paths in the foamed samples. In addition, the initial ion concentration in the sorption or release medium also influences the rate coefficients, resulting in larger rate coefficients when increasing the initial concentrations. For foamed hydrogels, however, an irregular release behavior was found when using very high ion concentrations, which we attribute to the volume shrinkage of the samples. Altogether, the obtained data suggest that the sorption and release rate can be adjusted by two different parameters: the ion concentration and the lengths of the diffusion path. As the diffusion path is directly determined by the pore diameter and, to a certain extent, by the pore opening diameter, tailoring the sorption and release rate might be achieved by adjusting these parameters via microfluidic foaming. Our findings are highly relevant for the potential application of GM-based hydrogel foams in wastewater treatment or drug delivery, where a controllable sorption and release rate is of great importance. In future work, the influence of the pH and the temperature on the sorption and release process should be studied. In addition, the sorption and release behavior of other drugs should be studied.

In the third part, the carboxyl groups in GM were chemically modified to introduce biotin as new functional groups to the hydrogel network. For this purpose, we synthesized a new gelatin derivative by tethering biotin-dPEG®4 moieties to GM using a two-step modification procedure. TNBS- and HABA/Avidin assays as well as ^{1}H-NMR analysis confirmed the biotinylation of GM. Furthermore, a high methacryloyl group content was maintained, which is essential for the cross-linking of polymer chains. In addition

, a high methacryloyl group content is important for ensuring a sufficiently low viscosity for microfluidic foaming. After having generated foamed and non-foamed hydrogels based on the new gelatin derivative, we showed that the streptavidin-conjugated model enzyme horseradish

peroxidase (Strep-HRP) can be successfully immobilized on the materials. This demonstrates that the biotin groups are available for bioconjugation. Thus, the modification of carboxyl groups introduces a new functionality to the hydrogel foams, which might also be used to immobilize other streptavidin-conjugated biomolecules. As many streptavidin-conjugated biomolecules are commercially available, a versatile bioconjugation platform might be created, which might also be used for e.g. biosensing or for protein purification. The influence of the hydrogel morphology on the substrate conversion rate was assessed by comparing foamed to non-foamed hydrogels. The substrate conversion rate was twelve times higher in foamed hydrogels, which might be ascribed to an increased amount of immobilized enzyme due to the larger surface area of the foamed samples. However, the amount of immobilized enzyme could not be quantified due to the porous structure of the foamed hydrogel. Thus, future work should focus on developing a new quantification method based on e.g. eluting Strep-HRP from the hydrogels. Furthermore, it should be examined whether the substrate conversion rate can be tailored by adjusting the surface area of the foamed hydrogels, which is directly determined by the pore diameter and can thus be easily adjusted via microfluidic foaming.

5. Materials and Methods

5.1 Chemicals

All chemicals that were used in this work are listed in Table 5.1. Dialysis was performed using membranes from *Medicell International* (United Kingdom, molecular weight cutoff 12-14 kDa). All chemicals were used as received, except Strep-HRP, from which aliquots were prepared that were stored at -20 °C until further use. All solutions were prepared with deionized water.

Table 5.1: Chemicals used in the thesis at hand.

Chemical	Abbreviation	Supplier
gelatin (type B, bovine bone, 232 bloom, batch #635621 and #641819)		Gelita (Germany)
methacrylic anhydride	MAAnh	Sigma Aldrich (Germany)
sodium 3-trimethylsilylpropionate-2,2,3,3-d_4	TMSP	Merck (Germany)
perfluorohexane (98 %, 85 % *n*-isomer)		abcr (Germany), Sigma Aldrich (Germany)
D_2O		deutero (Germany), eurisotop (United Kingdom)
lithium phenyl-2,4,6-trimethyl-benzoyl phosphinate	LAP	carbosynth (United Kingdom)
Plantacare 2000 UP (active content ~ 53%, water as solvent		Cognis (now BASF, Germany)
methylene blue		S3 chemicals (Germany)
phosphate buffered saline	PBS	Sigma Aldrich (Germany)
metoprolol tartrate		Sigma Aldrich (Germany)
ethanol (absolute)		VWR (Germany)
sodium chloride		VWR (Germany)
Ethylene diamine	EDA	Sigma Aldrich (Germany)

1-ethyl-3-(3-dimethylaminopropyl)carbodiimide	EDC	Sigma Aldrich (Germany)
NHS-dPEG®4-biotin		Sigma Aldrich (Germany)
2,4,6-trinitrobenzenesulfonic acid (1 M in H_2O)	TNBS	Sigma Aldrich (Germany)
glycine		Sigma Aldrich (Germany)
4'-hydroxyazobenzene-2 carboxylic acid/Avidin reagent	HABA/Avidin reagent	Sigma Aldrich (Germany)
bovine serum albumin	BSA	Sigma Aldrich (Germany)
2,2′-azino-bis(3-ethylbenzothiazoline-6-sulfonic acid) (liquid substrate system)	ABTS	Sigma Aldrich (Germany)
sodium hydroxide		VWR (Germany)
sodium hydrogencarbonate		VWR (Germany)
1 N hydrochloric acid (Titrisol)		Merck (Germany)
streptavidin-conjugated horseradish peroxidase (1 mg mL^{-1})	Strep-HRP	abcam (United Kingdom)
sodium dodecyl sulfate (lot 184257)	SDS	fisher scientific (Germany)

5.2 Synthesis and characterization of gelatin derivatives

5.2.1 Synthesis of gelatin derivatives

Gelatin methacryloyl: Gelatin methacryloyl (GM10) was synthesized and characterized according to a procedure described by *Claaßen* et al. [Cla18a]. 25.21 g gelatin type B were dissolved in 250 mL deionized water at 40 °C. To this end, gelatin from batch #635621 was used in **Publication I**, whereas gelatin from batch #641819 was used in **Publication II** and **III**. Once the gelatin was completely dissolved, the temperature was decreased to 37 °C. 13.15 mL (90.46 mmol) MAAnh were added to the solution. As this corresponds to a ten-fold molar excess with respect to free amino groups in gelatin (0.35 mmol g^{-1} according to *van den Bulcke* et al. [Bul00]), the synthesized gelatin derivative is denoted as GM10. The pH of the reaction mixture was adjusted to 7.25 using 4 M NaOH, and was kept between 7.0 and 7.4 throughout the reaction. To this end, an automatic titration device (*Titrino*, *Metrohm*, Switzerland) was used. After a reaction time of 5 h, the crude product was filtered, and the pH was adjusted to

8.5 using 1 M NaOH. The crude product was stored at 8 °C for two days. Afterward, the solution was sterile filtered, and dialyzed against deionized water for 5 days. The purified product was freeze-dried using an *Alpha 1-2 LD* lyophilizer from *Christ* (Germany). Typically, a yield of 70 – 80 % was obtained.

Gelatin methacryloyl aminoethyl: Gelatin methacryloyl aminoethyl (GM10E) was synthesized according to a procedure modified after *Claaßen* et al. [Cla19]. 4 g of GM10 which were estimated to contain a carboxyl group amount of 4.51 mmol (1 eq., based on the carboxyl group content in gelatin type B (1.128 mmol g^{-1} [Sew18])), were dissolved in 40 mL deionized water at 37 °C. 204 µL (184 mg, 3.05 mmol, 0.68 eq.) EDA were added to the solution. The pH was quickly adjusted to 4.5 using 1 N HCl. Afterward, 65 mg (0.34 mmol, 0.075 eq.) EDC were dissolved in 220 µL of deionized water and the solution was quickly added to the reaction mixture. The reaction mixture was stirred for 18 h and was subsequently filtered to remove the precipitate that formed during the reaction. To remove ionic impurities, the filtered product was dialyzed against a 9 g L^{-1} NaCl solution for two days. Afterward, the solution was dialyzed against deionized water for 2 days. The purified product was freeze-dried using an *Alpha 1-2 LD* lyophilizer from *Christ* (Germany). 3.43 g of GM10E (86 %) were obtained.

Biotinylated gelatin methacryloyl: Biotinylated gelatin methacryloyl (GM10EB) was synthesized by tethering biotin-dPEG®4 to GM10E. To this end, 2 g of GM10E (containing 0.14 mmol, 1 eq., amino groups) were dissolved in 39 mL of PBS at room temperature. 113.7 mg (1.36 eq.) NHS-dPEG®4-biotin were dissolved in 900 µL PBS and were added to the reaction mixture. After a reaction time of 18 h, the reaction mixture was sterile filtered, yielding a slightly opalescent solution. The crude product was dialyzed against deionized water for 6 days. Afterward, the solution was sterile filtered and subsequently freeze-dried using an *Alpha 1-2 LD* lyophilizer from *Christ* (Germany). 1.72 g (86 %) of GM10EB was obtained. Figure 5.1 shows the chemical structure of NHS-dPEG®4-biotin.

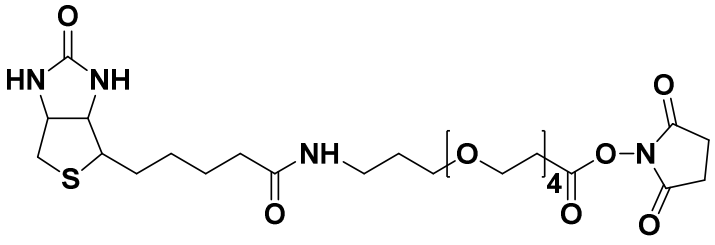

Figure 5.1: Chemical structure of NHS-dPEG®4-biotin.

5.2.2 Characterization of gelatin derivatives

^{1}H-NMR analysis: To determine the methacryloyl group content (*DM*) of GM10, GM10E and GM10EB, ^{1}H-NMR analysis in D_2O was used [Cla18a]. The spectra were recorded with a *Bruker Avance* NMR spectrometer. TMSP was used as an internal standard. The *DM* can be calculated according to

$$DM = \frac{\int \text{methacryloyl}}{\int \text{TMSP}} \cdot \frac{9\text{H}}{1\text{H}} \cdot \frac{n(\text{TMSP})}{m(\text{gelatin derivative})}, \tag{5.1}$$

where $\int$ methacryloyl is the integral of the methacryloyl protons (5.9 – 5.6 ppm), $\int$ TMSP is the integral of the TMSP protons (-0.2 – 0.2 ppm), n(TMSP) is the amount of TMSP in D_2O, and m(gelatin derivative) is the mass of gelatin derivative dissolved in D_2O. The obtained *DM* values varied between 0.88 mmol g^{-1} and 0.97 mmol g^{-1}. The exact *DM* values of the used gelatin derivatives are given in the relevant experimental sections (see Sections 5.3.1 and 5.3.2).

TNBS assay: To determine the amino group contents (*DE*) of GM10, GM10E, and GM10EB, the TNBS assay was performed. To this end, a 0.01 % (w/v) TNBS solution was prepared by diluting a 1 M TNBS solution with 0.1 M $NaHCO_3$ (pH = 8.5). Afterward, 200 µL of the TNBS solution are added to 500 µL of a 1 mg mL^{-1} gelatin derivative solution in 0.1 M $NaHCO_3$. The mixture was incubated at 37 °C under slight agitation in the dark. After 2 h, the reaction was stopped by adding 250 µL of a 10 % SDS solution and 125 µL of 1 N HCl. The absorbance of the solutions at 335 nm was measured in cuvettes with a pathlength of 2 mm, using a *Lambda 25* UV/VIS spectrometer from *Perkin Elmer* (Germany). The experiments were repeated three times. A calibration curve was obtained by performing the TNBS assay for glycine solution with concentrations of 0, 0.026, 0.053, 0.106, and 0.132 µmol mL^{-1} in 0.1 M $NaHCO_3$.

HABA/Avidin assay: To determine the biotin content (*DB*) in GM10EB, the HABA/Avidin assay was performed. Firstly, the HABA/Avidin mixture was reconstituted in 10 mL of deionized water. Afterward, 133 µL of a 0.55 mg mL^{-1} GM10EB solution in PBS were added to 1.2 mL HABA/Avidin mixture. A *Lambda 25* UV/VIS spectrometer from *Perkin Elmer* (Germany) was used to measure the absorbance of the solution at 500 nm before and after the addition of the GM10EB solution. To this end, cuvettes with a pathlength of 5 mm were used. The experiment was performed in triplicates. A calibration curve was generated by performing

the HABA/Avidin assay for NHS-dPEG®4-biotin solutions with concentrations of 0, 56, 111, 166, and 222 nmol mL^{-1} in PBS.

5.3 Preparation of foamed and non-foamed hydrogels

5.3.1 Preparation of foamed hydrogels

Preparation of polymer solutions: Gelatin derivative solutions that were used to prepare foamed hydrogels contained 0.14 wt. % of LAP, 0.1 wt. % of Plantacare 2000 UP, and 20 wt. % of GM10, GM10E, or GM10EB, respectively. Deionized water was used to prepare the solutions. All flasks were wrapped in aluminum foil to prevent premature activation of the photo initiator. In **Publication I**, the solution was additionally stored at 8 °C until further use. The *DM* values of gelatin derivatives used to prepare foamed hydrogels are listed in Table 5.2.

Table 5.2: *DM* values of gelatin derivatives used to prepare foamed hydrogels in different publications.

Publication	gelatin derivative	*DM* / mmol g^{-1}
I	GM10	0.88
II	GM10	0.88
III	GM10	0.88
	GM10E	0.97
	GM10EB	0.94

Microfluidic foaming: To produce liquid foam templates, a homemade polycarbonate microfluidic chip (Figure 5.2) was used. The chip was fabricated by micro-milling at the *Polish Academy of Sciences*, Warsaw, and had a constriction of 70 µm.

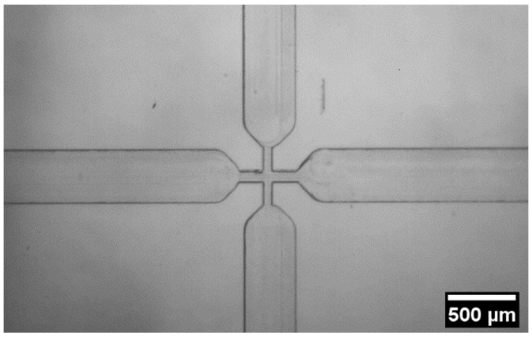

Figure 5.2: Polycarbonate microfluidic chip with a constriction of 70 µm.

The gas phase was pressure controlled, using an *OB1MK1* pressure controller from *Elveflow* (France). To prevent oxygen inhibition during cross-linking of polymer solutions, nitrogen was used as the gas phase. Furthermore, traces of perfluorohexane were added to the gas phase to prevent coarsening. To this end, the outlet of the pressure controller was connected to a glass bottle filled with perfluorohexane. The glass bottle was sealed with a *Vaplock GL45* cap from *fisher scientific* (Germany) and connected to the inlet of the microfluidic chip. The polymer solutions were injected with a *Pump 11 Elite* syringe pump from *Harvard Apparatus* (United States), which allows for controlling the liquid flow rate of the polymer solutions. An *SMZ 745T* bright field microscope from *Nikon* (Japan). equipped with a *KL 500* light source from *Schott* (Germany) was used to monitor the bubbling inside the microfluidic chip. To prevent premature activation of the photo initiator, the light source was covered with a UV-absorbing foil and the tubing was wrapped with aluminium foil. The bright field microscope was connected to an *EoSensCL* high speed camera from *Mikrotron* (Germany). Images were taken with the *MBDirector2KIT* software (version 1.7.11). Figure 5.3 shows an image of the setup. To collect the generated bubbles, a tube was connected to the outlet channel of the microfluidic chip.

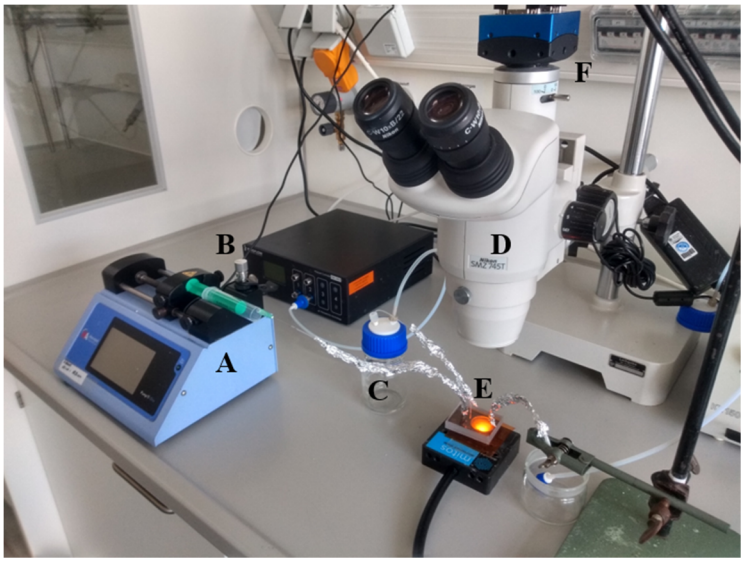

Figure 5.3: Image of the setup used for microfluidic foaming. (A) Syringe pump, (B) pressure controller, (C) glass bottle filled with perfluorohexane, (D) bright field microscope, (E) microfluidic chip, (F) high speed camera.

The same setup was used to generate liquid foams in all publications. However, in **Publication I**, the gas fraction of the liquid foams was additionally adjusted via two different methods, which are described in the following.

Variation of the gas fraction – addition of liquid: To be able to add polymer solution to the generated foam, the setup was slightly modified. A second tube was connected to the outlet channel, which was used to add the same polymer solution. The liquid flow rate of the additional polymer solution v_A was controlled using a *Pump 11 Elite* syringe pump from *Harvard Apparatus* (United States). To avoid feedback loops on the bubble pinch-off at the constriction, the polymer solution was added outside the microfluidic chip. Both tubes were slanted to enable the mixing of the generated foam with the additional liquid. Figure 5.4 shows a schematic drawing of the setup. This setup can also be used to add cross-linking agents to liquid foams [And18a].

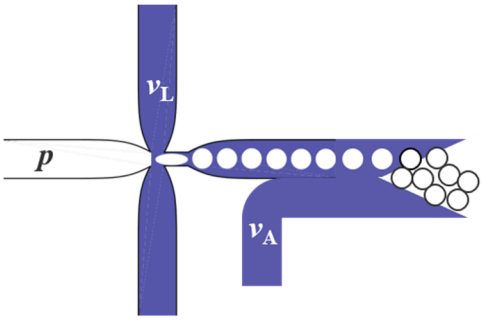

Figure 5.4: Schematic drawing of the experimental setup used to add polymer solution to the generated bubbles. Reprinted from [Deh21a], Copyright 2021, with permission from Elsevier.

Variation of the gas fraction – bubbling frequency: To vary the bubbling frequency, the ratio of liquid flow rate and gas pressure was kept constant at 0.1 µL min^{-1} mbar^{-1}, while continually increasing the absolute values of both parameters from 20 µl min^{-1} and 200 mbar to 80 µl min^{-1} and 800 mbar. Figure 5.5 shows bubbles produced at with different bubbling frequencies. The relation between the bubbling frequency and the gas fraction of the generated foams was first examined for an aqueous surfactant solution [Gar04] but has never been used to tailor the pore opening diameters in polymer foams.

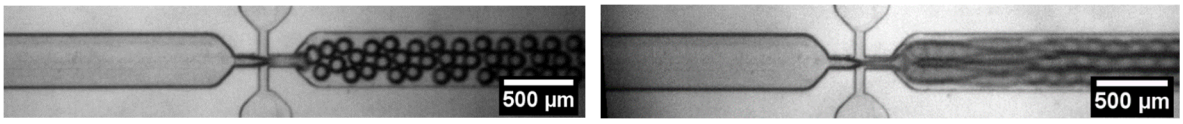

Figure 5.5: Generation of bubbles at different liquid flow rates and gas pressures. (left) v_L = 20 µl min^{-1}, p = 200 mbar, (right) v_L = 80 µl min^{-1}, p = 800 mbar. Adapted from [Deh21a], Copyright 2021, with permission from Elsevier.

The gas pressures p and liquid flow rates v_L and v_A used to produce liquid foams in different publications are listed in Table 5.3.

Table 5.3: Gas pressures p and liquid flow rates v_L and v_A used for the preparation of liquid foam templates based on different gelatin derivatives in different Publications.

Publication	gelatin derivative	gas pressure p / mbar	liquid flow rate v_L / µL min^{-1}	flow rate of additional liquid v_A / µL min^{-1}
I	GM10	260	7	0
		260	7	2
		260	7	3
		260	7	5
		260	7	8
		260	7	11
I	GM10	200	20	0
		300	30	0
		400	40	0
		500	50	0
		600	60	0
		700	70	0
		800	80	0
II	GM10	25	500	0
III	GM10	25	500	0
	GM10E	20	300	0
	GM10EB	20	290	0

Characterization of bubble diameters: To determine the bubble diameters of the generated liquid foams, one drop of the generated foams was collected on a microscope slide. To obtain a bubble monolayer, the foam was diluted with the same polymer solutions that was also used for microfluidic foaming. Images of the bubbles were taken with an *EoSensCL* highspeed camera from *Mikrotron* (Germany) using the *MBDirector2KIT* software (version 1.7.11). Note that the images must be taken quickly, as the bubbles increase in volume over time due to the presence of perfluorohexane. The images were analyzed using the software *ImageJ* (version 1.52p). At least 40 bubble diameters were measured for each sample.

Collection and curing of liquid foam templates: The generated foams were collected in sample containers that were placed under a stream of nitrogen to avoid oxygen inhibition during

cross-linking. In **Publication I**, cylindrical PDMS molds with a diameter of 4 mm and a height of 2 mm were used to collect the samples. In **Publication II** and **III**, cylindrical aluminum molds with a diameter of 2 cm and a height of 2 mm were used to collect the samples. As soon as the sample containers were completely filled, they were covered with a quartz glass pane and irradiated for 4.5 min with UV-A light, using an *Omnicure Series 1500* UV lamp from *Excelitas Technologies* (United States). The UV lamp had a maximum emission spectrum between 360 nm and 370 nm and was operated at 15 % intensity. The samples were placed at a distance of 5 cm to the light guide tip.

Sample processing: In **Publication I**, the samples were frozen for 30 min at -60 °C directly after curing. Afterward, they were freeze-dried using an *Alpha 1-2 LD* lyophilizer from *Christ* (Germany) and stored at room temperature until further use. In **Publication II** and **III**, smaller samples were punched out of the cross-linked hydrogel foam by using a biopsy punch with a diameter of 4 mm. To avoid the formation of ice crystals that might potentially alter the structure and might influence further measurements, the samples were not freeze-dried. Instead, they were washed in deionized water for 3 days at 8 °C to remove residual photo initiator and surfactant. Afterward, the samples were washed in ethanol for one day at 8 °C to sterilize them and to ensure fast evaporation during sample drying. The washing media were changed twice a day. The samples were dried at 60 °C until a constant weight was obtained and were stored at room temperature until further use.

5.3.2 Preparation of non-foamed hydrogels

Preparation of polymer solutions: Gelatin derivative solutions that were used to prepare foamed hydrogels contained 0.14 wt. % of LAP and 20 wt. % of GM10, GM10E or GM10EB, respectively. In **Publication II**, the polymer solution additionally contained 0.1 wt. % of Plantacare 2000 UP. Deionized water was used to prepare the solutions. All flasks were wrapped in aluminum foil to prevent premature activation of the photo initiator. The *DM* values of gelatin derivatives used to prepare non-foamed hydrogels are listed in Table 5.4.

Table 5.4: *DM* values of gelatin derivatives used to prepare non-foamed hydrogels in different Publications.

Publication	gelatin derivative	*DM* / mmol g^{-1}
II	GM10	0.88
III	GM10	0.94
	GM10E	0.97
	GM10EB	0.94

Curing of polymer solutions: The polymer solutions were filled into cylindrical PDMS molds with a diameter of 4 mm and a height of 2 mm. Afterward, the sample containers were covered with a quartz glass pane and were irradiated for 4.5 min with UV-A light, using a *Omnicure Series 1500* UV lamp from *Excelitas Technologies* (United States). The UV lamp had a maximum emission spectrum between 360 nm and 370 nm and was operated at 15 % intensity. The samples were placed at a distance of 5 cm to the light guide tip.

Sample processing: The cured samples were washed in deionized water for 3 days at 8 °C to remove residual photo initiator. Afterward, the samples were washed in ethanol for one day at 8 °C to sterilize them and to ensure a fast evaporation during sample drying. The washing media were changed twice a day. The samples were dried at 60 °C until a constant weight was obtained and were stored at room temperature until further use.

5.4 Characterization of foamed hydrogels

Measurement of gas fraction: The gas fraction ϕ of the hydrogel foams was determined gravimetrically. It holds for the gas fraction

$$\phi = 1 - \frac{m}{w \cdot V_l \cdot \rho}, \tag{5.2}$$

where m is the dry mass of the hydrogel foams, w is the mass fraction of the polymer, V_l is the sample volume in the liquid state, and ρ is the density of the polymer solution. All samples were characterized in triplicates. The density of the polymer solution was determined with a *DMA 5000 M* density meter from *Anton Paar* (Germany). For GM10 solutions with a polymer content of 20 wt. %, a density of $\rho = 1.056$ g cm^{-3} was obtained.

Sample staining: To stain the prepared hydrogel foams, samples with a mass of approximately 2 mg and a volume of 25 mm^3 were immersed into 2 g of a 5 mg L^{-1} methylene blue solution. The samples were slightly agitated at room temperature. After 32 h, the samples were removed from the methylene blue solutions and were immersed in 2 g of deionized water. The samples were washed with deionized water for at least 12 h under slight agitation to remove unbound methylene blue from the gel and the sample pores. The sorption of methylene blue for exemplary samples was followed by UV/VIS spectroscopy using a *Lambda 25* UV/VIS spectrometer from *Perkin Elmer* (Germany).

Confocal fluorescence microscopy: The stained samples were characterized with a *LSM 710* confocal fluorescence microscope from *Zeiss* (Germany) equipped with the *Zen Black* software (version 16.0.0.0). 3D z-stacks consisting of a series of 2D pictures taken along the z-axis were recorded. The distance between two pictures in the 3D stack was 9.6 µm. The samples were placed onto a sample holder from *ibidi* (Germany). A drop of deionized water was placed on top of the samples to prevent drying of the samples during the measurement. An excitation wavelength of 633 nm was used and emitted light was collected between 642 and 747 nm. As only a few pore layers of the sample can be visualized due to light scattering, the samples were cut vertically and horizontally to visualize longitudinal sections and cross-sections of the sample. The first pore layers of the samples have an ordered morphology due to the crystallization of the bubbles caused by the confinement of the sample mold. As the ordered domains are merely surface effects [Mea15], the first pore layers are not considered for further analysis. All samples were characterized in triplicates.

Picture analysis: The obtained pictures were analyzed using the software *ImageJ* (version 1.52p). A logarithmic transformation was applied to all pictures to account for skewed intensities when measuring areas deep inside the hydrogel foam. At least 40 pore diameters D_p and pore opening diameters d_p were measured for each sample. The pore diameter and pore opening diameter were only measured from pictures where both parameters were in the focal plane. This is also exemplary shown in Figure 5.6. If pore opening diameters were in a slightly elliptical shape, the major axis was considered the pore opening diameter.

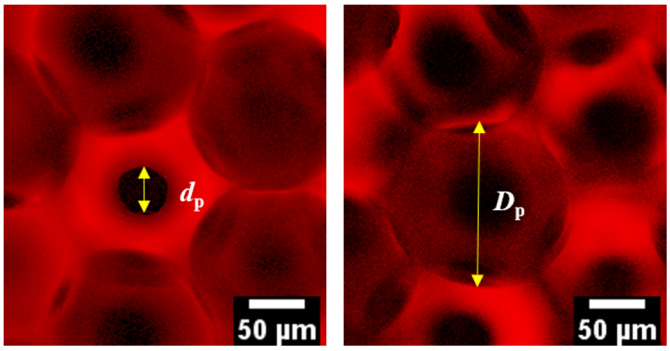

Figure 5.6: 2D pictures of a pore opening (left) and a pore (right) within the same sample. Both pictures show different z-positions within the 3D stack to focus either on the pore opening or the pore. The hydrogel foams are based on GM10. Reprinted from [Deh21a], 2021, with permission from Elsevier.

5.5 Batch sorption and release measurements

5.5.1 Batch sorption measurements

Metoprolol calibration curve: Calibration curves were generated by measuring the absorption of metoprolol tartrate solutions with metoprolol concentrations between 0.04 µmol mL^{-1} and 6 µmol mL^{-1} at a wavelength of 274 nm. To this end, a *Lambda 25* UV/VIS spectrometer from *Perkin Elmer* (Germany) was used. For metoprolol concentrations between 0.04 µmol mL^{-1} and 1.0 µmol mL^{-1}, cuvettes with a pathlength of 10 mm were used. For metoprolol concentrations between 1 µmol mL^{-1} and 6 µmol mL^{-1} cuvettes with a pathlength of 2 mm were used, as in this concentration range, the measured absorption is close to the detection limit of the spectrometer when using cuvettes with a pathlength of 10 mm, which might lead to an inaccurate determination of concentrations.

Sorption isotherms: Sorption isotherms were measured for foamed and non-foamed GM10 hydrogels. The foamed samples had a dry mass between 1.2 and 1.7 g and the non-foamed samples had a dry mass between 5.2 and 5.5 mg. One sample was used for each measurement. All samples were swollen in deionized water for 24 h. Prior to each experiment, the surface of the swollen samples was blotted dry to remove excess water. Afterward, the samples were immersed in 3 mL of a metoprolol tartrate solution with concentrations between 0.06 µmol mL^{-1} and 8 µmol mL^{-1}. The samples were placed on an orbital platform shaker (45 rpm) at room temperature. After 96 h, the UV/VIS spectra of the supernatants were

measured to determine the metoprolol concentration in the supernatant. It holds for the amount of sorbed metoprolol per mass of hydrogel, $q_{e,a}$,[1]

$$q_{e,a} = \frac{(c_0 - c_{e,a}) \cdot V_a}{m}, \tag{5.3}$$

where c_0 is the initial concentration of metoprolol, $c_{e,a}$ [2] is
the equilibrium concentration of metoprolol in the supernatant, V_a is the volume of the metoprolol solution, and m is the dry mass of the samples. The obtained data were fitted to the Langmuir model [Lan18]. It holds

$$q_{e,a} = q_{max} \frac{K_s c_{e,a}}{1 + K_s c_{e,a}}. \tag{5.4}$$

q_{max} is the maximum sorption capacity, K_s is the equilibrium constant, and $c_{e,a}$ is the equilibrium concentration of ions in the surrounding medium. For the regression, the data points were weighted using the reciprocal of the probability density function via the kernel density estimate. Hailey Poole measured the sorption isotherms.

Sorption kinetics: The sorption kinetics were measured for foamed and non-foamed GM10 hydrogels. The samples had a dry mass between 5.2 and 5.3 mg. As one foamed sample had a mass of approximately 1.4 mg, multiple samples had to be used to achieve a mass of 5.2 mg to 5.3 mg. All samples were swollen in deionized water for 24 h. Afterward, the surface of the samples was blotted dry to remove excess water, and the samples were immersed in 3 mL of a 0.2 µmol mL^{-1} or 1 µmol mL^{-1} metoprolol solution. The sorption kinetics were directly measured in a cuvette with a pathlength of 10 mm. Between measurements, the cuvettes were placed onto an orbital platform shaker (45 rpm) at room temperature. At different time points, the absorption of the supernatant was measured using a *Lambda 25* UV/VIS spectrometer from *Perkin Elmer* (Germany). The amount of sorbed metoprolol at a time t per mass of hydrogel, $q_{t,a}$, was determined according to

[1] Note that q depends on the time t. For $t \to \infty$, q is defined as $q_{e,a}$, while for any other value of t, q is defined as q_t to ensure better readability.
[2] Note that c depends on the time t. For $t \to \infty$, c is defined as $c_{e,a}$, while for any other value of t, c is defined as c_t to ensure better readability.

$$q_{t,\mathrm{a}} = \frac{(c_0 - c_t) \cdot V_\mathrm{a}}{m}, \tag{5.5}$$

with c_t being the metoprolol concentration in the supernatant at a time t. All experiments were performed in triplicates. The obtained data were fitted to the pseudo-first-order equation developed by Lagergren [Lag98]. It reads

$$q_{t,\mathrm{a}} = q_{\mathrm{e,a}}(1 - \mathrm{e}^{-k_\mathrm{a} t}). \tag{5.6}$$

k_a is the sorption rate coefficient. For the regression, the data points were weighted using the reciprocal of the probability density function via the kernel density estimate. Hailey Poole measured one replicate of the sorption kinetics for foamed and non-foamed hydrogels.

5.5.2 Batch release measurements

To measure the release of metoprolol, the calibration curves generated in section 5.5.1 were used.

Release isotherms: Release isotherms were measured for foamed and non-foamed GM10 hydrogels. The samples had a dry mass between 5.4 and 5.6 mg. As one foamed sample had a mass of approximately 1.4 mg, multiple samples had to be used to achieve a mass of 5.4 mg to 5.6 mg. To load the samples with metoprolol, they were first swollen in deionized water for 24 h. Afterward, the surface of the samples was blotted dry to remove excess water. The samples were immersed in 3 mL of a 1 µmol mL^{-1} metoprolol solution and were placed on an orbital platform shaker (45 rpm) at room temperature. After 96 h, the UV/VIS spectra of the supernatants were measured to determine the metoprolol concentration in the supernatant. To this end, a *Lambda 25* UV/VIS spectrometer from *Perkin Elmer* (Germany) was used. The samples loaded with metoprolol were placed in 3 mL of sodium chloride solutions with concentrations ranging from 0 µmol mL^{-1} to 10 µmol mL^{-1}. In addition to that, samples loaded with metoprolol were also placed in 3 mL of PBS solution. All samples were placed on an orbital platform shaker (45 rpm) at room temperature. After 96 h, the concentration of metoprolol in the supernatant was determined via UV/VIS spectroscopy. It holds for the percentage of released metoprolol

$$\text{percent released} = \frac{c_{\text{e,d}}}{c_0 - c_{\text{e,a}}} \cdot 100\ \%, \tag{5.7}$$

where $c_{\text{e,d}}$ is the equilibrium concentration of released metoprolol. Hailey Poole measured the release isotherm for non-foamed samples.

Release kinetics: The release kinetics were measured for foamed and non-foamed GM10 hydrogels with a dry mass between 5.2 and 5.3 mg. As one foamed sample had a mass of approximately 1.4 mg, multiple samples had to be used to achieve a mass of 5.2 mg to 5.3 mg. To load the samples with metoprolol, they were first swollen in deionized water for 24 h. Afterward, the surface of the samples was blotted dry to remove excess water, and the samples were immersed in 3 mL of a 1 µmol mL^{-1} metoprolol solution. After 96 h, the UV/VIS spectra of the supernatants were measured to determine the metoprolol concentration in the supernatant. To this end, a *Lambda 25* UV/VIS spectrometer from *Perkin Elmer* (Germany) was used. The loaded samples were immersed in 3 mL of a 1 µmol mL^{-1} or 10 µmol mL^{-1} sodium chloride solution. In addition, 3 mL of PBS were used as release medium. The release kinetics were directly measured in a cuvette with a pathlength of 10 mm. The cuvettes were placed onto an orbital platform shaker (45 rpm) at room temperature. At different time points, the absorption of the supernatant was measured. It holds for the amount of metoprolol released per mass of hydrogel at a time t, $q_{\text{e,a}} - q_{t,\text{d}}$,

$$q_{\text{e,a}} - q_{t,\text{d}} = \frac{c_{t,\text{d}} \cdot V_{\text{d}}}{m}, \tag{5.8}$$

with $q_{\text{t,d}}$ being the amount of sorbed metoprolol per mass of hydrogel at a time t, $c_{t,\text{d}}$ being the concentration of metoprolol in the release medium at a time t, and V_{d} being the volume of the release medium. All experiments were performed in triplicates. To analyze the obtained data, the values were fitted to equation 5.9. It holds for $q_{\text{e,a}} - q_{t,\text{d}}$

$$q_{\text{e,a}} - q_{t,\text{d}} = q_{\text{e,d}}\,(1 - \text{e}^{-k_{\text{r}}t}), \tag{5.9}$$

where $q_{\text{e,d}}$ is the amount of metoprolol released per mass of hydrogel in equilibrium and k_{r} is the release rate coefficient. The data points were weighted using the reciprocal of the probability density function via the kernel density estimate.

5.6 Enzyme immobilization and characterization of substrate conversion

Loading of Strep-HRP onto hydrogels: Strep-HRP was loaded onto foamed and non-foamed hydrogels based on GM10, GM10E, and GM10EB. To this end, all samples were swollen for 24 h in 2 mL of PBS under slight agitation. The swelling medium was changed once. Afterward, the samples were placed in 500 µL of a 1 µg mL^{-1} Strep-HRP solution in PBS. The loading time was 24 h. The samples were washed with 500 µL PBS until no relevant amount of Strep-HRP was detected in the supernatant. To detect Strep-HRP in the supernatant, 200 µL of ABTS substrate were added to 200 µL of washing solution. After thoroughly mixing the solutions, they were placed on an orbital platform shaker (90 rpm) in the dark. After a reaction time of 30 min, the reaction was stopped by adding 400 µL of 1 % SDS in deionized water. The absorption of the solution at 416 nm was measured using a *Lambda 25* spectrometer from *Perkin Elmer* (Germany). To this end, cuvettes with a pathlength of 2 mm were used. Typically, a washing time of 48 h was necessary during which the washing medium was changed 6 times. All solutions, except the ABTS substrate, contained 0.1 % (w/v) BSA to minimize non-specific protein adsorption. All experiments were conducted at room temperature.

ABTS staining: To visualize the Strep-HRP immobilization on different gelatin derivatives, Strep-HRP loaded foamed and non-foamed hydrogels based on GM10, GM10E, and GM10EB were placed in 400 µL ABTS substrate solution under slight agitation. All samples had a dry mass between 5.1 and 5.3 mg. After a reaction time of 30 min, the samples were removed from the ABTS substrate solution and 400 µl of 1 % SDS in deionized water were added to the supernatant to stop the reaction. The absorbance of the solution between 700 nm and 400 nm was measured using a *Lambda 25* UV/VIS spectrometer from *Perkin Elmer* (Germany). Cuvettes with a path length of 2 mm were used.

ABTS conversion: To compare the ABTS conversion for Strep-HRP immobilized on foamed and non-foamed hydrogels based on GM10EB, the samples were placed in 2.5 mL ABTS substrate solution. All samples had a dry mass between 5.6 and 5.7 mg. The ABTS conversion was directly measured inside a cuvette with a pathlength of 10 mm. The cuvettes were sealed with a Teflon stopper and were placed horizontally on an orbital platform shaker at 115 rpm. All experiments were conducted at room temperature. The absorbance of the solution between 700 – 400 nm was measured at different time intervals using a *Lambda 25* UV/VIS spectrometer from *Perkin Elmer* (Germany).

References

[Abo13]: Homaei, A. A.; Sariri, R.; Vianello, F.; Stevanato, R. Enzyme Immobilization: An Update. *J. Chem. Biol.* **2013**, *6*, 185–205.

[Ago07]: Agostinelli, E.; Belli, F.; Tempera, G.; Mura, A.; Floris, G.; Toniolo, L.; Vavasori, A.; Fabris, S.; Momo, F.; Stevanato, R. Polyketone Polymer: A New Support for Direct Enzyme Immobilization. *J. Biotechnol.* **2007**, *127* (4), 670–678.

[Ahm15]: Ahmed, E. M. Hydrogel: Preparation, Characterization, and Applications: A Review. *J. Adv. Res*. **2015**, *6* (2), 105–121.

[Ahs20]: Ahsan, A.; Farooq, M. A.; Parveen, A. Thermosensitive Chitosan-Based Injectable Hydrogel as an Efficient Anticancer Drug Carrier. *ACS Omega* **2020**, *5* (32), 20450–20460.

[Alb02]: Alberts, B., Johnson, A., Lewis, J. Molecular Biology of the Cell. 4th. edition, **2002**, *Garland Science*, *Taylor & Francis*, New York.

[Ali07]: Ali, I.; Gupta, V. K. Advances in Water Treatment by Adsorption Technology. *Nature Protoc.* **2007**, *1* (6), 2661–2667.

[Ald19]: Aldana, A. A.; Malatto, L.; Atiq, M.; Rehman, U.; Boccaccini, A. R.; Abraham, G. A. Fabrication of Gelatin Methacrylate (GelMA) Scaffolds with Nano- and Micro-Topographical and Morphological Features. *nanomaterials* **2019**, *9* (1), 120.

[And17]: Andrieux, S.; Drenckhan, W.; Stubenrauch, C. Highly Ordered Biobased Scaffolds : From Liquid to Solid Foams. *Polymer.* **2017**, *126*, 425–431.

[And18a]: Andrieux, S.; Drenckhan, W.; Stubenrauch, C. Generation of Solid Foams with Controlled Polydispersity Using Microfluidics. *Langmuir* **2018**, *34* (4), 1581–1590.

[And18b]: Andrieux, S.; Quell, A.; Stubenrauch, C.; Drenckhan, W. Liquid foam templating – A route to tailor-made polymer foams. *Adv. Colloid Interface Sci.*, **2018**, *256*, 276-290.

[Ard04]: Arditty, S. Fabrication, Stability and Rheological Properties of Particle-Stabilized Emulsions, PhD Thesis, University of Bordeaux, **2004**.

[Ast08]: T. Aste, D. Weaire: The pursuit of perfect packing, 2nd edition. **2008**, *CRC Press*, Boca Raton.

[Atk08]: Atkins, P.W.; de Paula, J. Kurzlehrbuch Physikalische Chemie, 4th edition. **2008**, *WILEY-VCH Verlag GmbH & Co. KGaA*, Weinheim.

[Aug06]: Augst, A. D.; Kong, H. J.; Mooney, D. J. Alginate Hydrogels as Biomaterials. *Macromol. Biosci.* **2006**, *6* (8), 623–633.

[Bab96]: Babel, W. Gelatine - Ein Vielseitiges Biopolymer. *Chemie unserer Zeit* **1996**, *30* (2), 86–95.

[Bar08]: Barbetta, A.; Massimi, M.; Di Rosario, B.; Nardecchia, S.; De Colli, M.; Devirgiliis, L. C.; Dentini, M. Emulsion Templated Scaffolds That Include Gelatin and Glycosaminoglycans. *Biomacromolecules* **2008**, *9* (10), 2844–2856.

[Bar09]: Barbetta, A.; Gumiero, A.; Pecci, R.; Bedini, R.; Dentini, M. Gas-in-Liquid Foam Templating as a Method for the Production of Highly Porous Scaffolds. *Biomacromolecules* **2009**, *10* (12), 3188–3192.

[Bas20]: Bashir, S.; Hina, M.; Iqbal, J.; Rajpar, A. H.; Mujtaba, M. A.; Alghamdi, N. A.; Wageh, S.; Ramesh, K.; Ramesh, S. Fundamental Concepts of Hydrogels: Synthesis, Properties, and Their Applications. *Polymers* **2020**, *12* (11), 2702.

[Ber02]: Berglund, G. I.; Carlsson, G. H.; Smith, A. T.; Szöke, H.; Henriksen, A.; Hajdu, J. The Catalytic Pathway of Horseradish Peroxidase at High Resolution. *Nature* **2002**, *417*, 463–468.

[Big08]: Bigi, A.; Cojazzi, G.; Panzavolta, S.; Rubini, K.; Roveri, N. Mechanical and Thermal Properties of Gelatin Films at Different Degrees of Glutaraldehyde Crosslinking. *Biomaterials* **2001**, *22* (8), 763–768.

[Bon06]: Bonnaillie, L. M.; Wool, R. P. Thermosetting Foam with a High Bio-Based Content from Acrylated Epoxidized Soybean Oil and Carbon Dioxide. *J. Appl. Polym. Sci.* **2006**, *105* (3), 1042–1053.

[Bro89]: Brown, M.; Pietrzyk, J. Anion-Cation Separations on a Mixed Bed Alumina-Silica Column. *J. Chromatogr.* **1989**, *466*, 291–300.

[Bue13]: Bueno, V. B.; Bentini, R.; Catalani, L. H.; Freitas, D.; Petri, S. Synthesis and Swelling Behavior of Xanthan-Based Hydrogels. *Carbohydr. Polym.* **2013**, *92* (2), 1091–1099.

[Buf86]: Buffham, B. A.; Mason, G.; Meacham, R. I. Sorption-Effect Chromatography. *J. Chromatogr. Sci.* **1986**, *24* (6), 265–269.

[Bul00]: Van Den Bulcke, I.; Bogdanov, B.; De Rooze, N.; Schacht, E.; Cornelissen, M.; Berghmans, H. Structural and Rheological Properties of Methacrylamide Modified Gelatin Hydrogels, *Biomacromolecules*, **2000**, *1*(1), 31-38.

[Bur11]: Burdick, J. A.; Prestwich, G. D. Hyaluronic Acid Hydrogels for Biomedical Applications. *Adv. Healthc. Mater.* **2011**, *23* (12), 41–56.

[Che06]: Cheng, J.; Shao, M. Y.; Peng, Z. Horseradish Peroxidase Immobilized on Aluminum-Pillared Interlayered Clay for the Catalytic Oxidation of Phenolic Wastewater. *Water Res.* **2006**, *40* (2), 283–290.

[Che12]: Chen, Y.; Lin, R.; Qi, H.; Yang, Y.; Bae, H.; Melero-Martin, J. M.; Khademhosseini, A. Functional Human Vascular Network Generated in Photocrosslinkable Gelatin Methacrylate Hydrogels. *Adv. Funct. Mater.* **2012**, *22* (10), 2027–2039.

[Cho08]: Choi, D.; Lee, W.; Kim, D.-N.; Park, J.; Koh, W.-G. Fabrication of Macroporous Hydrogel Membranes Using Photolithography for Enzyme Immobilization. *J. Chem. Technol. Biotechnol.* **2008**, *83*, 252–259.

[Cla18a]: Claaßen, C.; Claaßen, M. H.; Truffault, V.; Sewald, L.; Tovar, G. E. M.; Borchers, K.; Southan, A. Quantification of Substitution of Gelatin Methacryloyl: Best Practice and Current Pitfalls. *Biomacromolecules* **2018**, *19* (1), 42–52.

[Cla18b]: Claaßen, C.; Claaßen, M. H.; Gohl, F.; Tovar, G. E. M.; Borchers, K.; Southan, A. Photoinduced Cleavage and Hydrolysis of O-Nitrobenzyl Linker and Covalent Linker Immobilization in Gelatin Methacryloyl Hydrogels. *Macromol. Biosci.* **2018**, *18* (9), 1–13.

[Cla19]: Claaßen, C.; Rebers, L.; Claaßen, M. H.; Borchers, K.; Tovar, G. E. M.; Southan, A. Expanding the Range of Available Isoelectric Points of Highly Methacryloylated Gelatin. *Macromol. Chem. Phys.* **2019**, *220* (14), 1–9.

[Cla20]: Claus, J.; Eickner, T.; Grabow, N.; Kragl, U.; Oschatz, S. Ion Exchange Controlled Drug Release from Polymerized Ionic Liquids. *Macromol. Biosci.* **2020**, *20* (9), 2000152.

[Coc21]: Cocarta, A.; Hobzova, R.; Trchova, M.; Svojgr, K.; Kodetova, M. 2-Hydroxyethyl Methacrylate Hydrogels for Local Drug Delivery: Study of Topotecan and Vincristine Sorption/Desorption Kinetics and Polymer-Drug Interaction by ATR-FTIR Spectroscopy. *Macromol. Chem. Phys.* **2021**, *222* (13), 2100086.

[Coh59]: Cohen, M.; Turnbull, D. Molecular Transport in Liquids and Glasses. *J. Chem. Phys.* **2004**, *31* (5), 1164–1169.

[Col12]: Colosi, C.; Costantini, M.; Barbetta, A.; Pecci, R.; Bedini, R.; Dentini, M. Morphological Comparison of PVA Scaffolds Obtained by Gas Foaming and Microfluidic Foaming Techniques. *Langmuir* **2013**, *29* (1), 82–91.

[Col15]: Collins, D. J.; Neild, A.; Liu, A.; Ai, Y. The Poisson Distribution and beyond: Methods for Microfluidic Droplet Production and Single Cell. *Lab Chip* **2015**, *15*, 3439–3459.

[Cos15]: Costantini, M.; Colosi, C.; Jaroszewicz, J.; Tosato, A.; Wojciech, S.; Dentini, M.; Garstecki, P.; Barbetta, A. Microfluidic Foaming : A Powerful Tool for Tailoring the Morphological and Permeability Properties of Sponge-like Biopolymeric Scaffolds. *ACS Appl. Mater. Interfaces* **2015**, *7*, 23660–23671.

[Cos16]: Costantini, M.; Colosi, C.; Mozetic, P.; Jaroszewicz, J.; Tosato, A.; Rainer, A.; Trombetta, M.; Wojciech, Ś.; Dentini, M.; Barbetta, A. Correlation between Porous Texture and Cell Seeding Efficiency of Gas Foaming and Microfluidic Foaming Scaffolds. *J. Mater. Chem. B* **2016**, *62*, 668–677.

[Cos19]: Costantini, M.; Jaroszewicz, J.; Kozoń, Ł.; Szlązak, K.; Święszkowski, W.; Garstecki, P.; Stubenrauch, C.; Barbetta, A.; Guzowski, J. 3D-Printing of Functionally Graded Porous Materials Using On-Demand Reconfigurable Microfluidics. *Angew. Chemie - Int. Ed.* **2019**, *131* (23), 7702-7707.

[Dab21]: Dabrowski, M. L.; Stubenrauch, C. Methacrylate-Based Polymer Foams with Controllable Pore Sizes and Controllable Polydispersities via Foamed Emulsion Templating. *Adv. Eng. Mater.* **2021**, *23* (3), 2001013.

[Das02]: Das, P. K.; Caaveiro, J. M. M.; Luque, S.; Klibanov, A. M. Binding of Hydrophobic Hydroxamic Acids Enhances Peroxidase's Stereoselectivity in Nonaqueous Sulfoxidations. *J. Am. Chem. Soc.* **2002**, *124* (5), 7294–7299.

[Dav01]: Davis, B. G.; Boyer, V. Biocatalysis and Enzymes in Organic Synthesis. *Nat. Prod. Rep.* **2001**, *18*, 618–640.

[Deh19]: Dehli, F.; Rebers, L.; Stubenrauch, C.; Southan, A. Highly Ordered Gelatin Methacryloyl Hydrogel Foams with Tunable Pore Size. *Biomacromolecules* **2019**, *20* (7), 2666–2674.

[Deh21a]: Dehli, F.; Southan, A.; Drenckhan, W.; Stubenrauch, C. Tailoring and Visualising Pore Openings in Gelatin-Based Hydrogel Foams. *J. Colloid Interface Sci.* **2021**, *588*, 326–335.

[Deh21b]: Dehli, F.; Poole, H.; Stubenrauch, C.; Southan, A. Gelatin-Based Foamed and Non-Foamed Hydrogels for Sorption and Controlled Release of Metoprolol. *ACS Appl. Polym. Mater.* **2021**, *3* (11), 5674–5682.

[Deh22]: Dehli, F.; Stubenrauch, C.; Southan, A. New gelatin-based hydrogel foams for improved substrate conversion of immobilized horseradish peroxidase, *Macrom. Biosci.*, **2022**, 2200139.

[Dje21]: Djemaa, I. Ben; Auguste, S.; Drenckhan-Andreatta, W.; Andrieux, S. Hydrogel Foams from Liquid Foam Templates: Properties and Optimisation. *Adv. Colloid Interface Sci.* **2021**, *294*, 102478 1-20.

[Dre10]: Drenckhan, W.; Langevin, D. Current Opinion in Colloid & Interface Science Monodisperse Foams in One to Three Dimensions. *Curr. Opin. Colloid Interface Sci.* **2010**, *15* (5), 341–358.

[Dre15]: Drenckhan, W.; Saint-Jalmes, A. The Science of Foaming. *Adv. Colloid Interface Sci.* **2015**, *222*, 228–259.

[Dut17]: Dutta, K.; Hu, D.; Zhao, B.; Ribbe, A. E.; Zhuang, J.; Thayumanavan, S. Templated Self-Assembly of a Covalent Polymer Network for Intracellular Protein Delivery and Traceless Release. *J. Am. Chem. Soc.* **2017**, *139* (16), 5676–5679.

[Els17a]: Elsing, J.; Stefanov, T.; Gilchrist, M. D.; Stubenrauch, C. Monodisperse Polystyrene Foams via Polymerization of Foamed Emulsions: Structure and Mechanical Properties. *Phys. Chem. Chem. Phys.* **2017**, *19*, 5477-5485.

[Els17b]: Elsing, J.; Quell, A.; Stubenrauch, C. Toward Functionally Graded Polymer Foams Using Microfluidics. *Adv. Eng. Mater.* **2017**, *19*, 1700195.

[Esc13]: Escobar, P.; Teresinha, M.; Eduardo, C.; Gonçalves, C.; Fagundes-klen, M. R.; Bergamasco, R.; Antonio, E.; Yahico, P.; Suzaki, R. Nickel(II) and Zinc(II) Removal Using Amberlite IR-120 Resin: Ion Exchange Equilibrium and Kinetics. *Chem. Eng. J.* **2013**, *221*, 426–435.

[Eve71]: Everett, D. H. Manual of Symbols and Terminology for Physicochemical Quantities and Units, Appendix II: Definitions, Terminology and Symbols in Colloid and Surface Chemistry, *Pure and Applied Chemistry* **1972**, *31* (4), 577-638.

[Fai09]: Fairbanks, B. D.; Schwartz, M. P.; Bowman, C. N.; Anseth, K. S. Biomaterials Photoinitiated Polymerization of PEG-Diacrylate with Lithium Phenyl-2,4,6-Trimethylbenzoylphosphinate: Polymerization Rate and Cytocompatibility. *Biomaterials* **2009**, *30* (35), 6702–6707.

[Gar04]: Garstecki, P.; Gitlin, I.; DiLuzio, W.; Whitesides, G. M. Formation of monodisperse bubbles in a microfluidic flow-focusing device. *Appl. Phys. Lett.* **2004**, *85* (13), 2649–2651.

[Gei14]: Geise, G. M.; Paul, D. R.; Freeman, B. D. Fundamental Water and Salt Transport Properties of Polymeric Materials. *Prog. Polym. Sci.* **2014**, *39* (1), 1–42.

[Gre08]: Green, D. W.; Perry, R. H. Perry's Chemichal Engineers' Handbook, 8th Edition, *MacGraw-Hill Education*, **2008**, New York.

[Gre72]: Gregory, J.; Dhond, R. V. Wastewater Treatment by Ion Exchange. *Water Res.* **1972**, *6* (6), 681–694.

[Gui09]: Guillermic, R. M.; Salonen, A.; Emile, J.; Saint-Jalmes, A. Surfactant Foams Doped with Laponite: Unusual Behaviors Induced by Aging and Confinement. *Soft Matter* **2009**, *5*, 4975–4982.

[Gup10]: Gupta, N. V.; Shivakumar, H. Development of a Gastroretentive Drug Delivery System Based on Superporous Hydrogel. *Trop. J. Pharm. Res.* **2010**, *9* (3), 257–264.

[Hae07]: Haeberle, S.; Zengerle, R. Microfluidic Platforms for Lab-on-a-Chip Applications. *Lab Chip* **2007**, *7* (9), 1081–1220.

[Hag12]: Hager, W. H. Wilfrid Noel Bond and the Bond Number. *J. Hydraul. Res.* **2012**, *50* (1), 3–9.

[Han09]: Hanefeld, U.; Gardossi, L.; Magner, E. Understanding Enzyme Immobilisation. *Chem. Soc. Rev.* **2009**, *38* (2), 453–468.

[Hec98]: Heck, R. L. A Review of Commercially Used Chemical Foaming Agents for Thermoplastic Foams. *J. Vinyl Addit. Technol.* **1998**, *4* (2), 113–116

[Hoa08]: Hoare, T. R.; Kohane, D. S. Hydrogels in Drug Delivery: Progress and Challenges. *Polymer*. **2008**, *49* (8), 1993–2007.

[Höh21]: Höhler, R.; Seknagi, J.; Kraynik, A. Capillary Pressure, Osmotic Pressure and Bubble Contact Areas in Foams. *Soft Matter* **2021**, *17*, 6995–7003.

[Hoc12]: Hoch, E.; Schuh, C.; Hirth, T.; Tovar, G. E. M.; Borchers, K. Stiff Gelatin Hydrogels Can Be Photo-Chemically Synthesized from Low Viscous Gelatin Solutions Using Molecularly Functionalized Gelatin with a High Degree of Methacrylation. *J. Mater. Sci. Mater. Med.* **2012**, *23* (11), 2607–2617.

[Hoc13]: Hoch, E.; Hirth, T.; Tovar, G. E. M.; Borchers, K. Chemical Tailoring of Gelatin to Adjust Its Chemical and Physical Properties for Functional Bioprinting. *J. Mater. Chem. B* **2013**, *1* (41), 5675–5685.

[Hof03]: Hofstetter, T. B.; Schwarzenbach, R. P.; Haderlein, S. B. Reactivity of Fe(II) Species Associated with Clay Minerals. *Environ. Sci. Technol.* **2003**, *37* (3), 519–528.

[Hom13]: Homaei, A. A.; Sariri, R.; Vianello, F.; Stevanato, R. Enzyme Immobilization: An Update. *J. Chem. Biol.* **2013**, *6*, 185–205.

[Hsi16]: Hsieh, W.; Liu, Y.; Lee, Y.; Rimando, M. G.; Lin, K.; Lee, O. K. Matrix Dimensionality and Stiffness Cooperatively Regulate Osteogenesis of Mesenchymal Stromal Cells. *Acta Biomater.* **2016**, *32*, 210–222.

[Jun11]: Jung, U. Y.; Park, J. W.; Han, E. H.; Kang, S. G.; Lee, S.; Jun, C. H. Facile One-Step Catalytic Grafting of N-Hydroxysuccinimidyl-Ester-Functionalized Methallylsilane onto Silica for Enzyme Immobilization. *Chem. - An Asian J.* **2011**, *6* (2), 638–645.

[Kap97]: Kapeluich, Y. L.; Rubtsova, M. Y.; Egorov, A. M. Enhanced Chemiluminescence Reaction Applied to the Study of Horseradish Peroxidase Stability in the Course of P-Iodophenol Oxidation. *J. Biolumin. Chemilumin.* **1997**, *12* (6), 299–308.

[Kim10]: Kim, S.; Iyer, G.; Nadarajah, A.; Frantz, J. M.; Spongberg, A. L. Polyacrylamide Hydrogel Properties for Horticultural Applications. *Int. J. Polym. Anal. Charact.* **2010**, *15*, 307–318.

[Klo16]: Klotz, B. J.; Gawlitta, D.; Rosenberg, A. J. W. P.; Malda, J.; Melchels, F. P. W. Gelatin-Methacryloyl Hydrogels: Towards Biofabrication-Based Tissue Repair. *Trends Biotechnol.* **2016**, *34* (5), 394–407.

[Kra13]: Krainer, F. W.; Glieder, A. An Updated View on Horseradish Peroxidases: Recombinant Production and Biotechnological Applications. *Appl. Microbiol. Biotechnol.* **2015**, *99*, 1611–1625.

[Lag98]: Lagergren, S.Y. Zur Theorie der soganannten Adsorption gelöster Stoffe, *Kunglinga Svenska Vetenkapsakademiens: Handlingar*, **1898**, *24*, 1-39.

[Lan18]: Langmuir, I. The Adsorption of Gases on Plane Surfaces of Glass, Mica and Platinum. *J. Am. Chem. Soc*. **1919**, *40* (1914), 1361–1403.

[Lan20]: Langlois, V.; Kaddami, A.; Pitois, O.; Perrot, C. Acoustics of Monodisperse Open-Cell Foam: An Experimental and Numerical Parametric Study. *J. Acoust. Soc. Am.* **2020**, *148* (3), 1767–1778.

[Lee87]: Lee, P. I., Good, W. R., *Controlled-release technology: Pharmaceutical application,* **1987***,* ACS symposium series 0097-6156; 348, American Chemical Society, Washington, DC.

[Lee07]: Lee, S.-T.; Park, C. B.; Ramesh, N. S. Polymeric Foams: Science and Technology (Polymeric Foam Series), **2007**, *CRC Press, Taylor & Francis Group, LLC,* Boca Raton, London, New York.

[Lee13]: Lee, Y.; Huang, J.; Wang, Y.; Lin, K. Integrative Biology Compliant Substrates of Controlled Negative Curvature. *Integr. Biol.* **2013**, *5*, 1447–1455.

[Li10]: Li, Y.; Gao, F.; Wei, W.; Qu, J. B.; Ma, G. H.; Zhou, W. Q. Pore Size of Macroporous Polystyrene Microspheres Affects Lipase Immobilization. *J. Mol. Catal. B Enzym.* **2010**, *66* (1–2), 182–189.

[Li18]: Li, Y.; Ogorzalek, T. L.; Wei, S.; Zhang, X.; Yang, P.; Jasensky, J.; Brooks, C. L.; Marsh, E. N. G.; Chen, Z. Effect of Immobilization Site on the Orientation and Activity of Surface-Tethered Enzymes. *Phys. Chem. Chem. Phys.* **2018**, *20* (2), 1021–1029.

[Lin11]: Lin, J. Y.; Lin, W. J.; Hong, W. H.; Hung, W. C.; Nowotarski, S. H.; Gouveia, S. M.; Cristo, I.; Lin, K. H. Morphology and Organization of Tissue Cells in 3D Microenvironment of Monodisperse Foam Scaffolds. *Soft Matter* **2011**, *7* (21), 10010–10016.

[Liv93]: Livnah, O.; Bayer, E. A.; Wilchek, M.; Sussman, J. L. Three-Dimensional Structures of Avidin and the Avidin-Biotin Complex. *Proc. Natl. Acad. Sci. U. S. A.* **1993**, *90* (11), 5076–5080.

[Lyu21]: Lyu, X.; Gonzalez, R.; Horton, A.; Li, T. Immobilization of Enzymes by Polymeric Materials. *Catalysts* **2021**, *11* (10), 1211–1226.

[Ma17]. Ma, J.; Wang, Y.; Liu, J. Biomaterials Meet Microfluidics: From Synthesis Technologies to Biological Applications. *micromachines* **2017**, *8*, 255.

[Mae13]: Maestro, A.; Drenckhan, W.; Rio, E.; Höhler, R. Liquid Dispersions under Gravity: Volume Fraction Profile and Osmotic Pressure. *Soft Matter* **2013**, *9*, 2531–2540.

[Maj17]: Majer, G.; Southan, A. Adenosine Triphosphate Diffusion through Poly(Ethylene Glycol) Diacrylate Hydrogels Can Be Tuned by Cross-Link Density as Measured by PFG-NMR. *J. Chem. Phys.* **2017**, *146*, 225101.

[Maj91]: Majima, T.; Schnabel, W.; Weber, W. Photoinitiators . Generation and Reactivity of O=Ṗ(C_6H_5)(O-) Radical Anions. *Die Makromol. Chemie* **1991**, *192* (10), 2307–2315.

[Mar93]: Marchesiello, M.; Geniès, E. A Theoretical Model for an Amperometric Glucose Sensor Using Polypyrrole as the Immobilization Matrix. *J. Electroanal. Chem.* **1993**, *358* (1–2), 35–48.

[Mat18]: Matsumoto, T.; Isogawa, Y.; Tanaka, T.; Kondo, A. Streptavidin-Hydrogel Prepared by Sortase A-Assisted Click Chemistry for Enzyme Immobilization on an Electrode. *Biosens. Bioelectron.* **2018**, *99*, 56–61.

[Mea15]: Meagher, A. J.; Whyte, D.; Banhart, J.; Hutzler, S.; Weaire, D.; García-Moreno, F. Slow Crystallisation of a Monodisperse Foam Stabilised against Coarsening. *Soft Matter* **2015**, *11* (23), 4710–4716.

[Men21]: Menold, P.; Helmut, C.; Stubenrauch, C. Mineral Plastic Foams. *Mater. Horizons* **2021**, *8*, 1222–1229.

[Mit20]: Mitura, S.; Sionkowska, A.; Jaiswal, A. Biopolymers for Hydrogels in Cosmetics: Review. *J. Mater. Sci. Mater. Med.* **2020**, *31* (50), 1–14.

[Miy15]: Miyawaki, O.; Omote, C.; Meitushira, K. Thermodynamic analysis of sol-gel transition of gelatin in terms of water activity in various solutions, *Biopolymers*, **2015**, 103 (12), 685-691.

[Mon18]: Monteiroa, N.; Thrivikramana, G.; Athirasalaa, A.; Tahayeria, A.; Françaab, C.M.; Ferracanea, J.L.; Bertassoni, L.E. Photopolymerization of cell-laden gelatin methacryloyl hydrogels using a dental curing light for regenerative dentistry, *Dental Materials*, 2018, *34*(3), 389-399.

[Net09]: Net, A. Van Der; Gryson, A.; Ranft, M.; Elias, F.; Stubenrauch, C.; Drenckhan, W. Highly Structured Porous Solids from Liquid Foam Templates. *Colloids Surfaces A Physicochem. Eng. Asp.* **2009**, *346* (1–3), 5–10.

[Nic00]: Nichifor, M.; Cristea, D.; Carpov, A. Sodium Cholate Sorption on Cationic Dextran Hydrogel Microspheres. 1. Influence of the Chemical Structure of Functional Groups. *Int. J. Biol. Macromol.* **2000**, *28*, 15–21.

[Nic10]: Nichol, J. W.; Koshy, S. T.; Bae, H.; Hwang, C. M.; Yamanlar, S.; Khademhosseini, A. Cell-Laden Microengineered Gelatin Methacrylate Hydrogels. *Biomaterials* **2010**, *31* (21), 5536–5544.

[Par96]: Park, H.; Park, K. Hydrogels in Bioapplications. *Hydrogels Biodegrad. Polymers Bioapplications, ACS Symp. Ser.* **1996**, *Chapter 1*, 2–10.

[Pet12]: Petkova, G. A.; Záruba, K.; Pavel, Ž.; Král, V. Gold and Silver Nanoparticles for Biomolecule Immobilization and Enzymatic Catalysis. *Nanoscale Res. Lett.* **2012**, *7*, 287.

[Pie04]: Pierre, A. C. The Sol-Gel Encapsulation of Enzymes. *Biocatal. Biotransformation* **2004**, *22* (3), 145–170.

[Pie09]: Pieróg, M.; Gierszewska-Drużyńska, M.; Ostrowska-Czubenko, J. Effect of Ionic Crosslinking Agents on Swelling Behaviour of Chitosan Hydrogel Membranes. *Prog. Chem. Appl. Chitin Its Deriv.* **2009**, *XIV*, 75–82.

[Pit20a]: Pitois, O.; Kaddami, A.; Langlois, V. Permeability of Monodisperse Solid Foams. *Transp. Porous Media* **2020**, *134*, 635–649.

[Pit20b]: Pitois, O.; Kaddami, A.; Langlois, V. Capillary Imbibition in Open-Cell Monodisperse Foams. *J. Colloid Interface Sci.* **2020**, *571*, 166–173.

[Pot96]: Potter, K.; McFarland, E. W. Ion transport studies in calcium alginate gels by magnetic resonance spectroscopy. *Solid State Nucl. Magn. Reson.* **1996**, *6*, 323–331.

[Prin88]: Princen, H.M. Pressure/Volume/Surface Area Relationships in Foams and Highly Concentrated Emulsions : Role of Volume Fraction. *Langmuir*, **1988**, *4*(1), 164–169.

[Raj20]: Raju, R. R.; Liebig, F.; Klemke, B.; Koetz, J. Ultralight Magnetic Aerogels from Janus Emulsions. *RSC Adv.* **2020**, *10* (13), 7492–7499.

[Ram98]: Ramshaw, J.A.M.; Shah, N.K.; Brodsky, B. Gly-X-Y Tripeptide Frequencies in Collagen: A Context for Host–Guest Triple-Helical Peptides, *Journal of Structural Biology*, **1998,** *122*(1-2), 86-91.

[Rat72]: Ratner, B. D.; Miller, I. F. Interaction of Urea with Poly (2-Hydroxyethyl Methacrylate) Hydrogels. *J. Polym. Sci. Part A-1*. **1972**, *10* (8), 2425–2445.

[Reb19]: Rebers, L.; Granse, T.; Tovar, G.; Southan, A.; Borchers, K. Physical Interactions Strengthen Chemical Gelatin Methacryloyl Gels. *Gels* **2019**, *5* (4), 1–13.

[Rio14]: Rio, E.; Drenckhan, W.; Salonen, A.; Langevin, D. Unusually Stable Liquid Foams. *Adv. Colloid Interface Sci.* **2014**, *205*, 74–86.

[Rod05]: Rodriguez-Perez, M. A. Crosslinked Polyolefin Foams: Production, Structure, Properties and Applications. *Adv. Polym. Sci.* **2005**, *184*, 97–126.

[Rot90]: Rott, N. Note on the History of the Reynolds Number. *Annu. Rev. Fluid Mech.* **1990**, *22*, 1–11.

[Rud12]: Rudzinski, W. E.; Dave, A. M.; Vaishnav, U. H.; Kumbar, S. G.; Kulkarni, A. R.; Aminabhavi, T. M. Hydrogels as Controlled Release Devices in Agriculture. *Des. Monomers Polym.* **2012**, *5* (1), 39–65.

[Sew18]: Sewald, L.; Claaßen, C.; Götz, T.; Claaßen, M. H.; Truffault, V.; Tovar, G. E. M.; Southan, A.; Borchers, K. Beyond the Modification Degree: Impact of Raw Material on Physicochemical Properties of Gelatin Type A and Type B Methacryloyls. 2018, 1800168.

[She82]: Sheets, J. J.; Vickery, L. E. Proximity of the Substrate Binding Site and the Heme-Iron Catalytic Site in Cytochrome P-450scc. *Proc. Natl. Acad. Sci.* **1982**, *79* (19), 5773–5777.

[Sir13]: Sirova, M.; Vlierberghe, S. Van; Matyasova, V.; Rossmann, P.; Schacht, E.; Dubruel, P.; Rihova, B. Immunocompatibility Evaluation of Hydrogel-Coated Polyimide Implants for Applications in Regenerative Medicine. *J. Biomed. Mater. Res. - Part A* **2013**, *102* (6), 1982–1990.

[Sla09]: Slaughter, B. B. V; Khurshid, S. S.; Fisher, O. Z.; Khademhosseini, A.; Peppas, N. A. Hydrogels in Regenerative Medicine. *Adv. Mater.* **2009**, *21* (32–33), 3307–3329.

[Son09]: Sone, H.; Fugetsu, B.; Tanaka, S. Selective Elimination of Lead(II) Ions by Alginate/Polyurethane Composite Foams. *J. Hazard. Mater.* **2009**, *162* (1), 423–429.

[Squ05]: Squires, T. M. Microfluidics: Fluid Physics at the Nanoliter Scale. *Rev. Mod. Phys.* **2005**, *77*, 977–1026.

[Ste02]: Steen, P. E. Van Den; Dubois, B.; Nelissen, I.; Rudd, P. M.; Dwek, R. A.; Opdenakker, G. Biochemistry and Molecular Biology of Gelatinase B or Matrix Metalloproteinase-9 (MMP-9), *Crit. Rev. Biochem. Mol. Biol.* **2002**, *37* (6), 375–536.

[Ste21]: Steck, K.; Hamann, M.; Andrieux, S.; Muller, P.; Kékicheff, P.; Stubenrauch, C.; Drenckhan, W. Fluorocarbon Vapors Slow Down Coalescence in Foams. *Adv. Mater. Interfaces* **2021**, *8* (20), 2100723.

[Sun16]: Sun, B.; Jiang, J.; Shi, N.; Xu, W. Application of Microfluidics Technology in Chemical Engineering for Enhanced Safety. *Process Saf. Prog.* **2016**, *35* (4), 365–373.

[Tch08]: Tcholakova, S.; Denkov, N. D.; Lips, A. Comparison of Solid Particles, Globular Proteins and Surfactants as Emulsifier. *Phys. Chem. Chem. Phys.* **2008**, *10*, 1608–1627.

[Tes10]: Testouri, A.; Honorez, C.; Barillec, A.; Langevin, D.; Drenckhan, W.; Highly Structured Foams from Chitosan Gels. *Macromolecules* **2010**, *43*, 6166–6173.

[Tes12]: Testouri, A. Highly structured polymer foams from liquid foam templates using milifluidic lab-on-a-chip techniques, PhD thesis, University of Paris – XI, **2012**.

[Tes13]: Testouri, A.; Ranft, M.; Honorez, C.; Kaabeche, N.; Ferbitz, J.; Freidank, D.; Drenckhan, W. Generation of Crystalline Polyurethane Foams Using Millifluidic Lab-on-a-Chip Technologies. *Adv. Eng. Mater.* **2013**, *15* (11), 1086–1098.

[Tra71]: Traub, W.; Plez, K. A. The Chemistry and Structure of Collagen. *Adv. Protein Chem.* **1971**, *25*, 243–352.

[Tri19]: Trinh, V. H.; Langlois, V.; Guilleminot, J.; Perrot, C.; Khidas, Y.; Pitois, O. Tuning Membrane Content of Sound Absorbing Cellular Foams: Fabrication , Experimental Evidence and Multiscale Numerical Simulations. *Mater. Des.* **2019**, *162*, 345–361.

[Uhl15]: Uhlirova, T.; Gregorova, E.; Pabst, W.; Necina, V. Preparation of Cellular Alumina Ceramics via Biological Foaming with Yeast and Its Microstructural Characterization via Stereological Relations. *J. Eur. Ceram. Soc.* **2015**, *35* (1), 187–196.

[Var11]: Varade, D.; Carriere, D.; Arriaga, L. R.; Fameau, A.-L.; Rio, E.; Langevin, D.; Drenckhan, W. On the Origin of the Stability of Foams Made from Catanionic Surfactant Mixtures. *Soft Matter* **2011**, *7*, 6557–6570.

[Var17]: Varaprasad, K.; Malegowd, G.; Jayaramudu, T.; Mohan, M.; Sadiku, R. A Mini Review on Hydrogels Classification and Recent Developments in Miscellaneous Applications. *Mater. Sci. Eng. C* **2017**, *79*, 958–971.

[Vei00]: Veitch, N. C.; Smith, A. T. Horseradish Peroxidase. *Adv. Inorg. Chem.* **2001**, *51*, 107–162.

[Voi10]: Voigt, R. Pharmzeutische Technologie, 11th edition, *Deutscher Apotheker Verlag*, **2010**, Stuttgart.

[Wal01]: Walde, P.; Ichikawa, S. Enzymes inside Lipid Vesicles: Preparation, Reactivity and Applications. *Biomol. Eng.* **2001**, *18* (4), 143–177.

[Wan99]: Wang, C.; Stewart, R. J.; Kopec, J. Hybrid Hydrogels Assembled from Synthetic Polymers and Coiled-Coil Protein Domains. *Nature* **1999**, *397*, 417–420.

[Wea90]: Weaire, D.; Pageron, V. Frustrated Froth: Evolution of Foam Inhibited by an Insoluble Gaseous Component. *Philos. Mag. Lett.* **1990**, *62* (6), 417–421.

[Wea99]: Weaire, D.; Hutzler, S. The physics of foams, *Clarendon Press*, *Oxford University Press*, **1999**, New York.

[Wic60]: Wichterle, O.; Lim, D. Hydrophilic Gels for Biological Use, *Nature*, **1960**, *185*, 117-118.

[Won09]: Wong, J. C. H.; Tervoort, E.; Busato, S.; Gonzenbach, U. T.; Studart, R.; Ermanni, P.; Gauckler, L. J. Macroporous Polymers from Particle-Stabilized Foams. *J. Mater. Chem.* **2009**, *19*, 5129–5133.

[Won10]: Wong, J. C. H.; Rotello, V.; Tervoort, E.; Busato, S.; Gonzenbach, U. T.; Studart, R.; Ermanni, P.; Gauckler, L. J. Designing Macroporous Polymers from Particle-Stabilized Foams. *J. Mater. Chem.* **2010**, *20* (27), 5553–5764.

[Woo10]: Woo, E.; Ponvel, K. M.; Ahn, I. S.; Lee, C. H. Synthesis of Magnetic/Silica Nanoparticles with a Core of Magnetic Clusters and Their Application for the Immobilization of His-Tagged Enzymes. *J. Mater. Chem.* **2010**, *20* (8), 1511–1515.

[Wu20]: Wu, Z.; Chen, X.; Yuan, B.; Fu, M. A Facile Foaming-Polymerization Strategy to Prepare 3D MnO2 Modified Biochar-Based Porous Hydrogels for Efficient Removal of Cd (II) and Pb (II). *Chemosphere* **2020**, *239*, 124745 1-11.

[Yau16]: Yau, G.; Heng, G.; Timchenko, V. Numerical Investigation on the Velocity Fields during Droplet Formation in a Micro Fluidic T-Junction. *Chem. Eng. Sci.* **2016**, *139*, 99–108.

[Yao04]: Yao, C.; Liu, B.; Chang, C. Preparation of Networks of Gelatin and Genipin as Degradable Biomaterials. *Mater. Chem. Phys.* **2004**, *83* (2–3), 204–208.

[Yin18]: Yin, J.; Yan, M.; Wang, Y.; Fu, J.; Suo, H. 3D Bioprinting of Low-Concentration Cell-Laden Gelatin Methacrylate (GelMA) Bioinks with a Two-Step Cross-Linking Strategy. *ACS Appl. Mater. and Interfaces* **2018**, *10* (8), 6849–6857.

[Zai80]: Zaitsu, K.; Yosuke Ohkura. New Fluorogenic Substrates for Horseradish Sensitive Assays for Hydrogen Peroxide and the Peroxidase. *Anal. Biochem.* **1980**, *113* (1), 109–113.

[Zha03]: Zhang, G.; Shuang, S.; Dong, C.; Pan, J. Study on the Interaction of Methylene Blue with Cyclodextrin Derivatives by Absorption and Fluorescence Spectroscopy. *Spectrochim. Acta Part A* **2003**, *59*, 2935–2941.

[Zha12]: Zhang, H.; Xia, H.; Zhao, Y. Poly(Vinyl Alcohol) Hydrogel Can Autonomously Self-Heal. *ACS Macro Lett.* **2012**, *1* (11), 1233–1236.

[Zha13]: Zhao, Y.; Gordon, M. J.; Tekeei, A.; Hsieh, F.; Suppes, G. J. Modeling Reaction Kinetics of Rigid Polyurethane Foaming Process. *J. Appl. Polym. Sci.* **2013**, *130* (2), 1131–1138.

Publication I

Journal of Colloid and Interface Science 588 (2021) 326–335

Contents lists available at ScienceDirect

Journal of Colloid and Interface Science

journal homepage: www.elsevier.com/locate/jcis

Regular Article

Tailoring and visualising pore openings in gelatin-based hydrogel foams

Friederike Dehli [a], Alexander Southan [b], Wiebke Drenckhan [c], Cosima Stubenrauch [a,d,*]

[a] Institute of Physical Chemistry, University of Stuttgart, Pfaffenwaldring 55, 70569 Stuttgart, Germany
[b] Institute of Interfacial Process Engineering and Plasma Technology, University of Stuttgart, Nobelstraße 12, 70569 Stuttgart, Germany
[c] Institut Charles Sadron, 23 rue de Loess, Strasbourg 67034, France
[d] Institute of Advanced Studies (USIAS), University of Strasbourg, F-67000, France

GRAPHICAL ABSTRACT

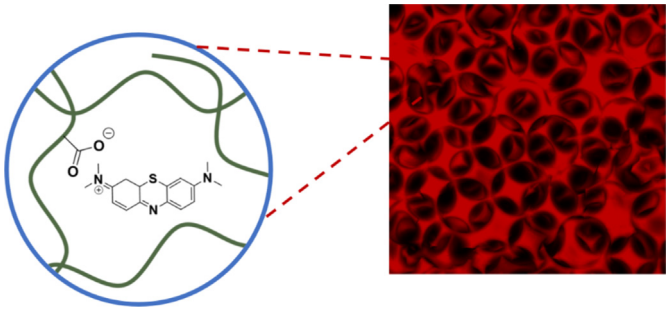

ARTICLE INFO

Article history:
Received 27 July 2020
Revised 18 December 2020
Accepted 19 December 2020
Available online 24 December 2020

Keywords:
Foam templating
Gelatin methacryloyl
Microfluidics
Pore opening
Biopolymer scaffolds

ABSTRACT

Hypothesis: While tailoring the pore diameters in hydrogel foams has been demonstrated in numerous studies, fine control over the diameters of the pore openings is still a challenge. We hypothesise that this can be achieved by controlling the size of the thin films which separate the bubbles in the liquid foam template. If this is the case, systematic changes of the template's gas fraction ϕ (the higher ϕ, the larger are the thin films) will lead to corresponding changes of the pore opening diameter.
Experiments: Since the size of the thin films depends on both bubble size $\langle D_b \rangle$ and gas fraction ϕ, we need to decouple both parameters to control the film size. Thus, we generated foams with constant bubble sizes via microfluidics and adjusted the gas fractions via two different techniques. The foams were solidified using UV light. Subsequently, they were analysed with confocal fluorescence microscopy.
Findings: We were able to change the pore opening diameter $\langle d_p \rangle$ at a constant pore diameter $\langle D_p \rangle$ by adjusting the gas fraction of the foam template. The obtained $\langle d_p \rangle / \langle D_p \rangle$ ratios are between those obtained theoretically for disordered foams and FCC ordered foams, respectively.

1. Introduction

Hydrogel foams based on biopolymers such as alginate, hyaluronic acid or gelatin have gained increasing attention in the field of biomaterials science because they combine the porous foam structure with the unique material properties of a hydrogel. Hydrogels are three-dimensionally cross-linked hydrophilic polymer networks that swell to equilibrium in aqueous media [1,2]. Due to their high water content [3], as well as their biocompatibility and biodegradability [4–6], hydrogels based on biopolymers are studied extensively as functional materials in various fields, e.g. tissue engineering or drug delivery [7–10]. What is of particular interest in this context is the biopolymer gelatin, which contains amino acid sequences relevant for cell adhesion as well as cleavage sites

* Corresponding author at: Institute of Physical Chemistry, University of Stuttgart, Pfaffenwaldring 55, 70569 Stuttgart, Germany.
E-mail address: cosima.stubenrauch@ipc.uni-stuttgart.de (C. Stubenrauch).

https://doi.org/10.1016/j.jcis.2020.12.064
0021-9797/

for biodegradation [11,12]. However, the diffusion of small molecules such as drugs or nutrients through hydrogels is often hindered by the small mesh sizes (up to tens of nanometres) of the material [13–15]. Thus, the generation of hydrogel foams with pore diameters ranging from tens to hundreds of micrometres has been investigated thoroughly.

One suitable method for the generation of hydrogel foams based on biopolymers is liquid foam templating [16–19]. With the help of this technique, a liquid foam is generated from an aqueous polymer solution and is subsequently solidified by cross-linking the polymer. As the morphology of the hydrogel foam is determined by the structure of the liquid template, the key parameters of the material, i.e. the pore diameter and the pore opening diameter, can be fine-tuned by tailoring the liquid template. Both pore diameter and pore opening diameter play a key role for the material properties of polymeric foams [20,21]. In the field of tissue engineering, relations between the differentiation and colonization behaviour of cells on the one hand and the pore diameter as well as the pore opening diameter on the other hand have been demonstrated in numerous studies [22–25]. To tailor the structure of the liquid template and thus the morphology of the hydrogel foam, microfluidic foaming has been examined extensively [16,18,21,26]. With the help of this technique, a gas and a liquid phase are pushed through a chip with a micrometric constriction, which results in the pinch-off of bubbles. As this pinch-off occurs periodically, the generated bubbles have the same diameter, i.e. they are monodisperse. The bubble diameter of the liquid template and thus the pore diameter of the hydrogel foam can be conveniently tailored by varying the gas pressure and/or the liquid flow rate inside the microfluidic chip. This has been demonstrated for hydrogel foams based on chitosan, alginate and gelatin [16,18,21,26]. The bubble diameter is further determined by the size of the constriction. While previous studies focussed on the variation of the pore diameter, the variation of the pore opening diameter has received little attention up until now. The mechanism of the pore opening process is still not very well understood. However, it can be assumed that the contact of two neighbouring bubbles leads to the formation of a contact zone between them. As these contact zones are subject to capillary forces generated by the surrounding struts, the thickness of the contact zone is reduced to a surfactant double layer. During cross-linking and freeze-drying, these films break and pore openings are generated (see Fig. 1).

Generally speaking, in liquid foam templating, the pore opening diameter correlates, to a first approximation, directly with the diameter of the thin liquid film which separates neighbouring bubbles. For foams with a high gas fraction ϕ (>90%) one can show by means of a simple scaling argument that the diameter $\langle d_p \rangle$ of the pore opening is related to the pore diameter $\langle D_p \rangle$. It holds

$$\langle d_p \rangle \sim \left(1 - \sqrt{1-\Phi}\right)\langle D_p \rangle. \quad (1)$$

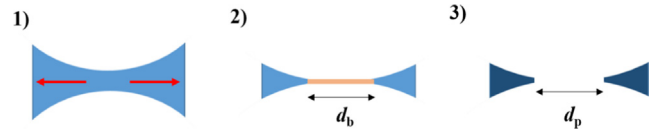

Fig. 1. Proposed mechanism for the generation of pore openings. (1) Drainage of the polymer solution (blue) between two neighbouring bubbles due to capillary forces (red arrows). (2) Expulsion of the polymer from the film generating a thin film with diameter d_b. (3) Upon solidification of the polymer (dark blue) the thin film ruptures and a pore opening with diameter d_p is generated. (For interpretation of the references to colour in this figure legend, the reader is referred to the web version of this article.)

For lower gas fractions, this relationship becomes a bit more complicated, as will be discussed in Section 3.3. Nevertheless, it shows the importance of decoupling the gas fraction and the pore size for explicit pore opening control. This was shown qualitatively for polyurethane foams by Testouri et al. [27]. A more systematic approach was developed for geopolymer- or gelatin-based foams that were generated from a foamed precursor solution which was then mixed with the geopolymer- or gelatin-containing dispersion/solution [21,28,29]. However, this approach is time-consuming, requires multiple formulations, and has high demands on foam stability. These requirements cannot always be met when using photo cross-linkable hydrogel formulations. The decoupling of pore size and gas fraction can also be achieved by varying the surfactant concentration, which was examined for systems based on alginate and methacrylated dextran [18,30]. Despite the fact that this is a very elegant concept, high surfactant concentrations are required, which limits potential applications.

In the present study, we used microfluidics for the generation of monodisperse liquid foams with a specific bubble diameter. The continuous phase of the foams consisted of an aqueous solution of gelatin methacryloyl. In order to tailor the pore opening diameter, we systematically adjusted the gas fraction of the foams independently of the bubble size using two different methods. In the first method, the polymer solution was added to the liquid foam template made at high gas fraction from the very same polymer solution. In the second method, the bubbling frequency during foam generation was tailored by varying the liquid flow rate and gas pressure while keeping the ratio of these parameters constant. This effect was examined by Garstecki et al. [31] for an aqueous surfactant solution, but has never been used to tailor the pore opening diameters in polymer foams. Another question we want to address is how hydrogel foams can be characterised. Typically, hydrogel foams are characterized by scanning electron microscopy, μ-CT or bright field microscopy. The downside of these methods is that they are expensive and time-consuming or do not adequately visualise the equilibrium state, i.e. the swollen state of the material. Here, we use confocal fluorescence microscopy to characterise the material in the swollen state. The paper is organised as follows: Firstly, we briefly report and discuss the use of confocal fluorescence microscopy for the characterisation of gelatin-based hydrogel foams. Secondly, we apply the two aforementioned approaches to decouple gas fraction and pore size. Finally, we compare the ratios of our experimentally determined pore opening diameters and pore diameters with predictions by Princen [32] and Arditty [33] for disordered foams, as well as with predictions by Pitois et al. [28,34] for foams with an FCC order.

2. Experimental

2.1. Chemicals

Gelatin (Type B, 232 bloom, batch #635621) was purchased from Gelita (Germany). Methacrylic anhydride was purchased from Sigma Aldrich (Germany). Sodium 3-trimethylsilylpropionate-2,2,3,3-d4 was purchased from Merck (Germany). Perfluorohexane (98%, 85% *n*-isomer) was purchased from abcr (Germany). D_2O was purchased from Deutero (Germany). Lithium phenyl-2,4,6-trimethylbenzoylphosphinate (LAP) was purchased from Carbosynth (UK). Plantacare 2000 UP was donated from Cognis (now BASF). Methylene blue was purchased from S3 chemicals (Germany). All chemicals were used as received. Deionised water was used for all experiments.

2.2. Synthesis of gelatin methacryoyl

Gelatin methacryloyl (GM) was prepared and analysed according to a procedure described by Claaßen et al. [35] 25.01 g of gelatin were dissolved in 250 mL of water at 40 °C. After the gelatin was dissolved completely, the temperature was set to 37 °C. The pH was adjusted to 7.25 using a 4 M NaOH solution. 14.28 mL (89.5 mmol) of methacrylic anhydride were added dropwise. The amount of methacrylic anhydride corresponds to a 10-fold molar excess with respect to free amino groups in gelatin (0.35 mmol g^{-1}, according to van den Bulcke et al. [36]). Consequently, the resulting product is further denoted as GM10. The reaction mixture was stirred for 5 h while the pH was kept between 7.0 and 7.4 by addition of 4 M NaOH solution. The crude product was stored at 8 °C for two days, afterwards dialyzed for 5 days and freeze-dried using an Alpha 1 – 4 LSC lyophiliser from Christ (Germany). 18.2 g of GM10 were obtained, which corresponds to a yield of 73%. ^{1}H NMR analysis in D_2O was used to determine the degree of methacryloylation (*DM*). TMSP was used as a standard. A *DM* of 0.88 mmol g^{-1} was obtained.

2.3. Generation of gelatin methacryloyl foams

A solution of 20 wt% GM10, 0.14 wt% LAP and 0.1 wt% Plantacare 2000 UP was prepared with deionised water. The density of the solution was determined to be 1.056 g cm^{-3} by using a DMA 5000 M density meter from Anton Paar. All flasks were wrapped with aluminium foil and stored at 8 °C in the dark until further use to prevent early activation of the photo initiator. Liquid foams were produced using a polycarbonate chip produced by micromilling, with a constriction of 70 μm in diameter (Fig. 3). The flow of the gas phase was controlled by the gas pressure p. To this end, an OB1MK1 pressure controller from Elveflow was used, which was connected to a nitrogen tap. The pressure pump was also connected to a glass bottle containing a small amount of perfluorohexane. In this way, the gas phase contains traces of perfluorohexane, which hinders Ostwald ripening. The flow rate v of the liquid phase was controlled with a Pump 11 Elite Syringe Pump from Harvard Apparatus. Bubbling in the microfluidic chip was monitored with a Nikon SMZ 745 T bright field microscope using a Mikrotron EoSensCL high speed camera. The accessible range of bubble diameters that can be produced using this microfluidic chip was assessed by varying the gas pressure p and the liquid flow rate v_L. The obtained data can be found in the Supporting Information (Fig. S1).

2.3.1. Addition of polymer solution

A liquid flow rate v_L of 7 μL min^{-1} and a gas pressure of 260 mbar were used to produce the foams. To analyse the bubble diameter of the liquid foam, pictures of foam monolayers taken with the Mikrotron EoSensCL high speed camera were analysed manually using the software ImageJ. In order to be able to add additional polymer solution to the resulting foams, a setup with connected and slanted outlet channels was used, where the same polymer solution that was used for the foaming was added with a defined flow rate v_A. The liquid flow rate of the additional polymer solution is a direct control parameter for the liquid fraction of the generated foam. A scheme of the setup is depicted in Fig. 2. As the additional polymer solution was added outside the microfluidic chip, undesirable feedback-loops on the bubble pinch-off at the constriction are prevented.

This setup has been used previously [37] to add fast gelling cross-linking agents to liquid foams. The mixing of additional polymer solution with the foam is ensured by the moving bubbles. The flow rate v_A was set by a second syringe pump (Pump 11 Elite, Harvard Apparatus) and was varied from 0 μL min^{-1} to 11 μL min^{-1}.

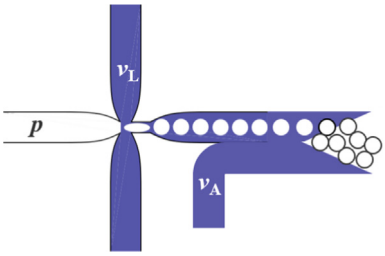

Fig. 2. Scheme of experimental setup used for the generation of liquid foam templates. The bubble size is determined by the gas pressure p and the liquid flow rate v_L, whereas the gas fraction can be controlled by the liquid flow rate v_A.

The resulting foams were collected in cylindrical PDMS moulds with a height of 2 mm and a diameter of 4 mm. By choosing this small sample height, we aimed to minimise the influence of drainage on the liquid foams. During the collection of the foams, the samples were overflown with nitrogen to prevent oxygen inhibition during cross-linking. The foams were covered with a quartz glass and irradiated immediately with UV-A light for 4.5 min. An Omnicure Series 1500 UV lamp with a maximum emission spectrum between 360 and 370 nm was used. The UV light guide tip had a distance of 5 cm to the samples and was operated at 15% intensity. After cross-linking, the samples were frozen at –60 °C for 30 min and freeze-dried. The dry samples were stored at room temperature until further use. The gas fraction ϕ of the foams was determined gravimetrically from the mass of the dried sample m, the sample volume in the liquid state V_l, the density ρ, and the concentration c of the polymer solution, using Eq. (2).

$$\phi = 1 - \frac{m}{c \cdot \rho \cdot V_l} \tag{2}$$

All experiments were carried out three times. All errors correspond to standard deviations.

2.3.2. Variation of the bubbling frequency

Liquid foams were generated by varying the liquid flow rate v_L stepwisely from 20 μL min^{-1} to 80 μL min^{-1}. The ratio of liquid flow rate to gas pressure was kept constant at 0.1 μL min^{-1} $mbar^{-1}$. As a result, the liquid fraction in the foam decreases with increasing liquid flow rate v_L, while a constant bubble size is maintained. Pictures of bubbles produced in the microfluidic chip at different liquid flow rates and gas pressures are depicted in Fig. 3.

As the production parameters were changed for each sample, the bubble diameters were determined for each sample as described in Section 2.3.1. The samples were collected, cross-linked and freeze-dried as described in Section 2.3.1. The gas fraction of the samples was determined as described in Section 2.3.1.

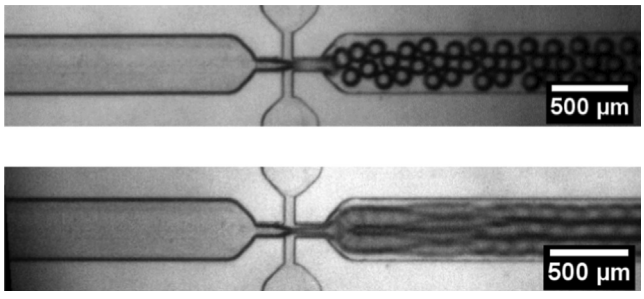

Fig. 3. Generation of bubbles inside the microfluidic chip at different liquid flow rates and gas pressures: (top) v_L = 20 μL min^{-1}, p = 200 mbar; (bottom) v_L = 70-μL min^{-1}, p = 700 mbar.

All experiments were carried out three times. All errors correspond to standard deviations.

2.4. Staining and absorption spectroscopy

As fluorescence microscopy relies on the excitation and emission of a fluorescing compound in the hydrogel matrix, a suitable dye which permanently stains the hydrogel had to be found. The isoelectric point of GM10 is 4.2, which leads to a negative net charge of the polymer in deionised water [38]. In contrast to that, the dye methylene blue (Fig. 4, left) is positively charged at a neutral pH.

To stain samples with methylene blue, freeze-dried GM10 foams, which had a mass of about 2 mg and a volume of about 25 mm^3, were immersed in 2 g of a 5 mg L^{-1} methylene blue solution under slight agitation (45 rpm) at room temperature. After 32 hrs of staining, the methylene blue solution was removed, and the samples were immersed in 2 g water for at least 12 h to remove unbound methylene blue from the gel phase as well as the pores. The samples were left at room temperature under slight agitation (45 rpm) until characterization with fluorescence microscopy. To follow the complete adsorption of the dye in the foam, the progressive reduction of the signal of the supernatant in the visible range was measured with a Lambda 25 UV/VIS spectrometer from Perkin Elmer at different times. The VIS absorption spectra of the supernatant after different immersion times are shown in Fig. 4 (right). After 29 h of immersion, almost no methylene blue can be detected in the supernatant. No methylene blue visibly leaches out of the material. The absorption and emission maxima of methylene blue are located at 664 nm and 684 nm, respectively [39].

2.5. Fluorescence microscopy

An LSM 710 confocal laser scanning microscope from Zeiss (Germany) equipped with the Zen Black software was used to characterise the stained samples. 3D z-stacks composed of 2D pictures along the z-axis of the sample were recorded. To prevent the samples from drying during the measurement, they were placed onto a droplet of water. Consequently, the pores of the sample are filled with water. The excitation wavelength was 633 nm. Emitted light was collected between 642 and 747 nm. To be able to not only visualise the surface of the sample but the inside, the samples were cut. The cutting was carried out both horizontally and vertically to obtain cross-sections and longitudinal sections. Please note that the surface of the samples displays an ordered morphology as the bubbles crystallise under the confinement of the sample mold walls and the quartz glass plate. Exemplary pictures of the ordered surface areas for samples discussed in Sections 3.2.1 and 3.2.2 are shown in the Supporting Information (Fig. S2). As the crystallised areas are merely surface effects that are relevant for the first bubble layers only [41], they are not considered for further analysis.

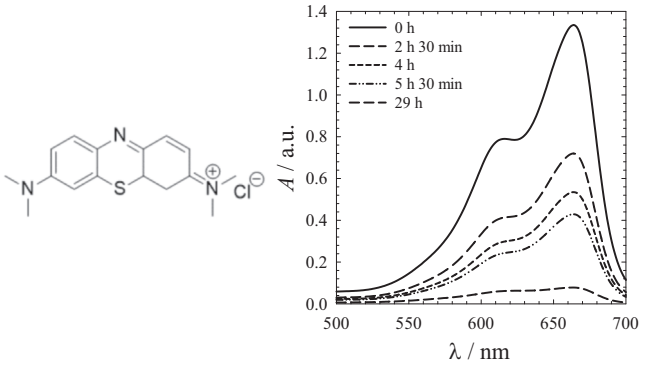

Fig. 4. (left) Chemical structure of methylene blue. (right) Absorption spectra of a 5 mg L^{-1} aqueous methylene blue solution after different immersion times of a GM10 foam.

2.6. Picture analysis

Compared to SEM, where the samples are cut at a random distance from the equatorial plane, stacks of 2D pictures can be recorded with confocal fluorescence microscopy. Thus, the acquired pore diameters were measured in pictures obtained close to the equatorial plane of the pores. Consequently, the maximum underestimation of the pore diameter depends on the distance of the 2D pictures in the stack, which is 9.6 μm in our case. As a result, the maximum underestimation of the pore diameter in our study is only between 0.26 μm and 0.33 μm. The obtained pictures were analysed using the software ImageJ (version 1.52p). A logarithmic transformation was applied to all pictures to account for skewed intensities due to light scattering when measuring deep inside the sample. Only 2D pictures of the 3D z-stack that captured either the pore diameter $\langle D_p \rangle$ or the pore opening diameter $\langle d_p \rangle$ in the focal plane were used (see Fig. 5). At least 40 pore and pore opening diameters were analysed manually for each sample. Since all samples were prepared three times, we have a total of 120 values for each pore diameter and each pore opening diameter. The corresponding size distributions are shown in the Supporting Information (Figs. S3-S6). When the pore opening diameters had slightly elliptical shapes in the 2D projections, the major axis was considered the pore opening diameter. All errors correspond to the standard deviation.

3. Results and discussion

3.1. Visualisation of GM10 hydrogel foams

One of the most important aspects to consider when tailoring the morphology of a material is a suitable characterization method. In this study, we want to demonstrate the possibility of using confocal fluorescence microscopy for the extensive characterization of GM10 hydrogel foams. A confocal fluorescence microscopy picture of a GM10 hydrogel foam stained with methylene blue which was immersed in water is shown in Fig. 6 (right). As can be seen in the picture, it is only the hydrogel matrix that fluoresces (red areas in the picture) but not the water that fills the pores of the matrix (black areas in the picture).

In a previous study, GM10 hydrogel foams were characterised using both SEM and bright field microscopy (Fig. 6, left and middle) [26]. SEM has often been used as a standard characterization technique for hydrogel foams [16,24,40], as it visualises the interconnected structure and the pore diameter of the material (Fig. 6, left). However, the material needs to be dried, which entails the formation of artefacts such as shrinkage. We have shown before that pore diameters in freeze-dried GM10 hydrogel foams are also smaller than pore diameters in GM10 foams swollen to equilibrium [26]. What is yet unknown is the behaviour of pore openings during drying in general and the degree of pore opening shrinkage relative to the shrinkage of the pore diameters in particular. Another method that has been used frequently for the characterization of hydrogel foams is μ-CT [19,24]. In this technique, the attenuation of X-rays by the material is detected and a 3D picture is reconstructed. The method is suitable for both dry and swollen samples. Although this method is undoubtedly the most precise method for the characterization of both dried and swollen hydrogel foams, several drawbacks should be considered. Firstly, the acquisition can take several hours, which is not very efficient if

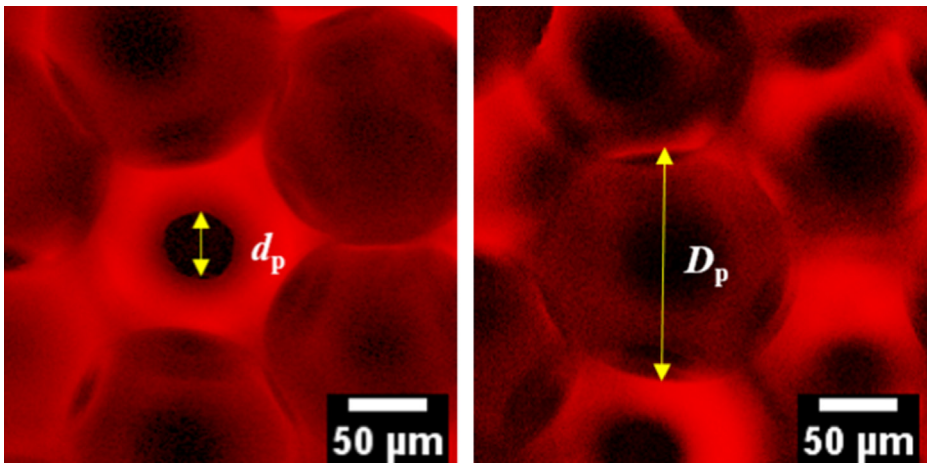

Fig. 5. Determination of pore opening diameter (left) and pore diameter (right). Note that the 2D pictures refer to the same area in the sample, but are taken at different z-positions in the 3D stack to focus either on the pore opening or on the pore.

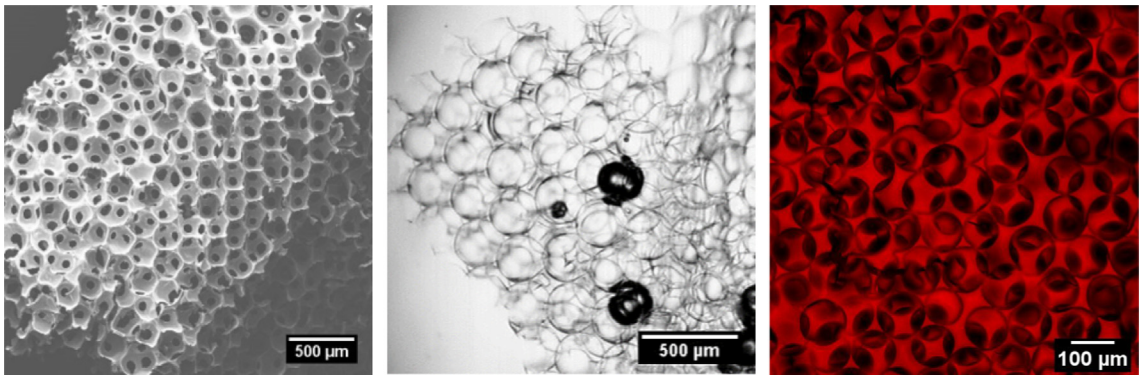

Fig. 6. Pictures of a GM foam visualised with SEM (left)[a], bright field microscopy (middle)[a] and confocal fluorescence microscopy (right, maximum intensity projection). [a]Adapted with permission from Dehli, F.; Rebers, L.; Stubenrauch, C.; Southan, A. Highly Ordered Gelatin Methacryloyl Hydrogel Foams with Tunable Pore Size, *Biomacromolecules*, 2019, *20*, 2666 – 2674. Copyright 2019 American Chemical Society.

multiple series of samples need to be characterised. Secondly, the acquisition time steeply increases with increasing resolution, which makes the characterization of the very thin pore opening boundaries even more time-consuming. Thirdly, the equipment is extremely expensive and only few research facilities have access to such instruments. Alternatively, the pore diameters of swollen hydrogel foams can be examined by bright field microscopy as the outlines of the pores (Fig. 6, middle) can be distinguished. However, due to the low contrast between the hydrogel matrix and the medium, detailed morphological structures such as pore openings are difficult to analyse. By contrast, confocal fluorescence microscopy enables the visualization of both pore and pore opening diameters in the swollen state due to the high contrast between the hydrogel matrix and the aqueous medium. Compared to what can be achieved by bright field microscopy, the interconnected structure can be visualised much better. As the picture acquisition time is only a matter of minutes, the method can be used to characterise multiple series of samples. However, there is a general limitation of confocal fluorescence microscopy when analysing porous materials. Due to the porous structure, some of the excitation light as well as the fluorescence emission are scattered when passing through the sample. Hence, the depth for picture acquisition is limited to approx. 220 µm in the case of GM10 hydrogel foams. As a result, thicker samples cannot be analysed without cutting them. Therefore, the samples must be cut and visualised several times to ensure thorough characterization. Nevertheless, confocal fluorescence microscopy can be considered an alternative to µ-CT for the visualization of swollen hydrogel foams when analysing the system described in this study.

3.2. Control of the pore opening diameter

3.2.1. Addition of polymer solution

To decouple the bubble diameter from the gas fraction, the liquid content of the foam templates was varied by adding polymer solution to the generated foam at flow rate v_A. The liquid foams were successfully cross-linked by irradiation with UV light to yield hydrogel foams. Cross-linked foams were swollen to equilibrium and analysed using confocal fluorescence microscopy. Pictures taken by confocal fluorescence microscopy are depicted in Fig. 7 together with the flow rate v_A of the additionally added polymer solution. The obtained values for pore diameters and pore opening diameters, as well as their ratios and gas fractions are listed in Table 1. Other than in Section 3.2.2, the bubble diameter ($\langle D_b \rangle$ = 174 ± 2 µm) was only measured once, since the experimental parameters used for bubble formation were not changed.

Looking at Fig. 7 and Table 1, one sees that the gas fraction decreased with increasing v_A from 82% to 66%, i.e. we decoupled bubble size and gas fraction. The pore opening diameter varied from 50 ± 11 µm to 27 ± 6 µm, respectively, while the pore diameter remained constant. Thus, the ratio of pore opening diameter and pore diameter could be adjusted between 0.15 and 0.28.

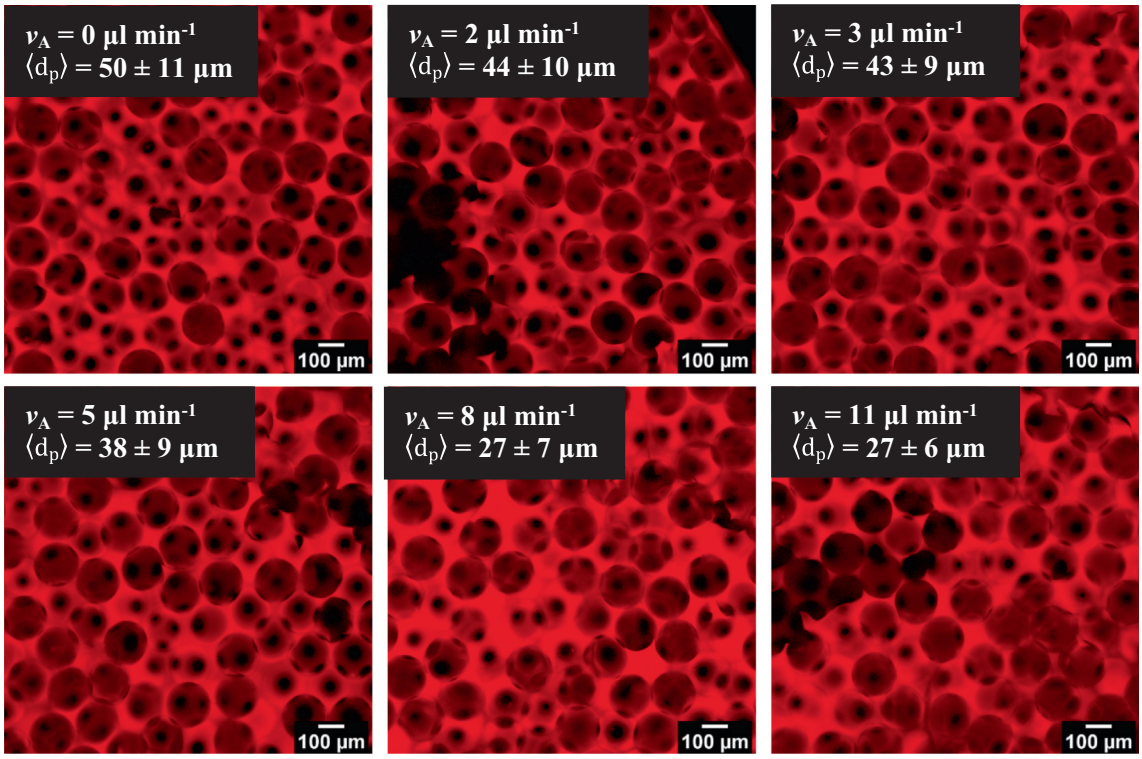

Fig. 7. Pictures of GM10 foams taken with confocal fluorescence microscopy. The flow rate v_A and the average pore opening diameter ⟨d_p⟩ are displayed in the inlets. The flow rate v_L and the gas pressure p during foam generation were kept constant at 7 µL min^{-1} and 260 mbar^{-1}, respectively.

Table 1
Liquid flow rates v_A of additionally added GM solution, pore diameters ⟨D_p⟩, pore opening diameters ⟨d_p⟩, the ratio ⟨d_p⟩/⟨D_p⟩, and the gas fraction of the liquid foams. The mean bubble diameter ⟨D_b⟩ of the generated liquid foam templates was 174 ± 2 µm.

v_A/µL min^{-1}	⟨D_p⟩/µm	⟨d_p⟩/µm	⟨d_p⟩/⟨D_p⟩	Gas fraction/%
0	178 ± 4	50 ± 11	0.28	82 ± 4
2	175 ± 4	44 ± 10	0.25	80 ± 1
3	181 ± 5	43 ± 9	0.24	79 ± 1
5	179 ± 3	38 ± 7	0.21	74 ± 1
8	178 ± 3	27 ± 7	0.15	67 ± 1
11	177 ± 4	27 ± 6	0.15	66 ± 0*

* As the gas fraction of samples produced with this liquid flow rate could only be determined from two samples which did not differ in weight, the obtained standard deviation is zero.

Fig. 7 also illustrates that the gas fraction influences the degree of pore ordering in the hydrogel foam. When no additional polymer solution is added to the sample (top, left), the pores are more ordered compared to samples where additional polymer solution is added (bottom, right). It was also found that the number of pore openings per pore decreases when polymer solution is added with high flow rates such as 8 µL min^{-1} and 11 µL min^{-1}. Note that adding polymer solution can only be used to tailor the pore opening diameter of foams with a high initial gas fraction and thus a large bubble size. We thus used a different method to tailor the pore opening diameters for foams with low initial gas fractions and thus smaller bubble sizes.

3.2.2. Variation of the bubbling frequency

To decouple the bubble diameter from the gas fraction, the bubbling frequency during microfluidic bubbling was varied by increasing gas pressure and liquid flow rate at a constant ratio. The resulting bubble diameters as well as their corresponding production parameters and the initial gas fraction are listed in Table 2. The resulting foams were successfully cross-linked by irradiation with UV-light and were swollen in water for confocal fluorescence microscopy. Pictures taken by confocal fluorescence microscopy are depicted in Fig. 8 together with the liquid flow rate v_L of the polymer solution during the production. The obtained values for pore diameters and pore opening diameters, as well as their ratios and the gas fraction are also listed in Table 2. Other than in Section 3.2.1, the bubble diameter was measured for each set of samples, as the experimental parameters for bubble formation were different. Looking at Table 2, one sees that we worked with a constant bubble diameter of ~140 µm, while the gas fraction increases from top to bottom. In addition, Table 2 and Fig. 8 illustrate that the pore opening diameter increases from 19 µm to 32 µm in the same direction, while the pore diameter remained constant. Thus, the ratio of pore opening diameter and pore diameter varied between 0.14 and 0.23. Similar to Section 3.2.1, foams with higher gas fractions are more ordered.

Please note that the gas fraction of foams produced with a liquid flow rate of 20 µL min^{-1} or 30 µL min^{-1} is below 63.5%, which corresponds to the critical packing limit for disordered foams. Theoretically, no pore openings should be observed for these samples. However, a drainage layer was observed at the bottom of the foams, which leads to an increased gas fraction in the foams and

Table 2
Liquid flow rates v_L and gas pressures p used to produce GM10 foams, bubble diameters$\langle D_b \rangle$, pore diameters $\langle D_p \rangle$, pore opening diameters $\langle d_p \rangle$, the ratio $\langle d_p \rangle / \langle D_p \rangle$, and the gas fraction of the liquid foams.

v_L/μL min^{-1}	p/mbar	$\langle D_b \rangle$/μm	$\langle D_p \rangle$/μm	$\langle d_p \rangle$/μm	$\langle d_p \rangle / \langle D_p \rangle$	Gas fraction/%
20	200	140 ± 5	131 ± 6	18 ± 4	0.14	60 ± 4
30	300	135 ± 3	133 ± 3	19 ± 5	0.14	54 ± 1
40	400	138 ± 3	136 ± 3	19 ± 4	0.14	65 ± 1
50	500	145 ± 4	138 ± 3	20 ± 5	0.15	68 ± 1
60	600	144 ± 2	140 ± 3	24 ± 6	0.17	71 ± 1
70	700	144 ± 3	144 ± 3	30 ± 7	0.21	75 ± 2
80	800	142 ± 2	142 ± 4	32 ± 8	0.23	76 ± 1

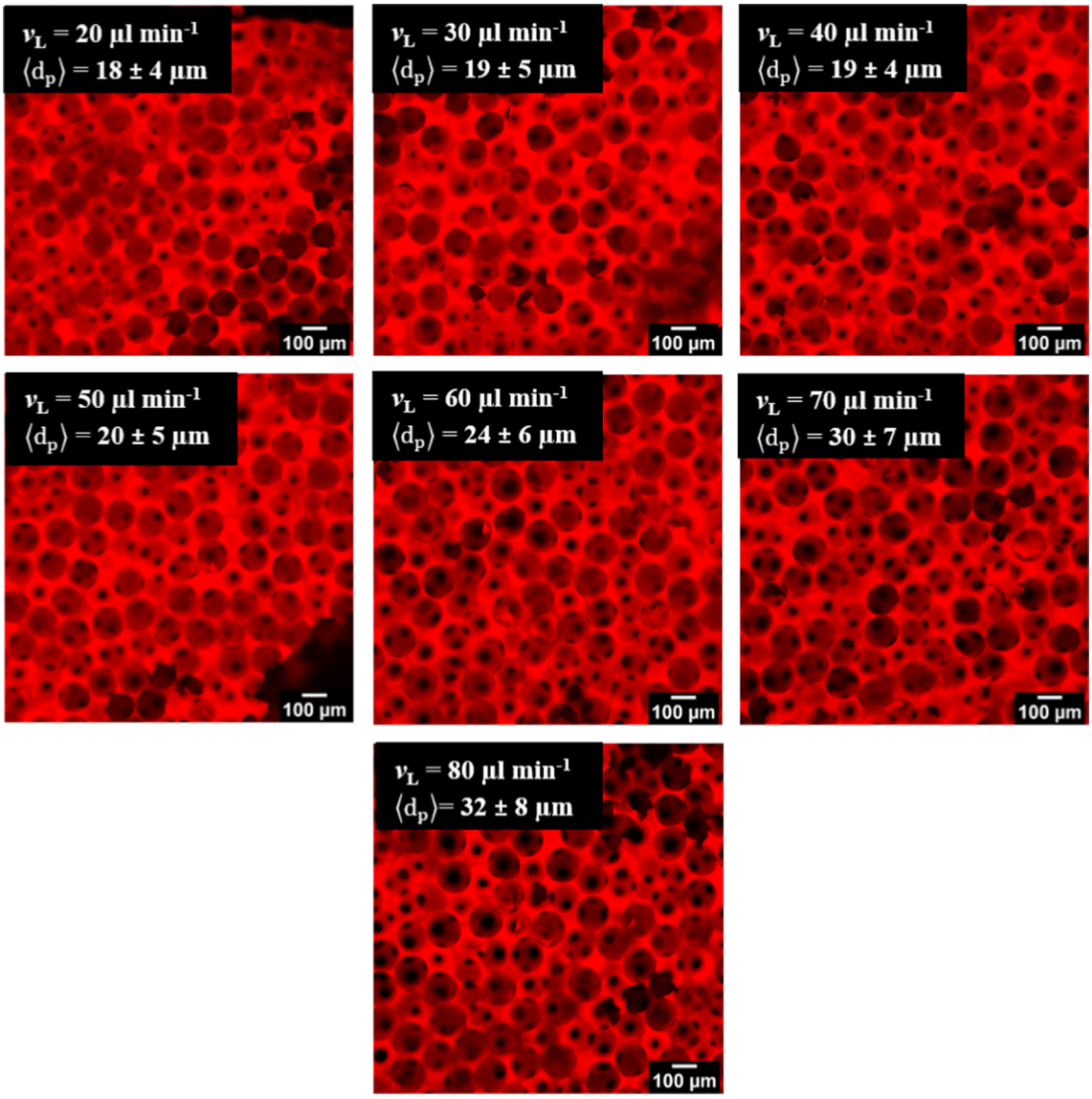

Fig. 8. Pictures of GM10 foams taken with confocal fluorescence microscopy. The flow rate v_L and the average pore opening diameter $\langle d_p \rangle$ are displayed in the inlets. The ratio of flow rate v_L and gas pressure p during foam generation was kept constant at 0.1 μL min^{-1} mbar^{-1}.

thus to the formation of pore openings. Consequently, the samples are not considered for further analysis in Section 3.3. For all other samples, no drainage layer was observed. To conclude one can say that the two techniques complement each other and allow generating hydrogel foams with controllable pore opening diameters at constant pore size.

3.3. Comparison of pore opening diameters to bubble contact zones of liquid foams

All experimentally obtained results for $\langle d_p \rangle / \langle D_p \rangle$ are plotted in Fig. 9. Combining all results from Sections 3.2.1 and 3.2.2, one sees that $\langle d_p \rangle / \langle D_p \rangle$ can be varied between 0.14 and 0.28. The variation of

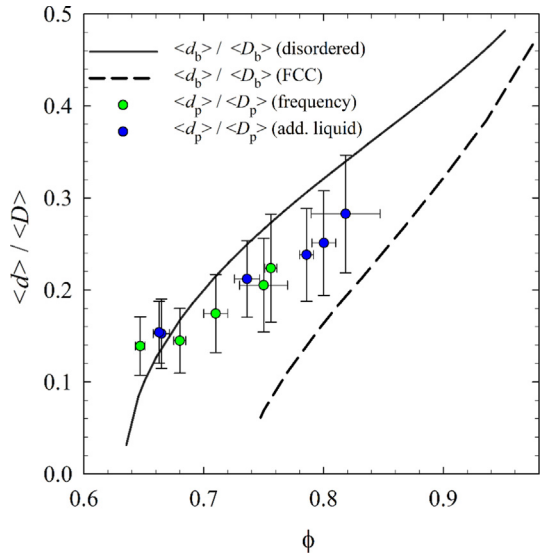

Fig. 9. Ratio of experimentally determined pore opening diameters $\langle d_p \rangle$ and pore diameters $\langle D_p \rangle$ obtained by adding liquid (blue data) and by varying the bubbling frequency (green data) plotted against the gas fraction ϕ of the foam. Also plotted are theoretical predictions calculated from Eq. (3) for disordered foams (solid line) or obtained by Surface Evolver simulations for ordered foams (dotted line) [34]. The errors are determined from an error propagation. (For interpretation of the references to colour in this figure legend, the reader is referred to the web version of this article.)

$\langle d_p \rangle / \langle D_p \rangle$ was also examined for geopolymer foams by systematically adding the geopolymer-dispersion to a precursor foam generated from an aqueous surfactant solution [28,29]. In these studies, the ratio of pore opening diameter to pore diameter was varied from 0.15 at low to 0.38 at very high gas fractions. Theoretically such high gas fractions could also be obtained for our system. However, since our gelatin-based hydrogel foams are cross-linked via radical polymerization, we encounter the more oxygen inhibition the higher the gas fraction is. Thus, a gas fraction of 82% represents the upper limit of the accessible pore opening diameters when generating foams under the conditions described in Section 2.3. By using a more rigorous inert gas atmosphere during foaming and cross-linking, larger gas fractions and thus also larger pore openings might be accessible. The lower limit of the pore opening diameters corresponds to a gas fraction of 65%. Even though liquid foams with gas fractions of less than 65% can be generated, these foams instantaneously start to drain. As this competes with the rapid cross-linking of the polymer chains, inhomogeneous foams are generated which cannot be reliably compared to foams with gas fractions above 65%. In a study by Costantini et al. [18], $\langle d_p \rangle / \langle D_p \rangle$ of alginate foams were varied by using surfactant concentrations between 0.6 wt% and 5 wt%. The ratio of pore opening diameter to pore diameter varied between 0.25 and 0.32. However, our techniques avoid the preparation and formulation of multiple solutions. Moreover, we can work at low surfactant concentrations which is of particular importance in applications such as tissue engineering.

To a first approximation, the pore opening diameters $\langle d_p \rangle$ are believed to be closely linked to the diameter of the contact zone $\langle d_b \rangle$ between touching bubbles in the liquid template. The ratio of this contact zone $\langle d_b \rangle$ and the bubble diameter $\langle D_b \rangle$ can be estimated based on the gas fraction ϕ of the liquid foam. A prediction of this relation was derived by Princen for polydisperse disordered foams [32] and adapted to monodisperse disordered systems by Arditty [33]

$$\frac{\langle d_b \rangle}{\langle D_b \rangle} = \frac{0.6}{\phi^{\frac{1}{3}}} \left(1 - \frac{1.74}{\left(\frac{\phi}{1-\phi} + 1.3 \right)^{\frac{1}{2}}} \right)^{\frac{1}{2}}. \quad (3)$$

To relate the gas fraction of the solid foam to that of the liquid template, we make the following assumption: As the bubble diameters of the liquid templates are almost equal to the pore diameters of the obtained hydrogel foams (see Tables 1 and 2), we assume that shrinkage during cross-linking and freeze-drying is counterbalanced by an isotropic swelling in water. Thus, the gas fraction in the hydrogel foam can be assumed to be equal to the gas fraction of the liquid template. The gas fractions of the liquid templates are listed in Tables 1 and 2. In Fig. 9 we also plot the predictions of Eq. (3) for disordered foams and those obtained from Surface Evolver simulations by Pitois et al. [28,34] for ordered foams (hexagonally close-packed - FCC). We can see that globally our data lies between the predictions for disordered and ordered foams, with a tendency to move from the disordered to the ordered case with increasing gas fraction. This tendency is confirmed by visual inspection of the samples, which, as discussed in Sections 3.2.1 and 3.2.2, show increased local ordering of the bubbles with increasing gas fraction. This can be explained by the fact that bubble interactions become stronger for increasing gas fraction, which, in turn, increases the driving force towards an energetically more favourable packing. For monodisperse foams, this packing is the FCC structure.

4. Conclusions

We describe two approaches to the independent variation of the pore diameter and the pore opening diameter in hydrogel foams generated by microfluidic bubbling. The pore opening diameter was decoupled from the pore diameter by varying the gas fraction of the templating foam at constant bubble size. To this end, two complementary methods were used. The liquid fraction was varied (1) by adding polymer solution to the generated liquid foams and (2) by changing the bubbling frequency. The pore openings were visualised with confocal fluorescence microscopy, which allows for a fast characterisation of the hydrogel foams in their equilibrium swollen state. We successfully varied the ratio of pore opening diameters to pore diameters $\langle d_p \rangle / \langle D_p \rangle$ between 0.14 and 0.28. As the pore openings are hypothesised to be generated by the rupture of thin films that form between neighbouring bubbles touching each other, the area of the thin films can be predicted based on surface area minimisations of bubble assemblies [32,33]. We show that our data lies in between the theoretical predictions obtained for disordered foams and Surface Evolver simulations for ordered (FCC) foams [34]. Our $\langle d_p \rangle / \langle D_p \rangle$ ratios correlate well with the predicted values for disordered foams at low gas fractions, indicating that the pore opening sizes are indeed determined by the thin film sizes in the template. For higher gas fractions, the ratios $\langle d_p \rangle / \langle D_p \rangle$ approach predicted values for FCC ordered foams. In other words, we observe an increasing degree of ordering for hydrogel foams with increasing gas fraction. Despite being of great importance in the field of biomaterials, the variation of the pore opening in chemically cross-linked polymer foams was examined in very few other studies. Costantini et al. [18] used different surfactant concentrations between 0.6 wt% and 5 wt% to vary the thin film area, while Testouri et al. [27] qualitatively examined the pore opening diameter in free standing foams subjected to drainage. The variation of the pore opening in geopolymer foams has been achieved by letting generated precursor foams drain and adding a cross-linking geopolymer dispersion afterwards

[28,29]. However, these approaches are either time-consuming or involve the formulation of multiple solutions. With the methods presented here, it is possible to systematically vary the influence of the gas fraction of the foam template on the pore opening size while working at low surfactant concentrations. By decoupling the bubble diameter from the gas fraction and thus the pore opening diameter from the pore diameter, it is now possible to independently study the influence of pore size and pore opening size on the behaviour of cells in tissue engineering, which is the subject of ongoing research. In addition to that, a new arena in the field of adsorption and release has opened up as the staining of the hydrogel foams for confocal microscopy relies on a cation exchange with methylene blue. This effect could be used for drug delivery or wastewater treatment where cationic drugs or pollutants are adsorbed on the hydrogel matrix.

CRediT authorship contribution statement

Friederike Dehli: Conceptualization, Methodology, Investigation, Visualization, Writing - original draft. **Alexander Southan:** Conceptualization, Writing - review & editing, Supervision. **Wiebke Drenckhan:** Conceptualization, Writing - review & editing, Supervision. **Cosima Stubenrauch:** Conceptualization, Writing - review & editing, Supervision.

Declaration of Competing Interest

The authors declare that they have no known competing financial interests or personal relationships that could have appeared to influence the work reported in this paper.

Acknowledgements

Friederike Dehli wants to thank Fabian Moczko for fruitful discussions. We thank Dr. Marco Costantini for the fabrication of the polycarbonate chip at the *Polish Academy of Sciences*, Warsaw. Friederike Dehli gratefully acknowledges financial support by the *Fonds der Chemischen Industrie*. The authors gratefully acknowledge the Technology Platform "Cellular Analytics" of the Stuttgart Research Center Systems Biology for their support and assistance in this work. Part of this work has been conducted within the IdEx Unistra framework (Chair W. Drenckhan) and has, as such, benefited from funding from the state, managed by the French National Research Agency as part of the "Investments for the future" program. The work was also supported by an ERC consolidator grant (agreement 819511-METAFOAM). Cosima Stubenrauch acknowledges a fellowship by the Institute of Advanced Studies at the University of Strasbourg (USIAS).

Appendix A. Supplementary material

Supplementary data to this article can be found online at https://doi.org/10.1016/j.jcis.2020.12.064.

References

[1] E.M. Ahmed, Hydrogel: preparation, characterization, and applications: A review, J. Adv. Res. 6 (2) (2015) 105–121, https://doi.org/10.1016/j.jare.2013.07.006.
[2] B.N.A. Peppas, J.Z. Hilt, A. Khademhosseini, R. Langer, Hydrogels in biology and medicine : from molecular principles to bionanotechnology, Adv. Mater. 18 (2006) 1345–1360, https://doi.org/10.1002/adma.200501612.
[3] J. Zhu, R.E. Marchant, Design properties of hydrogel tissue-engineering scaffolds, Expert Rev. Med. Devices 8 (5) (2011) 607–626, https://doi.org/10.1586/erd.11.27.
[4] J.Y. Lai, Y.T. Li, Functional assessment of cross-linked porous gelatin hydrogels for bioengineered cell sheet carriers, Biomacromolecules 11 (5) (2010) 1387–1397, https://doi.org/10.1021/bm100213f.
[5] K. Miyamoto, M. Sasaki, Y. Minamisawa, Y. Kurahashi, H. Kano, S.I. Ishikawa, Evaluation of in vivo biocompatibility and biodegradation of photocrosslinked hyaluronate hydrogels (HADgels), J. Biomed. Mater. Res. - Part A 70 (4) (2004) 550–559, https://doi.org/10.1002/jbm.a.30112.
[6] S.W.N. Ueng, L.J. Yuan, N. Lee, S.S. Lin, E.C. Chan, J.H. Weng, In vivo study of biodegradable alginate antibiotic beads in rabbits, J. Orthop. Res. 22 (3) (2004) 592–599, https://doi.org/10.1016/j.orthres.2003.09.001.
[7] Y. Luo, K.R. Kirker, G.D. Prestwich, Cross-linked hyaluronic acid hydrogel films new biomaterials, J. Control. Release 69 (2000) 169–184.
[8] A.D. Augst, H.J. Kong, D.J. Mooney, Alginate hydrogels as biomaterials, Macromol. Biosci. 6 (8) (2006) 623–633, https://doi.org/10.1002/mabi.200600069.
[9] C. Dollinger, S. Ciftci, H. Knopf-Marques, R. Guner, A.M. Ghaemmaghami, C. Debry, J. Barthes, N.E. Vrana, Incorporation of resident macrophages in engineered tissues: multiple cell type response to microenvironment controlled macrophage-laden gelatine hydrogels, J. Tissue Eng. Regen. Med. 12 (2) (2018) 330–340, https://doi.org/10.1002/term.2458.
[10] A. Barbetta, M. Massimi, B. Di Rosario, S. Nardecchia, M. De Colli, L.C. Devirgiliis, M. Dentini, Emulsion templated scaffolds that include gelatin and glycosaminoglycans, Biomacromolecules 9 (10) (2008) 2844–2856, https://doi.org/10.1021/bm800599d.
[11] J.W. Nichol, S.T. Koshy, H. Bae, C.M. Hwang, S. Yamanlar, A. Khademhosseini, Cell-laden microengineered gelatin methacrylate hydrogels, Biomaterials 31 (21) (2010) 5536–5544, https://doi.org/10.1016/j.biomaterials.2010.03.064.
[12] B. Ratnikov, E. Deryugina, J. Leng, G. Marchenko, D. Dembrow, A. Strongin, Determination of matrix metalloproteinase activity using biotinylated gelatin, Anal. Biochem. 286 (1) (2000) 149–155, https://doi.org/10.1006/abio.2000.4798.
[13] G. Majer, A. Southan, Adenosine triphosphate diffusion through poly(ethylene glycol) diacrylate hydrogels can be tuned by cross-link density as measured by PFG-NMR, J. Chem. Phys. 146 (22) (2017) 225101, https://doi.org/10.1063/1.4984979.
[14] O. Lieleg, K. Ribbeck, Biological hydrogels as selective diffusion barriers, Trends Cell Biol. 21 (9) (2011) 543–551, https://doi.org/10.1016/j.tcb.2011.06.002.
[15] N.A. Peppas, S.R. Lustig, And Relaxations of the macromolecular carrier in the diffusional release of conceptual and scaling relationships, Ann. New York Acad. Sci. 446 (1985) 26–41.
[16] S. Andrieux, W. Drenckhan, C. Stubenrauch, Highly ordered biobased scaffolds: from liquid to solid foams, Porous Polym.: A Special Issue Polym. 216 (2017) 425–431, https://doi.org/10.1016/j.polymer.2017.04.031.
[17] A. Barbetta, G. Rizzitelli, R. Bedini, R. Pecci, M. Dentini, Porous gelatin hydrogels by gas-in-liquid foam templating, Soft Matter 6 (8) (2010) 1785–1792, https://doi.org/10.1039/b920049e.
[18] M. Costantini, C. Colosi, J. Jaroszewicz, A. Tosato, S. Wojciech, M. Dentini, P. Garstecki, A. Barbetta, Microfluidic foaming : A powerful tool for tailoring the morphological and permeability properties of sponge-like biopolymeric scaffolds, ACS Appl. Mater. Interfaces 7 (2015) 23660–23671, https://doi.org/10.1021/acsami.5b08221.
[19] C. Colosi, M. Costantini, A. Barbetta, R. Pecci, R. Bedini, M. Dentini, Morphological comparison of PVA scaffolds obtained by gas foaming and microfluidic foaming techniques, Langmuir 29 (1) (2013) 82–91, https://doi.org/10.1021/la303788z.
[20] V. Langlois, V.H. Trinh, C. Lusso, C. Perrot, X. Chateau, Y. Khidas, O. Pitois, Permeability of solid foam: effect of pore connections, Phys. Rev. E 97 (5) (2018) 1–10, https://doi.org/10.1103/PhysRevE.97.053111.
[21] V.H. Trinh, V. Langlois, J. Guilleminot, C. Perrot, Y. Khidas, O. Pitois, Tuning membrane content of sound absorbing cellular foams: fabrication, experimental evidence and multiscale numerical simulations, Mater. Des. 162 (2019) 345–361, https://doi.org/10.1016/j.matdes.2018.11.023.
[22] L.R. Madden, D.J. Mortisen, E.M. Sussman, S.K. Dupras, J.A. Fugate, J.L. Cuy, K.D. Hauch, M.A. Laflamme, C.E. Murry, B.D. Ratner, Proangiogenic scaffolds as functional templates for cardiac tissue engineering, Proc. Natl. Acad. Sci. U. S. A. 107 (34) (2010) 15211–15216, https://doi.org/10.1073/pnas.1006442107.
[23] G. Lutzweiler, J. Barthes, G. Koenig, H. Kerdjoudj, J. Mayingi, F. Boulmedais, P. Schaaf, W. Drenckhan, N.E. Vrana, Modulation of cellular colonization of porous polyurethane scaffolds via the control of pore interconnection size and nanoscale surface modifications, ACS Appl. Mater. Interfaces 11 (22) (2019) 19819–19829, https://doi.org/10.1021/acsami.9b04625.
[24] M. Costantini, C. Colosi, P. Mozetic, J. Jaroszewicz, A. Tosato, A. Rainer, M. Trombetta, Ś. Wojciech, M. Dentini, A. Barbetta, Correlation between porous texture and cell seeding efficiency of gas foaming and microfluidic foaming scaffolds, Mater. Sci. Eng. C 62 (2016) 668–677, https://doi.org/10.1016/j.msec.2016.02.010.
[25] S.H. Oh, T.H. Kim, G.Il. Im, J.H. Lee, Investigation of pore size effect on chondrogenic differentiation of adipose stem cells using a pore size gradient scaffold, Biomacromolecules 11 (8) (2010) 1948–1955, https://doi.org/10.1021/bm100199m.
[26] F. Dehli, L. Rebers, C. Stubenrauch, A. Southan, Highly ordered gelatin methacryloyl hydrogel foams with tunable pore size, Biomacromolecules 20 (7) (2019) 2666–2674, https://doi.org/10.1021/acs.biomac.9b00433.
[27] A. Testouri, M. Ranft, C. Honorez, N. Kaabeche, J. Ferbitz, D. Freidank, W. Drenckhan, Generation of crystalline polyurethane foams using millifluidic

lab-on-a-chip technologies, Adv. Eng. Mater. 15 (11) (2013) 1086–1098, https://doi.org/10.1002/adem.201300077.
[28] O. Pitois, A. Kaddami, V. Langlois, Permeability of monodisperse solid foams, Transp. Porous Media 134 (3) (2020) 635–649, https://doi.org/10.1007/s11242-020-01461-6.
[29] V. Langlois, A. Kaddami, O. Pitois, C. Perrot, Acoustics of monodisperse open-cell foam: an experimental and numerical parametric study, J. Acoust. Soc. Am. 148 (3) (2020) 1767–1778, https://doi.org/10.1121/10.0001995.
[30] M. Costantini, C. Colosi, J. Guzowski, A. Barbetta, J. Jaroszewicz, W. Swieszkowski, M. Dentini, P. Garstecki, Highly ordered and tunable PolyHIPEs by using microfluidics, J. Mater. Chem. B 2 (2014) 2290–2300, https://doi.org/10.1039/c3tb21227k.
[31] P. Garstecki, I. Gitlin, W. Diluzio, G.M. Whitesides, E. Kumacheva, H.A. Stone, Formation of monodisperse bubbles in a microfluidic flow-focusing device, Appl. Phys. Lett. 85 (13) (2004) 2649–2651, https://doi.org/10.1063/1.1796526.
[32] H.M. Princen, Pressure/volume/surface area relationships in foams and highly concentrated emulsions: role of volume fraction, Langmuir 4 (1) (1988) 164–169, https://doi.org/10.1021/la00079a030.
[33] Arditty, S. Fabrication, Stability and Rheological Properties of Particles-Stabilized Emulsions PhD Thesis, University of Bordeaux, 2004.
[34] O. Pitois, A. Kaddami, V. Langlois, Capillary Imbibition in open-cell monodisperse foams, J. Colloid Interface Sci. 571 (2020) 166–173, https://doi.org/10.1016/j.jcis.2020.03.013.
[35] C. Claaßen, M.H. Claaßen, V. Truffault, L. Sewald, G.E.M. Tovar, K. Borchers, A. Southan, Quantification of substitution of gelatin methacryloyl: best practice and current pitfalls, Biomacromolecules 19 (1) (2018) 42–52, https://doi.org/10.1021/acs.biomac.7b01221.
[36] A.I. Van Den Bulcke, B. Bogdanov, N. De Rooze, E.H. Schacht, M. Cornelissen, H. Berghmans, Structural and rheological properties of methacrylamide modified gelatin hydrogels, Biomacromolecules 1 (1) (2000) 31–38, https://doi.org/10.1021/bm990017d.
[37] S. Andrieux, W. Drenckhan, C. Stubenrauch, Generation of solid foams with controlled polydispersity using microfluidics, Langmuir 34 (4) (2018) 1581–1590, https://doi.org/10.1021/acs.langmuir.7b03602.
[38] L. Sewald, C. Claaßen, T. Götz, M.H. Claaßen, V. Truffault, G.E.M. Tovar, A. Southan, K. Borchers, Beyond the modification degree: impact of raw material on physicochemical properties of gelatin type A and type B methacryloyls, Macromol. Biosci. 18 (12) (2018) 1–10, https://doi.org/10.1002/mabi.201800168.
[39] G. Zhang, S. Shuang, C. Dong, J. Pan, Study on the interaction of methylene blue with cyclodextrin derivatives by absorption and fluorescence spectroscopy, Spectrochim. Acta Part A 59 (2003) 2935–2941, https://doi.org/10.1016/S1386-1425(03)00123-9.
[40] A. Barbetta, A. Carrino, M. Costantini, M. Dentini, Polysaccharide based scaffolds obtained by freezing the external phase of gas-in-liquid foams, Soft Matter 6 (20) (2010) 5213–5224, https://doi.org/10.1039/c0sm00616e.
[41] A.J. Meagher, D. Whyte, J. Banhart, S. Hutzler, D. Weaire, F. García-Moreno, Slow crystallisation of a monodisperse foam stabilised against coarsening, Soft Matter 11 (23) (2015) 4710–4716, https://doi.org/10.1039/c4sm02412e.

SUPPORTING INFORMATION

Tailoring and visualising pore openings in gelatin-based hydrogel foams

Friederike Dehli[1], Alexander Southan[2], Wiebke Drenckhan[3], Cosima Stubenrauch[1,4*]

[1] Institute of Physical Chemistry, University of Stuttgart,
Pfaffenwaldring 55, 70569 Stuttgart, Germany

[2] Institute of Interfacial Process Engineering and Plasma Technology,
University of Stuttgart, Nobelstraße 12, 70569 Stuttgart, Germany

[3] Institut Charles Sadron, 23 rue de Loess, Strasbourg, 67034, France

[4] Institute of Advanced Studies (USIAS), University of Strasbourg, F-67000 France

*Corresponding Author : cosima.stubenrauch@ipc.uni-stuttgart.de, 0049 711 685-64470

Calibration of microfluidic chip

The range of accessible bubble sizes was obtained by varying the liquid flow rate or the gas pressure. Figure S1 depicts the obtained bubble sizes as a function of the gas pressure and the liquid flow rate, respectively.

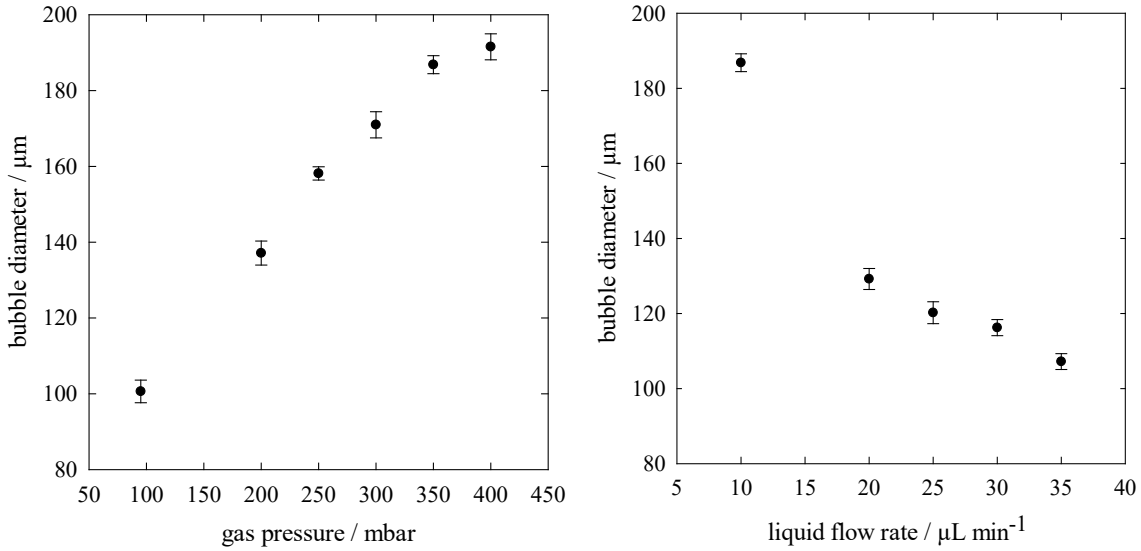

Figure S1: Bubble sizes of liquid foams as a function of (left) the gas pressure at a liquid flow rate of 10 µL min^{-1} and (right) the liquid flow rate at a gas pressure of 350 mbar.

Surface areas of samples

The surfaces of the samples display an ordered morphology - the bubbles crystallise at the sample mold walls and the quartz glass plate. Exemplary images of the first bubble layer for different samples are depicted in Figure S2.

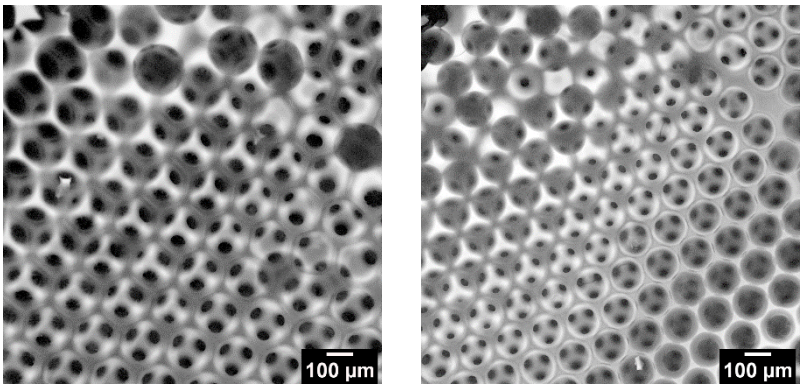

Figure S2: Pictures of surface layers for different samples: (left) The sample was prepared according to the method described in Section 2.3.1. Additional liquid was added with a flow rate of 3 µL min^{-1}. (right) The sample was prepared according to the method described in Section 2.3.2. A liquid flow rate of 50 µL min^{-1} and a gas pressure of 500 mbar was used.

Distributions of pore diameters and pore opening diameters

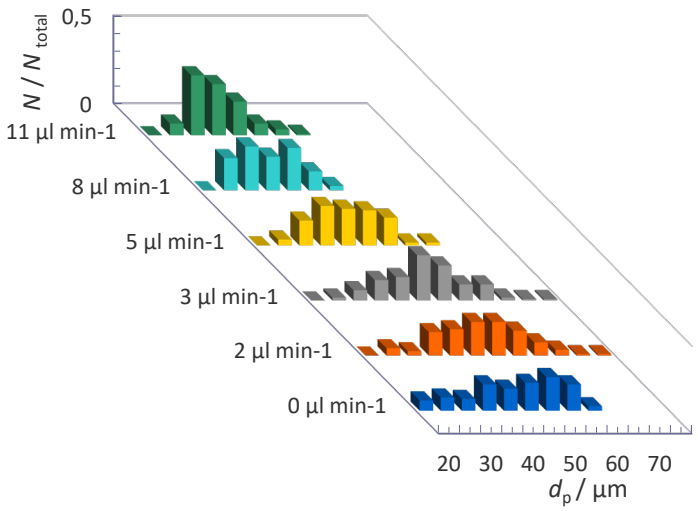

Figure S3: Distribution of pore opening diameters when additional polymer solution was added to the liquid templates (see Sections 2.3.1 and 3.2.1).

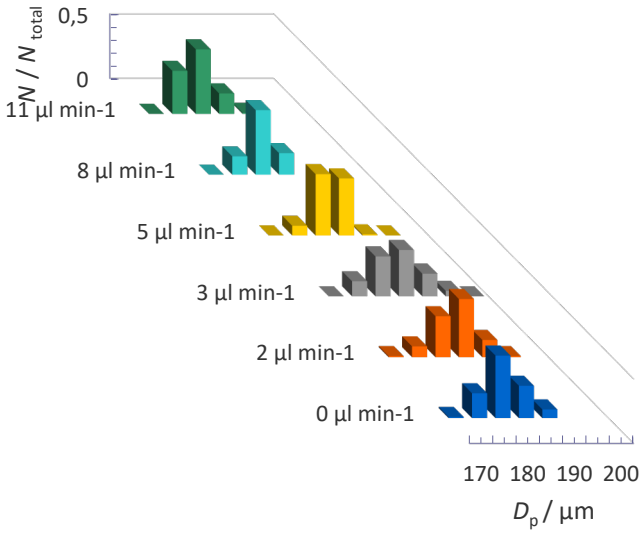

Figure S4: Distribution of pore diameters when additional polymer solution was added to the liquid templates (see Sections 2.3.1 and 3.2.1).

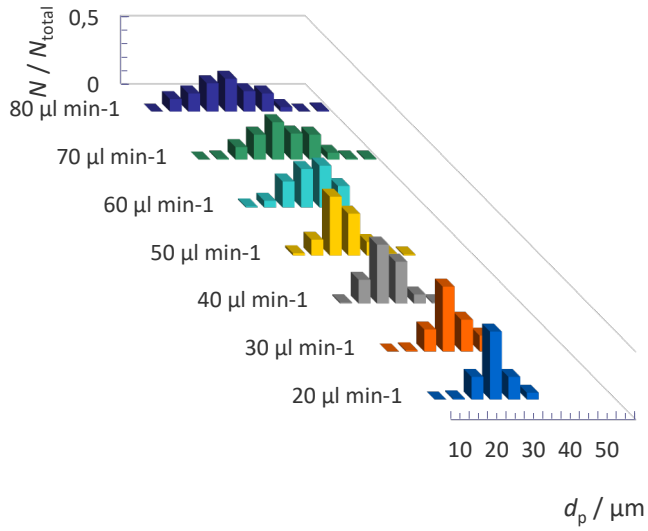

Figure S5: Distribution of pore opening diameters for samples produced with different bubbling frequencies (see Sections 2.3.2 and 3.2.2).

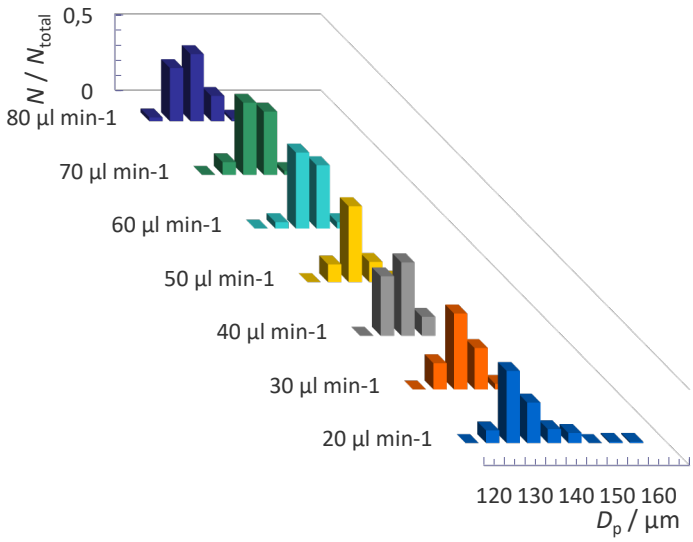

Figure S6: Distribution of pore diameters for samples produced with different bubbling frequencies (see Sections 2.3.2 and 3.2.2).

Publication II

ACS APPLIED POLYMER MATERIALS

pubs.acs.org/acsapm Article

Gelatin-Based Foamed and Non-foamed Hydrogels for Sorption and Controlled Release of Metoprolol

Friederike Dehli, Hailey Poole, Cosima Stubenrauch, and Alexander Southan*

Cite This: *ACS Appl. Polym. Mater.* 2021, 3, 5674−5682 Read Online

ACCESS | Metrics & More | Article Recommendations

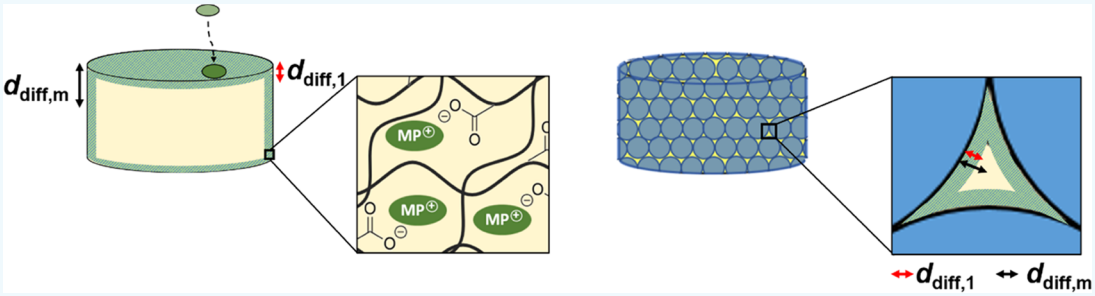

ABSTRACT: The influence of gelatin methacryloyl hydrogel morphology on the sorption and release behavior of metoprolol was studied for both equilibrium and non-equilibrium conditions. For samples examined in equilibrium conditions, no influence of the sample morphology was observed. The maximum sorption capacity q_{max} was determined to be 530 μmol g^{-1}. Furthermore, up to 100% of the sorbed drug was released from both foamed and non-foamed samples upon immersion into salt solutions, which demonstrates the regenerability of the material. By contrast, the sample morphology strongly influenced the sorption and release kinetics. We found that the sorption and release rate coefficients k increased up to 10 times for foamed hydrogels as compared to non-foamed hydrogels. Furthermore, k increased with increasing ion concentration in the sorption and release medium. This effect was more pronounced for non-foamed hydrogels. The obtained results indicate that the sorption and release rate can be controlled by the morphology of the sorbents and, to some extent, by the ion concentration of the surrounding medium.

KEYWORDS: *metoprolol, foam templating, desorption, porous hydrogel, drug delivery*

1. INTRODUCTION

Hydrogels are three-dimensional hydrophilic polymer networks that are swollen in water and are generated by chemical or physical cross-linking of polymer chains. Due to their high water content[1,2] as well as their ability to be fabricated in a variety of shapes,[3,4] hydrogels have gained a lot of attention as functional materials in fields such as tissue engineering,[5,6] drug delivery,[7] or wastewater treatment.[8] Furthermore, hydrogels are also attractive materials for ion exchange if suitable functional groups within the hydrogels are provided. As the meshes of hydrogels are generally permeable for small molecules,[9] the sorption of ions can not only take place at the surface of the hydrogels, i.e., at the interface between the hydrogels and the surrounding medium, but also inside the hydrogels. Thus, the material fraction available for sorption is increased considerably compared to other polymeric materials. The most widely used hydrogels for the sorption of ions are based on poly(styrene sulfonate)[10] or poly(acrylic acid).[11] However, these materials entail several drawbacks such as their lack of biodegradability or the non-renewable origin of their building blocks. Consequently, hydrogels[12−15] or hydrogel composites[16−18] based on various biopolymers have been examined extensively as materials for the sorption of ions due to their low cost, biocompatibility, and biodegradability.[19,20] For example, the removal of the cationic dye methylene blue from aqueous solutions was demonstrated not only for hydrogels based on cellulose−graft−acrylic acid[21] but also for chitosan−halloysite composite hydrogels.[8] Furthermore, foamed hydrogels have also been examined for the sorption of heavy metal ions[13,18] or organic dyes[15,22] via ion exchange. If the pores of the foamed hydrogel are interconnected, the sorbate first diffuses through the pores before entering the hydrogel matrix, where the sorption takes place. From our perspective, the sorption behavior of foamed hydrogels has not yet been sufficiently compared with their non-foamed counterparts and, by the same token, the influence of the

Received: August 5, 2021
Accepted: September 23, 2021
Published: October 7, 2021

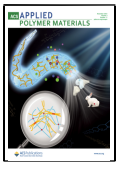

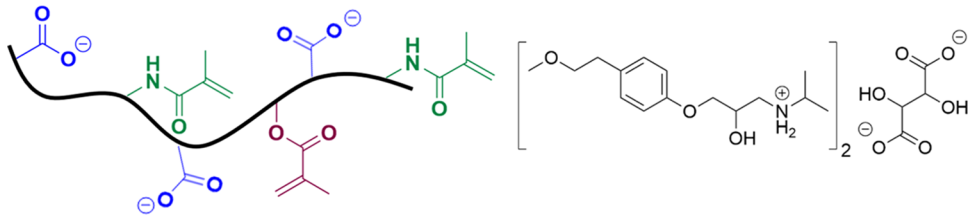

Figure 1. Chemically modified gelatin (left) and the chemical structure of metoprolol tartrate (right).

foamed hydrogel morphology on the sorption and release behavior has not been characterized thoroughly.

One way to generate foamed hydrogels with a defined morphology is foam templating.[23,24] In this technique, a liquid foam based on an aqueous polymer solution is generated and subsequently solidified. During solidification, the structure of the liquid foam is retained and serves as a template for the structure of the solid foam. Consequently, the morphology of the foamed hydrogel can be efficiently tailored by adjusting the structure and properties of the liquid foam. This approach has recently been used to generate hydrogel foams with defined pore diameters and pore opening diameters based on the biopolymer gelatin by adjusting the bubble diameter and the liquid fraction via microfluidic techniques.[25,26] In these studies, the solidification of the liquid templates was enabled using methacryl-modified gelatin, which can be cross-linked by irradiation with UV light in the presence of a suitable photoinitiator. Gelatin methacryloyl can be synthesized by modification of the amine and hydroxyl groups in the polypeptide side chains (Figure 1, left) with methacrylic anhydride.[27] The physicochemical properties as well as the generation of gelatin methacryloyl hydrogels have been characterized thoroughly in the recent years.[27−30] By contrast, foamed hydrogels based on gelatin methacryloyl were only investigated in two studies.[25,26]

When using gelatin-based hydrogels for ion exchange, the methods for preparing gelatin hydrogels have to be carefully considered. Unmodified gelatin is a polypeptide that is generated by either acidic (type A) or alkaline (type B) hydrolysis of collagen.[31] The reaction conditions during hydrolysis considerably influence the charge distribution on the polypeptide. While gelatin type A has an isoelectric point of 8.8,[32] which closely resembles that of native collagen,[31] gelatin type B has an isoelectric point of 4.9.[32] This decrease is due to the conversion of the amino acids asparagine and glutamine into aspartic and glutamic acid under basic conditions. Upon methacryloylation of amine groups in amino acid side chains (Figure 1, left), the isoelectric point is further decreased to 4.5 for gelatin type A and to 4.1 for gelatin type B.[32] As this results in a net negative charge at a neutral pH, hydrogels based on gelatin methacryloyl are potential materials for the sorption of cations via ion exchange. In fact, gelatin has often been used as part of a polymer mixture whose sorption capability is studied.[12,16,17] However, the contribution of gelatin regarding the sorption of ions remains unclear and has not yet been thoroughly characterized. One aspect that is also highly relevant in the field of sorption is the reusability of the material, especially for adsorbers used, e.g., in wastewater treatment. Sorbed ions can be released from hydrogels by changing the pH value[16] or by immersing the material in salt solutions.[33] This effect can also be applied in the field of drug delivery and controlled release if ionic drugs are sorbed on the hydrogel.[34] Especially in drug delivery, the control of the release rate is of utmost importance.

In this study, we examine the sorption and release behavior of gelatin methacryloyl hydrogels with different sample morphologies. To this end, foamed hydrogels with a defined pore diameter generated by liquid foam templating are compared with non-foamed hydrogels. To examine whether sorption and release on the net negatively charged gelatin methacryloyl hydrogels take place via ionic interactions, the cationic drug metoprolol (Figure 1, right) is used as a model sorbate. We chose metoprolol because (i) it is a β-blocker that is often used for treating cardiovascular diseases,[35] (ii) it is a micropollutant in surface water,[36] and (iii) it can be easily quantified using UV/Vis spectroscopy. To examine the sorption and release behavior in equilibrium, sorption and release isotherms are measured. Furthermore, the sorption and release behaviors under non-equilibrium conditions are studied by measuring the kinetics for differently concentrated sorption and release media.

2. MATERIALS AND METHODS

2.1. Chemicals. Gelatin (type B, 232 bloom, batch #641819) was donated by Gelita (Germany). Methacrylic anhydride, phosphate buffered saline (PBS), and metoprolol tartrate were purchased from Sigma Aldrich (Germany). Methylene blue was purchased from S3 Chemicals (Germany). Plantacare 2000 UP was donated by Cognis (Germany, now BASF) and lithium phenyl-2,4,6-trimethylbenzoyl-phosphinate (LAP) was purchased from Carbosynth (U.K.). Perfluorohexane (95, 85% *n*-isomer) was purchased from abcr (Germany). Ethanol (absolute) and sodium chloride (NaCl) were purchased from VWR (Germany). All chemicals were used as received and deionized water was used for all experiments.

2.2. Synthesis of Gelatin Methacryloyl. Gelatin methacryloyl was synthesized and characterized according to a procedure described elsewhere.[25,27] Briefly, 13.65 mL of methacrylic anhydride was added to a solution of 25.01 g of gelatin type B at 37 °C. As the amount of methacrylic anhydride corresponds to a 10-fold molar excess compared to free amine groups (0.35 mmol g^{-1} according to Van Den Bulcke et al.[37]), the modified gelatin is further denoted as GM10. The pH was adjusted to 7.25 using a 4 M NaOH solution. Thus, the counter ions of the carboxylic acids in the resulting GM10 are only sodium ions, which will translate into the hydrogels prepared below for sorption and release experiments. After 5 h of reaction time, the crude product was filtered, stored at 8 °C for 2 days, and dialyzed against deionized water for 5 days. The purified product was freeze-dried and the degree of methacryloylation was determined via ^{1}H NMR to be 0.88 mmol g^{-1}.[27]

2.3. Sample Preparation. Both foamed and non-foamed hydrogels were prepared using an aqueous solution of 20 wt % GM10, 0.14 wt % LAP, and 0.1 wt % Plantacare 2000 UP.

2.3.1. Foamed Hydrogels. Monodisperse foamed hydrogels were prepared using liquid foam templating.[25] The liquid foam templates were generated by microfluidic bubbling using a home-made polycarbonate microfluidic chip with a confined coflow geometry. The microfluidic chip was manufactured by micromilling and had a constriction of 70 μm. The polymer solution was pushed through the

https://doi.org/10.1021/acsapm.1c00968
ACS Appl. Polym. Mater. 2021, 3, 5674−5682

chip by applying a liquid flow rate of 25 μL min^{-1} and a gas pressure of 500 mbar. Traces of perfluorohexane were added to the gas phase to prevent coarsening. The resulting bubble diameter was D_b = 154 ± 2 μm. The liquid foam was collected in a cylindrical aluminum mold with a height of 2 mm and a diameter of 2 cm and covered with a quartz glass pane. The foams were irradiated immediately with UV-A light for 4.5 min using an Omnicure Series 1500 UV lamp with a maximum emission spectrum between 360 and 370 nm. The UV lamp was operated at 15% and the light guide tip had a distance of 5 cm to the samples. Smaller samples with a height of 2 mm and a diameter of 4 mm were punched out of the cross-linked hydrogel foam using a biopsy punch. The cross-linked samples were washed for 3 days with deionized water and 1 day with ethanol to both sterilize the samples and to ensure rapid evaporation of the solvent during the drying process. The washing medium was changed twice a day. To avoid the generation of additional pores due to the formation of ice crystals during freezing, the samples were not freeze-dried like in previous studies[25,26] but were dried at 60 °C until a constant mass was reached. The samples were stored at room temperature until further use. To characterize the pore diameter and pore opening diameter of the swollen hydrogel foams, three random samples were stained with methylene blue according to a procedure described elsewhere[26] and examined with confocal fluorescence microscopy. The resulting pore diameter was D_p = 147 ± 3 μm and the resulting pore opening diameter was d_p = 26 ± 6 μm. A representative image of the generated foams is depicted in Figure 2.

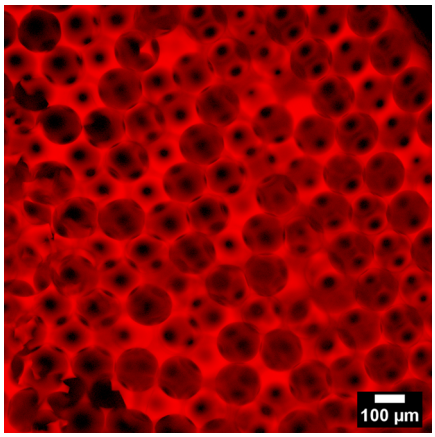

Figure 2. Confocal fluorescence microscope image of a foamed hydrogel sample stained with methylene blue. The resulting pore diameter was D_p = 147 ± 3 μm and the resulting pore opening diameter was d_p = 26 ± 6 μm.

2.3.2. Non-foamed Hydrogels. The polymer solution was poured into cylindrical molds with a height of 2 mm and a diameter of 4 mm and covered with a quartz glass pane. Curing by UV irradiation and subsequent washing and drying were done identical to the procedure described for foamed hydrogels.

2.4. UV/Vis Spectroscopy. A Lambda 25 UV/Vis spectrometer from PerkinElmer (Germany) was used to determine metoprolol concentrations present in the supernatants in sorption and release experiments. The absorption at the maximum wavelength (274 nm) was used for the analysis of the experimental data. Calibrations for metoprolol measurements were carried out using two different cuvettes. For cuvettes with a pathlength of 10 mm, standard solutions with concentrations between 0.04 and 1.0 μmol mL^{-1} were used. For cuvettes with a pathlength of 2 mm, standard solutions with concentrations between 1 and 6 μmol mL^{-1} were used. Cuvettes with a pathlength of 2 mm were only used where measured metoprolol concentrations exceeded 1.74 μmol mL^{-1}. At this concentration, the measured absorption exceeds 2.5 when using a cuvette with a pathlength of 10 mm. This extent of absorption is close to the detection limit of the spectrophotometer used at hand and might lead to an inaccurate determination of the concentration.

2.5. Sorption Measurements. To determine the sorption isotherms for foamed and non-foamed hydrogels, the dry samples were swollen in deionized water for 24 h. The dry mass of the gels was between 5.2 and 5.5 mg for the non-foamed samples and between 1.2 and 1.7 mg for the foamed samples. One sample was used for each measurement. The surface of the swollen hydrogel samples was blotted dry to remove excess water and the samples were immersed into 3 mL of metoprolol solutions with concentrations ranging from 0.06 to 8 μmol mL^{-1}. Please note that all concentrations refer to metoprolol concentrations instead of metoprolol tartrate concentrations, i.e., the metoprolol concentration is twice as big as the metoprolol tartrate concentration. The samples were placed onto an orbital platform shaker (45 rpm) at room temperature. After 96 h, the UV absorption spectrum of the supernatant was measured. The amount $q_{e,a}$ of sorbed metoprolol per mass of hydrogel was determined according to eq 1

$$q_{e,a} = \frac{(c_0 - c_{e,a})V_a}{m} \quad (1)$$

with c_0 being the initial concentration of metoprolol and $c_{e,a}$ being the equilibrium concentration of metoprolol in the supernatant. V_a is the volume of the metoprolol solution and m is the dry mass of the hydrogel.

To measure the sorption kinetics, dry foamed and non-foamed samples were swollen in deionized water for 24 h. The dry mass of the samples varied between 5.2 and 5.3 mg. As one foamed sample specimen corresponded to a mass of ∼1.4 mg, multiple foamed samples were used to achieve a mass between 5.2 and 5.3 mg. Afterward, the surface of the samples was blotted dry to remove excess water and the samples were immersed into cuvettes with a pathlength of 10 mm containing 3 mL of a 0.2 or a 1 μmol mL^{-1} metoprolol solution. The samples were placed on an orbital platform shaker (45 rpm) at room temperature. The concentration in the supernatant was determined at different time points via UV/Vis spectroscopy and the amount q_t of metoprolol present per mass of hydrogel at a time t was determined according to eq 2

$$q_t = \frac{(c_0 - c_t)V_a}{m} \quad (2)$$

with c_t being the concentration of metoprolol in the supernatant at a time t. All of the kinetic measurements were carried out in triplicates.

2.6. Release Measurements. To load the hydrogel samples for the release isotherms, the dry samples were swollen in deionized water for 24 h. Afterward, the surface of the swollen hydrogel samples was blotted dry to remove excess water and the samples were immersed into 3 mL of metoprolol solution with a concentration of 1 μmol mL^{-1}. The samples were placed onto an orbital platform shaker (45 rpm) at room temperature. After 96 h, the UV absorption spectrum of the supernatant was measured to determine the equilibrium concentration $c_{e,a}$ after sorption. To determine the release isotherms, the samples were placed into 3 mL of NaCl solution with concentrations ranging from 0 to 10 μmol mL^{-1}. Additionally, samples were also placed in 3 mL of PBS solution. The concentration of metoprolol in the supernatant was determined after 96 h, and the percentage of metoprolol being released from the hydrogel was determined from the initial loading concentration c_0, the equilibrium concentration after sorption $c_{e,a}$, and the equilibrium concentration $c_{e,d}$ after desorption, according to eq 3

$$\text{percent released} = \frac{c_{e,d}}{c_0 - c_{e,a}} \times 100\% \quad (3)$$

To measure the release kinetics, both foamed and non-foamed samples with dry masses between 5.2 and 5.3 mg were swollen in water and loaded with metoprolol as described above. As one foamed sample specimen corresponds to a mass of ∼1.4 mg, multiple foamed samples were used to achieve a mass between 5.2 and 5.3 mg. The loaded hydrogels were immersed in a cuvette with a pathlength of 10

https://doi.org/10.1021/acsapm.1c00968
ACS Appl. Polym. Mater. 2021, 3, 5674−5682

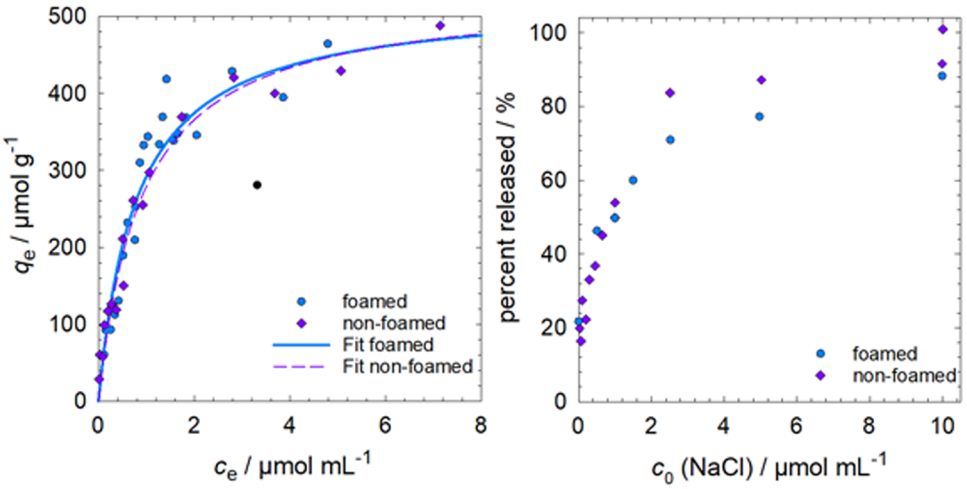

Figure 3. (Left) Metoprolol concentrations $q_{e,a}$ inside foamed and non-foamed hydrogels against equilibrium concentrations $c_{e,a}$ of metoprolol in the surrounding medium. The lines represent fits according to eq 5. The data point marked in black was not included in the non-linear regression. (Right) Percentage of released metoprolol against initial sodium chloride concentrations for both foamed and non-foamed hydrogels. Prior to the release experiments, the samples were loaded with 248 ± 10 µmol g^{-1} metoprolol.

mm containing 3 mL of a 1 or 10 µmol mL^{-1} NaCl solution and the UV absorption spectrum of the supernatant was measured after different time intervals. Between measurements, the samples were placed onto an orbital platform shaker (45 rpm) at room temperature. The amount of metoprolol released at a time t per mass of hydrogel, $q_{e,a} - q_{t,d}$, was calculated according to eq 4

$$q_{e,a} - q_{t,d} = \frac{c_{t,d} V_d}{m} \tag{4}$$

with $c_{t,d}$ being the concentration of metoprolol in the release medium at time t, V_d is the volume of the release medium, and m is the dry mass of the hydrogel. All kinetic measurements were carried out in triplicates.

3. RESULTS AND DISCUSSION

3.1. Sorption and Release Isotherms. To assess the interaction of metoprolol with both foamed and non-foamed hydrogels in the equilibrium state, sorption and release isotherms were measured. Sorption isotherms were determined by calculating the equilibrium concentrations $q_{e,a}$ of metoprolol inside the hydrogel and plotting them against the corresponding equilibrium concentrations $c_{e,a}$ of metoprolol in the surrounding medium (Figure 3, left). For both foamed and non-foamed hydrogels, $q_{e,a}$ initially increased with increasing $c_{e,a}$ values until a plateau was reached. The data points were subsequently analyzed using the Langmuir model (eq 5).[38] In this model, it is assumed that a specific amount of equal sorption sites are provided by the sorbent. Each sorption site can sorb only one molecule and the sorption sites are accessible to all sorbate molecules. Furthermore, no interactions between neighboring sorption sites and sorbed molecules occur. It holds

$$q_{e,a} = q_{max} \frac{K_s c_{e,a}}{1 + K_s c_{e,a}} \tag{5}$$

where q_{max} is the sorption capacity and K_s is the equilibrium constant, which is the ratio of the sorption and desorption rate constants. The values for K_s and q_{max} obtained by non-linear regression are summarized in Table 1.

The obtained values for K_s and q_{max} differed only slightly between foamed and non-foamed hydrogels. Thus, it can be concluded that the morphology of the material does not influence the equilibrium sorption behavior. This indicates that metoprolol can enter the hydrogel through the surface of the material, i.e., that there is no size exclusion and that metoprolol has the same accessibility to sorption sites in both materials. For both foamed and non-foamed hydrogels, K_s is close to 1 mL µmol^{-1}, implying that the rate constants of sorption and desorption are approximately the same. Although a direct comparison between metoprolol and heavy metal ions is not possible, we note that the K_s value is two orders of magnitude larger in the case of systems such as alginate/polyurethane foams for which K_s values of up to 11 mL µmol^{-1} were obtained for the sorption of heavy metal ions.[13]

Table 1. Langmuir Isotherm Parameters K_s and q_{max} for the Sorption of Metoprolol onto Foamed and Non-foamed Hydrogels Obtained by Fitting the Data to Equation 5[a]

	K_s/mL µmol^{-1}	q_{max}/µmol g^{-1}
foamed	1.3	522
non-foamed	1.1	531

[a]The data points were weighted using the reciprocal of the probability density function via the kernel density estimate.

The maximum sorption capacity q_{max} reached approximately 520−530 µmol g^{-1} for both foamed and non-foamed hydrogels, which corresponds to 142 mg g^{-1}. When analyzing the amino acid composition of gelatin type B, which was used for this study, 427 µmol g^{-1} aspartic acid and 701 µmol g^{-1} glutamic acid were found.[32] Thus, the theoretical maximum sorption capacity is 1128 µmol g^{-1}, assuming that sorption of metoprolol takes place at the carboxyl groups of gelatin. The fact that this is approximately twice as high compared to the experimentally determined value might be due to incomplete dissociation of metoprolol tartrate in aqueous solutions.

To demonstrate the reusability of the material, the hydrogels were loaded with 248 ± 10 µmol g^{-1} metoprolol and subsequently immersed into differently concentrated sodium chloride solutions. The percentage of metoprolol released from the hydrogel was plotted against the initial sodium chloride concentration (Figure 3, right). Equally to the equilibrium sorption behavior, it was found that the morphology had no

https://doi.org/10.1021/acsapm.1c00968
ACS Appl. Polym. Mater. 2021, 3, 5674−5682

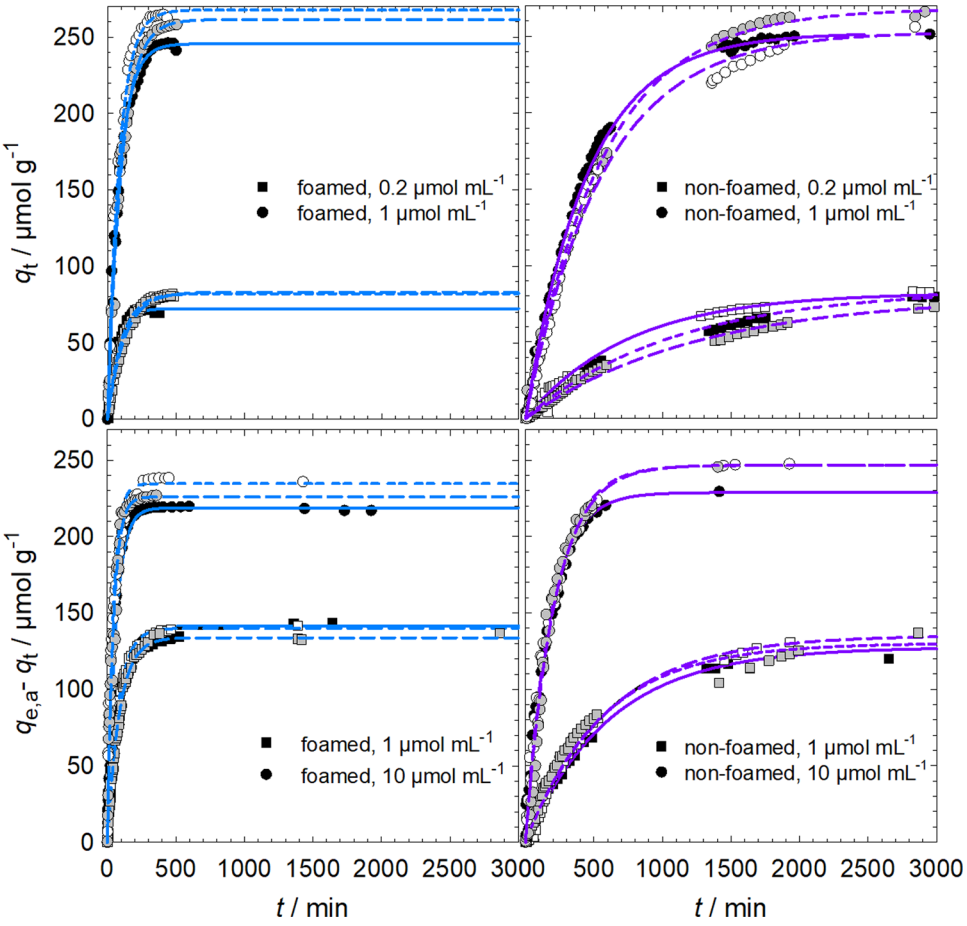

Figure 4. (Top) Sorption kinetics: Metoprolol concentrations q_t inside foamed (left) and non-foamed (right) hydrogels against time t. Solutions with c_0 (Metoprolol) = 1 and 0.2 μmol mL^{-1} were used as starting points. The solid and dashed lines represent the fits according to eq 6. (Bottom) Release kinetics: Amount of released metoprolol, $q_{e,a} - q_t$, for foamed (left) and non-foamed (right) hydrogels against time t. Prior to the release, the samples were loaded with 254 ± 10 μmol g^{-1} metoprolol. Solutions with c_0 (NaCl) = 10 and 1 μmol mL^{-1} sodium chloride were used as release medium. The solid and dashed lines represent the fits according to eq 7.

significant influence on the equilibrium release behavior, either. It was observed that for both foamed and non-foamed hydrogels, the percentage of released metoprolol increased with increasing sodium chloride concentration from ∼20% at a concentration of 0 μmol mL^{-1} (deionized water) to 90−100% at a concentration of 10 μmol mL^{-1}. The release of up to 20% metoprolol upon immersion into deionized water can be ascribed to the weak interaction between metoprolol and gelatin, which is also indicated by the low K_s value. When increasing the sodium chloride concentration, a plateau is reached where up to 100% of metoprolol is released, which demonstrates that the material is fully regenerable by immersing it into a salt solution. This also substantiates that the sorption and release of metoprolol and sodium takes place via ion exchange, which is again confirmed by the fact that 100% of sorbate is released by immersion in PBS, a buffer that matches the ion concentrations and osmolarity of the human body. PBS has a total salt concentration of 151 μmol mL^{-1}. In addition to immersion in salt solutions[34] at a constant pH value, hydrogels for ion exchange are often regenerated by immersing the material in, e.g., HCl solutions and thus changing the pH value.[16] However, this method is not suitable for the materials examined in this study as gelatin is a polypeptide and thus sensitive to hydrolysis at high or low pH values.

3.2. Sorption and Release Kinetics. To study the time-dependent interaction of metoprolol with both foamed and non-foamed hydrogels, the sorption kinetics as well as the release kinetics were examined. Two different initial metoprolol concentrations, namely, 0.2 and 1 μmol mL^{-1}, were used for measuring the sorption kinetics, and the amount of metoprolol inside the hydrogels, q_t, was plotted against time t (Figure 4, top left and top right). For both foamed and non-foamed hydrogels, as well as for both initial sorbate concentrations c_0, the value of q_t initially increased with increasing time until a plateau was reached, which represents the equilibrium concentration $q_{e,a}$ of metoprolol inside the hydrogels. It was observed that $q_{e,a}$ is the same for both foamed and non-foamed samples if the same initial sorbate concentrations c_0 are used. This confirms again that the sample morphology does not influence the equilibrium state. By contrast, the initial slope of the $q_t(t)$ curves, which is related to the sorption rate coefficient k_1, varies considerably between foamed and non-foamed hydrogels as well as for initial sorbate ion concentrations.

To determine the sorption rate coefficients, the kinetic data were analyzed using the pseudo-first-order kinetic model[39]

$$q_t = q_{e,a}(1 - e^{-k_1 t}) \quad (6)$$

https://doi.org/10.1021/acsapm.1c00968
ACS Appl. Polym. Mater. 2021, 3, 5674−5682

Table 2. Kinetic Parameters k_1 and $q_{e,a}$ for the Sorption of Metoprolol on Foamed and Non-foamed Hydrogels Using Different Metoprolol Concentrations c_0 as well as Kinetic Parameters k_2 and $q_{e,d}$ for the Release of Metoprolol from Foamed and Non-foamed Hydrogels Using Different Sodium Chloride Concentrations c_0[a]

		c_0 (Metoprolol)/μmol mL^{-1}	k_1/h^{-1}	$q_{e,a}$/μmol g^{-1}
sorption	foamed	0.2	0.64 ± 0.19	79 ± 6
		1	0.67 ± 0.07	258 ± 11
	non-foamed	0.2	0.061 ± 0.017	82 ± 2
		1	0.12 ± 0.015	258 ± 9
		c_0 (NaCl)/μmol mL^{-1}	k_2/h^{-1}	$q_{e,d}$/μmol g^{-1}
release	foamed	1	0.71 ± 0.05	139 ± 4
		10	1.27 ± 0.23	227 ± 8
	non-foamed	1	0.102 ± 0.005	131 ± 4
		10	0.31 ± 0.03	241 ± 10

[a]Prior to the release experiments, all samples were loaded with 254 ± 10 μmol g^{-1} metoprolol. The values are obtained by non-linear regression and the listed errors are standard deviations. The data points were weighted using the reciprocal of the probability density function via the kernel density estimate.

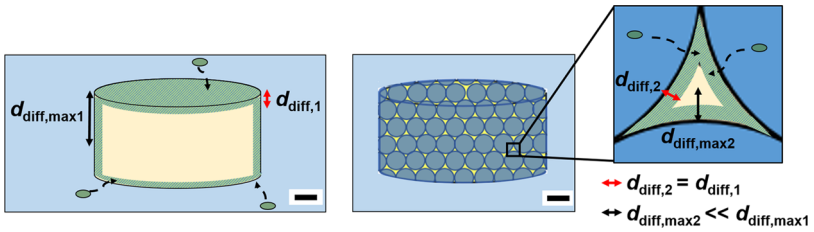

Figure 5. (Left) Schematic drawing of the sorption process in non-foamed hydrogels. The metoprolol molecule (green) crosses the surface of the hydrogel matrix (yellow) and diffuses through the meshes of the hydrogel. The average distance a metoprolol molecule has covered at a given time t is denoted as $d_{diff,1}$, whereas the maximum distance to the surface is denoted as $d_{diff,max1}$. The scale bar is 500 μm. (Right) Schematic drawing of the sorption process in foamed hydrogels. The blue circles represent the water-filled pores, whereas the hydrogel matrix is illustrated in yellow. The average distance a metoprolol molecule has covered at a given time t is denoted as $d_{diff,2}$. Note that $d_{diff,max2}$ is much shorter compared to the non-foamed hydrogel. As a result, a bigger fraction of the available hydrogel matrix is penetrated by the metoprolol solution at a given time t. The scale bar is 500 μm.

The values for $q_{e,a}$ and k_1 obtained by non-linear regression are summarized in Table 2. Furthermore, the release kinetics were examined by immersing both foamed and non-foamed hydrogels, which were loaded with 254 ± 10 μmol g^{-1} metoprolol into sodium chloride solutions. Two different sodium chloride concentrations were used, namely, 1 and 10 μmol mL^{-1}, and the amount of metoprolol released from the hydrogels, $q_{e,a} - q_t$, was plotted against time t (Figure 4, bottom left and bottom right). Similar to the sorption kinetics, the values of $q_{e,a} - q_t$ initially increased with increasing time until a plateau was reached, which represents the equilibrium amount $q_{e,d}$ of metoprolol released per mass of hydrogel. Again, $q_{e,d}$ was the same for foamed and non-foamed hydrogels if the same initial sodium chloride concentrations were used, confirming that the sample morphology does not influence the equilibrium state. Furthermore, one sees that the sample morphologies, as well as the sodium chloride concentrations, strongly influence the initial slope of the curves, which is related to the release rate coefficient k_2. To determine release rate coefficients, the kinetic data were analyzed using the expression

$$q_{e,a} - q_t = q_{e,d}(1 - e^{-k_2 t}) \quad (7)$$

The values for $q_{e,d}$ and k_2 obtained by non-linear regression are also summarized in Table 2.

Looking at Table 2 and comparing foamed with non-foamed hydrogels, one sees that the sorption rate coefficient k_1 obtained for an initial metoprolol concentration of 0.2 μmol mL^{-1} is 10-fold higher for foamed hydrogels. For an initial metoprolol concentration of 1 μmol mL^{-1}, a 6-fold increase in k_1 was found. This large increase in k_1 for both initial metoprolol concentrations can be ascribed to the difference in both the surface area and diffusion path for foamed and non-foamed hydrogels. The surface is defined as the interface between the hydrogel matrix and the surrounding medium, whereas the diffusion path is the distance a metoprolol molecule has to cover until sorption occurs at a specific sorption site. During the sorption process for both foamed and non-foamed hydrogels, the sorbate crosses the surface of the hydrogel and diffuses through the meshes of the polymer network until it sorbs onto the polymer network (Figure 5). In case of foamed materials with interconnected pores, the sorbate additionally has to diffuse through the water-filled pores before entering the hydrogel matrix, which is due to the swelling step in deionized water. However, the diffusion coefficient D_w of metoprolol in water should be much larger compared to the diffusion coefficient of metoprolol inside the hydrogel D_h. The latter depends on parameters such as the cross-linking density, polymer concentration, and amount of charged groups inside the hydrogel. For calcium alginate hydrogels, the diffusion coefficient of copper ions inside the hydrogels was reported to be 25% of the diffusion coefficient of free copper ions.[40] Thus, the initial diffusion through the interconnected pores in foamed hydrogels, which are first filled with deionized water and which have to be passed before the drug reaches the hydrogel matrix, should not affect the equilibration time significantly. Note that the properties of the hydrogel (e.g., the equilibrium swelling degree) may change

https://doi.org/10.1021/acsapm.1c00968
ACS Appl. Polym. Mater. 2021, 3, 5674−5682

during the sorption of ions, which, in turn, influences D_h. Also, D_h can be expected to depend on the local occupation of sorption sites, which out of equilibrium is a function of time and location. Thus, D_h will also depend on time and location.

For a more detailed understanding, it is useful to define a characteristic diffusion time τ that a metoprolol molecule needs to travel an average distance d_{diff}[41]

$$\tau \sim \frac{d_{diff}^2}{D_h} \tag{8}$$

If one assumes a relatively small curvature of the hydrogel surface A, d_{diff} is correlated to the penetrated volume V by

$$d_{diff} = \frac{V}{A} \tag{9}$$

By combining eqs 8 and 9, it is obvious that a reduction of the maximum diffusion path through the hydrogel meshes will result in a much faster penetration of the entire sample volume, leading to shorter equilibration times.

Figure 5 visualizes the sorption process for both foamed and non-foamed hydrogels. Due to the larger surface area in foamed hydrogels, the volume V of the hydrogel that is penetrated by the metoprolol solution at a given time t is much larger for an equal distance d_{diff}. As a result, foamed hydrogels have a shorter equilibration time and thus a larger sorption rate coefficient k_1. The equilibrium state is reached when metoprolol is distributed evenly on the polymer network.

The difference in the diffusion path between foamed and non-foamed hydrogels can also be illustrated via the maximum distance $d_{diff,max}$ from the center of the hydrogel to its surface. For non-foamed hydrogels, $d_{diff,max1}$ can be estimated to be 1 mm (see Section 2.3) based on the cylindrical shape of the sample (Figure 5). For foamed hydrogels, $d_{diff,max2}$ is much shorter and can be estimated assuming a hexagonal closed packing of pores with a volume fraction of 74% and a pore diameter D_p. In this case, $d_{diff,max2}$ equals the radii of octahedral (eq 10) and tetrahedral voids (eq 11) between the pores of the hydrogel foam

$$d_{diff,max2} = (\sqrt{2} - 1)\frac{D_p}{2} \approx 0.207 \times D_p \tag{10}$$

$$d_{diff,max2} = \left(\frac{\sqrt{6}}{2} - 1\right)\frac{D_p}{2} \approx 0.112 \times D_p \tag{11}$$

In this study, foams with a pore diameter D_p = 147 μm were used, which corresponds to $d_{diff,max2}$ = 30 μm (octahedral voids) or $d_{diff,max2}$ = 17 μm (tetrahedral voids).

During the release, which is essentially the sorption of sodium ions on the sorption sites, the reverse process takes place. First, the sodium ions cross the surface of the hydrogels and diffuse through the meshes of the hydrogel until they are sorbed at the sorption sites. As a result, metoprolol is displaced from the sorption sites, diffuses through the polymer network, and is finally released into the surrounding medium by crossing the hydrogel surface. Equilibrium is attained when the sodium ions are evenly distributed on the polymer network. Again, the equilibration time should depend on both the surface area and the diffusion path. Indeed, similar trends like those for the sorption kinetics can be observed for the release kinetics. Comparing foamed to non-foamed samples, the release rate coefficient k_2 is ~7-fold higher for an initial sodium chloride concentration of 1 μmol mL^{-1} and ~4-fold higher for an initial sodium chloride concentration of 10 μmol mL^{-1}. Note that at a concentration of 1 μmol mL^{-1} metoprolol or sodium chloride, the rate constants k_1 and k_2 are identical for both foamed and non-foamed hydrogels. This further indicates that the sorption and release are complementary processes.

As both the surface area and $d_{diff,max}$ directly depend on D_p, it might be possible to adjust the rate of sorption and release by tailoring the pore radius of the foamed hydrogels. This could be of particular relevance in fields such as wastewater treatment or drug delivery, where a controlled removal of water contaminants or a controlled release of ionic drugs is desirable.

In addition to the effect of the sample morphology, a second parameter, namely the initial metoprolol or sodium chloride concentration, can be identified to influence both k_1 and k_2. For the sorption of metoprolol, this effect is more pronounced for non-foamed hydrogels, where a 2-fold increase in k_1 was found when increasing the initial metoprolol concentration from 0.2 to 1 μmol mL^{-1}. For foamed hydrogels, k_1 is approximately the same for both sorbate concentrations. Similar trends can again be observed for the release kinetics. When increasing the sodium chloride concentration from 1 to 10 μmol mL^{-1}, a 3-fold increase in k_1 was found for non-foamed hydrogels, whereas a 2-fold increase in k_1 was observed for foamed hydrogels. The influence of the concentration on the rate coefficients can be explained by considering that the rate coefficients describe the mass transfer of the sorbate into and out of the gel. The mass transfer is in turn influenced by the gradient of q_t or $q_{e,a} - q_t$ inside the hydrogel matrix. Both q_t and $q_{e,a} - q_t$ are related to the sorbate concentrations via the Langmuir isotherm, which is only linear for small values of c_e. If higher c_e values are obtained, the gradients of q_t or $q_{e,a} - q_t$ should differ for different concentrations due to the non-linearity of the Langmuir isotherm, which in turn should lead to different rate coefficients. However, the relation between the rate coefficients and the sorbate concentrations is far more complex because the diffusion coefficient of metoprolol in the hydrogel is influenced by, e.g., the equilibrium swelling degree, which may change during the sorption and release process. When comparing the influence of the concentration for different hydrogel morphologies, one sees that the effect of the concentration is higher for non-foamed hydrogels as compared to foamed hydrogels. This might again be ascribed to the larger diffusion path, which increases the time until equilibrium is attained. This effect is especially pronounced for the sorption kinetics of foamed hydrogels, where almost equal values for k_1 were obtained. The difference in k_2 on the other hand is more obvious, which can be ascribed to the fact that the difference in initial sodium chloride concentration is larger. Similar to the influence of the morphology, the influence of the initial concentrations on the sorption and release rate coefficients is also important for potential application fields such as wastewater treatment and drug delivery, where a control over the rate coefficients is of practical relevance.

Finally, when looking at the amounts of released metoprolol for different sodium chloride concentrations (Table 2), one can learn something about the relative affinity of metoprolol and sodium to the sorption sites. All samples were loaded with metoprolol using a solution with a concentration of 1 μmol mL^{-1}. When immersing the materials in a 1 μmol mL^{-1} sodium chloride solution, ~139 μmol mL^{-1} metoprolol was released, which corresponds to 55%. By contrast, ~241 μmol mL^{-1} metoprolol, which corresponds to 95%, was released

https://doi.org/10.1021/acsapm.1c00968
ACS Appl. Polym. Mater. 2021, 3, 5674−5682

when immersing the materials in a 10 μmol mL^{-1} sodium chloride solution. As the volume of sorption and release medium is the same, the ratios of metoprolol to sodium chloride are 1:1 and 1:10, respectively. Interestingly, this results in a release of 55% and 95%, which would be expected if both ions had approximately the same affinity to the sorption sites.

4. CONCLUSIONS

In this study, the sorption and release behavior of gelatin-based hydrogels were examined for two different morphologies using the cationic molecule metoprolol as a model drug. The sorption and release behavior in equilibrium conditions was characterized by measuring the sorption and release isotherms. When analyzing the sorption isotherm, we found that the equilibrium constant K_s is close to 1 mL μmol^{-1} for both foamed and non-foamed hydrogels, indicating a relatively weak interaction between metoprolol and hydrogels based on gelatin methacryloyl. Furthermore, the maximum sorption capacity was determined to be $q_{max} \approx 530$ μmol g^{-1} for both sample morphologies, which is approximately half of the theoretically expected value. The release of sorbed metoprolol was controlled by immersing the samples in sodium chloride solutions, which shows that the material can be fully regenerated. Consequently, the material can be reused in potential applications. The results show that the sample morphology has no influence on either sorption or release behavior in equilibrium. The sorption and release behavior under non-equilibrium conditions were characterized by kinetic measurements, which was subsequently used to determine the rate coefficients. In contrast to the equilibrium behavior, the sample morphology had a pronounced effect on the rate coefficients, which increased up to 10-fold for foamed hydrogels. This effect might be ascribed to the increased surface area and decreased diffusion path through the hydrogel. The rate coefficients could be further increased by increasing the ion concentrations in the surrounding medium. The observed effect was more prominent for non-foamed hydrogels, which might again be due to the increased diffusion path and surface area of the hydrogel. Future work will focus on elucidating the role of the diffusion path by further varying the sample morphology, which can be achieved by varying the pore diameter and pore opening diameter. Furthermore, the influence of temperature and the pH value will be examined. Once the influence of each parameter is determined, our concept of controlling sorption and release rates with foamed gelatin methacryloyl hydrogels can be applied for different drugs.

Our findings for both equilibrium and non-equilibrium conditions are highly relevant for potential applications such as drug delivery or wastewater treatment. The interaction between sorbate and sorbent is important for the efficiency and the amount of drug loading or the removal of contaminants. Our results clearly show that the rate of sorption and release can be adjusted by tailoring the sample morphology as well as the ion concentration. As the pore diameter of the hydrogel foams can be efficiently adjusted by microfluidic techniques, tailor-made materials for the sorption and release of cationic molecules can easily be generated.

AUTHOR INFORMATION

Corresponding Author

Alexander Southan − *Institute of Interfacial Process Engineering and Plasma Technology, University of Stuttgart, 70569 Stuttgart, Germany;* orcid.org/0000-0001-7530-1690; Email: alexander.southan@igvp.uni-stuttgart.de

Authors

Friederike Dehli − *Institute of Physical Chemistry, University of Stuttgart, 70569 Stuttgart, Germany*

Hailey Poole − *Institute of Physical Chemistry, University of Stuttgart, 70569 Stuttgart, Germany*

Cosima Stubenrauch − *Institute of Physical Chemistry, University of Stuttgart, 70569 Stuttgart, Germany;* orcid.org/0000-0002-1247-4006

Complete contact information is available at: https://pubs.acs.org/10.1021/acsapm.1c00968

Author Contributions

F.D.: conceptualization, experimental design, investigation, writing—original draft; H.P.: investigation; C.S.: conceptualization, writing—review and editing, supervision; A.S.: conceptualization, writing—review and editing, supervision. All authors have given approval to the final version of the manuscript.

Notes

The authors declare no competing financial interest.

ACKNOWLEDGMENTS

The authors thank Dr. Wiebke Drenckhan for fruitful discussions. F.D. gratefully acknowledges financial support by the Fonds der Chemischen Industrie via the Kékulé Stipend. H.P. gratefully acknowledges funding within the DAAD Program Study Scholarships—Master Studies for All Academic Disciplines, 2020/21, No. 57507833.

REFERENCES

(1) Ahmed, E. M. Hydrogel: Preparation, Characterization, and Applications: A Review. *J. Adv. Res.* **2015**, *6*, 105−121.

(2) Peppas, B. N. A.; Hilt, J. Z.; Khademhosseini, A.; Langer, R. Hydrogels in Biology and Medicine: From Molecular Principles to Bionanotechnology. *Adv. Mater.* **2006**, *18*, 1345−1360.

(3) Zhang, Y. S.; Khademhosseini, A. Advances in Engineering Hydrogels. *Science* **2017**, *356*, No. eaaf3627.

(4) Li, H.; Tan, C.; Li, L. Review of 3D Printable Hydrogels and Constructs. *Mater. Des.* **2018**, *159*, 20−38.

(5) Barbetta, A.; Massimi, M.; Di Rosario, B.; Nardecchia, S.; De Colli, M.; Devirgiliis, L. C.; Dentini, M. Emulsion Templated Scaffolds That Include Gelatin and Glycosaminoglycans. *Biomacromolecules* **2008**, *9*, 2844−2856.

(6) Nichol, J. W.; Koshy, S. T.; Bae, H.; Hwang, C. M.; Yamanlar, S.; Khademhosseini, A. Cell-Laden Microengineered Gelatin Methacrylate Hydrogels. *Biomaterials* **2010**, *31*, 5536−5544.

(7) Naskar, S.; Sharma, S.; Kuotsu, K. Formulation, Characterization and Antihypertensive Activity of Metoprolol Succinate Loaded Gelatin Nanoparticles. *J. Drug Delivery Sci. Technol.* **2019**, *53*, No. 101214.

(8) Peng, Q.; Liu, M.; Zheng, J.; Zhou, C. Adsorption of Dyes in Aqueous Solutions by Chitosan-Halloysite Nanotubes Composite Hydrogel Beads. *Microporous Mesoporous Mater.* **2015**, *201*, 190−201.

(9) Majer, G.; Southan, A. Adenosine Triphosphate Diffusion through Poly(Ethylene Glycol) Diacrylate Hydrogels Can Be Tuned by Cross-Link Density as Measured by PFG-NMR. *J. Chem. Phys.* **2017**, *146*, No. 225101.

(10) Vaslow, F.; Boyd, G. E. Thermodynamic Properties in the Exchange of Silver with Sodium Ions in Cross-Linked Polystyrene Sulfonate Cation Exchangers. *J. Phys. Chem. A* **1966**, *70*, 2295−2299.
(11) Xie, J.; Xinrong, L.; Jifu, L. Absorbency and Adsorption of Poly(Acrylic Acid-Co-Acrylamide) Hydrogel. *J. Appl. Polym. Sci.* **2007**, *106*, 1606−1613.
(12) Hui, B.; Zhang, Y.; Ye, L. Structure of PVA/Gelatin Hydrogel Beads and Adsorption Mechanism for Advanced Pb(II) Removal. *J. Ind. Eng. Chem.* **2015**, *21*, 868−876.
(13) Sone, H.; Fugetsu, B.; Tanaka, S. Selective Elimination of Lead(II) Ions by Alginate/Polyurethane Composite Foams. *J. Hazard. Mater.* **2009**, *162*, 423−429.
(14) Zhou, G.; Luo, J.; Liu, C.; Chu, L.; Crittenden, J. Efficient Heavy Metal Removal from Industrial Melting Effluent Using Fixed-Bed Process Based on Porous Hydrogel Adsorbents. *Water Res.* **2018**, *131*, 246−254.
(15) Mittal, H.; Babu, R.; Alhassan, S. M. Utilization of Gum Xanthan Based Superporous Hydrogels for the Effective Removal of Methyl Violet from Aqueous Solution. *Int. J. Biol. Macromol.* **2020**, *143*, 413−423.
(16) Raju, R. R.; Liebig, F.; Klemke, B.; Koetz, J. Ultralight Magnetic Aerogels from Janus Emulsions. *RSC Adv.* **2020**, *10*, 7492−7499.
(17) Ruiz, C.; Vera, M.; Rivas, B. L.; Sánchez, S.; Urbano, B. F. Magnetic Methacrylated Gelatin-: G-Polyelectrolyte for Methylene Blue Sorption. *RSC Adv.* **2020**, *10*, 43799−43810.
(18) Wu, Z.; Chen, X.; Yuan, B.; Fu, M. L. A Facile Foaming-Polymerization Strategy to Prepare 3D MnO2 Modified Biochar-Based Porous Hydrogels for Efficient Removal of Cd(II) and Pb(II). *Chemosphere* **2020**, *239*, No. 124745.
(19) Lai, J. Biocompatibility of Chemically Cross-Linked Gelatin Hydrogels for Ophthalmic Use. *J. Mater. Sci. Mater. Med.* **2010**, *21*, 1899−1911.
(20) Ratnikov, B.; Deryugina, E.; Leng, J.; Marchenko, G.; Dembrow, D.; Strongin, A. Determination of Matrix Metalloproteinase Activity Using Biotinylated Gelatin. *Anal. Biochem.* **2000**, *286*, 149−155.
(21) Zhou, Y.; Fu, S.; Liu, H.; Yang, S.; Zhan, H. Removal of Methylene Blue Dyes From Wastewater Using Cellulose-Based Superadsorbent Hydrogels. *Polym. Eng. Sci.* **2011**, *51*, 2417−2424.
(22) Wang, Y.; Liu, X.; Wang, H.; Xia, G.; Huang, W.; Song, R. Microporous Spongy Chitosan Monoliths Doped with Graphene Oxide as Highly Effective Adsorbent for Methyl Orange and Copper Nitrate (Cu(NO3)2) Ions. *J. Colloid Interface Sci.* **2014**, *416*, 243−251.
(23) Barbetta, A.; Gumiero, A.; Pecci, R.; Bedini, R.; Dentini, M. Gas-in-Liquid Foam Templating as a Method for the Production of Highly Porous Scaffolds. *Biomacromolecules* **2009**, *10*, 3188−3192.
(24) Lin, J. Y.; Lin, W. J.; Hong, W. H.; Hung, W. C.; Nowotarski, S. H.; Gouveia, S. M.; Cristo, I.; Lin, K. H. Morphology and Organization of Tissue Cells in 3D Microenvironment of Monodisperse Foam Scaffolds. *Soft Matter* **2011**, *7*, 10010−10016.
(25) Dehli, F.; Rebers, L.; Stubenrauch, C.; Southan, A. Highly Ordered Gelatin Methacryloyl Hydrogel Foams with Tunable Pore Size. *Biomacromolecules* **2019**, *20*, 2666−2674.
(26) Dehli, F.; Southan, A.; Drenckhan, W.; Stubenrauch, C. Tailoring and Visualising Pore Openings in Gelatin-Based Hydrogel Foams. *J. Colloid Interface Sci.* **2021**, *588*, 326−335.
(27) Claaßen, C.; Claaßen, M. H.; Truffault, V.; Sewald, L.; Tovar, G. E. M.; Borchers, K.; Southan, A. Quantification of Substitution of Gelatin Methacryloyl: Best Practice and Current Pitfalls. *Biomacromolecules* **2018**, *19*, 42−52.
(28) Hoch, E.; Hirth, T.; Tovar, G. E. M.; Borchers, K. Chemical Tailoring of Gelatin to Adjust Its Chemical and Physical Properties for Functional Bioprinting. *J. Mater. Chem. B* **2013**, *1*, 5675−5685.
(29) Rebers, L.; Granse, T.; Tovar, G.; Southan, A.; Borchers, K. Physical Interactions Strengthen Chemical Gelatin Methacryloyl Gels. *Gels* **2019**, *5*, No. 4.
(30) Rebers, L.; Reichsöllner, R.; Regett, S.; Tovar, G. E. M.; Borchers, K.; Baudis, S.; Southan, A. Differentiation of Physical and Chemical Cross-Linking in Gelatin Methacryloyl Hydrogels. *Sci. Rep.* **2021**, *11*, No. 3256.
(31) Babel, W. Gelatine-Ein Vielseitiges Biopolymer. *Chemie Unserer Zeit* **1996**, *30*, 86−95.
(32) Sewald, L.; Claaßen, C.; Götz, T.; Claaßen, M. H.; Truffault, V.; Tovar, G. E. M.; Southan, A.; Borchers, K. Beyond the Modification Degree: Impact of Raw Material on Physicochemical Properties of Gelatin Type A and Type B Methacryloyls. *Macromol. Biosci.* **2018**, *18*, No. 1800168.
(33) Luo, Y.; Kirker, K. R.; Prestwich, G. D. Cross-Linked Hyaluronic Acid Hydrogel FIlms New Biomaterials. *J. Controlled Release* **2000**, *69*, 169−184.
(34) Claus, J.; Eickner, T.; Grabow, N.; Kragl, U.; Oschatz, S. Ion Exchange Controlled Drug Release from Polymerized Ionic Liquids. *Macromol. Biosci.* **2020**, *20*, No. 2000152.
(35) Nellore, R. V.; Singh Rekhi, G.; Hussain, A. S.; Tillman, L. G.; Augsburger, L. L. Development of Metoprolol Tartrate Extended-Release Matrix Tablet Formulations for Regulatory Policy Consideration. *J. Controlled Release* **1998**, *50*, 247−256.
(36) Petrie, B.; Barden, R.; Kasprzyk-Hordern, B. A Review on Emerging Contaminants in Wastewaters and the Environment: Current Knowledge, Understudied Areas and Recommendations for Future Monitoring. *Water Res.* **2015**, *72*, 3−27.
(37) Van Den Bulcke, A. I.; Bogdanov, B.; De Rooze, N.; Schacht, E. H.; Cornelissen, M.; Berghmans, H. Structural and Rheological Properties of Methacrylamide Modified Gelatin Hydrogels. *Biomacromolecules* **2000**, *1*, 31−38.
(38) Langmuir, I. The Adsorption of Gases on Plane Surfaces of Glass, Mica and Platinum. *J. Am. Chem. Soc.* **1918**, *40*, 1361−1403.
(39) Lagergren, S. Y. *Zur Theorie Der Sogenannten Adsorption Gelöster Stoffe*; Kungliga Svenska Vetenskapsakademiens: Handlingar, 1898; Vol. *24*, pp 1−39.
(40) Potter, K.; McFarland, E. W. Ion transport studies in calcium alginate gels by magnetic resonance spectroscopy. *Solid State Nucl. Magn. Reson.* **1996**, *6*, 323−331.
(41) Atkins, P. W.; de Paula, J. *Kurzlehrbuch Physikalische Chemie*, 4th ed.; WILEY-VCH Verlag GmbH & Co. KgaA: Weinheim, 2008; p 501.

https://doi.org/10.1021/acsapm.1c00968
ACS Appl. Polym. Mater. 2021, 3, 5674−5682

Publication III

RESEARCH ARTICLE

Macromolecular Bioscience
www.mbs-journal.de

New Gelatin-Based Hydrogel Foams for Improved Substrate Conversion of Immobilized Horseradish Peroxidase

*Friederike Dehli, Cosima Stubenrauch, and Alexander Southan**

Hydrogel foams provide an aqueous environment that is very attractive for the immobilization of enzymes. To this end, functional polymers are needed that can be converted into hydrogel foams and that enable bioconjugation while maintaining high enzyme activity. The present study demonstrates the potential of biotinylated gelatin methacryloyl (GM10EB) for this purpose. GM10EB is synthesized in a two-step procedure with gelatin methacryloyl (GM10) being the starting point. Successful biotinylation is confirmed by 2,4,6-trinitrobenzene sulfonic acid and 4'-hydroxyazobenzene-2-carboxylic acid/avidin assays. Most importantly, a high methacryloyl group content (DM) is maintained in GM10EB, so that solutions of GM10EB show both a sufficiently low viscosity for microfluidic foaming and a pronounced curing behavior. Thus, foamed and nonfoamed GM10EB hydrogels can be prepared via radical crosslinking of the polymer chains. Within both sample types, biotin groups are available for bioconjugation, as is demonstrated by coupling streptavidin-conjugated horseradish peroxidase to the hydrogels. When assessing the substrate conversion rate r_A in foamed hydrogels by enzymatic conversion of 2,2′-azino-bis(3-ethylbenzothiazoline-6-sulfonic acid), a value for r_A 12 times higher than the value for nonfoamed hydrogels of the same mass is observed. In other words, r_A can be successfully tailored by the hydrogel morphology.

1. Introduction

Hydrogels are crosslinked, hydrophilic polymer networks that can absorb and retain large amounts of water or biological fluids.[1,2] In the past few years, hydrogels have received increased attention in the field of materials science due to their easily adjustable physical shapes,[3,4] their high water content,[5] and their biocompatibility.[6,7] Hydrogels are particularly interesting for fields of application such as drug delivery[8] or tissue engineering.[9,10] Furthermore, hydrogels have been investigated as solid support materials for the immobilization of enzymes with the aim of facilitating their recovery and reuse.[11–13] Enzymes are highly specific, yet, at the same time, delicate biocatalysts that are used in various fields, including food technology,[14] sensing,[15] or synthetic chemistry.[16] Due to their high water content, hydrogels provide a suitable physiological environment for enzymes, and are therefore believed to increase their stability.[17] To date, the most widely used methods to immobilize enzymes have been entrapment,[18] enzyme crosslinking,[19] covalent attachment,[20] or adsorption.[21] However, these methods entail several drawbacks, for example, the decrease of enzyme activity due to damaged protein functional groups, the limitation of mass transfer, or the leaching of enzymes from their supports.[22] Ultimately, this results in a decreased rate of enzyme substrate conversion per mass of solid support. A much more promising approach is the immobilization of enzymes via the biotin-streptavidin interaction, which provides strong attachment while avoiding additional chemical protein modification. For glucose dehydrogenase (GDH) immobilized via the biotin-streptavidin interaction it was found that after several days the enzyme activity of GDH was considerably higher compared to enzymes immobilized via crosslinking.[23] In addition, this technique is extremely versatile, because many biotin- or streptavidin-conjugated biomolecules are easily accessible.

Another aspect that influences the rate of enzyme substrate conversion is the shape of the hydrogel. Glucose oxidase immobilized inside poly(ethylene glycol) hydrogel membranes with a microtubular structure showed a rate of H_2O_2 formation, which was 1.5 times higher than that of nonstructured hydrogels.[24] This effect can be attributed to an increase in contact between substrate solution and encapsulated enzymes as a result of the larger surface area. However, since the materials used in that study were prepared by photolithography, only samples with a height of up to 800 µm could be studied. Much larger samples of porous materials can be prepared by means of foam templating.[25–27] In this approach, a liquid foam template is formed from an aqueous

F. Dehli, C. Stubenrauch
Institute of Physical Chemistry
University of Stuttgart
Pfaffenwaldring 55, 70569 Stuttgart, Germany
A. Southan
Institute of Interfacial Process Engineering and Plasma Technology
University of Stuttgart
Nobelstraße 12, 70569 Stuttgart, Germany
E-mail: alexander.southan@igvp.uni-stuttgart.de

The ORCID identification number(s) for the author(s) of this article can be found under https://doi.org/10.1002/mabi.202200139

DOI: 10.1002/mabi.202200139

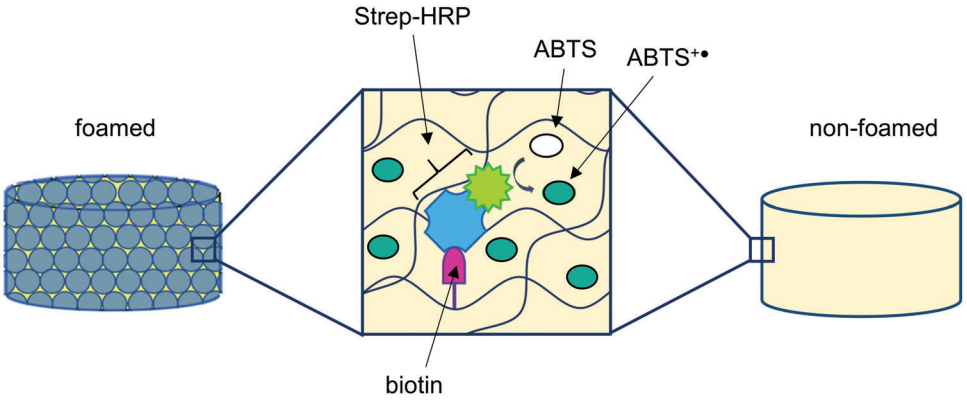

Figure 1. Schematic depiction of Strep-HRP immobilization and conversion of colorless ABTS to bluish-green $ABTS^{+}\bullet$ on foamed (left) and nonfoamed (right) samples.

polymer solution, and is subsequently solidified by crosslinking the polymer chains. During crosslinking, the structure of the liquid template is retained. In this way, the structure of the resulting porous materials, which are also called foamed hydrogels, can be tailored by adjusting the structure of the liquid template.[28–31] This has also been demonstrated for the generation of foamed hydrogels based on gelatin methacryloyl: By adjusting the structure of the liquid template via microfluidic methods, foamed hydrogels with defined pore diameters and pore opening diameters were generated.[32,33] Gelatin methacryloyl is a derivative of the biopolymer gelatin, which is generated by methacryloylation of amine and hydroxy residues in the polypeptide side chains and allows for radical crosslinking of the polymer chains.[34,35] The generation of gelatin methacryloyl hydrogels, as well as their physicochemical properties, have been examined thoroughly.[36–38] Moreover, it was demonstrated that available carboxyl groups in polypeptide side chains can be used for further polymer modification and that the biotin group can withstand the radical curing chemistry of gelatin methacryloyl.[39,40]

In this study, we aim to provide a method for preparing functional hydrogel foams based on gelatin methacryloyl that can further be used to immobilize enzymes via the biotin-streptavidin interaction. To this end, biotin groups are tethered to available carboxyl groups of gelatin methacryloyl via a two-step synthesis. This modification route leads to a dual functionalization of gelatin, which allows for processing by microfluidics as well as for reliable crosslinking via the methacryloyl groups. Furthermore, the generated polymers allow for the immobilization of streptavidin-conjugated enzymes after hydrogel formation (**Figure 1**). The influence of the hydrogel shape on the rate of substrate conversion will then be assessed by comparing foamed with nonfoamed hydrogels. To our best knowledge, the synthesis of biotinylated gelatin methacryloyl as well as the generation of foamed and nonfoamed hydrogels based on this polymer have not been examined to date. The present study is divided into three sections: (1) the synthesis and characterization of biotinylated gelatin methacryloyl, (2) the generation of foamed and nonfoamed hydrogels based on this polymer, and (3) the immobilization of a suitable enzyme, followed by the comparison of the enzyme substrate conversion for different hydrogel shapes. As a suitable enzyme, we chose horseradish peroxidase (HRP), which catalyzes the oxidation of colorless 2,2′-azino-bis(3-ethylbenzothiazoline-6-sulfonic acid) (ABTS) to bluish-green radical cations $ABTS^{+}\bullet$ (Figure 1). This allows easily assessing both enzyme immobilization and substrate conversion by means of UV/Vis spectroscopy.

2. Results and Discussion

2.1. Synthesis and Characterization of Biotinylated Gelatin Methacryloyl

To synthesize biotinylated gelatin methacryloyl, a two-step procedure with gelatin methacryloyl (GM10) being the starting point was developed (**Figure 2**). During the first reaction step, the carboxyl groups of GM10 are partially modified with ethylene diamine (EDA), using 1-ethyl-3-(3-dimethylaminopropyl)carbodiimide (EDC) as a coupling agent. In this way, primary amino groups are introduced into the polymer, which can then be used in the second reaction step to tether biotin moieties to the polymer backbone. The resulting polymers are denoted as GM10E (Step 1) and GM10EB (Step 2).

The first reaction step was performed following a procedure previously described by Claaßen et al.,[39] which was modified for the study at hand. Compared to the original procedure, less EDA and EDC were used to obtain a lower degree of modification. This was done to avoid a significant increase of the isoelectric point of GM10E compared to GM10, as it was described for higher degrees of modification.[39] An increase in IEP might cause significant differences in nonspecific protein adsorption between the gelatin derivatives during the immobilization of Strep-HRP. Furthermore, only a low amount of functional groups is required for immobilizing enzymes. Like in the previous report, EDA was added in large excess with respect to the coupling agent EDC to avoid EDC-mediated crosslinking of the polymer chains. Indeed, visual observation of GM10E solutions showed that the reaction product was completely soluble in both water and phosphate-buffered saline (PBS), i.e., that the polymer chains are not crosslinked. The content of primary amino groups (DE) in both GM10 and GM10E was quantified with the 2,4,6-trinitrobenzene sulfonic acid (TNBS) assay. The obtained values are listed in **Table 1**. In accordance with previous results,[39] no

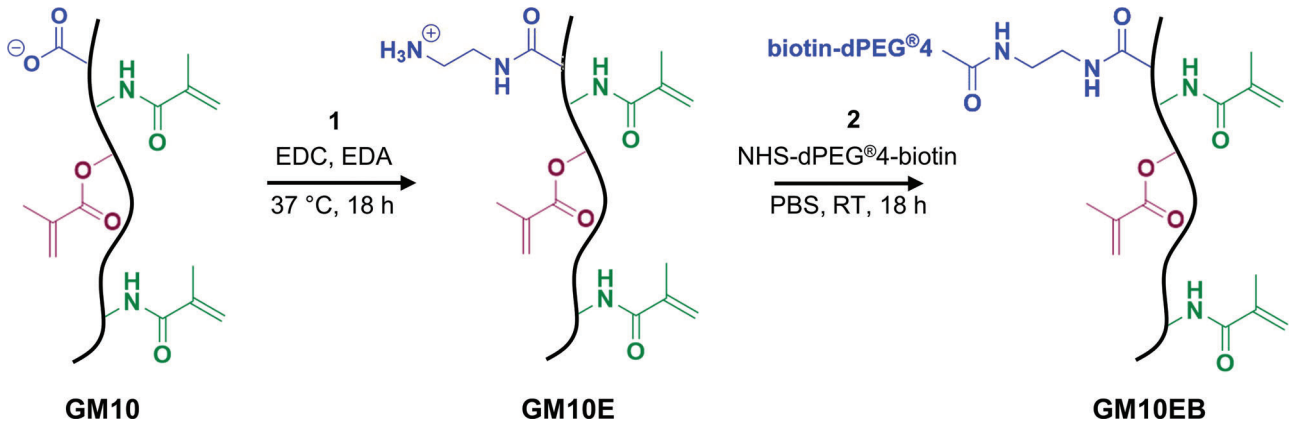

Figure 2. Reaction scheme for the biotinylation of gelatin methacryloyl (GM10). Step 1: Modification of GM10 with EDA, resulting in GM10E. Step 2: Biotinylation of GM10E with NHS-dPEG4-biotin, resulting in GM10EB.

Table 1. Methacryloyl group content (DM), amino group content (DE), and biotin content (DB) of the gelatin derivatives prepared in this study. The biotin content for GM10EB was determined indirectly with the TNBS assay and directly with the HABA/avidin assay. The errors are standard deviations, except for DB (TNBS) for which the error was derived from error propagation.

Gelatin derivative	DM [mmol g^{-1}]	DE [μmol g^{-1}]	DB (TNBS) [μmol g^{-1}]	DB (HABA/avidin) [μmol g^{-1}]
GM10	0.94	−2 ± 2	–	–
GM10E	0.97	71 ± 2	–	–
GM10EB	0.94	38 ± 1	33 ± 3	26 ± 2

amino groups were detected in GM10 (DE = −2 ± 2 μmol g^{-1}). By contrast, an amino group content of DE = 71 ± 2 μmol g^{-1} was obtained for GM10E, which corresponds to a modification of 6.3% of the total carboxyl groups or 0.8% of all amino acids.[36] The effect of this modification on the isoelectric point (IEP) of GM10E compared to GM10 was estimated using pK_a values of the amino acid residues according to Bjellqvist et al.,[41] similar to a previously described method.[39] According to this calculation, GM10 has an IEP of 4.2, whereas GM10E has an IEP of 4.4, which is only slightly higher. Consequently, significant differences in nonspecific protein adsorption are not to be expected with the PBS buffer used. In addition, the obtained GM10E was examined with ^{1}H-NMR spectroscopy (**Figure 3**, middle).

Compared to the ^{1}H-NMR spectrum of GM10 (Figure 3, top), two additional shoulders appear at 3.50 and 3.15 ppm, which belong to the two CH_2 groups of EDA.[39] The signals are considerably smaller compared to previously published work,[39] which is due to the lower DE in the study at hand. In addition, the methacryloyl group content (DM), which is important both for the formation of hydrogels via radical crosslinking as well as for the viscosity of the solutions used in microfluidic foaming, was determined from the ^{1}H-NMR spectra using sodium 3-trimethylsilyl-propionate-2,2,3,3-d4 (TMSP) as an internal standard (Table 1). It was found that the DM of GM10E remained virtually unchanged compared to GM10. This is in contrast to previously published work, where the DM was decreased by 23% after modification with EDA.[39] We attribute this observation to the

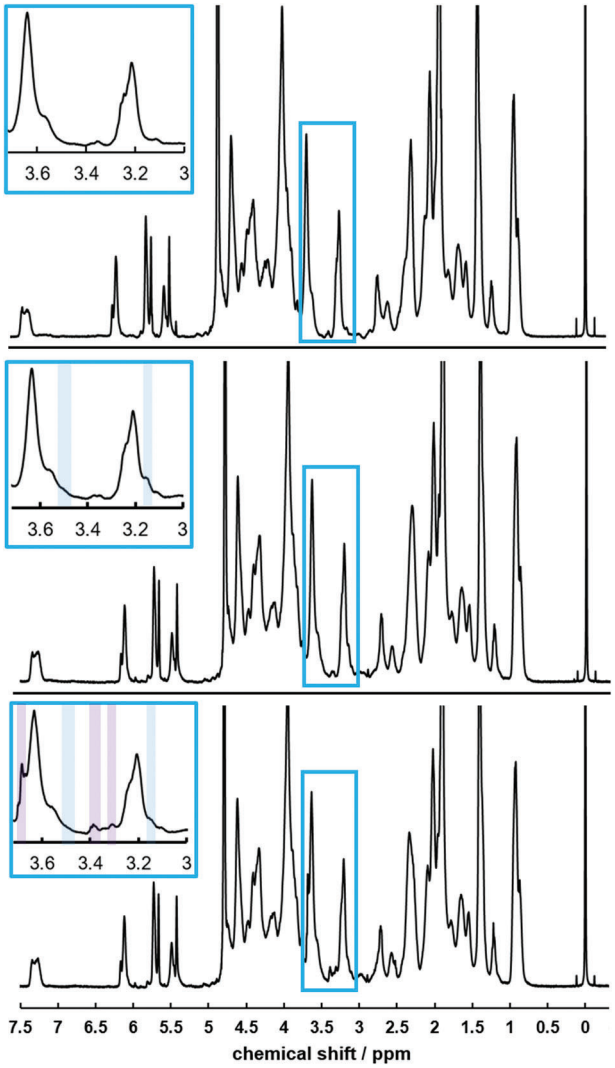

Figure 3. ^{1}H-NMR spectra of GM10 (top), GM10E (middle), and GM10EB (bottom) in D_2O. The insets display signals between 3.0 and 3.7 ppm. EDA-related signals are marked in blue, while dPEG4-related signals are marked in purple.

use of less EDA in the study at hand, which leads to fewer EDA-related side reactions, i.e., aminolysis or hydrolysis of methacryloyl groups.

In the second reaction step, GM10E was biotinylated by reaction of the amine groups with biotin-dPEG4-NHS (Figure 7). Visual observation of GM10EB solutions showed that the obtained polymer was completely soluble in PBS and demineralized water, yielding a slightly opalescent solution. Since a successful biotinylation of GM10E should lead to a lower amount of primary amino groups, the TNBS assay was again performed for GM10EB (Table 1). Indeed, it was found that compared to GM10E (DE = 71 ± 2 μmol g^{-1}), the amino group content in GM10EB is reduced by 47% to DE = 38 ± 1 μmol g^{-1}. Consequently, the biotin group content (DB) can be determined by subtracting the DE of GM10EB from the DE of GM10E. In this way, a biotin content of DB (TNBS) = 33 ± 3 μmol g^{-1} was obtained (Table 1). The difference corresponds to a total biotinylation of 3.2% of the carboxyl groups in GM10 or 0.4% of all amino acids. The IEP of GM10EB was again calculated as described above, and a slightly decreased IEP of 4.3 was found. In addition, the biotin content was also directly quantified with the 4'-hydroxyazobenzene-2-carboxylic acid (HABA)/avidin assay, where the molecule HABA is coordinatively bound to the protein avidin from which it is displaced after the addition of biotin. This process results in a color change at 500 nm, which can be used to quantify the biotin content. According to the HABA/avidin assay, the biotin content in GM10EB was DB (HABA/avidin) = 26 ± 2 μmol g^{-1} (Table 1), which is in good agreement with the value determined with the TNBS assay. The fact that DB (HABA/avidin) was slightly lower compared to DB (TNBS) might be ascribed to steric hindrance, as biotin in GM10EB is bound to a macromolecule. Another explanation could be that traces of coordinatively bound EDA were still present in GM10E, leading to an overestimation of the DE in GM10E and thus to an apparently higher DB (TNBS) in GM10EB. Furthermore, the reaction product was examined with ^{1}H-NMR spectroscopy (Figure 3, bottom). Comparing the ^{1}H-NMR spectra of GM10EB and GM10E, one sees that three new signals appear at 3.68, 3.39, and 3.31 ppm, which might either belong to the CH_2 groups of the tetra(ethylene glycol) spacer or might result from a shift in the signals of the CH_2 groups that belong to EDA. However, no quantitative conclusion can be drawn since the signals are quite small and are superimposed by other signals of the polymer. The DM of GM10EB was again determined as before (Table 1) and was found to be unchanged, confirming that a high degree of methacryloylation was maintained during the reaction.

Taken together, the results of the HABA/avidin assay and of the TNBS assay demonstrate a successful biotinylation of gelatin methacryloyl. This finding is supported by the respective ^{1}H-NMR spectra. Furthermore, a high degree of methacryloylation was maintained during polymer modification. Consequently, GM10EB solutions should have sufficiently low viscosities for microfluidic foaming and enough polymerizable groups for hydrogel generation.

2.2. Preparation and Characterization of Foamed and Nonfoamed Hydrogels

Nonfoamed hydrogels with all gelatin derivatives (GM10, GM10E, and GM10EB) could be prepared straightforwardly by UV-initiated curing of the respective polymer solutions. This confirms that the amino and biotin functionalization did not interfere with the radical crosslinking reaction. However, the visual appearance of the hydrogels was different between the three derivatives. For GM10EB, slightly opaque samples were obtained, while samples based on GM10 and GM10E were optically clear (Figure S4, Supporting Information). During several washing, drying, and re-swelling steps, the opacity in GM10EB samples did not change.

Table 2. Liquid flow rate ν_L and gas pressure p used to generate liquid foam templates from different gelatin derivatives, as well as bubble diameters D_b of liquid foam templates, pore diameters D_p, and pore opening diameters d_p of crosslinked samples. All listed errors are standard deviations.

Gelatin derivative	ν_L [μL min^{-1}]	p [mbar]	D_b [μm]	D_p [μm]	d_p [μm]
GM10	25	500	154 ± 2	147 ± 3	26 ± 6
GM10E	20	300	140 ± 3	128 ± 4	26 ± 6
GM10EB	20	290	154 ± 2	127 ± 3	31 ± 7

Furthermore, foamed hydrogels based on GM10, GM10E, and GM10EB could be prepared by means of foam templating, using very similar procedures for the different gelatin derivatives. To prepare foamed hydrogels, liquid foam templates with a defined bubble size D_b were generated by microfluidic foaming. The bubble diameter D_b of the liquid foam templates as well as the gas pressure p and liquid flow rate ν_L during microfluidic foaming are listed in **Table 2**.

Looking at D_b, one sees that liquid foams with very similar bubble diameters between 140 and 154 μm were obtained from solutions of different gelatin derivatives, i.e., the bubble size can be easily controlled in all cases by means of microfluidic foaming. However, small adjustments in p and ν_L were necessary, which indicates that the polymer modifications in GM10E and GM10EB entail a certain change in the physicochemical properties of their aqueous solutions. Irradiation of the liquid templates with UV-light yielded foamed hydrogels with interconnected pores, which were characterized with confocal fluorescence microscopy (**Figure 4**).[33] The values obtained for the pore diameters D_p and for the pore opening diameters d_p are listed in Table 2.

The pore opening diameter d_p is similar for all generated samples. However, comparing the bubble diameter D_b with the pore diameter D_p for different gelatin derivatives, one sees for all three gelatin derivatives that a shrinkage took place during crosslinking. The change of the pore diameter compared to the bubble diameter can be expressed as $\frac{D_b - D_p}{D_b}$. In fact, the pore diameter of GM10EB decreased by 18% compared to the bubble size of the liquid templates. For foamed hydrogels based on GM10 and GM10E, a decrease of 5% and 9% was observed, respectively. While a shrinkage of 5% is almost in the error range of the values for D_b and D_p, and might therefore be neglected, a shrinkage of 9% and 18% is more pronounced, which indicates that the additional modification of the polymer also results in a different behavior during crosslinking. This effect needs to be considered if foamed hydrogels with predefined pore diameters are required. For the present study, the achieved pore diameters allow comparing GM10, GM10E, and GM10EB hydrogel foams as well as comparing the foamed hydrogel with

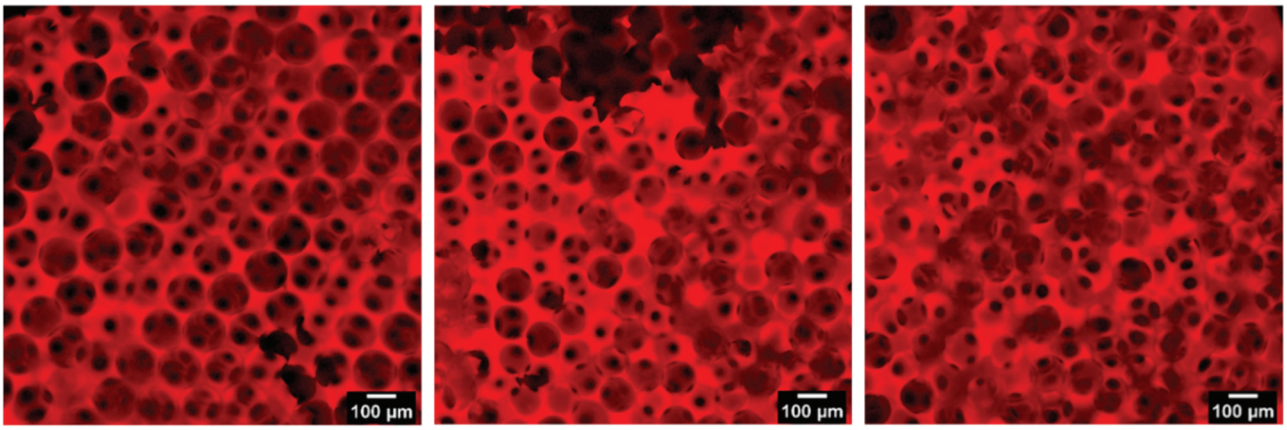

Figure 4. Confocal fluorescence microscopy images of foamed hydrogels stained with methylene blue, prepared with GM10 (left), GM10E (middle), and GM10EB (right).

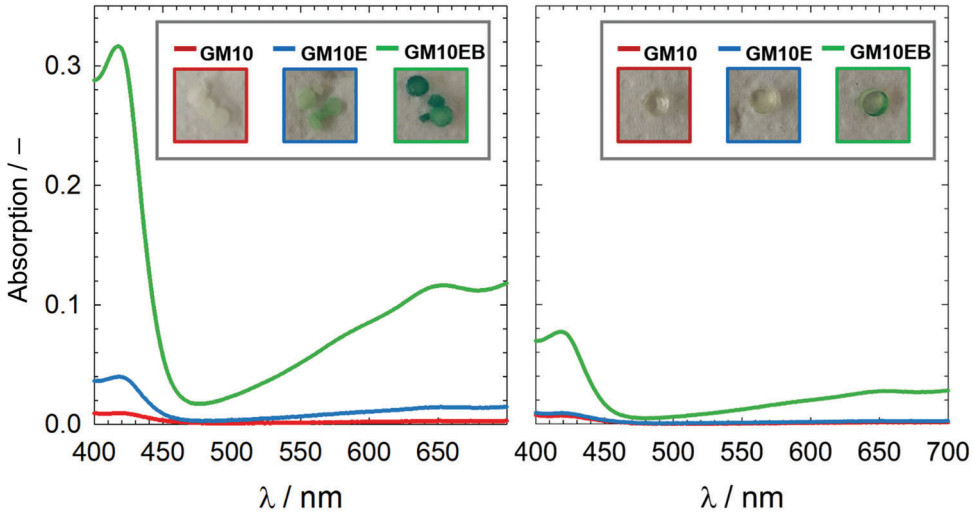

Figure 5. Representative UV/Vis–spectra of the supernatants after a reaction time of 30 min of the ABTS assay, using foamed hydrogels (left) and nonfoamed hydrogels (right). The reaction was stopped by the addition of 1% SDS solution. The insets show photos of the corresponding hydrogel samples.

their nonfoamed counterparts, as described in the following section.

2.3. Strep-HRP Immobilization and ABTS Conversion

2.3.1. Strep-HRP Immobilization on Different Gelatin Derivatives

To be able to immobilize streptavidin-conjugated enzymes effectively on the generated GM10EB hydrogels, the biotin groups have to be intact and accessible after radical crosslinking. In addition, it has to be shown that the biotin functionalization indeed leads to an enhanced immobilization of streptavidin-conjugated enzymes, i.e., that nonspecific adsorption is less important. To examine both aspects, both foamed and nonfoamed hydrogels prepared with GM10, GM10E, and GM10EB were exposed to a Strep-HRP solution, followed by several washing steps. Note that the conjugation of Strep-HRP to the biotin moieties was performed after hydrogel formation. This is because a large number of radicals are generated during crosslinking of the polymer chains, which can damage the protein structure of Strep-HRP. In addition, subsequent treatment of the generated materials involves both an organic solvent and elevated temperatures, which might also damage the protein structure. As Strep-HRP catalyzes the oxidation of colorless ABTS to bluish-green $ABTS^{+}\bullet$, the presence of Strep-HRP was determined with the ABTS assay. Both the obtained UV/Vi spectra of the supernatants after a reaction time of 30 min and the photos of the corresponding hydrogel samples are shown in **Figure 5**. Comparing the UV/Vis spectra of the supernatants for different gelatin derivatives, one sees that the absorption for GM10EB hydrogels (green lines) is considerably higher than the absorption for GM10 and GM10E hydrogels (red and blue lines) regardless of the sample morphology.

Accordingly, foamed and nonfoamed samples based on GM10EB have a pronounced green staining (Figure 5, insets), which indicates the presence of Strep-HRP. By contrast, the foamed and nonfoamed samples based on GM10 and GM10E (Figure 5, insets) appear either less stained or colorless. However, even though some samples appear completely colorless, the corresponding UV/Vis spectra of the supernatants show nonzero absorptions, which demonstrates that a certain degree of nonspecific protein adsorption takes place. However, since the difference between biotin-containing and biotin-free hydrogels is very pronounced, it can be concluded that Strep-HRP is predominantly immobilized via the biotin-streptavidin interaction and that nonspecific interactions can be neglected. Note that the amount of Strep-HRP present in the loading solution is only 4.7 pmol. By contrast, GM10EB samples contain ≈170 nmol of biotin, which was estimated from the biotin content determined with the TNBS assay (see Section 2.1). Due to this large excess of biotin moieties, Strep-HRP probably binds to biotin moieties at or close to the surface before it reaches the bulk of the hydrogel. This effect might also be enhanced by a hindered diffusion of Strep-HRP inside the hydrogel matrix due to its large hydrodynamic radius.[40]

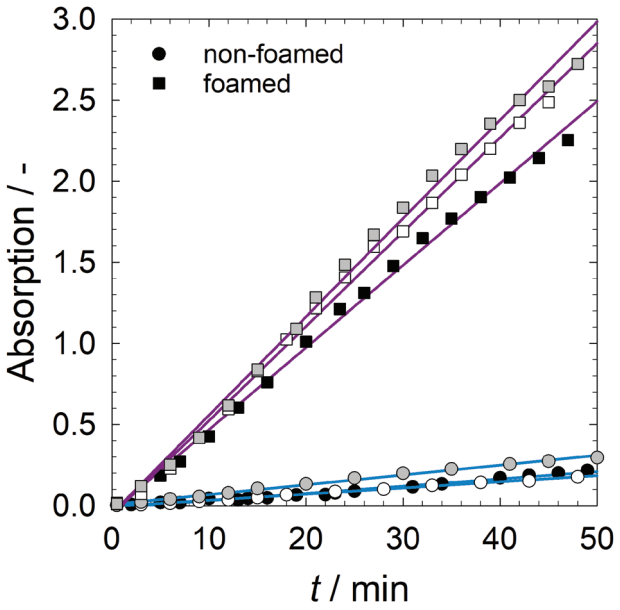

Figure 6. Time-dependent absorption of the ABTS solutions at 416 nm for foamed and nonfoamed Strep-HRP-loaded GM10EB hydrogels. Three independent measurements for each hydrogel type are shown.

2.3.2. ABTS Conversion Rate

Looking at Figure 5 and comparing the UV/Vis spectra of foamed samples with those of nonfoamed samples, one sees that the supernatants of the foamed samples display a greater color intensity. As the color intensity is directly related to the amount of generated $ABTS^{+}\bullet$, this observation indicates a difference in ABTS conversion rate for different hydrogel shapes. The conversion rate was quantified by following the time-dependent color development of the supernatants of foamed and nonfoamed GM10EB samples by means of UV/Vis spectroscopy. The corresponding absorptions of the ABTS solutions at 416 nm are shown in **Figure 6**.

The substrate conversion rate r_A was defined as the slope of the linear regression line. For the nonfoamed samples, a rate of $r_A = 0.29 \pm 0.07\ h^{-1}$ (mean ± standard deviation) was obtained, while the foamed samples had a twelve times higher rate of $r_A = 3.4 \pm 0.3\ h^{-1}$ (mean ± standard deviation). We ascribe the increased r_A values of the foamed samples compared to the nonfoamed samples to a different enzyme distribution within the hydrogel depending on the sample shape. As explained in Section 2.3.1, most of the enzyme is likely immobilized near the hydrogel surface. Consequently, the larger surface area of the foamed samples provides a larger amount of easily accessible binding sites during enzyme loading. This might lead to an increased amount of immobilized enzyme, which, in turn, results in an increased rate of substrate conversion. In addition, in the nonfoamed samples enzymes can generally be immobilized further away from the sample surface than in the foamed samples due to different characteristic diffusion lengths.[42] Thus, the shorter diffusion lengths inside the hydrogel matrix of the foamed hydrogels might cause a faster transport of both substrate and product to the immobilized enzyme and back into the supernatant, respectively, which leads to an increased substrate conversion rate. Note, however, that the diffusion path length of substrate molecules inside the hydrogel matrix is also largely influenced by their enzymatic conversion.[43] For glucose oxidase immobilized in poly(pyrrole) films it was demonstrated that substrate conversion only takes place in an active layer that is located 200–400 nm from the surface, which is due to the rapid substrate conversion. Further insight into the prevailing mechanism can be gained by quantifying the amount of immobilized Strep-HRP. However, commonly used methods, such as the quantification of Strep-HRP in the supernatant before and after hydrogel loading, cannot be easily applied as the porous structure impedes an accurate quantification of proteins in the washing solutions. Nevertheless, the obtained results demonstrate that the substrate conversion rate can be tailored by the shape of the hydrogel. The overall substrate conversion for $t \to \infty$ is however most likely determined by the enzyme amount itself and should be independent of the sample structure, provided that the enzyme is stable for sufficiently long times. Our findings are highly relevant for applications where the substrate conversion rate needs to be adjusted, such as in biocatalysis. Depending on the type of application, a lower or higher substrate conversion rate can be achieved by using foamed or nonfoamed hydrogels. However, one unequivocal advantage of the immobilization of enzymes on foamed hydrogels is that they allow for a more efficient use of the generated polymer since the bulk of nonfoamed samples does not contribute to the ABTS-conversion if the reaction takes place at the surface of the material. An increased surface area could also be generated by using microspheres or thin sheets based on GM10EB. However, compared to these materials, a foam offers several advantages. First of all, a foam is monolithic and can be easily prepared in various sizes and shapes. Compared to spheres or sheets, a foam might therefore be easier to handle in batch processes, as it can be removed from the reaction mixture in one piece. Compared to thin sheets, a foam might also provide improved mechanical stability.

3. Conclusions

We developed foamed gelatin-based hydrogels which improve the substrate conversion of immobilized enzymes by a factor of 12 compared to their nonfoamed counterparts. To achieve this aim we 1) synthesized—for the first time—biotinylated gelatin methacryloyl (GM10EB) by modifying the carboxylate groups in gelatin methacryloyl in a two-step procedure, 2) generated foamed and nonfoamed hydrogels based on this derivative, and 3) compared the substrate conversion of foamed and nonfoamed hydrogel after immobilizing the enzyme Strep-HRP via the biotin-streptavidin interaction. We showed that GM10EB solutions meet all requirements for a crosslinkable material with properties which are suitable for microfluidic foaming and simultaneously provide intact and accessible biotin groups. Future perspectives of foamed GM10EB hydrogels include the conjugation with other streptavidin-modified (bio)molecules. In this way, a versatile bioconjugation platform can be created that might be used not only in the field of enzyme immobilization but also for various other applications such as protein purification or biosensing. In addition, the substrate conversion rate could further be adjusted by tailoring the pore diameter of the samples via microfluidic techniques. Last but not least, the favorable GM10EB solution properties might facilitate the development of highly functional and individually structured hydrogel materials by means of other processing techniques like inkjet printing or two-photon polymerization.

4. Experimental Section

Chemicals: Methacrylic anhydride (MAAnh), EDA, PBS, EDC, NHS-dPEG4-biotin, TNBS solution 1 M in H_2O, glycine, HABA/avidin reagent, bovine serum albumin (BSA), and ABTS liquid substrate system were purchased from Sigma Aldrich (Germany). NaOH, NaCl, $NaHCO_3$, and ethanol absolute were purchased from VWR. Gelatin (type B, 232 bloom, bovine bone, batch #641819) was donated by Gelita (Germany). Plantacare 2000 UP was donated by Cognis (now BASF, Germany). D_2O was purchased from Merck (Germany) and eurisotop (UK). Perfluorohexane was purchased from abcr (Germany) and Sigma Aldrich (Germany). TMSP was purchased from Merck and deutero (Germany). The following chemicals were purchased from suppliers given in parentheses: 1 N hydrochloric acid (Titrisol, Merck, Germany), methylene blue (S3 chemicals, Germany) lithium phenyl-2,4,6-trimethyl benzoyl phosphinate (LAP, Carbosynth, UK), streptavidin-conjugated horseradish peroxidase (Strep-HRP, 1 mg mL^{-1}, abcam, UK), sodium dodecyl sulfate (SDS, lot 184257, fisher scientific, Germany). Dialysis was performed using dialysis membranes (molecular weight cutoff 12-14 kDa) from Medicell International Ltd. (UK). All chemicals except Strep-HRP were used as received. Upon arrival, Strep-HRP was thawed to prepare aliquots that were stored at −20 °C until further use.

Synthesis of Gelatin Methacryloyl: Gelatin methacryloyl (GM10) was synthesized and characterized according to a previously described procedure.[35] Briefly, gelatin type B (25.44 g) was dissolved in 250 mL of deionized water at 40 °C. Once the gelatin was completely dissolved, the temperature was adjusted to 37 °C and 14.3 mL MAAnh were added. The amount of added MAAnh corresponds to a tenfold molar excess with respect to the amount of free amine groups (0.35 mmol g^{-1} according to van den Bulcke et al.[44]). Thus, the corresponding derivative is denoted as GM10. The pH of the reaction mixture was kept between 7.0 and 7.4 by the addition of 4 M NaOH solution. After a reaction time of 5 h, the reaction mixture was filtrated using a sterile filter and stored at 8 °C for 2 d. Afterward, the crude product was dialyzed against deionized water for 5 d and then freeze-dried. A yield of 73%–77% was obtained. The degree of methacryloylation (DM) was determined by means of ^{1}H-NMR (500 MHz) in D_2O using TMSP as an internal standard.[35]

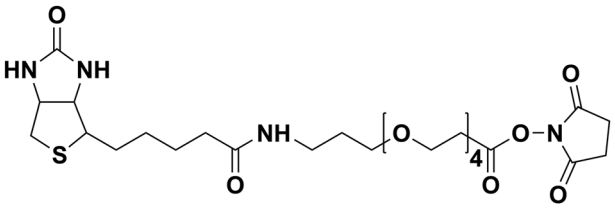

Figure 7. Chemical structure of NHS-dPEG4-biotin.

Synthesis of Gelatin Methacryloyl Aminoethyl: Gelatin methacryloyl aminoethyl (GM10E) was synthesized using a modified procedure described by Claaßen et al.[39] 4.0 g of GM10 (DM = 0.94 mmol g^{-1}) were dissolved in 80 mL of deionized water. 4 g of GM10 were estimated to contain a carboxyl group amount of 4.51 mmol (1 eq.), based on the carboxyl group content in gelatin type B (1.128 mmol g^{-1}).[36] The temperature was adjusted to 37 °C. 204 µL (184 mg, 3.05 mmol, 0.68 eq.) EDA was added and the pH of the solution was quickly adjusted to 4.5 using 1 N HCl. Subsequently, EDC (65 mg, 0.34 mmol, 0.075 eq.) was dissolved in 220 µL deionized water and was quickly added to the reaction mixture. After a reaction time of 18 h, the precipitate that was formed during the reaction was removed by filtering the crude product with a sterile filter. The filtrate was subsequently dialyzed against a 9 g L^{-1} sodium chloride solution for two days to remove any ionic impurities. Afterward, the product was dialyzed against deionized water for two days and then freeze-dried. The purified product (3.43 g, 86%) was analyzed by means of ^{1}H-NMR (500 MHz) in D_2O. In addition, the DM was determined using TMSP as an internal standard, as described above for gelatin methacryloyl.

Synthesis of Biotinylated Gelatin Methacryloyl: Biotinylated gelatin methacryloyl (GM10EB) was synthesized by dissolving 2.0 g GM10E (containing 0.14 mmol, 1 eq., amine groups) in 39 mL PBS at room temperature. Afterward, 113.7 mg (1.36 eq.) NHS-dPEG4-biotin was dissolved in 900 µL PBS and was quickly added to the reaction mixture. The chemical structure of NHS-dPEG4-biotin is shown in **Figure 7**. The solution was stirred for 18 h at room temperature. The crude product was filtrated with a sterile filter and the slightly opalescent solution was subsequently dialyzed against deionized water for 6 d. The visual appearance of the polymer solution was unaffected by several filtering steps as well as dialysis, thus indicating that the opalescence is not caused by impurities or bacterial contamination The purified product was again sterile filtered and subsequently freeze-dried. The purified product (1.72 g, 86%) was analyzed by means of ^{1}H-NMR (500 MHz) in D_2O. In addition, the DM was determined using TMSP as an internal standard as described above.

2,4,6-Trinitrobenzenesulfonic Acid Assay: The amine group contents of GM10, GM10E, and GM10EB were determined using the TNBS assay. Briefly, a 0.01% (w/v) TNBS solution was prepared by diluting a 1 M TNBS solution with 0.1 M $NaHCO_3$ (pH = 8.5). 250 µL of this solution were added to 500 µL of a 1 mg mL^{-1} gelatin derivative solution in 0.1 M $NaHCO_3$. The mixture was reacted at 37 °C under slight agitation in the dark. After 2 h of reaction time, 250 µL of a 10% SDS solution in deionized water as well as 125 µL of 1 N HCl were added. The assay was performed in triplicates. A standard curve was generated by performing the TNBS assay with glycine solutions at concentrations of 0, 0.026, 0.053, 0.106, and 0.132 µmol mL^{-1} in 0.1 M $NaHCO_3$. The absorbance of the solutions at 335 nm was measured using a Lambda 25 UV/Vis spectrometer from Perkin Elmer (Germany). Cuvettes with a path length of 2 mm were used. The obtained values are visualized in Figure S1 (Supporting Information).

4′-Hydroxyazobenzene-2-carboxylic acid/avidin Assay: The biotin content of GM10EB was determined using the HABA/avidin assay. Briefly, the commercially available HABA/avidin mixture was reconstituted in 10 mL of deionized water. 133 µL of a 0.55 mg mL^{-1} GM10EB solution in PBS was added to 1.2 mL of the HABA/avidin solution. The assay was performed in triplicates. A standard curve was generated by performing the

HABA/avidin assay with NHS-dPEG4-biotin solutions in PBS at concentrations of 0, 56, 111, 166, and 222 nmol mL^{-1}. The absorbance of the solution at 500 nm before and after the addition of GM10EB was measured using a Lambda 25 UV/Vis spectrometer from Perkin Elmer (Germany). Cuvettes with a path length of 5 mm were used. The obtained values are visualized in Figure S2 (Supporting Information).

Preparation of Nonfoamed and Foamed Hydrogels: All polymer solutions that were used for the preparation of nonfoamed and foamed hydrogels contained 0.14 wt% LAP and 20 wt% of GM10, GM10E, or GM10EB, respectively. The solutions used for preparing foamed hydrogels additionally contained 0.1 wt% of the surfactant Plantacare 2000 UP. Deionized water was used to prepare all solutions.

Foamed Hydrogels: To prepare foamed hydrogel samples, liquid foam templating was used, similar to a previously described procedure.[33] Briefly, liquid foam templates were generated using a homemade polycarbonate microfluidic chip with a flow-focusing geometry that had a constriction of 70 µm. The gas pressures p, as well as liquid flow rates vL that were used to push the polymer solutions through the microfluidic chip, are summarized in Table 2. To prevent coarsening, traces of perfluorohexane were added to the gas phase. The bubble sizes D_b of the generated liquid foam templates were analyzed according to a procedure described previously[32] and are summarized as well in Table 2. Cylindrical aluminum molds (2 cm in diameter and 2 mm in height) were used to collect the liquid foam templates. The liquid foam templates were immediately covered with a quartz glass pane and subsequently irradiated with UV-A light for 4.5 min, using a UV lamp (Omnicure Series 1500, 15% intensity) with a maximum emission spectrum between 360 and 370 nm. The light guide tip had a distance of 5 cm to the samples. Smaller hydrogel foam samples with a diameter of 4 mm and a height of 2 mm were punched out of the crosslinked material using a biopsy punch. The samples were washed for 3 d with deionized water and 1 d with ethanol. To enable long-term storage, the samples were subsequently dried at 60 °C until a constant weight was reached. To determine the pore diameter D_p and pore opening diameter d_p in the swollen state, three random samples were analyzed via confocal fluorescence microscopy. Staining and image analysis was done according to a procedure described before using the software ImageJ (version 1.53f51).[33]

Nonfoamed Hydrogels: The polymer solutions were poured into PDMS molds with a diameter of 4 mm and a height of 2 mm that were covered with a quartz glass pane. Curing, washing, and drying of the samples was identical to the procedure described for foamed hydrogels.

Loading of Streptavidin-Conjugated Horseradish Peroxidase onto Foamed and Nonfoamed Hydrogels: To load Strep-HRP onto hydrogel samples, the dried samples were swollen for 24 h in 2 mL PBS under slight agitation. The swelling solution was changed once. Afterward, the samples were placed in 500 µL of PBS solution containing 1 µg mL^{-1} Strep-HRP. After 24 h, the samples were washed with 500 µL of PBS until no relevant amount of Strep-HRP was detectable in the supernatant. The determination of Strep-HRP in the washing solutions is shown in Figure S3 (Supporting Information). Typically, the samples were washed for 48 h and the washing medium was changed six times. Furthermore, the stability of Strep-HRP at room temperature was assessed by performing ABTS assays with a 25 ng mL^{-1} Strep-HRP solution at different time points (Figure S5, Supporting Information). To minimize nonspecific protein adsorption, all solutions contained 0.1% (w/v) BSA. All experiments were performed at room temperature.

2,2′-Azino-bis(3-ethylbenzothiazoline-6-sulfonic Acid Assay: After sample loading, the ABTS assay was performed using two different approaches. To visualize the effect of the hydrogel functionalization on the Strep-HRP immobilization, foamed and nonfoamed hydrogels were prepared with the gelatin derivatives GM10, GM10E, and GM10EB and loaded with Strep-HRP as described above. Each sample was placed in 400 µL ABTS substrate solution under slight agitation. All samples had a mass between 5.1 and 5.3 mg. After 30 min, the samples were removed from the ABTS substrate solution. 400 µL of 1% SDS in deionized water were added to the solution to stop the reaction. The absorbance of the solution between 400 and 700 nm was measured using cuvettes with a path length of 2 mm.

To compare the ABTS conversion rate by Strep-HRP immobilized on foamed and nonfoamed hydrogels, GM10EB samples with a dry mass between 5.6 and 5.7 mg were placed in 2.5 mL ABTS substrate solution inside a cuvette with a path length of 10 mm. The cuvettes were sealed with a Teflon stopper and the absorbance of the solution at 416 nm was measured at different time intervals. Between measurements, the cuvettes were placed horizontally on an orbital shaker at 115 rpm. All experiments were performed at room temperature. To measure the UV/Vis spectra, a Lambda 25 spectrometer from Perkin Elmer (Germany) was used.

Supporting Information

Supporting Information is available from the Wiley Online Library or from the author.

Acknowledgements

F.D. gratefully acknowledges financial support by the Fonds der Chemischen Industrie via the Kékulé Stipend. A.S. would like to thank the Ministry of Science, Research and Arts of the Federal State of Baden-Württemberg (Germany) for financial support within the *Leistungszentrum Mass Personalization* (https://www.mass-personalization.de/).

Open access funding enabled and organized by Projekt DEAL.

Conflict of Interest

The authors declare no conflict of interest.

Data Availability Statement

The data that support the findings of this study are available from the corresponding author upon reasonable request.

Keywords

bioconjugation, enzyme immobilization, foam templating, horseradish peroxidase, porous hydrogel

Received: April 5, 2022
Revised: May 24, 2022
Published online:

[1] E. M. Ahmed, *J. Adv. Res.* **2015**, *6*, 105.
[2] B. N. A. Peppas, J. Z. Hilt, A. Khademhosseini, R. Langer, *Adv. Mater.* **2006**, *18*, 1345.
[3] H. Li, C. Tan, L. Li, *Mater. Des.* **2018**, *159*, 20.
[4] Y. S. Zhang, A. Khademhosseini, *Science* **2017**, *356*, 500.
[5] J. Zhu, R. E. Marchant, *Expert Rev. Med. Devices* **2011**, *8*, 607.
[6] J. Lai, *J. Mater. Sci.: Mater. Med.* **2010**, *21*, 1899.
[7] K. Miyamoto, M. Sasaki, Y. Minamisawa, Y. Kurahashi, H. Kano, S. I. Ishikawa, *J. Biomed. Mater. Res., Part A* **2004**, *70*, 550.
[8] S. Naskar, S. Sharma, K. Kuotsu, *J. Drug Delivery Sci. Technol.* **2019**, *53*, 101214.
[9] J. W. Nichol, S. T. Koshy, H. Bae, C. M. Hwang, S. Yamanlar, A. Khademhosseini, *Biomaterials* **2010**, *31*, 5536.
[10] A. Barbetta, M. Massimi, B. Di Rosario, S. Nardecchia, M. De Colli, L. C. Devirgiliis, M. Dentini, *Biomacromolecules* **2008**, *9*, 2844.
[11] S. Jo, S. Park, Y. Oh, J. Hong, H. J. Kim, K. J. Kim, K. K. Oh, S. H. Lee, *Biotechnol. Bioprocess Eng.* **2019**, *24*, 145.

[12] H. Tümtürk, N. Karaca, G. Demirel, F. Şahin, *Int. J. Biol. Macromol.* **2007**, *40*, 281.
[13] S. S. Betigeri, S. H. Neau, *Biomaterials* **2002**, *23*, 3627.
[14] J. Adler-Nissen, *Trends Biotechnol.* **1987**, *5*, 170.
[15] B. W. Park, D. Y. Yoon, D. S. Kim, *Biosens. Bioelectron.* **2010**, *26*, 1.
[16] A. Schmid, J. S. Doderick, B. Hauer, A. Kiener, M. Wubbolts, B. Witholt, *Nature* **2001**, *409*, 258.
[17] M. Bilal, T. Rasheed, Y. Zhao, H. M. N. Iqbal, *Biol. Macromol.* **2019**, *124*, 742.
[18] S. Park, S. H. Kim, K. Won, J. W. Choi, Y. H. Kim, H. J. Kim, Y. H. Yang, S. H. Lee, *Carbohydr. Polym.* **2015**, *115*, 223.
[19] R. A. Sheldon, R. Schoevaart, L. M. Van Langen, *Biocatal. Biotransform.* **2005**, *23*, 141.
[20] T. Li, S. Li, N. Wang, L. Tain, *Food Chem.* **2008**, *109*, 703.
[21] T. Jesionowski, J. Zdarta, B. Krajewska, *Adsorption* **2014**, *20*, 801.
[22] X. Lyu, R. Gonzalez, A. Horton, T. Li, *Catalysts* **2021**, *11*, 1211.
[23] T. Matsumoto, Y. Isogawa, T. Tanaka, A. Kondo, *Biosens. Bioelectron.* **2018**, *99*, 56.
[24] D. Choi, W. Lee, D.-N. Kim, J. Park, W.-G. Koh, *J. Chem. Technol. Biotechnol.* **2008**, *83*, 252.
[25] A. Barbetta, G. Rizzitelli, R. Bedini, R. Pecci, M. Dentini, *Soft Matter* **2010**, *6*, 1785.
[26] C. Colosi, M. Costantini, A. Barbetta, R. Pecci, R. Bedini, M. Dentini, *Langmuir* **2013**, *29*, 82.
[27] M. Costantini, C. Colosi, J. Jaroszewicz, A. Tosato, S. Wojciech, M. Dentini, P. Garstecki, A. Barbetta, *ACS Appl. Mater. Interfaces* **2015**, *7*, 23660.
[28] S. Andrieux, W. Drenckhan, C. Stubenrauch, *Langmuir* **2018**, *34*, 1581.
[29] S. Andrieux, W. Drenckhan, C. Stubenrauch, *Polymer* **2017**, *126*, 425.
[30] A. Testouri, M. Ranft, C. Honorez, N. Kaabeche, J. Ferbitz, D. Freidank, W. Drenckhan, *Adv. Eng. Mater.* **2013**, *15*, 1086.
[31] M. Costantini, J. Jaroszewicz, Ł. Kozoń, K. Szlązak, W. Święszkowski, P. Garstecki, C. Stubenrauch, A. Barbetta, J. Guzowski, *Angew. Chem., Int. Ed.* **2019**, *5*, 7620.
[32] F. Dehli, L. Rebers, C. Stubenrauch, A. Southan, *Biomacromolecules* **2019**, *20*, 2666.
[33] F. Dehli, A. Southan, W. Drenckhan, C. Stubenrauch, *J. Colloid Interface Sci.* **2021**, *588*, 326.
[34] E. Hoch, C. Schuh, T. Hirth, G. E. M. Tovar, K. Borchers, *J. Mater. Sci.: Mater. Med.* **2012**, *23*, 2607.
[35] C. Claaßen, M. H. Claaßen, V. Truffault, L. Sewald, G. E. M. Tovar, K. Borchers, A. Southan, *Biomacromolecules* **2018**, *19*, 42.
[36] L. Sewald, C. Claaßen, T. Götz, M. H. Claaßen, V. Truffault, G. E. M. Tovar, A. Southan, K. Borchers, *Macromol. Biosci.* **2018**, *18*, 1800168.
[37] L. Rebers, T. Granse, G. Tovar, A. Southan, K. Borchers, *Gels* **2019**, *5*, 4.
[38] L. Rebers, R. Reichsöllner, S. Regett, G. E. M. Tovar, K. Borchers, S. Baudis, A. Southan, *Sci. Rep.* **2021**, *11*, 3256.
[39] C. Claaßen, L. Rebers, M. H. Claaßen, K. Borchers, G. E. M. Tovar, A. Southan, *Macromol. Chem. Phys.* **2019**, *220*, 1900097.
[40] C. Claaßen, M. H. Claaßen, F. Gohl, G. E. M. Tovar, K. Borchers, A. Southan, *Macromol. Biosci.* **2018**, *18*, 1800104.
[41] B. Bjellqvist, B. Basse, E. Olsen, J. E. Celis, *Electrophoresis* **1994**, *15*, 529.
[42] F. Dehli, H. Poole, C. Stubenrauch, A. Southan, *ACS Appl. Polym. Mater.* **2021**, *3*, 5674.
[43] M. Marchesiello, E. Geniès, *J. Electroanal. Chem.* **1993**, *358*, 35.
[44] A. I. Van Den Bulcke, B. Bogdanov, N. De Rooze, E. H. Schacht, M. Cornelissen, H. Berghmans, *Biomacromolecules* **2000**, *1*, 31.

Macromolecular Bioscience

Supporting Information

for *Macromol. Biosci.*, DOI 10.1002/mabi.202200139

New Gelatin-Based Hydrogel Foams for Improved Substrate Conversion of Immobilized Horseradish Peroxidase

*Friederike Dehli, Cosima Stubenrauch and Alexander Southan**

Supporting information

New gelatin-based hydrogel foams for improved substrate conversion of immobilized horseradish peroxidase

*Friederike Dehli, Cosima Stubenrauch, Alexander Southan**

1. TNBS Assay

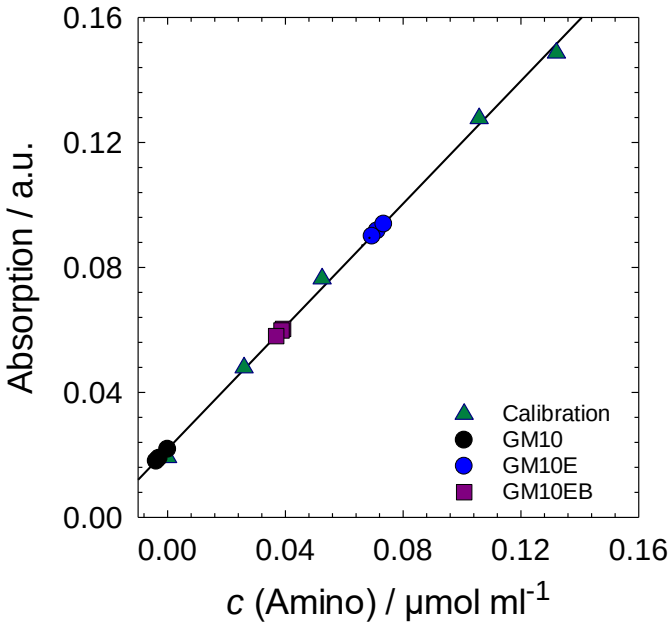

Figure S1: Standard curve (green) and obtained values for GM10 (black), GM10E (blue) and GM10EB (purple).

2. HABA/Avidin Assay

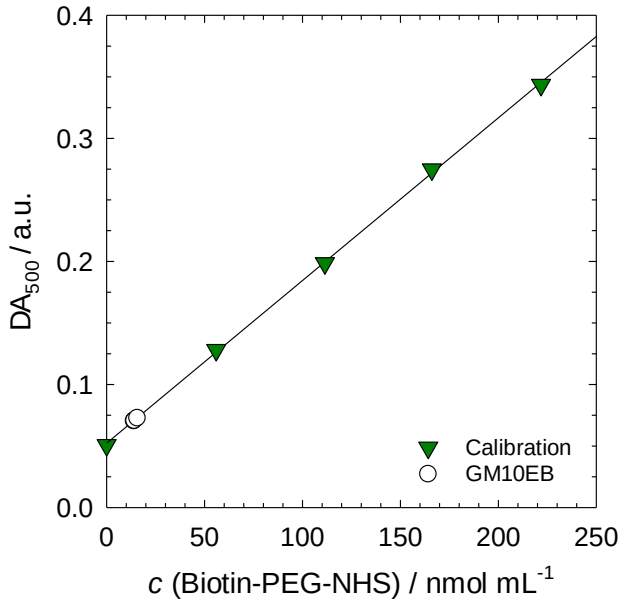

Figure S2: Standard curve (green) and obtained values for a 0.55 mg mL^{-1} GM10EB solution in PBS (white)

3. Determination of Strep-HRP in Washing Solutions

The presence of Strep-HRP in the washing solutions was determined by performing the ABTS assay after each washing step. Briefly, 200 µL of washing solution were added to 200 µL of ABTS substrate. The solutions were thoroughly mixed and placed on an orbital shaker (90 rpm) in the dark. After 30 min of reaction time, the reaction was stopped by adding 400 µL of 1 % SDS in deionized water. The absorption of the solution at 416 nm was measured in cuvettes with a pathlength of 2 mm using a *Lambda 25* spectrometer from *Perkin Elmer* (Germany). The absorption of the solutions at 416 nm plotted against the number of washing steps is displayed in Figure S3. All experiments were conducted at room temperature and all of the six washing steps were performed within 48 h.

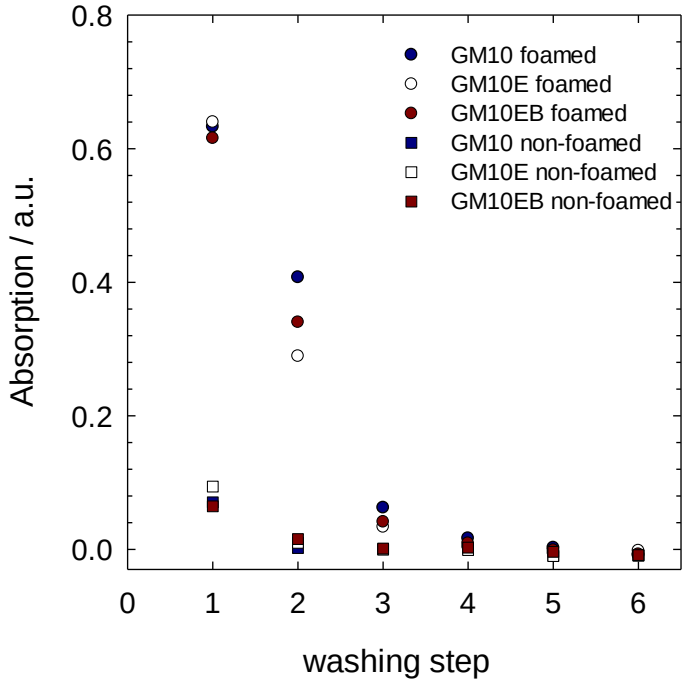

Figure S3: ABTS-absorption at 416 nm of solutions after each washing step.

It was observed that the absorption for foamed samples is much higher, i.e. the content of Strep-HRP in the washing solutions is larger compared to non-foamed samples. This is due to the loading solution being still present in the pores of the foamed hydrogels after the first washing steps. Nevertheless, the absorption rapidly decreased for both foamed and non-foamed samples and for all gelatin derivatives with increasing number of washing steps. After the 5th and 6th washing step, the absorption for all samples is close to zero. Thus, it was concluded that no relevant amount of Strep-HRP is present in the washing solutions and that the washing steps are sufficient to remove unbound Strep-HRP.

4. Photos of Nonfoamed Hydrogels

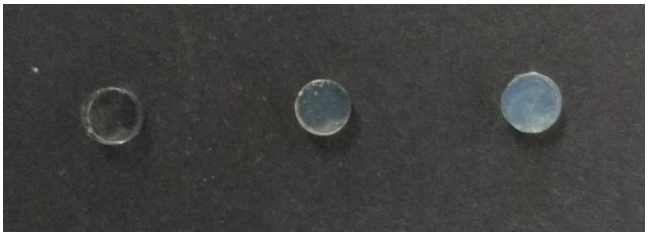

Figure S4: Photos of nonfoamed hydrogels based on GM10 (left), GM10E (middle) and GM10EB (right) swollen in PBS.

5. Stability of Step-HRP

The stability of Strep-HRP was assessed by performing ABTS assays with a 25 ng mL^{-1} Strep-HRP solution in PBS, containing 0.1 % (w/v) BSA at different time points. All experiments

were performed at room temperature. Briefly, 200 µL of the 25 ng mL^{-1} Strep-HRP solution in PBS were added to 200 µL of ABTS substrate. The solutions were thoroughly mixed and placed on an orbital shaker (90 rpm) in the dark. After 30 min of reaction time, the reaction was stopped by adding 400 µL of 1 % SDS in deionized water. The absorption of the solution at 413 nm was measured in cuvettes with a path length of 2 mm using a *Lambda 25* spectrometer from *Perkin Elmer* (Germany). Between measurements, the Strep-HRP solution was stored at room temperature. The absorption of the solutions at 413 nm plotted against the storage time of the Strep-HRP solution is displayed in Figure S5.

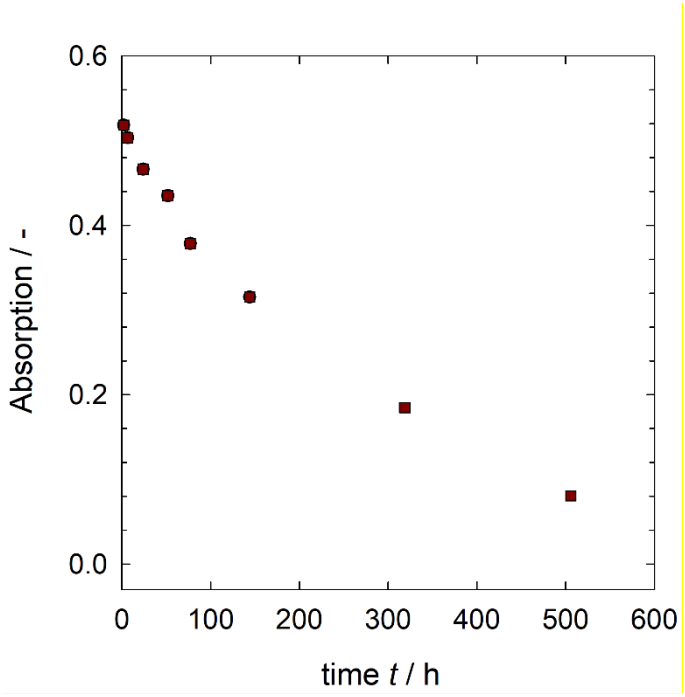

Figure S5: Absorption at 413 nm after ABTS conversion in 25 ng mL^{-1} Strep-HRP solutions plotted against the storage time. The Strep-HRP solutions were stored at room temperature.

As can be seen, the amount of converted ABTS decreases with increasing storage time of the Strep-HRP solution. However, no relevant reduction in enzyme activity is to be expected for the experimental times used in this study (< 1 h).